ARTI Report No. 20140-01

ELECTROSTATIC FORCES AND WATER SPRAYS FOR TEMPERATURE, HUMIDITY, AND INDOOR AIR QUALITY CONTROL

Final Report

Date Published – September 2008

Joshua L. Hensley and James E. Bryan

UNIVERSITY OF MISSOURI
Mechanical and Aerospace Engineering Department
E2411 Lafferre Hall
Columbia, MO 65211

Prepared for

AIR-CONDITIONING, HEATING, AND REFRIGERATION TECHNOLOGY INSTITUTE, INC
2111 Wilson Blvd, Suite 500, Arlington, Virginia 22201-3001

DISCLAIMER

This report was prepared as an account of work sponsored by the Air-Conditioning and Refrigeration Technology Institute, Inc. (ARTI). Neither ARTI, its research program financial supporters, or any agency thereof, nor any of their employees, contractors, subcontractors or employees thereof - makes any warranty, expressed or implied; assumes any legal liability or responsibility for the accuracy, completeness, any third party's use of, or the results of such use of any information, apparatus, product, or process disclosed in this report; or represents that its use would not infringe privately owned rights. Reference herein to any specific commercial product, process, or service by trade name, trademark, manufacturer, or otherwise, does not necessarily constitute nor imply its endorsement, recommendation, or favoring by ARTI, its sponsors, or any agency thereof or their contractors or subcontractors. The views and opinions of authors expressed herein do not necessarily state or reflect those of ARTI, its program sponsors, or any agency thereof.

Funding for this project was provided by (listed alphabetically):
- Air-Conditioning & Refrigeration Institute (ARI)
- Copper Development Association (CDA)
- Heating, Refrigeration and Air Conditioning Institute of Canada (HRAI)
- New York State Energy Research and Development Authority (NYSERDA)

CONTENTS

LIST OF FIGURES

LIST OF TABLES

NOMENCLATURE

A	area
b	radius of air volume around drop
C	capacitance, coefficient
C_d	drag coefficient
c	vapor concentration, absolute humidity
c_p	specific heat, heat capacity
D_v	binary diffusion coefficient
E	energy
E	electric field magnitude
$\mathbf{E}$	electric field vector
E_{xd}	rate of exergy destruction
$\mathbf{e}_f$	flow exergy
F	force
$\mathbf{F}$	force vector
g	gravitational constant
H	enthalpy, total
h	convection heat transfer coefficient or enthalpy
h_D	mass transfer coefficient
h_r	radiation heat transfer coefficient
h_f	enthalpy of liquid
h_{fg}	latent heat of vaporization
i_c	spray cloud current
k_{air}	thermal conductivity
L_c	coherent length of spray
l_e	length of electrode
M	molecular weight
M	mass, molar mass
m	mass
n	number in sample
P	pressure
p	pressure
q	charge
q	heat energy
Q	charge
Q	heat energy, total
RH	relative humidity
S_x	sample standard deviation
s	entropy
SHR	sensible heat ratio
T	temperature
t	time
U, U_∞	free stream velocity
u	velocity in x-direction, internal energy
V	volume, voltage, velocity
v_s	velocity of spray sheet

v_f	specific volume of liquid
v	specific volume, general
W	work, humidity ratio
R	radial distance
r_d	drop radius
r_e	radius of electrode
r_p	radius to particle
w_s	width of spray sheet
x	x distance
x_s	x-spacing
y	y distance
y_s	y-spacing
z	z distance

Non-dimensional numbers

Le	Lewis number
Nu	Nusselt number
Pe	Peclet number
Pr	Prandtl number
Re	Reynolds number
Sc	Schmidt number
Sh	Sherwood number

Greek symbols

μ	dynamic viscosity, mean
ν	kinematic viscosity
ρ	density (also charge density)
ε	effectiveness
ε_o	permittivity
ω	humidity ratio
α	thermal diffusivity
θ	temperature
τ	time constant, non-dimensional time
φ	angular reference
σ	conductivity, surface tension, std. dev.

Subscripts

CV	control volume
db	dry bulb
v	vertical
h	horizontal
p	partical
v	vapor
l	liquid

d	drop, liquid phase
e	exit (as in exiting the C.V.)
f	fluid, liquid
in	entering
w	water
wb	wet bulb
∞	free stream
a	air or air/vapor in free stream
o	initial, or reference to dead state
out	leaving
s	surface, saturated
avg	average
bar	barometric
ps	power supply
orif	orifice
i, *i*	initial or in (as in entering the C.V.)
moist	containing water
H_2O	water

Abbreviations

COP	Coefficient of performance
DOE	Department of Energy
DCHX	Direct Contact Heat Exchanger
LFE	Laminar Flow Element
RFT	Remote Flow Transmitter
UA	Overall heat transfer coefficient

EXECUTIVE SUMMARY

The overall scope of this research was to investigate using electrostatic forces and water sprays for temperature, humidity and indoor air quality control. With this knowledge, the feasibility of a direct contact heat exchanger (DCHX) for small-scale commercial and/or residential applications can be assessed. The research was divided into three areas: 1) spray charging; 2) spray collection; and 3) heat and mass transfer of the spray. The following is a summary of the results in these three areas.

It was initially hypothesized that there are two primary reasons to charge the spray used in the direct contact process: to assist in droplet collection and to increase the air cleaning capabilities. To test these hypotheses, a reliable method was needed to charge the sprays. The strategy follows that if the spray can be charged, then simple experiments will show how much charge can be imparted on the average drop. This would allow for more accurate modeling when calculating the force due to an electric field versus the drag or momentum force. The initial research effort focused on temperature and humidity control studies. Indoor air quality control study was not part of the initial effort and were planned as future research, if the temperature and humidity control studies were successful.

A simple induction charging nozzle was developed for use with a fully hydraulic, flat fan, water spray. Charging was achieved by passing the sheet portion of the spray between two, relatively small diameter, parallel electrodes to determine the optimum location resulting the maximum deposition current on a collection screen producing the maximum droplet charge. A simple, analytic model was also developed to gain fundamental knowledge about the relationships between the variables that determine the deposition current (x and y electrode position, power supply voltage, and nozzle pressure), and to aid in the prediction of the optimum electrode location. The model and experimental data agreed on the linear relationship between the applied voltage and the deposition current, and a nonlinear relationship between the nozzle operating pressure and deposition current. Differences between the model and experiments occurred as the electrode to electrode spacing (x-direction) decreased. Droplet impact issues were revealed from experiments as the x-spacing became very small resulting in decreased deposition current. This occurred for electrode spacing less than 20 mm when the electrodes were greater than 35 mm from the spray nozzle.

The spray momentum of the droplets was significantly greater than the Coulomb force produced on the droplets even though optimum charging was achieved on the water droplets for the flows, pressures and nozzles used in this study. Thus, the electrostatic force had no impact on controlling the droplet collection. However, it is important to note that the smallest spray nozzle used in the study produced average droplet sizes of 475 microns and analysis showed that the electrostatic force could have an impact on droplets in the ~100 micron range for the conditions experienced in this study.

The spray momentum and the small test section (15cm x 15 cm) used in this study resulted in significant droplet rebound. The best method for this size test section was to rotate the section 45^{o}, use a flat fan spray nozzle, and remove a section of the false wall separating the collection tray from the air stream. This minimized droplet rebound. The test section used in this study was limited in size due to the test capabilities of the wind tunnel system. The spray chamber for practically sized systems will be larger to allow for greater energy transfer and better spray collection.

The heat and mass transfer of the water spray was studied experimentally and analytically. An experimental apparatus and test methods were first developed to support the creation of a semi-empirical overall heat transfer coefficient correlation and numeric model which quantified the heat and mass transfer from a water spray. A low speed, temperature and humidity controlled wind tunnel was constructed to test a prototype DCHX test section which was 15 cm x 15 cm square, 60 cm long, and utilized flat-fan water sprays as the working fluid/surface. In the tests, the air face velocities were run at 1 and 3 m/s, air temperatures are 26.7 °C and 33 °C with relative humidity ranging from 32 to 68%, while water flow rates were varied from 3.0 to 5.5 kg/min at temperatures of 5 °C and 10 °C. The water spray nozzles used were varied, effectively varying the average drop size or spray surface area for a given flow rate. For the experimental conditions investigated, the following conclusions can be made: 1) heat transfer rate increases as water mass flow increases, relative humidity increases, and drop size decreases; 2) in general dehumidification and cooling occur for relative humidity greater than 56% for all conditions tested with greater heat and mass transfer occurring with increasing water flow rate, decreasing water temperature, and decreasing droplet size; and 3) humidification and sensible cooling increase for relative humidity less than 56% for all conditions tested with increasing water flow rate and decreasing droplet size.

A *UA* correlation was developed that was a function of the mean drop size, the free stream relative humidity, and the water flow rate – the three key driving variables for the system performance. The correlation was derived from a fundamental analysis of the system, the heart of which centers on forced convection on a single drop. The overall heat transfer correlation was found to capture the general behavior of the system, but in its present form, it does not lend itself for wholly accurate predictions of the overall heat transfer coefficient. A full spray model was also developed. The numeric model was found to trend well with the experimental results; however, the absolute magnitude of the simulated heat transfer was on average 50% less than what was measured in the experiments. Analysis of the model, correlation, and experiments revealed the most likely sources of the discrepancies were due to droplet entrainment and moisture accumulation in the test section, which was not accounted for in the correlation or model.

The experimental data is for discrete points of interest over a certain range of conditions, thus, there are gaps in the information. The correlation, which has some, but not all, of the experimental phenomenon incorporated, lends itself to bridge some of the gaps between the experimental data points. The analytic correlation further lends itself to be manipulated algebraically so that independent variable ranges may be identified for a desired overall heat transfer coefficient. Of course, this overall heat transfer does not fully identify the exit state of the air, so the model then becomes useful as it more precisely defines the details of the heat transfer problem. The model does not lend itself as an initial investigation tool given the associated computational intensity; however, the correlation can be rapidly applied for a first order analysis.

To design a direct contact heat exchanger (DCHX) for small-scale commercial and/or residential applications the system scale needs to be increased from what was studied in this research. Greater volumetric air flow is needed, which is easily achieved by increasing the cross section area. Ideally, the cross section should be increased in order to keep the face velocity low, a requirement to keep from entraining drops. However, with a larger cross section, the drops traverse a larger distance and thus take longer to exit the air stream. For example, smaller drops were found to produce the best results for cooling and dehumidification, but as the section increases in size smaller drops could start to evaporate if they are kept in the air stream too long. From the results and models presented in this work one could evaluate what average drop size and inlet water conditions could produce the required cooling and dehumidification (or humidification) for a given set of practical air section dimensions and inlet air conditions.

1.0 INTRODUCTION

1.1 Purpose

It has been argued that energy is the key research subject as it is the basis of all civilization and life as we know it [1]. Not surprisingly, there is great interest in finding new energy sources. However, new energy sources tend to be hard to come by, so most engineering work focuses towards conserving energy through improvement of end use technology. The question naturally follows: where would investments in technology and product development be most beneficial? One area would be the largest energy consumers, as they would have the largest net impact on total energy consumption. The Department of Energy in 1999 did this and investigated U.S. commercial building energy consumption [2]. The results of the study were clear: 30% (the largest single share) of the buildings' energy was consumed for HVAC purposes, and of the HVAC systems, unitary (roof top style) air conditioning systems consumed 54% of that energy share. For that reason, the DOE then compiled a list of the top 55 most promising technologies for improving HVAC efficiency. The direct contact heat exchanger ranked second with an estimated 35% increase in system coefficient of performance by their estimates. However, limited research has been performed in the area of direct contact heat exchangers (DCHXs) to compete with traditional coil style heat exchangers. Accordingly, the purpose of this work serves to provide a basis for DCHX design and implementation.

1.2 Scope

The DCHX in question is loosely based on air washer and evaporative cooler technology. The basic principles are the same: water is sprayed into direct contact with air, and energy transfers due to differences in temperature and/or vapor pressure. In the simplest case of evaporative cooling, warm air is sensibly cooled and humidified as its energy is released to provide the latent energy consumed when the water evaporates. This process is effective enough when the incoming air has a low degree of saturation. However, the process is so sensitive to the air's humidity content that this form of cooling is not feasible in most geographic regions. [3] Consequently, these efforts are focused on developing a true *heat exchanger*, having the capacity to work in a much wider range of applications.

Preliminary investigation [4][5] shows that a heat exchanger that sprays the working fluid (water) into direct contact with moist air has the potential to not only cool the air, but also dehumidify and clean the air as well, if properly employed. Thus, the resulting DCHX would be attractive as it is a true air conditioner, conditioning not only for temperature, but for humidity levels and indoor air quality. There are many facets to developing this heat exchanger, a number of which have been addressed in previous research and feasibility studies [4][5][6][7]. Without even considering the physical details of a DCHX design, many independent variables govern the ability to control temperature and humidity. Before design and development of a DCHX can take place, insight into the heat and mass transfer process must be gained to determine the performance of the system under various conditions.

Note that the approach taken in this work is unique in that it focuses on understanding the coupled heat and mass transfer and drop dynamics. Most air washers or cooling towers simply spray copious amounts of water into an air stream allowing the system to come to a completely saturated thermal equilibrium state. The strategy with the proposed DCHX will be to take advantage of the spray/chamber geometry and other operational variables (flow rates and temperatures) to be able to operate like a conventional cooling coil (that dehumidifies the air as it cools). The key here is recognizing that dehumidification only takes place for only part of the droplets lifetime. To illustrate this point, consider the following simple explanation that reveals the challenge, and thus, the purpose and importance of the background work with respect to development of a DCHX.

Imagine a water droplet entering a moist air stream. If the drop's temperature is below the dew point temperature of the air, a thermal boundary layer will form around the drop (neglecting interfacial phenomena). The air near the drop will be cooled below its dew point temperature and the excess moisture will condense on the nearest nucleation site, which happens to be the drop itself. In order to reach thermodynamic equilibrium, the droplet heats and grows as the surrounding air volume cools and dries. At this point, the air has been cooled and dehumidified, and if dehumidification was the goal, the process should be stopped by removing the drop from the air – consequently removing the excess moisture it has gained. If the drop is not removed, as it reaches thermal equilibrium, differences in vapor pressure between the drop and surrounding air will drive the drop to evaporate.

The latter scenario would constitute a loss of system control as the DCHX is reduced to a simple evaporative cooler. One needs to be able to control the droplets and remove them at the right time to make a DCHX work, which leads to the following question. What is the right time to remove the drop from the air stream and how does that time correspond to distance traveled, inlet temperatures, humidity, air velocity, drop size, etc.? Reduction of experimental data allows for the creation of correlations that answer these questions, ultimately guiding the development of a new kind of direct contact heat exchanger. Thus, the key objective of this work is to develop a functional relationship between the operational variables in a DCHX which can be used to guide future heat exchanger design.

2.0 BACKGROUND

The initial investigation into this problem started at the University of Missouri – Columbia in 2003 with an undergraduate Honors project, which entailed the design and construction of a low speed wind tunnel for use in later DCHX experimentation [4]. With the tunnel construction underway, a feasibility study was launched which evolved into a senior capstone project [5]. Based on the findings of that study, the DCHX concept showed promise and thus the decision was made to take the project to the next level as a Master's Thesis project that was completed in August of 2004. The results of the Master's project highlighted the key variables to consider when developing the DCHX at the Doctoral research level. The following sections include the key details and findings of these projects.

2.1 Supporting Work and Conclusions

2.1.1 Capstone Work – The Feasibility Study

The undergraduate capstone project investigated the feasibility for using a direct contact system for residential applications. After developing two rough designs, first cost and operational cost estimates were made. As the estimates were exceptionally conservative, the direct contact systems first cost was higher that a comparable sized system using direct expansion coils. The operational costs were projected to be lower than a conventional system, basically due to the DCHX systems calculated 30% higher system coefficient of performance (COP). The COP calculations were formulated using experimental data [7] to develop a *UA* value for the proposed system.

Preliminary experiments were conducted to gather data that were used in a factorial and ANOVA analysis. Analysis of the results reveals that the nozzle size (effectively, the drop size) used played the most significant role in determining the heat exchanger effectiveness (taken as the sensible effectiveness: q/q_{max}), followed by the water temperature, and then the air temperature.

The final consensus was that the DCHX system was technically feasible; however, it would require a substantial amount of engineering before it could be marketable.

2.1.2 Master's Work – The Single Drop Model

2.1.2.1 Synopsis

It was clear from the experiments in the feasibility study that two things needed immediate attention: droplet control was a critical factor and more insight into the drop/air interaction was needed.

The droplet control factor would be addressed primarily with a redesign of the test section, but also with an investigation into assisted collection via charged drops. The concept of charging the drops was thought to benefit the system in two ways. First, it was hypothesized that the space charge generated by the drops would aid in transporting the droplets to a grounded target surface in the collection tray. Secondly, it was hypothesized that the charged drops would act to supplement the inherent air cleaning characteristics as they could act as small electrostatic air cleaners. This would aid in collecting non-wetting media like oil mists, which air washers do not collect well. In any case, this additional electrostatic force was to be accounted for when modeling the drops.

The fundamental insight into the heat and mass transfer process was gained through the development of a numeric model. This model is detailed in [8], and will only be highlighted here. The model, which was adapted from one found in a then current journal [19], is based on a simple quasi-steady state energy balance between a drop of a given radius, r_d, and a volume of moist air of radius b surrounding the drop. The model consists of six ordinary differential equations which were solved simultaneously using MatLab's built in 'ode23s' solver. The variables in question are the drop's x and y position (and velocity), temperature, and radius, as well as the free stream temperature and vapor concentration, respectively:

$$\frac{d^2x}{dt^2} = \frac{\left(\frac{1}{2}\rho_{air} C_d A\left(\mathrm{U} - \frac{dx}{dt}\right)\left|\mathrm{U} - \frac{dx}{dt}\right| + \frac{Cv^2}{R}\cos\phi\right)}{m} \tag{1}$$

$$\frac{d^2y}{dt^2} = -g + \frac{\left(-\frac{1}{2}\rho_{air} C_d A\left(\frac{dy}{dt}\right)\left|\frac{dy}{dt}\right| + \frac{Cv^2}{R}\sin\phi\right)}{m} \tag{2}$$

$$\frac{dT_d}{dt} = \frac{3}{2\rho_w c_{pw} r_d^2}\left\{ k_{air}\,\mathrm{Nu}\left(T_\infty - T_d\right) - h_{fg} D_v \mathrm{Sh}\left(c_s - c\right)\exp\left[\frac{-3 r_d D_v t}{\left(b - r_d\right)^3}\right]\right\} \tag{3}$$

$$\frac{dr_d}{dt} = \frac{-D_v}{2\rho_w r_d}\mathrm{Sh}\left(c_s - c\right)\exp\left[\frac{-3 r_d D_v t}{\left(b - r_d\right)^3}\right] \tag{4}$$

$$\frac{dT_\infty}{dt} = \frac{-3 r_d}{2\left(b^3 - r_d^3\right)\left(\rho_{air} c_{pair} + c c_{pv}\right)}\left\{ k_{air}\,\mathrm{Nu}\left(T_\infty - T_d\right) + c_{pv} T_{air} D_v \mathrm{Sh}\left(c_s - c\right)\exp\left[\frac{-3 r_d D_v t}{\left(b - r_d\right)^3}\right]\right\} \tag{5}$$

$$\frac{dc}{dt} = \frac{3 r_d D_v}{2\left(b^3 - r_d^3\right)}\mathrm{Sh}\left(c_s - c\right)\exp\left[\frac{-3 r_d D_v t}{\left(b - r_d\right)^3}\right] \tag{6}$$

Given the number of variables, a 2^k style factorial analysis was used to investigate the single drop, heat and mass transfer problem. This approach would reveal which variables would have the most statistically significant impact on the heat and mass transfer process. A second factorial analysis was performed to investigate which fluid properties used in the computation had the most impact on the calculations.

2.1.2.2 Key Findings

The results of the factorial study showed that the most statistically significant variable was the free stream relative humidity, followed by the drop size and drop temperature. Note that no regard was given to humidity in the capstone work, but the order of significance of the drop size and water temperature was in agreement between these two studies. With this information, it was reasoned that future experimentation should focus on these key variables.

The effects of drop charging were only visible on the smallest of drops (~100 μm). This was a good effect, because the previous experimentation had shown that these are the most difficult drops to collect. Thus, at least theoretically, there is potential to use an electric field to help collect the very small drops.

The second factorial analysis showed that the diffusion coefficient used was, by a wide margin, the most sensitive property used in the model. This was reasonable considering the importance of the relative humidity and the mass transfer process in general.

2.1.3 Extension to HVAC Applications

The knowledge gained form the Master’s work was then applied to typical HVAC problems. In this work the single drop model is used in a case study for cooling and dehumidification in Atlanta, Georgia. The Atlanta study highlights the effects of the drop and air velocity and how they relate to identifying an ideal droplet diameter to maximize cooling and dehumidification.

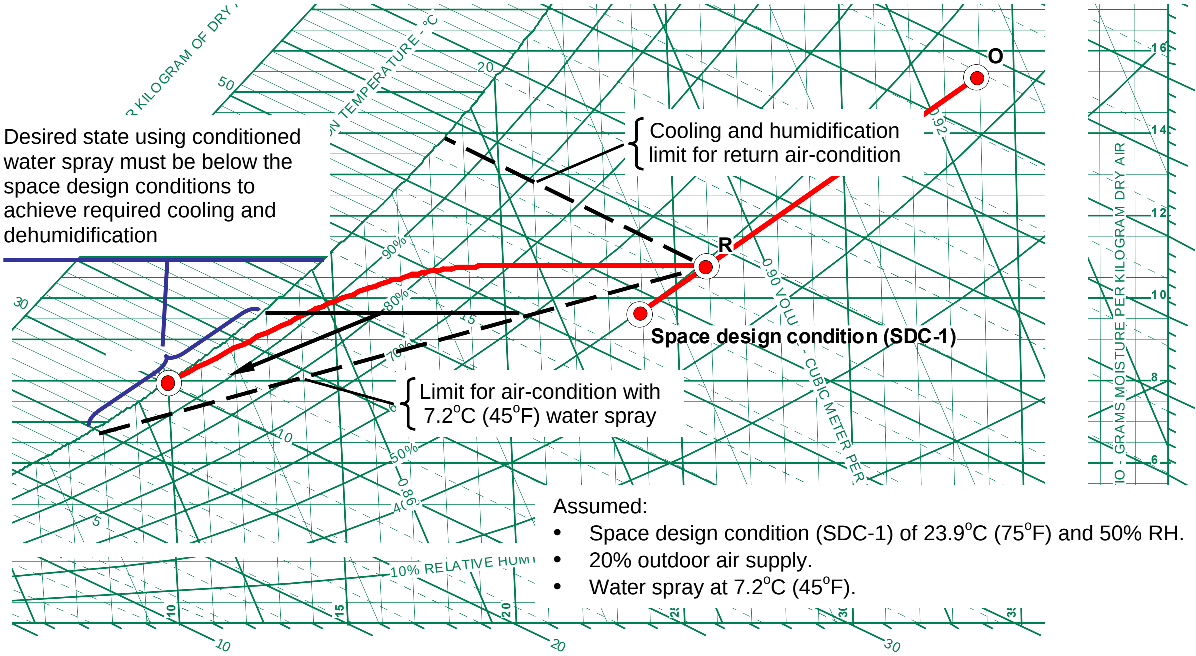

Desired state using conditioned water spray must be below the space design conditions to achieve required cooling and dehumidification

Cooling and humidification limit for return air-condition

Space design condition (SDC-1)

Limit for air-condition with 7.2°C (45°F) water spray

Assumed:

- Space design condition (SDC-1) of 23.9°C (75°F) and 50% RH.
- 20% outdoor air supply.
- Water spray at 7.2°C (45°F).

Figure 1 Psychrometric chart showing cooling space conditions for Atlanta, Georgia, and range of air conditions possible using a 7.2°C (45°F) water spray to cool air.

Upon analyzing the process from an HVAC standpoint, the system range of operation becomes immediately evident. An example is shown in Fig. 1. There is a clear region where the system could be expected to operate depending on the heat exchanger characteristics. The question then becomes a matter of *where* in this region will the DCHX operate. For instance, Fig. 2 shows the difference in droplet behavior for a 100 and 1000 µm drop. There are three graphs in Fig. 2 showing the heat and mass transfer as a function of time and the trajectory of the drops under different operating conditions. Under all conditions return air is cooled (indicated by drop heating); however as the drop diameter decreases air dehumidification (drop mass increase) changes to air humidification (drop mass decrease). As the drop diameter decreases, the rate of drop heating increases more rapidly, approaching the return air dew point. Once the drop temperature starts to exceed the dew point temperature of the return air, the drop will start to evaporate and its temperature will stabilize just below the return air dew point. For a 1 second flight time, the use of a 100 µm (0.004 in) drop spray would result in cooling and humidification whereas the use of a 1000 µm (0.039in) drop spray would result in cooling and dehumidification. From this example it is evident that an optimum droplet diameter exists to maximize cooling and dehumidification. The size and shape of the spray chamber will directly impact heat and mass transfer since it will establish the time the drop will be present in the air stream.

Another aspect explored with this work is the effect of the radius, *b*, of the volume of air surrounding the drop. To this point, *b* was set large with respect to the drop size such that it acted as an infinite expanse of air. As *b* is reduced to be on the order of the drop radius, the drops response diminishes. This effect is important because it limits how the real system would behave as a drop in a real spray would be surrounded by neighboring drops which would decrease the temperature and moisture gradients, thus reducing the drive to transfer heat and mass. This effect will be discussed further in later sections.

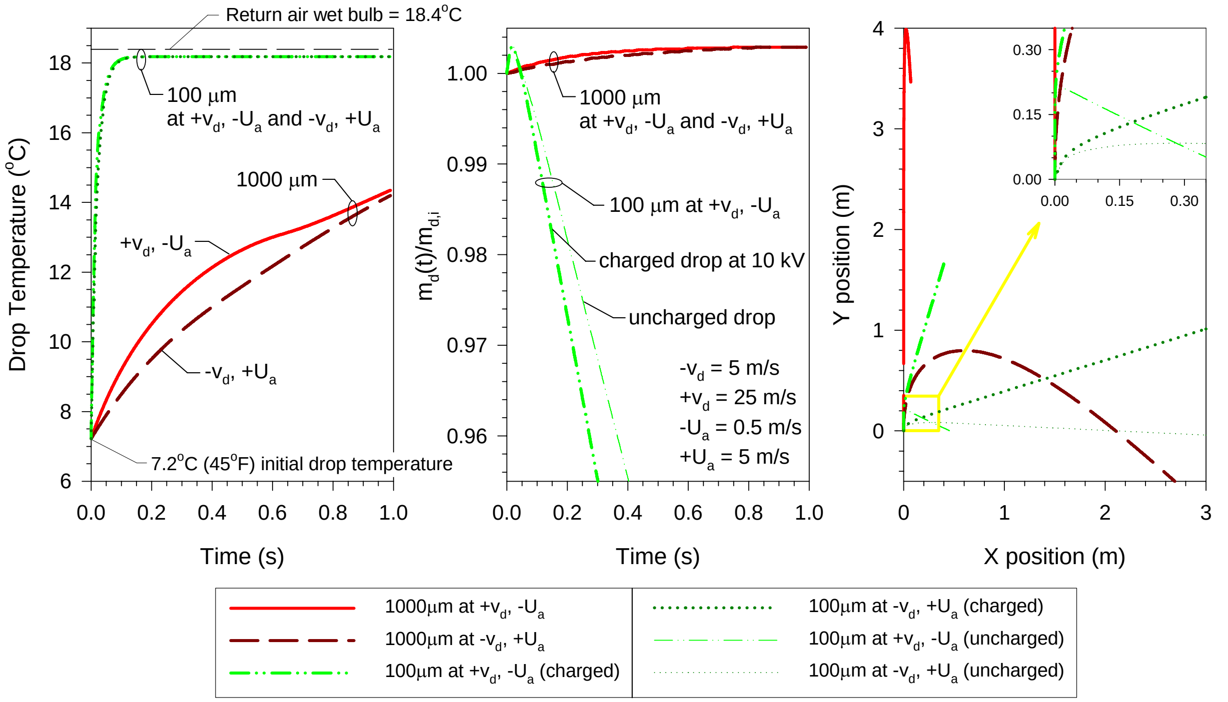

Figure 2 Model results showing water droplet heat and mass transfer as function of time and trajectory of 100 μm (0.004 in.) and 1000 μm (0.039 in.) drops under different operating conditions for the Atlanta, Georgia, conditions defined in Fig.1.

3.0 PROBLEM DESCRIPTION

3.1 Heat and Mass Transfer with Sprays

3.1.1 Definition of the Problem

Superficially, heat and mass transfer with sprays is a straightforward problem: drops experience heat and mass transfer given a potential difference between the drops' surfaces and the free stream temperatures and vapor concentrations. However, in the case of a real spray, *exact* modeling of heat and mass transfer is virtually impossible given the chaotic nature of the spray, beginning with the spray generation process. Further, after the spray is formed, the dynamic interaction between the droplets (coalescence and ruptures resulting from impacts) is another chaotic process being virtually impossible to define. Then, even if the spray dynamics were able to be defined precisely, the resulting heat and mass transfer calculations would be computationally intense. This breakdown has not even accounted for the coupled nature of the problem, i.e. heat transfer affects mass transfer which affects dynamics via the time varying drop size (which, if large enough, can be considered a deformable body adding more nonlinearity to the problem). Further still, the internal circulation of the drop is another fluid dynamics problem in and of itself, which can affect the heat and mass transfer of the system.

Thinking of the problem on this level reveals why a problem of this nature must first be approached experimentally. This is not to say that models cannot be made, though it is argued that the models available in the literature will be formed with a certain set of assumptions, and that because of those assumptions, they will not be applicable to this problem. As such, to understand the true behavior of the direct contact system in question (being of a certain geometry and operating under certain conditions), the experimental approach is the appropriate starting point for correlation development. Models may then be created – being tailored specifically to the problem (geometry) at hand – and then checked against the experimental data. Comparison between the fundamental model and the experimental results can help to understand some of the more subtle details of both analysis. In any case, any claims for development of a universal model would almost certainly be unrealistic. It is only prudent to begin the investigation by searching for existing knowledge that may be applicable to this problem. The following section introduces the work and salient conclusions of other researchers.

3.1.2 Literature Review

In the current literature, few sources have specific data or conclusions that apply directly to this direct contact heat and mass exchange with flat fan sprays investigation. What literature does exist about direct contact heat exchange in general seems to fall on either end of the spectrum of operation – the authors either model the overall process from a bulk flow standpoint, or they become entrapped in focusing on the most fundamental heat and mass transfer phenomena at the drop/bubble level, which turns into a complex and debatable subject. Jacobs [9] makes the argument that direct contact heat exchange is in no way a new field of heat transfer engineering (he traces some of the earliest publications to 1900 Germany), yet it does, however, lack the attention that surface type heat exchangers have received even though direct contact processes are widely used throughout industry. He attributes this lack of acknowledgement to a lack of experience on the part of textbook writers, who then transfer their lack of understanding to students who then continue the suppression of the subject.

So much direct contact research is focused on solid particle media, or at least heat transfer without phase change, and virtually always in a columnar form having the denser media almost always falling under its own weight [9][10][11][12]. When liquid sprays are analyzed by these researchers, inevitably it is in a saturated environment [9][11]. Further, most analysis neglect entrance and exit effects and focus on modeling according to bulk flow behavior in these columns [9][10][12], which is understandable given the complexity of the process.

The papers reviewed [6][7][9][10][11][12][13] do tend to agree on the key advantages of the direct contact process, namely the non-fouling factor of their performance, that is, there are no surfaces to corrode or otherwise degrade over time, deteriorating the heat exchanger performance. Further, this direct contact allows for more heat transfer for a given heat exchanger size which translates to lower driving temperature differentials. Yet another advantage is the lower pressure drop through the heat exchanger (relative to coil type heat exchangers). The final point involves the lower first cost of construction of a DCHX – a system that consists of little more than tubing, nozzles, a pump and a tank. Jacobs [9] goes further to note one generally accepted disadvantage of the direct contact process centering on the miscibility of the two fluid streams, in this case. However, it should be noted that this miscibility may be thought as an advantage in the current application as the transfer of mass allows for an extra degree of operational freedom.

Focusing our attention on Jacobs's [9] spray type heat exchanger comments reveals an interesting approach to modeling performance. He notes that it is best to utilize models based on individual drop heat exchange, however a number of researchers have investigated the use of volumetric heat transfer coefficients for preliminary design which utilize a void fraction or holdup coefficient. Jacobs [9] notes that the correlations he has found are highly dependant on the individual heat exchanger design and that using them on a different system would create suspicious results, in his opinion. He goes into some detail on the work of other researchers who focus their attention of the condensation problem for individual drops. Again, there is a considerable amount of effort focused on the interface accommodation problem and the internal heat transfer limitations of a drop which is complicated with the additional resistance of a condensate layer and gaseous absorption phenomena. Note, however, that the Master's model (section 2.1.2), which has mass transfer relations based on Fick's Law, avoids these issues directly through the use of a diffusion coefficient. Though it could be argued that the model is more simplistic in light of Jacobs's comments, it could also be said that the model is more easily applied and calibrated with experimental data.

A review by Sideman and Moalem-Maron [11] which focuses on direct contact technology for use in desalination processes, geothermal energy production, and emergency reactor cooling also points out the limitation of the technology due to the balance between the latent heat of condensation and the amount of sensible heat the liquid can absorb until saturation. Note that the proposed system does not operate under the same limitations given the chilled state of the water which allows for sensible heat transfer component. Unfortunately, Sideman and Moalem-Maron's [11] discussion on condensation on the surface of drops follows the assumptions of so many other researchers in that they model in a saturated vapor environment. Further, when they do introduce the issue of noncondensables, it is understood that the fraction of the air (in the steam environment) is small.

Bruckner and Mattick [14] discuss the use of a direct contact heat exchanger for use in high power space applications. They identify the key to successful operation, which is with separation of the heat exchange media following heat transfer. They discuss the use of a vortex chamber to accomplish this task as harnessing the liquid drops' momentum will be essential in a zero-g environment. It should be noted that the current research does not rely on this special vortex chamber geometry, even though it may be a good method. It is felt that this kind of dynamic operation would simply add to the complexity of the modeling and correlations at this time.

The authors [14] also note that in the design of their vortex style DCHX, the chamber diameter is linked to many parameters, namely: drop size, drop trajectory, drop temperature, gas velocity, and relative mass flow rate between the two media. They go on to say that the relations between these parameters are complex and thus are usually studied empirically. This is reassuring as these facts are in agreement with the conclusions of the Master's thesis [8].

Though the authors are focused on using liquids with very low vapor pressures, they agree that the key to proper operation of a DCHX lies with ensuring that the drops are not carried out of the heat exchanger with the gas stream and that the drops should only be allowed to leave after having exchanged the desired amount of energy. This strikes precisely to the point of needing to understand the time dependant state of the average drop in the DCHX – ultimately leading to optimization and maximizing efficiency, dehumidification, heat transfer, etc.

There are a few key papers that focus specifically on the topic of cooling air with a water spray, though most are focused on the evaporative cooling mode of operation. The papers tend to follow the same process highlighted by Jacobs: an attempt is made to develop some kind of model which is then checked with experimental data. But in every case where experimental data has been presented, the measurement methods detract form the value of the work [13][15][16][17][18], and the amount of data collected is limited at best. This highlights the importance of the development of good test equipment and experimental methods in this project.

A good example of the limits of experimental quality is shown by Kachhwaha et al. [16] who focus on hollow cone sprays, a different geometry than the flat fan style sprays under investigation in this project. The researchers attempt to model the hollow cone spray in a 0.6 x 0.6 x 2 m long duct. They also conducted experiments to characterize the spray (drop size, spray angle, etc.) and then determine heat and mass transfer in a wind tunnel. The hollow cone sprays are injected parallel with the direction of flow. The test section is angled such that the fallen water drains out the section exit while the remaining water is collected on a drift eliminator/screens section. The experimental data is questionable given the fact that the inlet temperature and humidity was not controlled, the water temperature was not controlled, the measurement methods for these fluids was questionable, and error propagation is not considered in the uncertainty analysis. Ultimately, the authors concluded that the experiments were too rudimentary to allow for correlation development. Nonetheless, the authors compared their model to the experimental data and found agreement within 15% by their calculations. The idea of their work is solid, however their methods are questionable. This project utilizes more sophisticated equipment, better experimental techniques, and a more straightforward model to achieve virtually the same goals. Kachhwaha et al. released a second paper which investigated a counter flow arrangement [17], and produced the same questionable results with their model agreeing within 30% of the experimental data.

Yoo and Kwon [13] have experimentally investigated the performance of a small scale DCHX. Unfortunately, their data is also questionable given the equipment used (for example, rotameters and Pitot tubes are used to measure water and air flow rates, respectively) and further, no confidence interval or error is presented and general typographical errors create a level of mistrust. Nevertheless, their experiments follow closely with those planned for this project. In general, however, the result trends presented agree with preliminary data found in past work, specifically the key result being that heat/mass exchange effectiveness increases with increasing water flow rate. The second obvious conclusion is that the inlet water temperature must be below the inlet air dew point temperature to achieve dehumidification. Again though, Yoo and Kwon's work can be misleading as they make claims about dehumidification, yet fail to mention what the inlet air moisture content is in almost all experiments. This limits direct comparison between this project and their work.

Chen and Trezek [15] are proponents of the spray energy release (SER) model which is derived from another semi-empirical approach. The goal of this SER model is to quantify the net energy released by the spray. These authors go further to see if the SER could be obtained by analysis of a single drop, ultimately reducing the amount of experimental work. Their final conclusion was that there was not enough available data to check their approach.

However, Chen and Trezek identify what they consider to be the three key parameters in evaluating a spray system performance: droplet heat transfer coefficient, local wet bulb temperature, and the size distribution of the droplets [15]. They analyze these parameters to gain insight into improving the accuracy and predictive techniques used to evaluate spray system performance. They develop a model based on Fickian diffusion for mass transfer and convective and radiative heat transfer terms. They later choose to drop the radiation terms, and further conclude that existing Nusselt number correlations are inherently inaccurate for modeling a spray drop and that any spray model must ultimately be calibrated with experimental data – a method adopted for this project.

The authors discuss the concept of a critical wind speed as it relates to the local wet bulb temperature. As the difference in the wet bulb temperatures between the droplet boundary layer and the ‘ambient’ drives the mass transfer, it is essential that the ‘ambient’ temperature be correctly defined for an accurate solution. The authors conclude that the relative mass flow rate of air past the drop must be above the critical wind speed to use the free stream wet bulb temperature in the calculations, otherwise some average of the boundary and free stream wet bulb temperatures must be used. This important point is accounted for in the Master’s model through the definition of the air volume around the drop (see section 2.1.2). Their final conclusion was that at lower wind speeds (<2.5 m/s) the thermal performance was significantly affected by the proper choice for a local wet bulb temperature. The nozzles used in the following experiments (section 4.3.5) and which will also be modeled (section 3.5), produce drops with relative velocities on the order of 15 m/s, well above the 2.5 m/s limit. However, the spray cloud density (as it relates to the air volume modeled) is still expected to play a role, which may be significant according to these authors.

Ni Bo has investigated air washer performance from an analytical standpoint [19][20] and from an experimental standpoint. The analytic work [19] was helpful in developing the Master’s model which will be expanded in this work. However, the work under consideration now is that dealing with his coupling of a numeric simulation with experimental results [18]. The conclusions of the work are typical: increasing air velocity and water/air ratio is favorable for humidifying efficiency. The model follows a Lagrangian approach and essentially takes the form of that introduced in section 2.1.2 being adjusted slightly to highlight the counterflow nature of the experiments. The measurement techniques are, again, questionable, which makes one suspicious when the agreement between the model and experimental data is presented. Further, the issue of what Ni Bo refers to as ‘nozzle density’ is merely mentioned as an aside, and more importantly still is that the value of the air volume surrounding the drop, *b* (see section 2.1.2), is not addressed at all. However, it is this authors feeling that these points (specifically the value of *b*) are critical to correctly applying the model. In any case, however, Ni Bo’s model and experimental trends are similar.

El-Morsi [7] presented a Ph.D. dissertation investigating the optimization of direct contact spray coolers. Given the limited amount of current literature, his literature review actually highlights some of the papers mentioned here. His conclusions agree that most work has been focused on transfer to single droplets or sprays with little regard for the specific cooling and dehumidification problem. Further, he notes that the complexity of this process does not lend itself to a simple model for all direct contact heat exchangers.

This author (JLH) is in agreement, and thus has focused these efforts on analyzing the specific DCHX operation, namely the flat fan spray operating in a cross flow orientation in a 0.15 x 0.15 m [6 x 6 in] test section. Note further that this scale of test section is far smaller than those found in the literature listed thus far.

El-Morsi [7] begins his work with experimental testing with a blow through wind tunnel with the test section consisting of a 0.2 m [7.9 in] diameter and 3.48 m [137 in] long stainless steel tube. A simple hole allows the water to drain from the test section and entrained moisture is prohibited from leaving the test section with the inclusion of drift eliminators. An important point to mention with the approach taken in the current work is that the spray is strategically removed from the air stream in efforts to prevent excess humidification. This is in stark contrast to all research found to date where the water is allowed to pool and saturate the test section environment. The significance of this point is that the effect of droplet diameter becomes more pronounced as the residence time of the drops becomes a major variable. As such, this variable can then be controlled or even optimized. El-Morsi, taking advantage of his test section geometry in a similar manner to this work, uses a full cone spray nozzle centrally located in his tubular test section. Though much more sophisticated than the research listed thus far, El-Morsi still relies on older measurement techniques, and thus limits the accuracy of his experimental data. Further, he actually ran only a few experiments (approximately 5 experiments).

El-Morsi [7] performs a numerical analysis with Fluent software taking advantage of the injection feature. His discussion of the solution process is based on the documentation section of the Fluent software with a few additional details, mostly concerning the availability and validity of different correlations. There were two classes of numeric simulations, one used a 'reflecting' wall boundary condition, and the second was an 'escaping' wall boundary. These would represent drops that either bounced off of the wall or adhered to the wall, respectively. El-Morsi notes that these boundaries should represent the limiting cases of thermal performance. The experimental data is actually bounded by the simulation results, but this does not necessarily make sense given that only 100 injections are used in the simulation and in the real situation, the corresponding mass flow rate would produce thousands of drops.

From his simulations, El-Morsi found that the effect of gravity did play a role as it produced temperature stratifications in his horizontal airflow due to droplets concentrating in the lower half of the chamber. He also found that the increase in droplet diameter produced a corresponding decrease in what he terms as spray chamber effectiveness (basically sensible heat exchanger effectiveness). He attributes the decrease in performance to a decreased spray tip penetration (essentially residence time) and decreased surface area. In fact, his parametric study revealed that the drop diameter was the principal factor affecting spray chamber effectiveness. The other two parameters were the spray tip penetration and the initial speed ratio of the drops.

El-Morsi then tries to develop analytic models to guide heat exchanger design. The models are based on the data generated with the numeric simulations. The issue of the 'reflect' and 'escape' boundary conditions, along with the gravity factor, complicates his derivations resulting in a set of equations that a designer would have to choose from which would ultimately just bound the performance of El-Morsi's steel tube DCHX.

In conclusion, El-Morsi notes that his limited amount of experimental data has detracted from the value of his work as his correlations are based predominantly on numeric simulations. His experimental work was actually geared more toward proving the concept of cooling and dehumidifying. Further, mass transfer is not featured in his correlations or simulations at all. He also acknowledges that the variation of nozzle characteristics (namely the spray angle) should be investigated.

3.2 Spray Charging

It was initially hypothesized that there are two primary reasons to charge the spray used in the direct contact process: to assist in droplet collection and to increase the air cleaning capabilities. To test these hypotheses, a reliable method was needed to charge the sprays. The strategy follows that if the spray can be charged, then simple experiments will show how much charge can be imparted on the average drop. This would allow for more accurate modeling when calculating the force due to an electric field versus the drag or momentum force. Further, the charge can be checked against other published research that investigates air cleaning with charged drops. That being said, this sub-project entailed the development and testing of a nozzle to charge water sprays. Joshua L. Hensley, Xin Feng, and James E. Bryan have submitted the details of this study for publication to the Journal of Electrostatics under the title of "Induction Charging Nozzle for Flat Fan Sprays".

Because the working fluid is conductive in nature (of conductivity $>10^{-4}$ S/m), an induction charging scheme was used for sake of practicality. After reviewing the existing literature, no acceptable nozzle design was found. The challenge remained to develop a fully hydraulic, flat fan spray induction charging system. It was felt that the simplest charging system should be designed for sake of reliability, predictability, and practicality. Thus, the system was based on passing the grounded, flat spray between two parallel, cylindrical electrodes held at a high potential. A concept sketch is shown in Fig. 3.

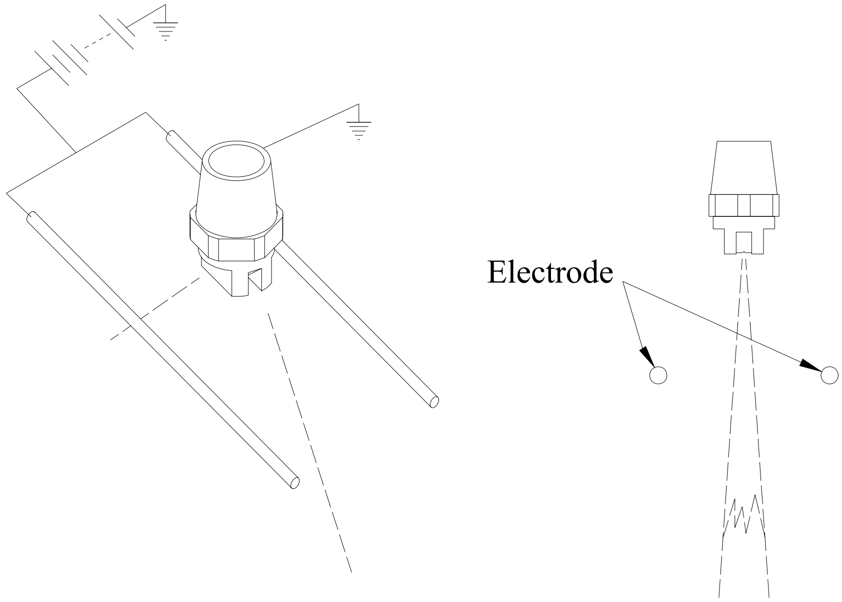

Figure 3 Electrode placement relative to the flat fan spray.

The induction charging process makes use of the conductive nature of the fluid which is normally a barrier for the other charging processes [9]. Assume a positively charged high voltage electrode is held near a spray stream. Because the liquid is conductive, negative free charges in the fluid move toward the electrode to neutralize the net charge in the region. At this point, the stream of water from the nozzle begins to break up due to natural surface instability phenomena, and as the droplets form, they essentially trap the negative free charges forming a net negatively charged drop. [21][22] Law [23] points out that in the ideal situation the droplets should form in the highest field region as this would produce the highest charge on the droplets for a given potential. He outlines a simple method to predict where this region would be and goes further to actually try to predict not only the current carried by the spray, but the expected charge to mass ratio for an average drop. This method was adopted and explored as a guide for this work. The theory is then tested with the construction and testing of an electrode system.

3.3 Spray Collection

One of the key strategies to developing the DCHX for cooling and dehumidifying air lies with the removal of the drops from the air stream after dehumidification takes place, that is, the drops must not be allowed to pool and saturate the free stream. It will be mentioned at this time that the spray charging study was successful; however, the charge imparted on the drops was not sufficient for creation of electric forces strong enough, relative to the momentum forces, to justify further use of the charged drops for collection purposes. A purely mechanical strategy was then sought to remove the drops from the air stream.

The free stream air must be segregated from the collection tray in a way that still allows the spray to pass freely into the collection tray. The basic solution was to create a 'false wall' that would allow both of these functions. The false wall material of choice was a polycarbonate honeycomb structured material with 6.4 mm [0.25 in] diameter cells.

The first generation of test section design was relatively naïve, as seen in Fig. 4. This section was used in the undergraduate capstone project, and even though there were severe droplet rebound issues, the section still functioned in cooling and dehumidifying air. The second generation of test section addressed the issues of air bypassing the spray, as well as spray impacting the walls by simply rotating the section 45° so that the walls would align with the edges of the flat fan spray. Further, this aligned the honeycomb cells with the spray edges. Though vastly superior to the first test section, the second generation test section still had droplet rebound issues that needed to be addressed. This preliminary testing [4][5] showed that the orientation, or alignment, of the cells with respect to the spray can impact the effectiveness of the honeycomb material. If the drops strike at a more normal angle to the cell wall, or of the drops impact the mouth of the cell, the resulting splatter is viewed as rebound, which constitutes a loss of system control. Thus, an investigation was launched to determine which orientation produced the fewest amount of reflected drops.

3.4 Correlation Development

The key contribution of this work is to develop design tools to aid in the future design, development, implementation, and operation of a direct contact heat exchanger. One tool will take the form of an equation that could be manipulated to solve, for example, the required water conditions to achieve balance with a given operating heat and humidity load.

Some thought has been invested in choosing which performance metric should be developed. That investigation is found in the Appendix (section 8.5). It was concluded that the overall heat transfer coefficient, *UA*, would be the most useful metric. Not only will this allow the DCHX to be compared to conventional heat exchanger coils used in the HVAC industry, but this value can also be used to directly calculate sensible heat transfer – typically the first question to be asked about the performance of a system.

The overall heat transfer coefficient is typically a sensible heat transfer metric. However, the experimental results (section 5.3) show that moisture content and removal significantly affects the sensible heat transfer. Thus, this information will have to appear somewhere in the correlation. This comes as no surprise as previous research [8] has shown that the relative humidity is a dominant variable in both the heat and mass transfer process. That work has also shown that the drop size is another driving factor. Thus, this drop size information should appear as a variable in the correlation. In addition, the water mass flow rate, which has a significant impact on the total energy that can be transported, should be a major variable in the correlation.

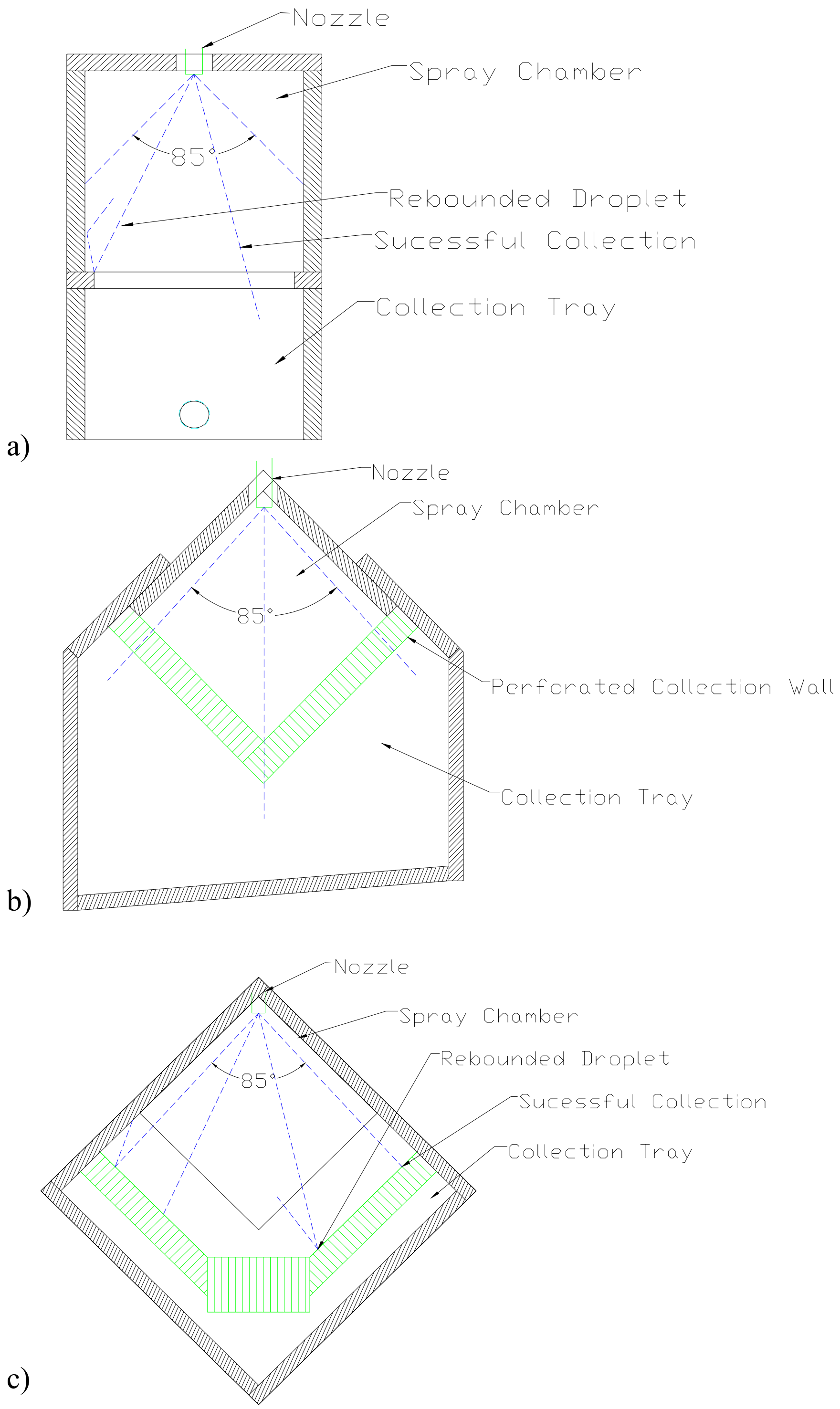

Figure 4 Cross section views of the first a), second b), and third c) generation wind tunnel test sections.

Lastly, the correlation should be based on some fundamental theory, i.e. the functional relation should not simply come from curve fits of the experimental data, rather, a form of the relation should first be developed based on some fundamental understanding of the problem, and then the experimental data should be fit to determine coefficients or other calibration parameters. Thus, one key to developing correlations is to have a large amount of data. The literature review showed the importance of a well developed test matrix. In this case though, the paramount problem lies with the fact that efforts must be made to strive for the development of generic equations of a fundamental nature that may be applicable to more than one operational design. To clarify this, it is known that data will be generated using a prototype test section which has been designed for sake of reliability, ease of testing, space and budget constraints, etc.; however, a real system is conceived to operate in an altogether different configuration. Knowing this from the onset provides foresight, which will guide the development of the correlations in a more generic format, i.e. a form that is not particularly dependant on the exact DCHX geometry, for example.

3.5 Development of Full Spray Model

There are two key tools to be developed in this work. The first tool is an equation, or correlation, describing the operation and variable relationships of the direct contact heat exchanger (see above). The second tool to be developed is a numeric model that quantifies the heat and mass transfer from a full spray. Note that in previous research (the Master's thesis [8]) a numeric model simulating the heat and mass transfer from a single drop was developed. This full spray model is an extension of that work. In this case, however, the single drop model will be called in a loop, and the sum of the energy transfer for the individual drops will be the effective energy transfer for the spray.

To understand the challenge of this work, some insight into the model construction must first be gained. It will be mentioned now that the model in the Master's thesis [8] has been re-derived from first principals. The derivation of the model may be found in the Appendix (section 8.1.1). The core model is a set of differential equations that describe the drop temperature, air temperature, drop size, and air vapor concentration as a function of time:

$$\frac{dT_d}{dt} = \frac{3}{2r_d^2 \rho_w c_{p,w}} \left[k_a Nu \left(T_\infty - T_d \right) - \left(u_{lv} + RT_d \right) D_v Sh \left(c_s - c \right) \right] \tag{7}$$

$$\frac{dT_\infty}{dt} = \frac{3r_d}{2\left(b^3 - r_d^3\right)\left(\rho_a c_{v,a} + c c_{v,v}\right)} \left[-k_a Nu \left(T_\infty - T_d \right) + \left(RT_d \right) D_v Sh \left(c_s - c \right) \right] \tag{8}$$

$$\frac{dr_d}{dt} = \frac{-D_v Sh \left(c_s - c \right)}{2\rho_w r_d} \tag{9}$$

$$\frac{dc}{dt} = \frac{3r_d}{2\left(b^3 - r_d^3\right)} \left(1 - \frac{c}{\rho_w} \right) D_v Sh \left(c_s - c \right) \tag{10}$$

The dynamic part of the model (the acceleration equations) is also listed in the Appendix, but these equations will not be listed here as they are not pertinent to this discussion.

The model is based on an energy balance between a single drop, and a volume of air (defined by a radius *b*). Equations (8) and (10), which describe the air temperature and air vapor concentration as a function of time, show this variable *b*. The challenge lies with determining the correct value of *b* to create an accurate simulation. This value changes with the number of drops in the spray as the number of neighboring drops increases, the value of *b* will decrease. The problem is further complicated by the fact that the spray fans. The result of this is the fact that in the real situation, *b* is time dependant and increases as the drop traverses the test section. Further, in the real spray drops can coalesce and/or be broken up via mid air impacts. For these reasons, it should be clarified that the model can only be calibrated with an "effective *b*." This topic will be addressed in more detail in section 5.4.

In studying the chaotic nature of sprays, it seemed a natural choice to adapt a Monte Carlo technique to generate a 'random' spray model. Fortunately, MatLab, the software used to solve the differential equation set, has built in 'random' number generators which allows for modification of the existing single drop model. In this case, a random number generator is used to determine the drop size, launch velocity, and launch angles (as the flat fan spray spreads not only in the purposefully induced direction, but also in an angle normal to the fan due to natural breakup phenomena. Note that normal distributions are used at this time for sake of simplicity, and these are felt to be good enough for the merit of this exercise. With the means and standard deviations known, the random numbers are used to calculate random variables:

$$Variable_{random} = X = Rand_{N(\mu=0,\sigma=1)} \times \sigma_{X,measured} + \mu_{X,measured}\,. \tag{11}$$

In Eq. (11), the random number generated by MatLab using "`randn`" is represented by $Rand_N$ because the random number is generated to follow a standard normal distribution. Note that other researchers have studied this problem in detail and concluded that the spray properties follow Gaussian distributions [16]. Once a matrix of initial conditions is then built by calling Eq. (11) in a loop for each random variable, the ordinary differential equation solver can then be called in a loop, being supplied with a new set of random initial conditions. The real challenge in the program then lies with efficiently handling the data returned from the solver loop, and extracting the appropriate data for energy and transfer calculations.

4.0 EXPERIMENTAL SYSTEMS

4.1 Spray Charging System

4.1.1 General Description

The pervasive goal of the experimental spray charging exercise was to find the electrode placement to induce maximum deposition current a given spray generation nozzle (Spraying Systems Co. H ¼-VV-SS 8005) and flow rate (1.3 l/min). To accomplish this, a method was developed for holding a pair of stainless steel, cylindrical electrodes in various locations and parallel to the sheet region of a flat fan spray (see Figs. 5 and 6). This new induction charging nozzle was then tested with the electrodes in a range of locations to map the deposition current as a function of electrode placement.

The nozzle was mounted on a boom to spray vertically downward into a collection tank (see Fig. 7). Before the spray reaches the tank, the deposition current was measured as the charged spray impacts a box (fabricated from aluminum screen mesh) located above the tank. The collection screen was only connected to an electrometer (Keithley model 610C) but otherwise electrically isolated from the system and any ground paths. The electrodes were maintained at a high voltage with a DC power supply (Glassman model PS/EH30R03.0). The nozzle pressure was monitored with a pressure transducer (Sensotec model ST JE/1835-13-02). The deposition current, power supply current and voltage, and the nozzle pressure are all wired into a Keithley model 7708 multiplexer card installed in a Keithley model 2701 ethernet multimeter/DAQ. The conductivity of the water was also measured before and after testing (YSI model 35 conductance meter) and found to lie in the range of 3×10^{-3} S/m.

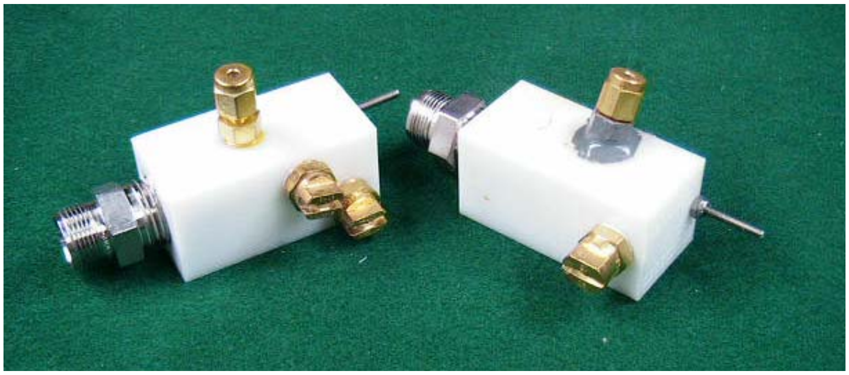

Figure 5 Spray nozzle holders shown without electrodes.

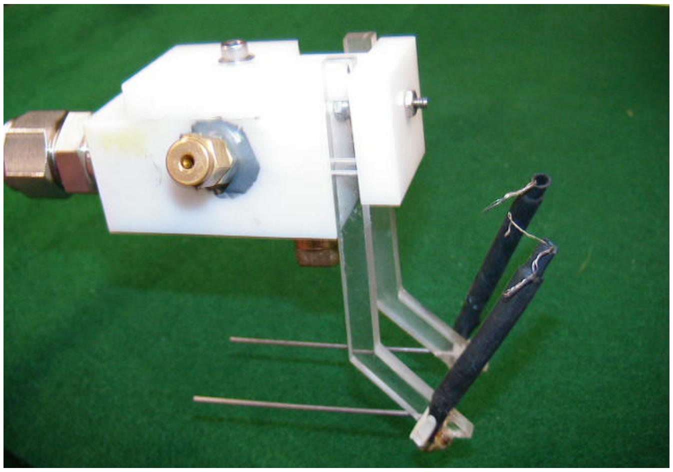

Figure 6 Spray nozzle holder with electrodes and high voltage leads in place.

Figure 7 Photograph of the experimental system arrangement.

4.1.2 Data Reduction

The experimental observations included measurement of four data streams: nozzle pressure, power supply voltage, power supply output current, and deposition current. Further, the stock calibration of the power supply and electrometer were used. The pressure transducer could be calibrated provided a reliable standard was available that could generate pressures to the 1.4 MPa [200 psig] sensor range. The pressure transducer was zeroed once in place and the pressure was double checked with a precision bourdon gage (Wallace & Tiernan model FA141). Note that the nozzle pressure is monitored as flow rate is directly coupled to operating pressure. Thus, given the water temperature variance is negligible, a consistent nozzle pressure will equate to a consistent flow rate. Thus, the specific operating pressure was not as important as consistency between runs. All equipment had linear relations between their output signals and inputs. The following equations were used in accordance with manufacturer recommendations for 0-10 VDC output signals:

$$i_{deposition}[\mathrm{mA}] = V_{signal}\left(\frac{10}{3}\right), \tag{12}$$

$$i_{ps}[\mathrm{mA}] = V_{signal}\left(\frac{3}{10}\right), \tag{13}$$

$$V_{ps}[\mathrm{kVDC}] = V_{signal}\left(\frac{30}{10}\right), \tag{14}$$

$$P_{nozzle}[\text{psig}] = V_{signal}\left(\frac{100}{2.25}\right). \qquad (15)$$

A minimum of 35 data points were collected for each experimental setting so simple means and standard deviations could be calculated.

4.1.3 Uncertainty Analysis

Some assumptions were made in the uncertainty analysis portion of this proof-of-concept experiment. As stated previously, factory calibration equations were used, and the measurements were taken directly, i.e. the electrometer simply measured charge collecting on the screen without further manipulation. Thus, with the equipment, or bias, error assumed negligible, only precision error remained which required no error propagation analysis. As more than 35 data points were collected per measurement, the variation in readings was assumed to follow a Gaussian distribution. Thus, the uncertainty for these measurements was calculated according to [24]

$$\text{Uncertainty} = 1.96\frac{S_x}{\sqrt{n}}. \qquad (16)$$

where S_x is the sample standard deviation and n is the number of measurements in the sample. The factor of 1.96 is used to ensure a standard 95% confidence interval.

The uncertainty of electrode position is 0.5 mm, based on the readout of the digital calipers and location jig used to position the electrodes.

4.1.4 Test Matrix

Aside from the shakedown tests and test to verify the analytic solution, the key experiments were run to find the optimum electrode position which would yield the maximum deposition current, or charge on the spray. Thus, the electrodes were to be held at various positions around the spray sheet and the resulting deposition current measured. In this way, the region around the spray would be mapped. The electrodes were incrementally moved to all combinations of ‘x’ and ‘y’ positions found in Table 1. Note that the positions are referenced to Fig. 31.

Table 1 Electrode positions, in millimeters as referenced to Fig. 31.

y_S	10	20	30	40	45	50	55	60	65	70	75
x_S	5	10	15	20	25	30					

4.2 Spray Collection System

It was reasoned that the cell orientation was the determining factor to control droplet rebound. Thus, the experimental strategy involved spraying water onto the honeycomb material and monitoring the resulting drop rebound. The honeycomb material was suspended over a collection tank so that a high speed camera (Photron Fastcam-PCI R2) could be focused on key regions where the spray impacted the collection surface. The frame rate, view size, filter settings, zoom, etc. were kept consistent between the tests to allow for direct comparison of the resulting high speed videos.

A number of potential designs were considered, however all designs reduced to basically three designs referred to as: 2P, 3P, and C (see Fig. 8) which were constructed and then tested.

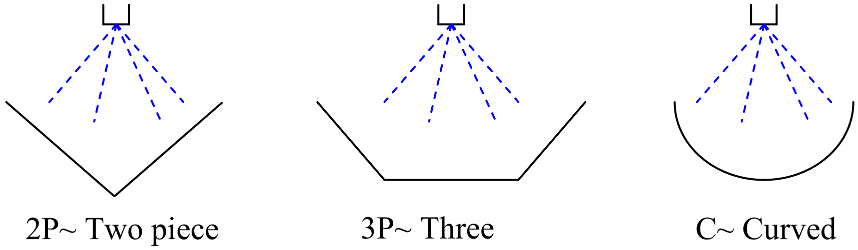

Figure 8 Sketches of the end view of the basic collection surfaces investigated by high speed imaging.

4.3 Wind Tunnel and Supporting Hardware

4.3.1 General Description

An instrumental portion of the project included the design and construction of a new air handler for the existing wind tunnel. One of the requirements of the new air handler was that it should be able to generate stable air flows up to 10 m/s (face velocity in the test section) while having uniform velocity profiles. Further, the air handler should have both temperature and humidity control. Thus, the air should be able to be not only humidified, but dehumidified as well. This was accomplished with a series of coils and a steam generator. Another goal was to be able to produce a range of air conditions from sub-zero air temperatures up to 35 C at 85% relative humidity. The final requirement was to make the wind tunnel a closed loop with a damper section that would allow the regulation of the amount of exhaust and make-up air. Closing the loop would also allow for the aforementioned temperature and humidity ranges to be exceeded.

Design of the new air handler began in January of 2006, with construction beginning in mid February of 2006. The air handler was online in August of 2006 (seen in Fig. 9).

4.2.3.1 Features

The main air handler frame is suspended by four adjustment screws to allow for leveling and height changes as required for variation in test section centerline heights (if the frame of the test section is rotated 45° the centerline changes). The body panels double as insulation panels as well as noise dampeners. Two ultra-violet lights were installed to combat bacteria growth. Provisions are in place to feed four heat exchange coils, however only two coils are installed at this time (the remaining two coils are still under construction). A steam generator is mounted onboard, which has been retrofitted with SCR controllers allowing the system to precisely maintain desired humidity levels at even the highest loads. The incorporation of turning vanes and dual purpose coils has balanced the flow to produce a symmetric air profile though the test section. Like the tunnel section, the air handler is mounted on a rigid base frame with six casters allowing easy movement once the ducting is disconnected.

Figure 9 The third generation wind tunnel. The air handler lies on the left half of the photo, while the test section and instrumentation is on the right half.

4.2.3.2 Performance

The air flow generated in the third generation tunnel is remarkably stable in comparison to the former systems. The maximum air flow breaches 450 cfm (9.2 m/s face velocity) in the open loop configuration (100% make-up) with an empty test section. Though slightly less than the design goal, this air flow is more than sufficient for future testing.

The temperature control is easily achieved; however, some issues arise with respect to humidity control at lower air flow rates. This is due to the fact that such a large steam generator was needed to introduce an adequate amount of moisture at the high flow rates that it tends to not have a fine enough resolution of moisture production at lower power levels. This problem is combated in part by dehumidifying the air prior to the generation manifold in order to compensate for the excess moisture created. In any case though, the variation in humidity is seen as uncertainty in measurements in the final analysis.

4.3.2 Detailed Descriptions

4.3.2.1 The Air Handler and Support Loop

A multifunctional small-scale wind tunnel was developed to test the DCHX prototype and generate data to be used in correlation development. The testing apparatus consists of a temperature and humidity controlled wind tunnel and a dedicated recirculating water supply loop designed to provide reliable testing conditions procedures and numerous testing capabilities on both the air and water side of the system. Schematics of the entire testing system can be seen in Figs. 10 and 11.

4.3.2.1.1 The Wind Tunnel

The new and current air-handler (Fig. 12) was designed with both the flow asymmetry and humidity control in mind. The new handler was expanded to incorporate auxiliary coils and a humidifier. Air enters the air handler through a damper system which allows for regulation of make-up air from 0-100% refresh. Air is driven through the wind tunnel by a 2 hp variable speed centrifugal blower. The blower is operated by a PowerFlex® 4 controller. The air is blown into the Primary A-Coil which is temperature controlled by Conditioning Loop 1. This Primary coil can be used to initially dehumidify the air if the need arises, preheat the air so that it can accept a greater amount of moisture, or provide an auxiliary load if necessary (as in the case of a closed loop configuration). The air then moves into the humidifying section of the air handler where steam is injected. The steam is introduced into the system by a VaporStream® VLC 9-1 humidifier which is manually regulated by a DriSteem® controller and a 0-10 VDC power supply. To prevent mold and mildew growth in the humidification section, the air handler is equipped with two UV lights. The air then moves through a second A-coil, the Set-Point Coil, for final temperature control. The Set-Point Coil temperature settings are supplied by Conditioning Loop 2. There are provisions for Auxiliary coils between the humidification section and the Set-Point coil and before the blower; however those coils are not presently installed.

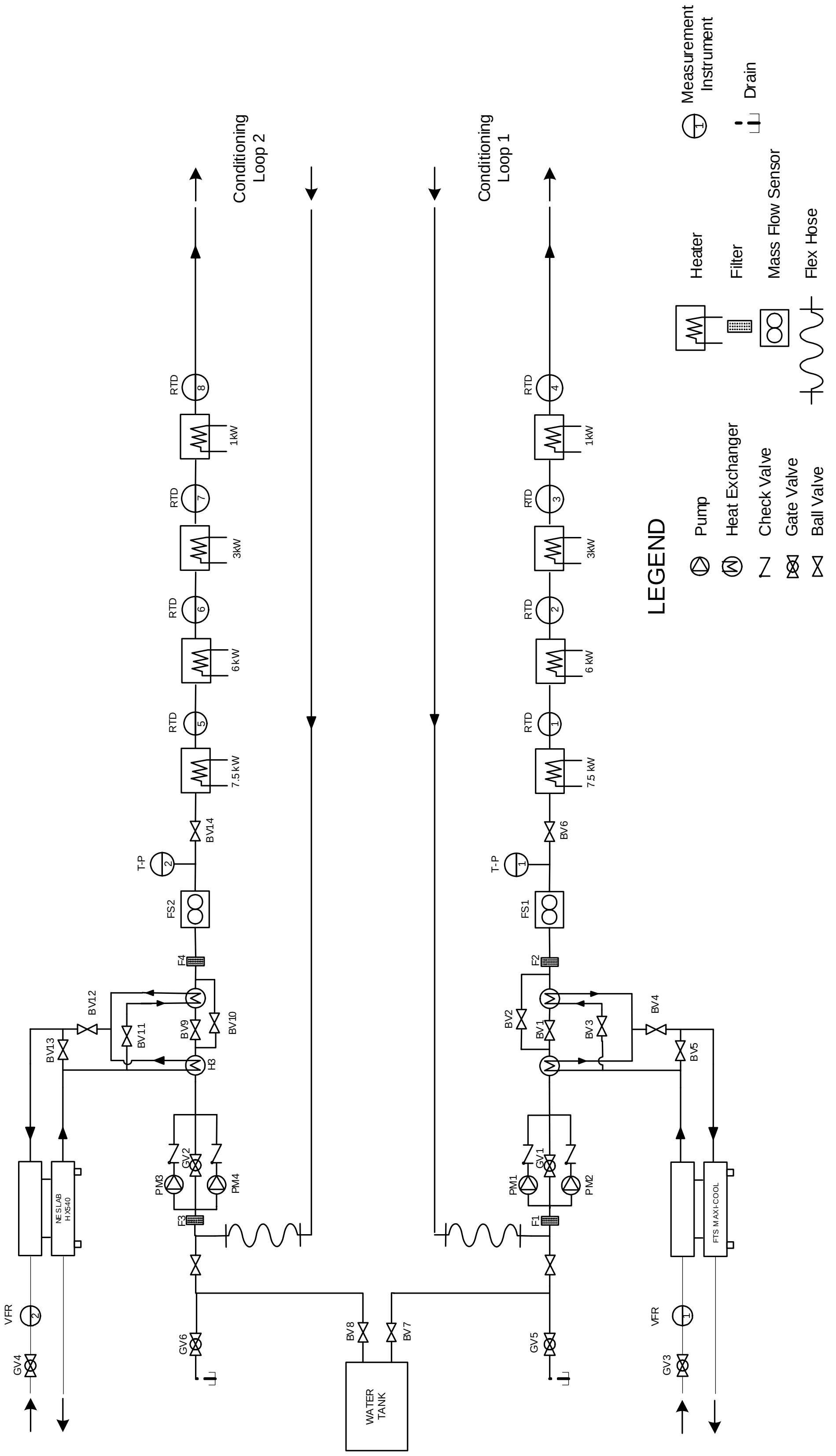

Figure 10 Schematic of the air handler support water loops.

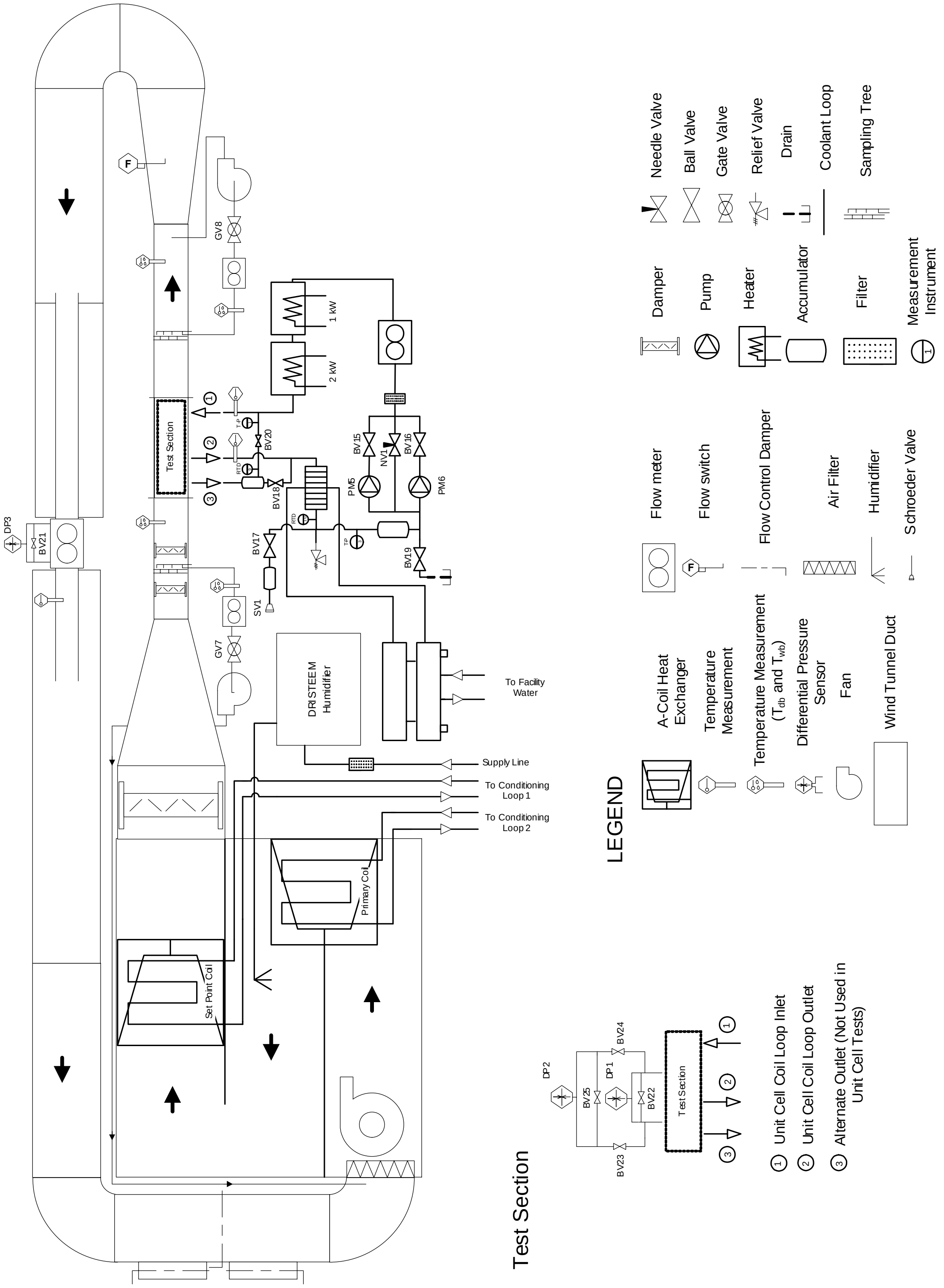

Figure 11 Schematic of the new air handler and spray water loop.

Figure 12 New and current air handler.

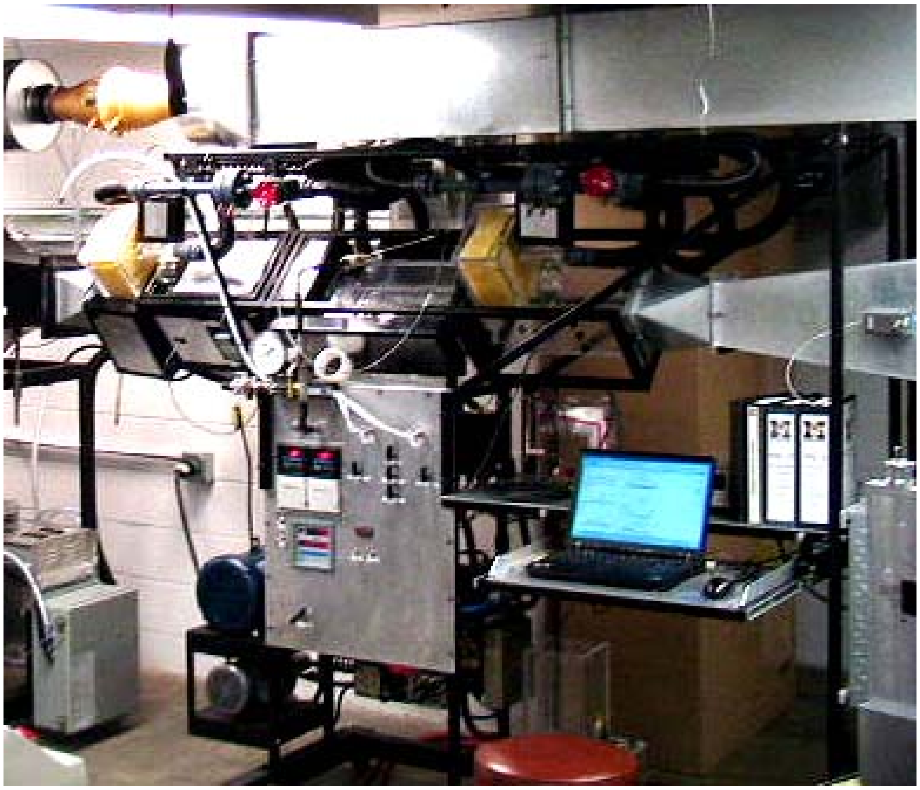

Figure 13 Wind tunnel with instrumentation sections.

From the Set Point coil, the air enters an 18" x 18" x 6" setting chamber, followed by a series of screens and honeycomb sections to straighten the flow. The air then enters the contraction nozzle which reduces the cross section from 18" x 18" to a 6" x 6". From there the air flows in to a rotation section (rotates the square geometry 45º), and then into another series of screens and honeycomb cores. Air is sampled for inlet dry bulb and wet bulb temperature measurements in between a series of screen and honeycomb straightening sections. The air's temperature and humidity is again measured by a secondary Dwyer® probe. The air then enters the test section which contains the spray nozzle, collection bin, false wall, and pressure taps (for pressure drop measurements across the spray). From there the air is again sampled for the outlet dry bulb and wet bulb temperature measurements.

The air then exits the acrylic duct work and then goes through another rotation section before it enters a steel diffusion section, increasing the duct size from 6" x 6" to 12" x 12". The air makes the return bend 180° back towards the air handler. On the return course, the air flows through a 4" diameter, 40" long duct to produce fully developed flow before it is measured by a laminar flow element meter (LFE). On the outlet of the LFE a thermistor measures the dry bulb air temperature before it enters another 4" diameter core to maintain stable flow through the LFE. The air then flows to the return damper to be recirculated or vented to the lab depending on the damper settings.

4.3.2.1.2 Air Handler Conditioning Loops

To ensure that air flow through the test coil was at specified conditions, two single-phase water loops were created to provide sufficient heating and cooling for the air handler coils. These water loops, Conditioning Loop 1 and Conditioning Loop 2, are built similarly but operate independently of one another to provide maximum control of the testing apparatus. The coils are connected to the conditioning loop by flexible hosing fitted with quick disconnect fittings.

Once the water enters the inlet of the conditioning loop it flows down a long stretch of copper tubing prior to entering a filter which prevents particulate buildup in the system. The conditioning water leaves the filter and enters parallel 3-hp and 1-hp pumps. These pumps are controlled by two Allen-Bradely® 1305 variable speed controllers mounted on the control panel. The water exits the pumps and flows into two 25 kW capacity Flat Plate® heat exchangers (see Fig. 14).

Conditioning Loop 1 is connected to a smaller 1 kW FTS® Maxi-Cool chiller, while Conditioning Loop 2 is connected to a larger 50 kW HX540 NESLAB® chiller providing broader range of water temperatures. Once exiting the heat exchangers, the water flow rate is measured by a Micro Motion® A351 Corriolis mass flow meter. A Micro Motion RFT 9739 controller is utilized to monitor flow on the loop's control panel. For final temperature control, the water enters a series of resistive heaters. The water flows first through a 7.5 kW heater and is followed by a 6kW, 3 kW, and 1 kW heater. At each heating element a RTD measures the water outlet temperature. These measurements are relayed back to Watlow® 96 controller, which monitors the firing of the heater elements. The conditioning loop heaters are shown in Fig. 15. Once through the heater series, the water exits the conditioning loop system through another quick disconnect and flows into the flex hose heading toward an air handler coil.

Figure 14 Flat Plate® heat exchangers in the Air Handler Conditioning Loop heater section.

Figure 15 Watlow® resistive heaters (1 kW, 3kW, 6kW, and 7.5kW) in the Air Handler Conditioning Loop.

Figure 16 Maxi-Cool chillers used for supplement heating and cooling for Air Handler Conditioning Loop and Refrigerant Loop.

Figure 17 HX540 NESLAB® chiller used for supplement cooling for Air Handler Conditioning Loop.

4.3.2.1.3 Spray Conditioning Loops

The water used in the actual DCHX loop is conditioned in a different loop contained in the wind tunnel base. The loop is constructed of ½" stainless steel tubing. Starting from the make-up tank, the water flows through a filter before entering a Flat Plate heat exchanger. Here the water is cooled as an FTS Maxi-cool chiller is circulating refrigerant on the opposing side of the heat exchanger. From there the water flows to an accumulator up-stream of two pumps to ensure that the pumps have a positive pressure head at all times. The water is pumped through the system by either a 1 hp or a 3 hp gear pump connected in parallel (see Fig. 18). Each pump is controlled by a PowerFlex® 4 controller. The water is pumped through a filter before it flows through a Micro Motion® Model D mass flow meter used for monitoring the flow rate (Fig. 19). After the water flows through the flow meter it enters the resistive heater section. Three 1 kW heaters are present for final temperature adjustment or auxiliary loading (see Fig. 20). One 1 kW heater cannot be adjusted and fires at full power when turned on. The other two 1 kW heaters are coupled in series and connected to a Watlow® 96 controller which can vary the output power from 0-100%. The water then flows out to a set of valves and a pressure gage so that the water may be bypassed (so that the loop can be brought to quasi-steady state) or delivered directly to the nozzle (see Fig. 21). The spray nozzle holder is fitted to hold a thermistor which measures the water temperature just before it is sprayed into the test section (see Fig. 21). After being sprayed into the test section, the water collects in the lower tray which is also fitted with a thermistor probe to measure the exiting water temperature. The water drains from the bin under its own weight to the make-up tank, where the cycle starts again.

Figure 18 Stacked 1-hp and 3-hp pumps for spray water loop.

Figure 19 Micro Motion® flow meter used for water flow measurement.

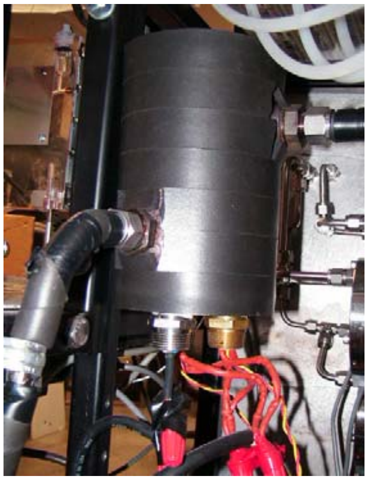

Figure 20 Heating section of spray water loop.

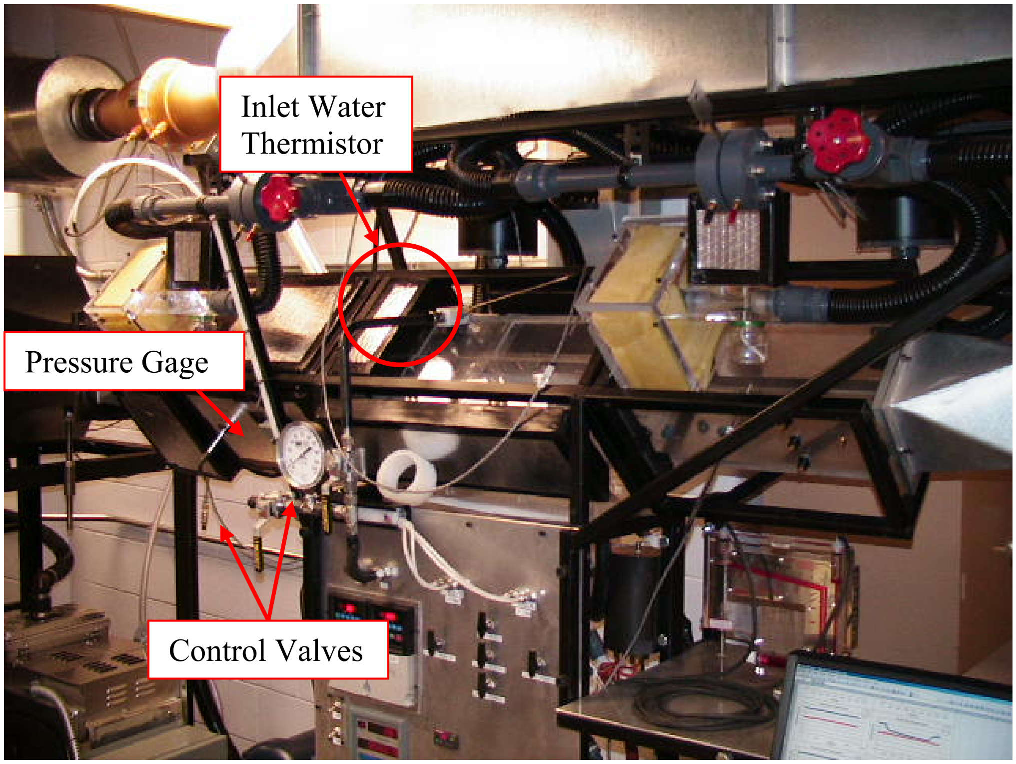

Figure 21 Wind tunnel showing the valve system, pressure monitor, and inlet water temperature thermistor.

4.3.2.2 Instrumentation

To effectively evaluate the DCHX performance, the experimental system must be extensively instrumented. The instrumentation was chosen primarily to maximize accuracy since total energy transfer of the small scale heat exchanger was less than 2 kW. On such a small scale, even small inaccuracies in measurement can become a sizeable percentage of the total measure.

4.3.2.2.1 Air Side Temperature Measurement

Determining the total heat transfer of a DCHX requires measurement of the air side heat transfer, or the change in air temperature and humidity. Thus, a sample of air is taken before and after the test section. The custom built air sampling/measuring systems (Fig. 22) were developed in accordance with ASHRAE Standard 33-2000 [25] and through constant upgrades of the wind tunnel. The air temperature measurement system consists of an air sampling device, a measurement section, a valve and orifice plate for air flow regulation and a fan (see Figs. 22-25).

3/8 inch copper tubes are used to sample the moist air 22 inches upstream from the test section and 2½ inches downstream from test section. The copper tubing is inserted into nylon compression fittings and manifolded together outside the wind tunnel in a series of elbow and T-fittings creating the sampling “tree”. Once the air exits the manifold it enters the acrylic measurement section. Each acrylic block suspends two 9 inch stainless-steel shielded 4-wire Thermoinc® thermistors, one measuring the dry bulb temperature measurement the other measuring the wet bulb temperature. The thermistor probes are sealed and held by compression fittings so that their tips are directly in the flow stream of the sampled air. For the wet bulb measurements, 3-5 inch long cotton wicks are loosely slid over the probe. The free end of the wick is suspended in a jar of distilled water. Two Dwyer® Temperature/Humidity Probe are also placed in the center of the duct and are used to check for abnormalities in the system and offer additional verification of the dry bulb temperature and relative humidity.

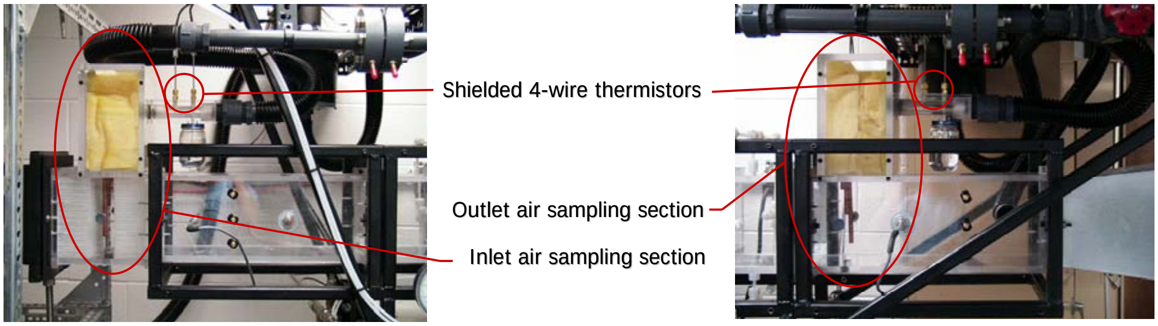

Figure 22 Air sampling and dry and wet bulb temperature measuring devices (Note that the wind tunnel is in a different configuration with insulation removed for clarity).

To accurately measure the wet bulb temperatures, an air velocity across the probes tips must be maintained between 3.6 m/s and 5.1 m/s in accordance to ASHRAE Standard 41.2 [26]. To supply this air velocity to the temperature measurement apparatus, air is pulled through each measurement apparatus by a 1/15 hp centrifugal blower, as shown by Fig. 23. Upstream of each fan is an orifice plate and gate valve, for measurement and regulation of the air velocity (Fig 24). Differential pressure measurements in the orifice plate are monitored by an inclined monometer to ensure that the correct air velocity flowed through each measurement apparatus. The sampled inlet air is returned to the air handler from the downstream side of the axial fan. The outlet sampled air is returned to the primary duct 12” downstream of the outlet sampling tree, so that the sampled air can be accounted for during air flow measurements.

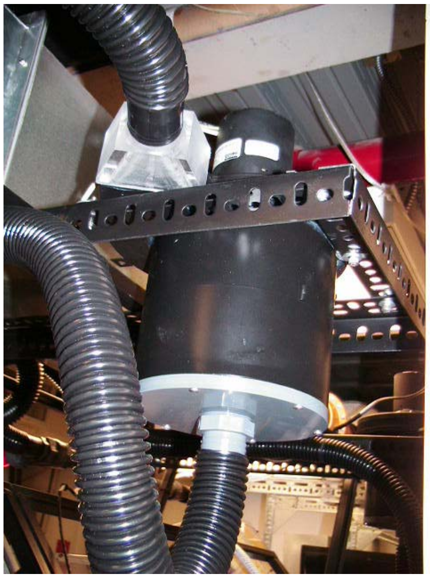

Figure 23 One of two blowers used to power the air sampling measurements.

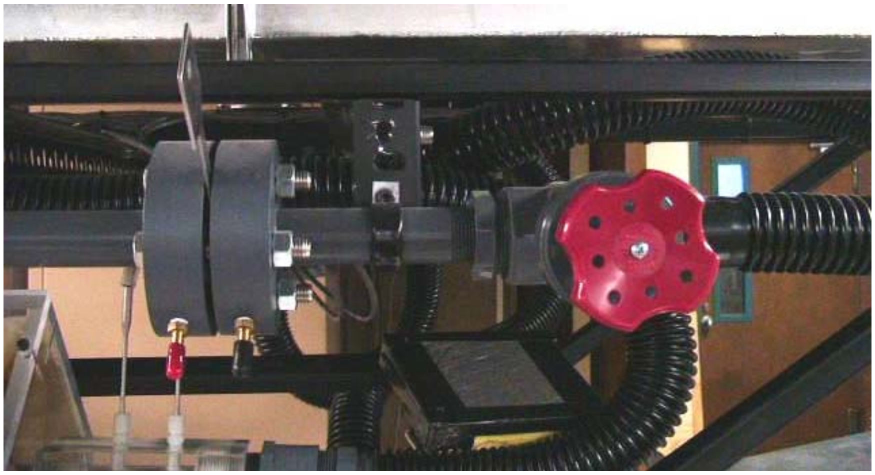

Figure 24 Air flow regulation for temperature measurement.

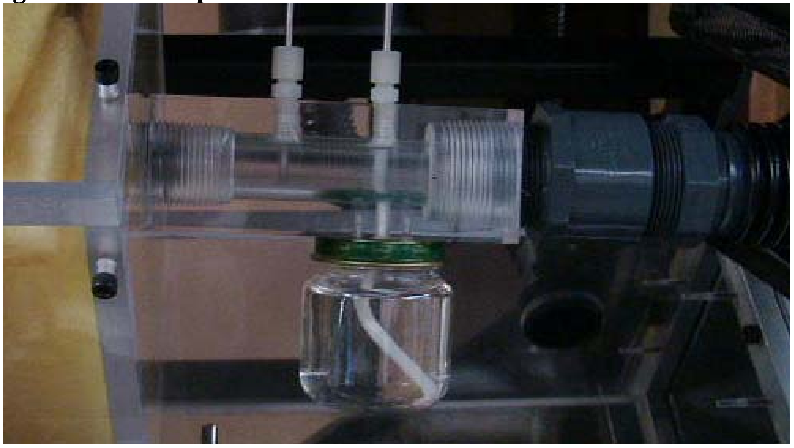

Figure 25 Air dry and wet bulb temperature measurement system.

4.3.2.2.2 Pressure Drop Measurement

To measure the pressure drop across the DCHX, two pressure taps have been incorporated into the test section. The 0.06 inch diameter taps were drilled flush to the wall centered along each wall face, 3 inches in front of the coil and 3 inches behind the spray as according to ASNI/ASHRAE 41.2 1987 [26]. On the outside of the test section ¼ inch NPT pipe threads were tapped into the backside of the pressure taps. Plastic compression fittings were inserted into the pipe threads and ¼ inch plastic tubing was used to connect the taps to the Validyne DP-103 differential pressure transducers. The transducers were connected together with ¼ inch stainless steel tubing and equipped with bypass valves (Fig. 26). The transducers were connected to a CD280 Multi-Channel Carrier Demodulator which converted the transducer output to a ±10VDC output for DAQ measurement.

The use of two transducers allows for a broader range in measurement as one of the transducer acts for pressure drops 0-.35 inches H_2O and the other a higher range to 2.22 inches of H_2O. To protect the low pressure transducer during high pressure ranges, shut off valves were inserted before and after the transducer to avoid over pressuring and damaging the diaphragm. From ASHRAE Standard 33-2000 6.2.4 [25] accuracy of pressure measurement is to be at least 0.005 inches of H_2O. With the current set up the typical pressure drop uncertainty across the coil for a given test is at this 0.005 inches of H_2O requirement. Calibration curves and detailed calibration procedures of the transducers can be seen in the Appendix section 8.2.

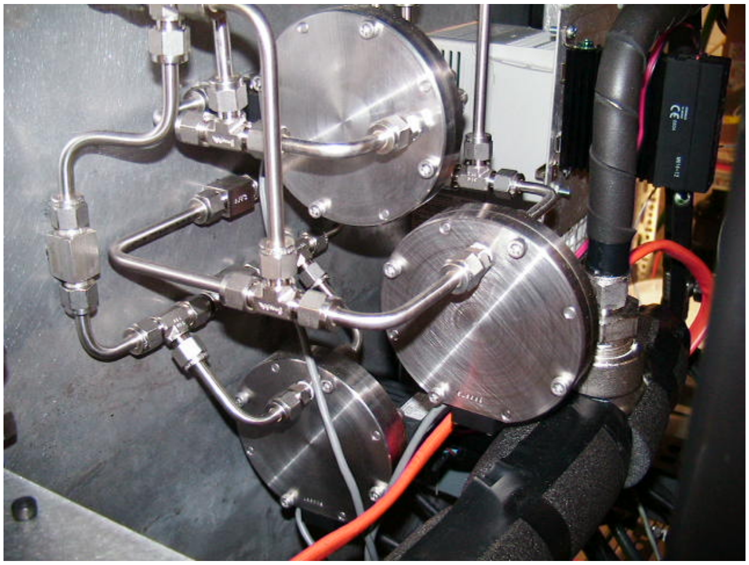

Figure 26 Differential pressure transducers for measuring pressure drop through the test section and through laminar flow element.

4.3.2.2.3 Air Flow Measurement

A pressure drop measurement across the Merriam® Laminar Flow Element (LFE) meter (model 50MC2-4-1, see Fig. 27) was obtained by connecting the orifice meter to a DP-103 Validyne® Differential Pressure Transducer with a range of 0-2.22 inches of H_2O. This transducer was connected to the same CD280 Multi-Channel Carrier Demodulator that the coil pressure drop transducers were connected to.

For accurate volumetric flows in the LFE, both the properties of the entering air and its absolute pressure are measured. The dry bulb temperature is measured by stainless-steel shielded four-wire Thermoinc® thermistors whose probe tip was inserted directly into the air flow at the outlet of the LFE. Assuming that no moisture in the air is lost between the outlet of the test section and inlet of the LFE, the humidity ratio at the test section outlet and LFE entrance are assumed equal. With the dry bulb temperature and humidity ratio, all needed air properties can be calculated. The absolute pressure is measured by a Princo Fortin Tube Mercurial Barometer, (Fig. 28).

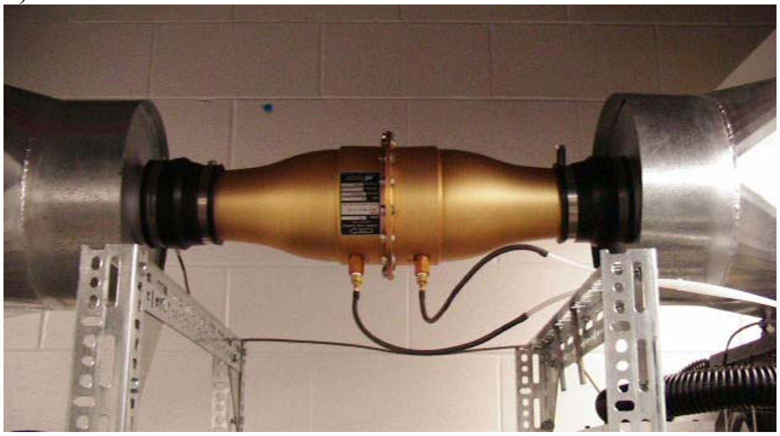

Figure 27 Laminar Flow Element used for air volumetric flow rate measurements.

Figure 28 Princo Fortin Tube Mercurial Barometer.

The calibrated LFE is used to determine the actual air volumetric flow rate using equations provided in the supplied operations manual [27]. The flow rate is obtained by measuring the differential pressure across the LFE and the outlet air temperature at the LFE. The calibration curve from the LFE (see Appendix) gives the uncorrected flow rate, $\dot{V}_{LFE}$, in terms of differential pressure. But, to correct for variations in the calibration, two correction factors must be considered. The first correction factor deals with the reference temperature of the *ΔP* sensor, and the second deals with viscous effects.

Because the calibration curve is given at a water reference temperature of 4˚C, the ratio water densities at there reference temperatures must be multiplied to the pressure drop across the LFE.

$$C_{\Delta P} = \frac{\left(\text{density of } \mathrm{H_2O} \text{ @ device temperature reference}\right)}{\left(\text{density of } \mathrm{H_2O} \text{ @ } 4°\mathrm{C}\right)} \tag{17}$$

The density of water at the device reference temperature can be obtained using water density tables for the ambient temperature, while also noting that the density of water at 4˚C is 999.969 kg/m^3 (62.426 lbs/ft^3).

To correct for vicious effects during calibration, the uncorrected flow rate is multiplied by a correction factor:

$$C_{\mu} = \left(\frac{\mu_{std}}{\mu_f}\right) = \frac{\left(\text{viscosity of flowing gas at } 70°\mathrm{F}\right)}{\left(\text{viscosity of flowing gas at flowing temperature}\right)}. \tag{18}$$

The μ_{std} or calibrated viscosity is given as 181.87 micropoise. The reference viscosity also in micropoise, μ_f, is more involved and defined as:

$$\mu_f = \left(\frac{14.58 T_{db,LFE}^{\ 3/2}}{110.4 + T_{db,LFE}}\right) \times \left(\frac{\mu_{wet}}{\mu_{dry}}\right), \tag{19}$$

where $T_{db,LFE}$ is the LFE dry-bulb temperature in Kelvin, μ_{wet} is the viscosity of moist air and μ_{dry} is the viscosity of dry air. Through the use of the Southerland equation the dry air viscosity can be given by,

$$\mu_{dry} = \frac{1.458 \times 10^{-6} \sqrt{T_{db,LFE}}}{1 + \dfrac{110.4}{T_{db,LFE}}}, \tag{20}$$

again where the $T_{db,LFE}$ is the LFE dry-bulb temperature in Kelvin. The wet air viscosity can be estimated by curve fitting Kestin and Whitelaw's [43] viscosity of wet air tabular data as a function of air temperature and mol fraction of water to air, as seen in Fig. 29.

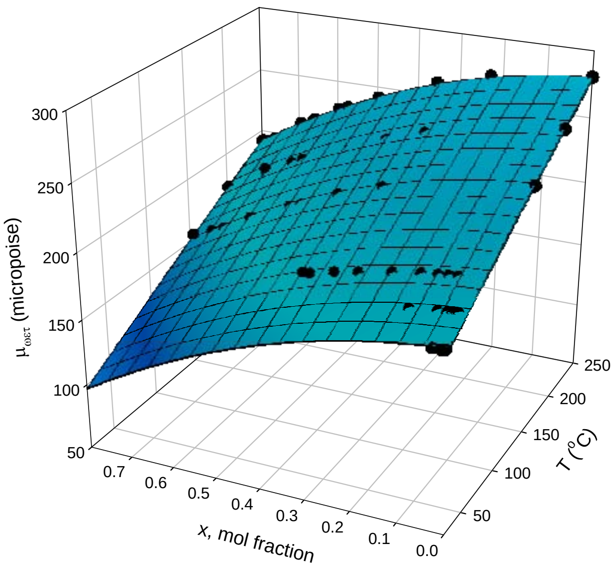

Figure 29 Three dimensional plot of viscosity with respect to mol fraction of and dry bulb temperature.

Using Sigma Plot software for the three-dimensional curve fit option the equation for wet air viscosity is estimated as,

$$\mu_{wet} = 174.1648 + 0.4556 T_{db,LFE} - 20.4213 X - 0.0001 T_{db,LFE}{}^{2} - 113.3991 X^{2} \tag{21}$$

where $T_{db,LFE}$ is the air temperature in °C and X is the mol fraction of water to air. The mol fraction of the air was calculated using

$$X = \frac{n_{H_2O}}{n_{air} + n_{H_2O}} = \frac{\dfrac{W}{M_{H_2O}}}{\dfrac{W}{M_{H_2O}} + \dfrac{1}{M_{air}}} \tag{22}$$

where n_{H2O} and n_{air} are the number of moles of water and air respectively, W is the humidity ratio and M_{H2O} and M_{air} are the molecular mass of water and air. The molecular mass of water is 18.016 g/mol and while the molecular mass of air is 28.97 g/mol. Assuming there is one mole of air, the ratio of number of moles of water to the total number of moles can be estimated.

The actual volumetric flow rate can then be calculated by multiplying this viscosity correction factor to the already pressure corrected LFE flow rate. Thus, the equation for the actual volumetric flow rate becomes

$$\dot{V}_{actual} = C_{\mu} \times \dot{V}_{LFE}\left(\Delta P, C_{\Delta P}\right). \tag{23}$$

With the actual volumetric flow rate known the actual air face velocity through the test coil can be calculated using,

$$\mathrm{U}_{actual} = \frac{\dot{V}_{actual}}{A_{duct}}, \tag{24}$$

where A_{duct} is the cross-sectional area of the duct. The velocity calculated through the test section assumes that the same volumetric flow rate through the LFE is the same as that of the test section. Thus, the air is treated as an incompressible fluid and the densities at the LFE and the test section are assumed constant in the flow calculations.

According to ASHRAE Standard 41.2-1987 [26] the accuracy of air flow measurement must be within 1.2% of the flow. The LFE is has accuracy of 1-2% with accuracy improving at higher flow rates. The calibration equations and uncertainty analysis are included in the Appendix, section 8.2.

4.3.2.2.4 Water Side Temperature Measurement

The calibration data and uncertainty analysis of the thermistors used to measure the water temperature can be seen in the Appendix. The inlet measurement is straight-forward, however the exiting water temperature measurement might not be as accurate as the rest of the system. The goal is to measure the temperature of the drops immediately after the traverse the test section, but that is not practically possible. So the drops, after coming together in the collection tray, form a pool of water. This pool's temperature is what is actually measured. Further, this pool sits on an acrylic floor of the test section, which may transfer some small amount of heat. These slight inaccuracies could play a role in energy balances or other metrics that rely on the water temperature information.

4.3.2.2.5 Water Flow Measurement

The water mass flow rate was measured with a D25 MicroMotion® flow meter. The flow meter was connected to a Model 9712 Remote Flow Transmitter (RTF), which converted the flow meter output to a frequency output for DAQ measurement. The RFT was also coupled with a MicroMotion® Digital Rate Totalizer which displays mass flow rate on the wind tunnel control panel. The flow meter was selected for its high accuracy and low maintenance. The calibration of the Micro Motion flow meter took place outside of the laboratory so detailed calibration procedures are not available. The uncertainty for the water flow measurements with the factory calibration was found to be 1-3% of the mass flow rate measurement.

4.3.2.2 Electrical Hardware

The data acquisition system (DAQ) used in this experimental investigation was an Intergra Series Keithley 2701 Ethernet enabled DAQ equipped with a Keithley 7708 multiplexer card. The DAQ was connected to an IBM ThinkPad Laptop through the computers Ethernet port. The data acquisition system, the 2701 DMM and IBM laptop, are shown in Fig. 30.

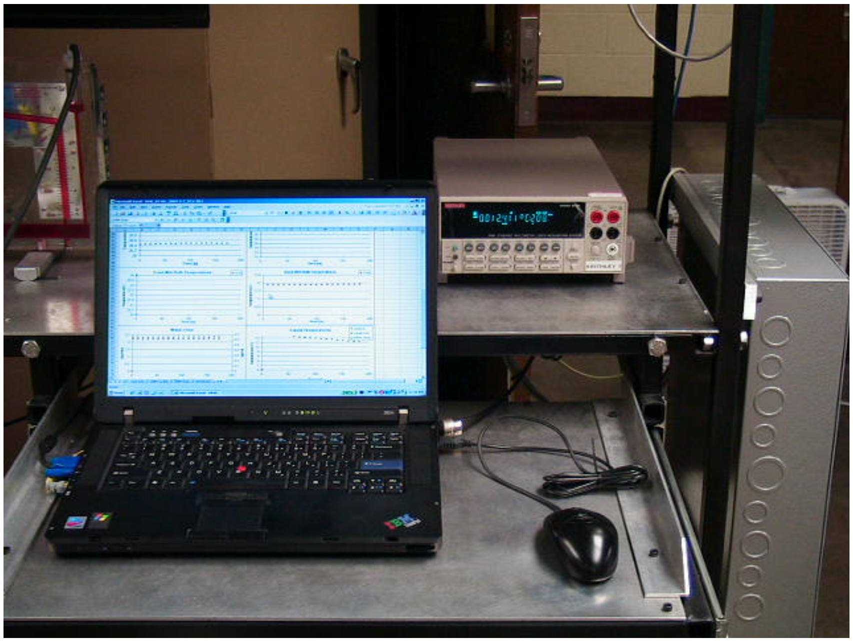

Figure 30 Kiethley 2701 DAQ with 7708 multiplexer card.

4.3.3 Data Reduction

The main data reduction follows the method outlined by ASHRAE [28] which is used to determine the moist air properties used in the energy calculations. This ASHRAE method will be outlined here.

The basic air side heat transfer rate must be calculated by using the actual air velocity:

$$Q_{air} = \dot{m}_{air}\left(h_{in} - h_{out}\right), \tag{25}$$

where $\dot{m}_{air}$, is the mass flow rate of water and h_{in} and h_{out} represent the inlet and outlet air enthalpies respectively. The enthalpy for both the inlet and outlet conditions is determined by [28]:

$$h = 1.006T_{db} + W(2501 + 1.805T_{db})\text{. [kJ/kg]} \tag{26}$$

Here T_{db} is the dry bulb temperature in °C, of the air and W is the humidity ratio.

The humidity ratio, W, is a function of the dry and wet bulb temperatures and the atmospheric pressure. These factors are related through the humidity ratio of moist air at saturation thermodynamic wet-bulb temperature,

$$W_{s,wb} = 0.62198\frac{p_{ws}}{p - p_{ws}}\text{, [kg/kg]} \tag{27}$$

where p is the atmospheric pressure in kPa and p_{ws} is the pressure of pure water in kPa. The saturation pressure was calculated by [28]

$$\ln p_{ws} = C_1/T_{wb} + C_2 + C_3T_{wb} + C_4T_{wb}^{\ 2} + C_5T_{wb}^{\ 3} + C_6\ln T_{wb} \tag{28}$$

$$
\begin{aligned}
C_1 &= -5.8002206E+03\\
C_2 &= 1.3914993E+00\\
C_3 &= -4.8640239E-02\\
C_4 &= 4.1764768E-05\\
C_5 &= -1.4452093E-08\\
C_6 &= 6.5459673E+00
\end{aligned}
$$

where T_{wb} is the wet-bulb temperature in Kelvin and p_{ws} is the pressure of pure water again in kPa. Finally, the humidity ratio, Eq. (29), can be solved with the factors calculated thus far:

$$W = \frac{(2501 - 2.381T_{wb})W_{s,wb} - 1.006(T_{db} - T_{wb})}{2501 + 1.805T_{db} - 4.186T_{wb}}, \text{ [kg/kg]} \tag{29}$$

To finish calculating the heat transfer on the air side the actual mass flow rate must be determined. The mass flow rate of the air is calculated by using the volumetric flow obtained from the LFE and its calibration curve,

$$\dot{m}_{air} = \frac{\mathrm{U}_{actual}}{v} A, \text{ [kg/s]} \tag{30}$$

where $\vec{v}_{actual}$ is the actual air face velocity provided by LFE, v is the moist air viscosity and A is the cross-sectional area of the wind tunnel. The cross-sectional area of the duct is 0.0232 m^3. The moist air viscosity is calculated using

$$v = \frac{0.2871(T_{db,LFE} + 273.15)(1 + 1.6078W)}{p} \text{ [m}^3\text{/kg].} \tag{31}$$

In Eq. (31) the $T_{db,LFE}$ represents the LFE dry-bulb temperature and W represents the humidity ratio at the outlet of the test coil. Solving for the air viscosity and the mass allows the air side heat transfer to be determined.

The water side heat transfer is much simpler, as seen in Eq. (32) [29]

$$Q_{H_2O} = \dot{m}_{H_2O} C_p (T_{in} - T_{out}), \text{ [W]} \tag{32}$$

where $\dot{m}_{H_2O}$ is the mass flow rate, T_{in} and T_{out} are the inlet and outlet water temperatures respectively and C_p is the specific heat of the water. The average of the inlet and outlet temperatures is used in a table [29] to find the specific heat of the water. It should be noted that T_{in} was not corrected due to the change in pressure across the spray nozzle. The temperature change was almost an order of magnitude less than the uncertainty.

4.3.4 Uncertainty Analysis

The uncertainty is calculated following standard uncorrelated variable error propagation models and statistical methods. The uncertainty of a given measurement Δf is given by

$$\Delta f = \left(\sum_j \left(\frac{\partial f}{\partial x_j} \Delta x_j \right)^2 \right)^{1/2} \tag{33}$$

where f is a function of x_j and the uncertainty of that variable, Δx_j. A detailed calculation is shown in Appendix, section 8.3. Note that a detailed discussion of the wind tunnel development and its uncertainties in operation are included in a Master's thesis by Sean C. Staed entitled "Creation of "Unit Cell" Concept for Air-to-Liquid Heat Exchanger Research and Development" [30].

In this type of analysis, the uncertainties increase as the measurement levels increase. This makes reporting the uncertainties somewhat challenging. Error bars are not included on the experimental results plots for sake of clarity. However, the average uncertainty will be listed here for the following results in section 5.3.1 and 8.6. Additionally, the measurements, results, and specific uncertainties for each measurement are reported in the Appendix, section 8.6.

Table 2 Average experimental uncertainties.

Average Measurement Uncertainty		
Measure	Reading	Average % of measure
Air Tdb [C]	0.05	0.60%
Air Twb [C]	0.06	0.60%
Air Flow [kg/m]	0.17	6.93%
Water T [C]	0.05	0.60%
Water Flow [kg/m]	0.01	0.27%
Average Response Uncertainty		
Qtotal [W]	29.6	7.87%
Qsens [W]	27.4	7.63%
Sensible *UA* [W/K]	1.2	4.68%

The experimental repeatability was checked during the calculation of *UA* (used in the correlation development as introduced in section 3.4). Given the time required to complete a test, it was not practical to rerun the entire series of tests. Therefore, certain specific tests were repeated, hopefully to reveal the worst cases for repeatability. In this repeatability study, the largest and smallest nozzles were investigated. The overall heat transfer coefficients for various tests are shown in Fig. 31 with the repeated tests being noted as "RX" in the legend. Note that this level of repeatability is considered quite satisfactory considering that over seven months (January to August) had passed since the first series of tests. This created a problem as the 32% relative humidity conditions could not be reproduced in the summer month (given the naturally higher relative humidity), however, the 56% and 68% conditions could be recreated, and thus, were investigated.

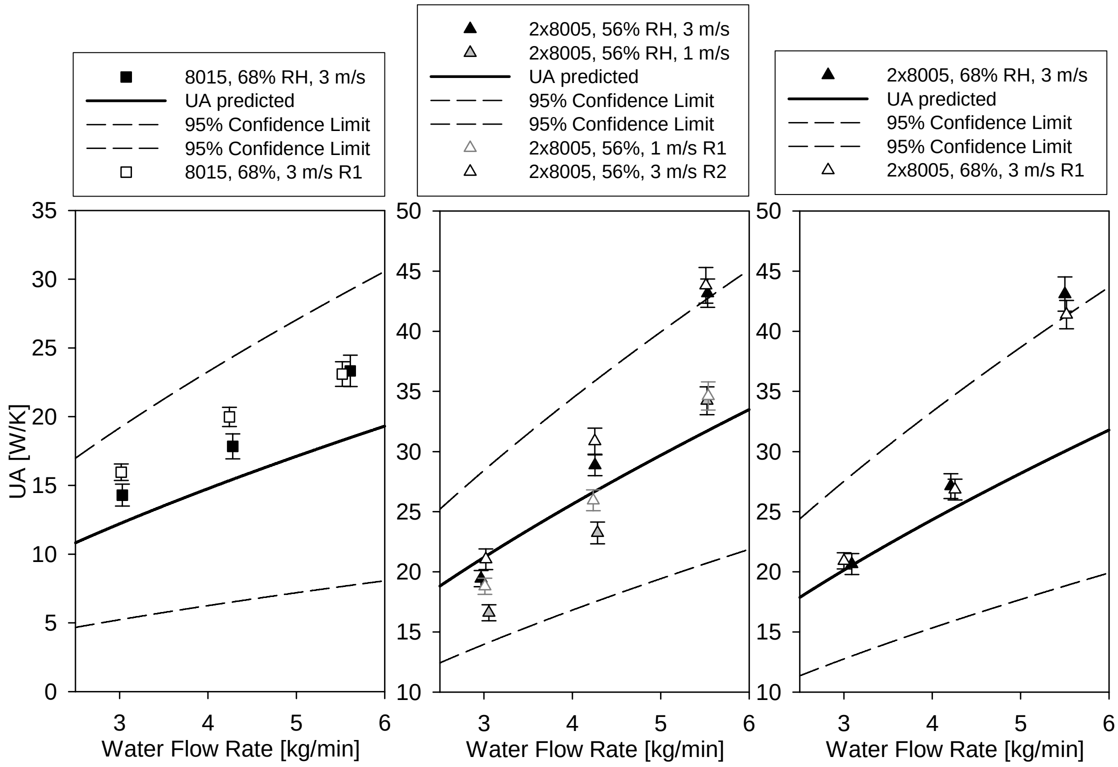

Figure 31 Repeatability results.

The seven-month gap potentially introduced a few key sources for error. One source of error was the laboratory conditions. The laboratory (room C1204, Lafferre Hall) lies on the main branch of an HVAC air handler. The old HVAC system is notorious for falling out of adjustment, consequently delivering most of its air to the laboratory in which testing took place. As such, the laboratory temperature in the winter months climbs well over 27 ºC, while plunging well below 19 ºC in the summer months. This change in the ambient temperatures could affect the data by accentuating error related to heat leakage; however, the repeatability tests do not show consistent deviation. This data, therefore, indicates that the system is relatively insensitive to the environment (well insulated).

The second source of error centers on the accumulation of scale on the drift eliminator and honeycomb cell walls. The presence of this hard scale affects the wetting characteristics on these surfaces. It is then reasoned that these surfaces then are more likely to hold water – possibly contributing to a saturation effect (described in more detail in section 5.5.2). Also, note that this same scale was present to a smaller degree in the nozzles. This could possibly change the spray characteristics slightly.

The final point to mention would be any changes to the instrument calibration. The random variation in repeatability also indicates that no major calibration changes occurred in the seven-month ageing. As a whole then, the system and methods appear to be robust.

4.3.5 Testing Matrix

The performance of the system is 'mapped' by experimental trials with the temperature and humidity controlled wind tunnel. The Master's work showed that some emphasis should be placed on the free stream humidity and the drop size, which is basically regulated by nozzle size. Thus, three settings are used for both of these variables. Further, though not addressed with the Master's work, the mass flow rate of the water will be incremented through three settings. Two water temperature settings and two air temperature settings will be used, as well as two airside flow rates. The values of these settings are listed in Table 3.

The 26.7 ºC dry bulb air temperature has been selected to represent typical return air conditions for HVAC applications. It should be noted that this test temperature has also been selected as it is used by Carrier when reporting the performance of some direct expansion coils [31]. The 33 ºC temperature is simply used to represent 'off design' HVAC conditions. The relative humidities, again, are chosen to approximately coincide with the Carrier data. The face velocities are chosen to lie slightly out of the range of typical velocities for direct expansion coils. The 5 ºC water temperature was chosen as a 'safety' low limit as their may be some issues in the future with operating any closer to the freezing point of water. The 10 ºC water temperature is taken to represent a possible working fluid temperature if an intermediate heat exchanger were used in conjunction with 7.5 ºC chilled water supplied by a district loop.

The water flow rates are restricted by the nozzles selected. The goal is to have as wide a droplet size distribution as possible between the three nozzles. The maximum system operating pressure is set to be approximately 100 psi. At this pressure, the 8009 capacity nozzle will just reach 5.5 kg/min of flow. Two 8005 nozzles must be mounted in a special housing in order to achieve this 5.5 kg/min flow at approximately 90 psi. At the other end of the spectrum, the largest nozzle (8015) will flow 3 kg/min at 9 psi. In general, as the pressure is reduced below approximately 10 psi, the nozzle's fan pattern begins to decrease substantially; and consequently, the spray does not fan to cover the full cross section of the test chamber resulting in blow-by. Thus the 8015 is the largest nozzle that can be used with the 8009 and 2x8005 pairing.

It should be noted that a Laser Doppler system could be used to investigate the actual nozzles used to determine more accurate the drop size information. Though this information is not entirely necessary in light of practical applications, it may be useful in other investigations related to modeling the full spray.

The chosen test settings align with other experimental work by Yoo and Kwon [13]. For their experiments in a 30 cm x 30 cm [11.8 inch x 11.8 inch] test section, they use air velocities of 1-3 m/s (equating to a volumetric flow rate of 0.09-0.27 m^3/s) and water flow rates ranging 6-21 kg/min, inlet air temperatures of 24-38 ºC, and water temperatures of 4-16 ºC [13]. Simple math shows that the approximate ratio of volumetric air flow to volumetric flow rate of water for Yoo and Kwon's work for the low air flow rate ranges from 257 to 900, and for the high air flow rate it ranges from 771 to 2700. The same ratios for this work range from 250 to 460, and 760 to 1400 for the low and high air flow settings, respectively. This means that under some settings, when these ratios are approximately equal, the results could be compared for a kind of spray chamber effectiveness. This effectiveness might be described through ε-NTU methods as no inlet moisture content is provided by Yoo and Kwon [13].

Table 3 Independent variable values.

Air Temperature (dry bulb) [ºC (ºF)]	
26.7 (80.0)	
33.0 (91.4)	
Relative Humidity [%]	
32	
56	
68	
Air Flow Rate	
Face Velocity [m/s (ft/s)]	**Mass Flow Rate [kg/s]**
1 (3.3)	0.026
3 (9.8)	0.086
Water Temperature [ºC (ºF)]	
5.0 (41)	
10.0 (50)	
Water Flow Rate [kg/min (gpm)]	
3.00 (0.8)	
4.25 (1.1)	
5.50 (1.4)	
Nozzle	
Part Number (Spray Systems Co)	**Drop Size* [microns]**
8005	475
8009	690
8015	860

*Drop diameter estimated from nozzle manufacturer data. See discussion later in this section.

5.0 RESULTS

5.1 Spray Charging

5.1.1 Theoretical Analysis

The concept sketch for the charging system is detailed in Fig. 32. The system utilizes two, relatively small diameter, cylindrical electrodes. As pointed out by Law [23], electrode capacitance increases with size. The increase in capacitance results in an increased charge on the electrodes for a given potential, which may ultimately translate to an increased spray cloud current. Given this, the immediate conclusion is to maximize the size (and charge) on the electrodes.

However, increasing the size of the electrodes increases the risk of droplet deposition on them for two reasons. First, size increase effectively increases the target area for droplet deposition. Secondly, the larger charge acts to increase the Coulombic force which attracts the newly formed, oppositely charged drops back to deposit on the electrodes provided the drops have insufficient momentum to escape the field. In either case, without some way to continuously clean the electrodes, reverse ionization is more probable at higher voltages. The logic behind the proposed small electrode design is that the chance of droplet impact will be reduced due to the smaller target area. Further, the small electrodes cannot support the formation of large droplets which can, under the right conditions, form Taylor cones that lead to reverse ionization. This phenomenon has been shown to reduce the effect of the induction charging process [32]. It was further hypothesized that strategic placement of smaller electrodes can counter their loss of capacitance. This being said, a model was created to predict where that optimum region would be, and then make some estimation as to the expected charge on the spray/drops.

The spray current was developed to be a function of easily measured independent variables (note that the details of development may be found in the Appendix, section 8.1.2):

$$i_c = \frac{\varepsilon_o V_{ps} l_e}{3\ln\left(\frac{x_s}{r_e}\right)} \frac{x_s}{\left(x_s^2 + y^2\right)^{3/2}} \left(\frac{a_2 + b_2\sqrt{p}}{A_{orif}\sqrt{p}}\right) \tan\left(\frac{1}{2\left(a_1 + \frac{b_1}{p}\right)}\right). \tag{34}$$

The merit of this exercise is revealed by Fig. 33 as a clear region is defined wherein the droplets would receive the maximum charge.

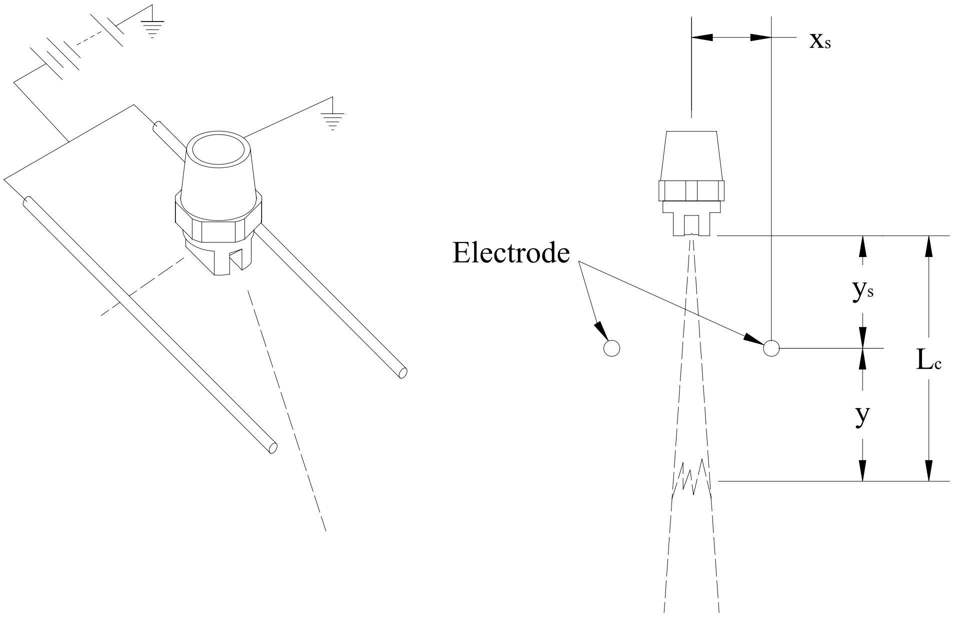

Figure 32 Electrode placement relative to the flat fan spray.

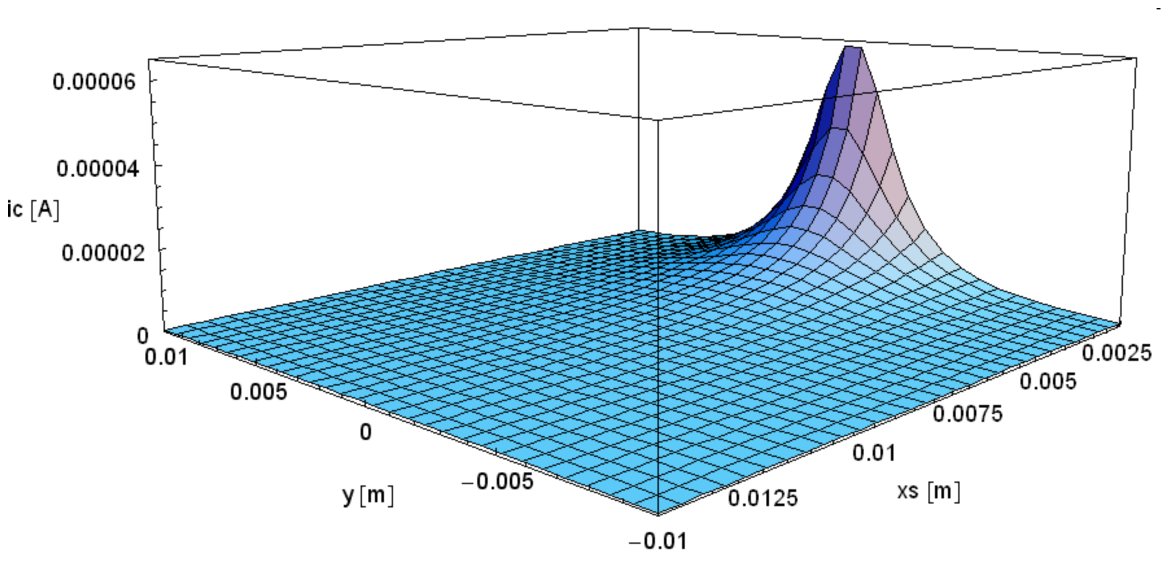

Figure 33 Analytic output of Eq. (34) showing how the spray cloud current increases as the electrodes are brought closer to the spray and into the droplet formation zone at *y*=0.

Though helpful in understanding the physics of the problem, this simple model was expected to have limited accuracy with respect to calculating the actual spray cloud, or deposition current for reasons addressed later. In any event, the firm conclusions to be drawn are that the deposition current should increase as the x-spacing of the electrodes is reduced and as the electrodes are brought into the region where the most droplets are being formed. Comparison of this simple model with experimental results highlights the significance of spray hydrodynamics on drop charging.

5.1.2 Experimental Results and Discussion

A few points concerning the nozzle's performance were first checked during shakedown testing. The hypothesis that the small electrodes would not experience the electrode wetting and subsequent reverse ionization was first tested. To do this, a negative voltage was applied to the electrodes as negative ion injection occurs more easily in air [33]. The system was run as the electrodes were charged to -2 kV DC and moved to various locations around the spray sheet. It was noticed that any substantial droplet deposition only occurred when the electrodes x-spacing was reduced below approximately 10 mm, especially when y_s (Fig. 32) increased. This results from the fact that the spray spreads in the direction normal to the induced factory spray angle, and is therefore closer to the electrodes at larger y-spacings. Once the electrodes were sufficiently wet, the power supply voltage was increased until corona discharge (reverse ionization) was observed. The limiting voltage was found to be approximately -7 kV DC. At this point though, the discharge did not occur from the ends of the electrodes, but from a drop that had formed into a Taylor cone on one of the electrode holders, as shown in Fig. 34. The only drop large enough to form into a sharp point and begin to emit was actually located on the head of a screw that held the electrodes in place. The other drops present on the electrodes did not form into injection sites.

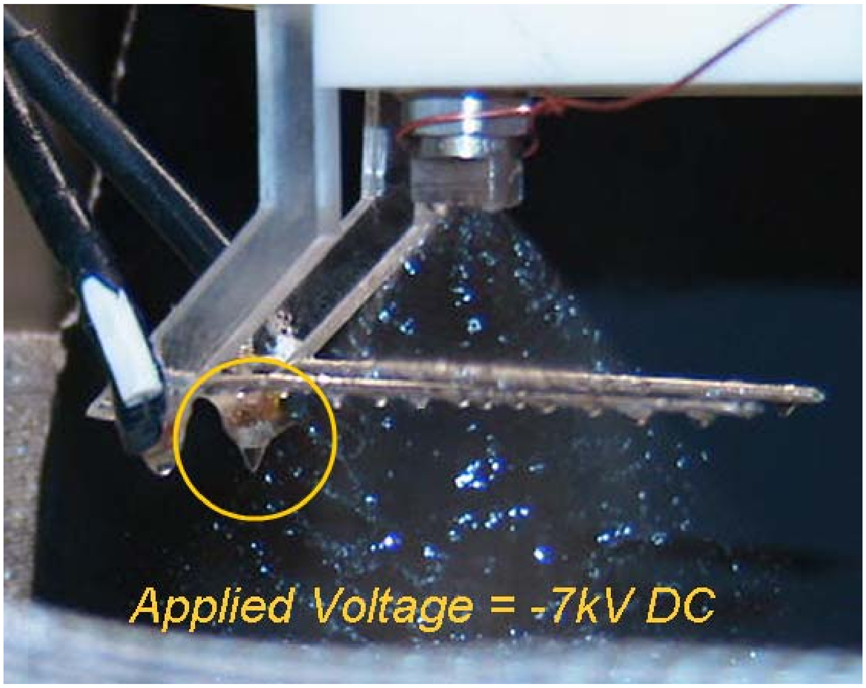

Figure 34 Photograph showing the nozzle operation at its limiting potential of -7 kV DC. Note the circle highlighting the only point of injection. The drops on the electrodes were too small to form into injection sites.

The repeatability of the system was investigated by varying the power supply voltage for a given electrode spacing. The system produced the same relation between deposition current and applied voltage (within the limits of error) for both upscale and downscale measurements. This point was reinforced as more data was amassed.

Another aspect of the system to be checked was the linear response to power supply voltage as indicated by the model. Figure 35a shows that the system did respond linearly to the power supply changes as predicted by the analytic solution.

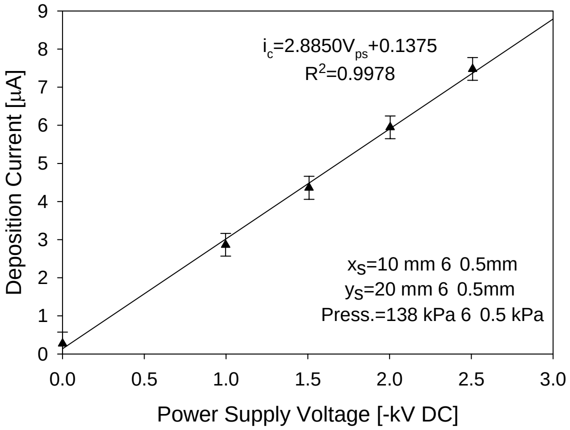

Figure 35a Linear response of deposition current as a function of power supply voltage.

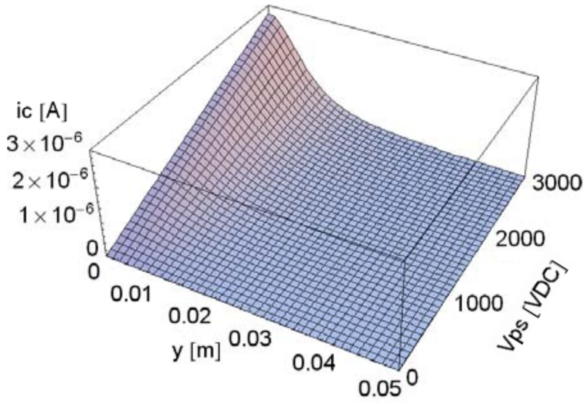

Figure 35b Analytic solution for deposition current as a function of the distance from the electrodes to the droplet formation zone (*y*) and power supply voltage.

Note though that in referencing between the analytic and experimental figures, the y-spacing, y_s, in the experimental data presented refers to the distance between the nozzle and the electrode. The y-spacing, y, in the analytic results is the distance between the electrodes and the theoretical droplet formation zone (ref. Fig. 32).

Inspection of Figs. 35a and 35b reveals that the analytic solution tends to underestimate the deposition current, contrary to what was reasoned in the previous section. The explanation of these differences requires a better understanding of the assumptions imbedded in the model which is derived in the Appendix, section 8.1.2. The spray current, Eq. (34), is directly proportional to the width of the spray at breakup. This width is calculated as a function of the spray angle, and perhaps more importantly, the coherent length. As Fig. B2 (in the Appendix) reveals, these variables are very difficult to quantify. Thus, any error in calculating the coefficients in Eqs. (B10) and (B11) directly translates to an error with the model. It appears that the coherent length was initially underestimated. This directly translates to the calculation of a smaller value for a spray width, and ultimately, the spray cloud current. Further, the real spray sheet has some finite thickness, ultimately resulting in a reduction in the distance between the spray sheet surface and the electrode surface (which also has a finite radius). Figure 33 gives insight into the effect of these variations in x-spacing as the sensitivity to the electrodes proximity to the breakup region is clearly deduced by the slope of the analytic solution.

In the real situation, the electrodes produce a field that charges all of the drops being formed. Those drops forming at farther distances from the electrodes are simply being charged to a lesser extent as the field there is weaker. This gives some merit to the larger parallel plate electrodes as they would essentially sustain a stronger field over the larger region in which the droplets form. However, it is felt that the smaller electrodes are still favorable for the aforementioned reasons, and that these results merely justify the efforts of this exercise. It is clear that the small electrodes will be most effective with a better understanding of the physics of not only the electrostatics of the problem, but the hydrodynamic aspects of the problem as well.

The last point verified during shakedown testing was the relation between the nozzle flow rate and deposition current. The nozzle pressure was varied for a fixed electrode spacing and voltage. The resulting deposition current is shown in Fig. 36a and the analytical solution is shown in Fig. 36b. Again, the predicted deposition current is lower than what was measured experimentally. This variation is explained with the previous reasoning.

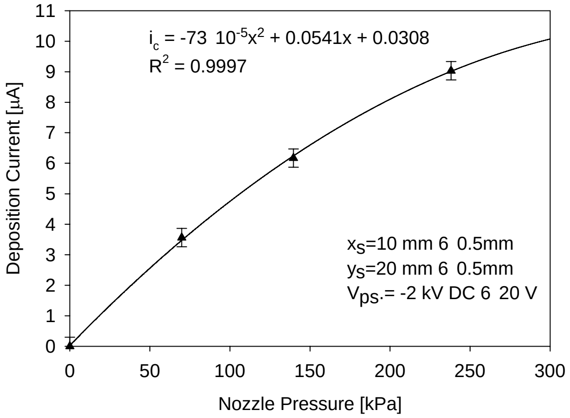

Figure 36a Deposition current as a function of nozzle pressure.

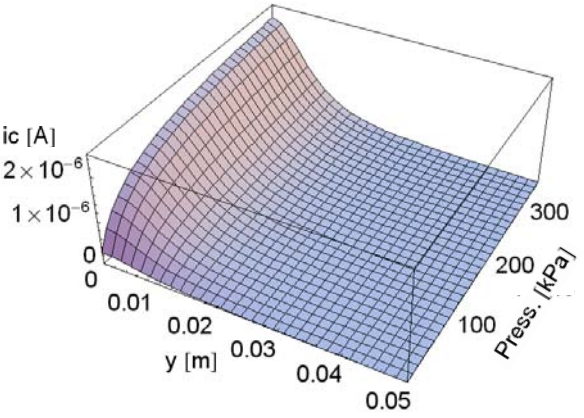

Figure 36b Analytic solution for deposition current as a function of the distance from the electrodes to the droplet formation zone (y) and nozzle pressure.

The main efforts of this exercise are geared toward finding the optimum electrode placement for a given spray generation nozzle. The model indicates that there exists a well defined optimum region. The intention of this exercise is to "map" the region around the spray in order to see if and where this optimum region is located with respect to a real spray. This mapping was carried out by fixing the power supply voltage at +2 kV DC with the nozzle pressure being maintained at 138 ± 0.7 kPa. The electrodes were then incrementally moved around the spray sheet region, and the corresponding deposition current was recorded and averaged. Figure 37 reveals how the analytic model trends for the same voltage and pressure values use in generating the measured experimental results, found in Fig. 38. Note that the individual data points in Fig. 38 have been connected for ease of visualization only. The actual experimental data has been included in the Appendix, section 8.4. Included in the tables is the average measured power supply current which should be zero in the theoretic case of induction charging. The presence of this current indicates current "leakage." In this case, most of this current is expected to arise from the droplets impacting the electrodes.

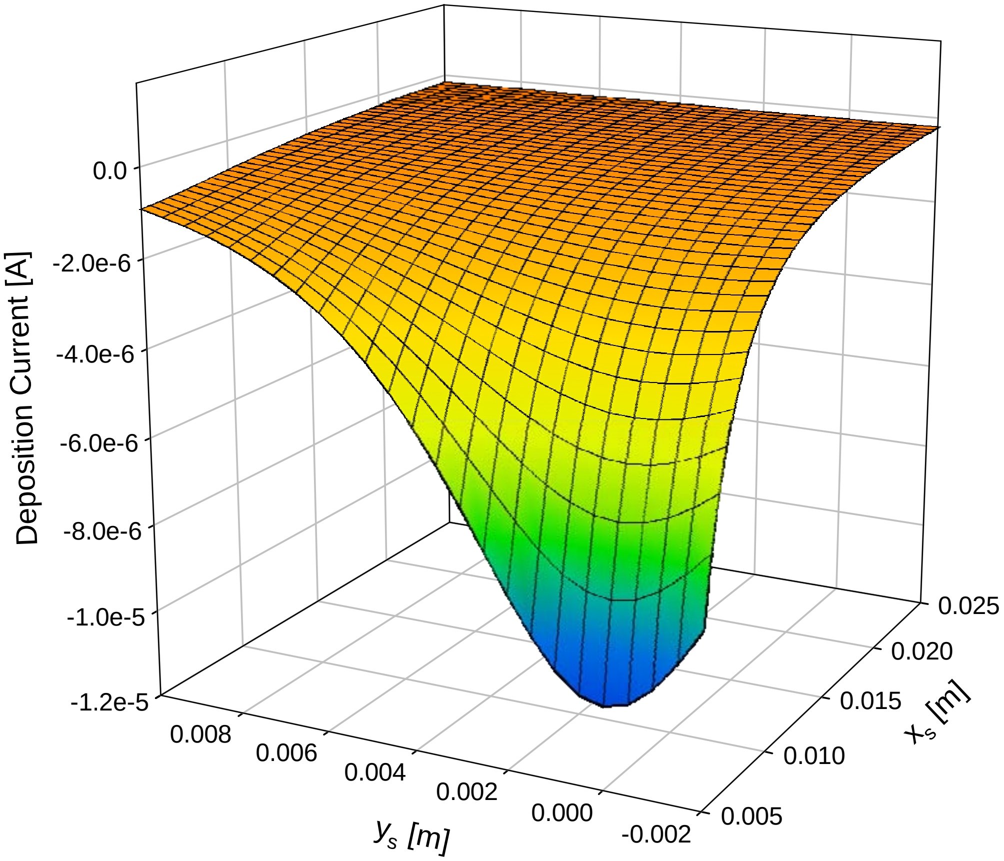

Figure 37 Analytic solution for deposition current as a function of electrode placement.

It is clear that the deposition current increases as the x-spacing decreases, as predicted by the analytic results. However, the experimental data does not show the same strong asymptotic behavior like the analytic solution as x_s becomes small. This is because more drops strike the electrodes as they are moved towards the spray. The negatively charged drops, after striking the electrodes, become positively charged, which results in a reduction of the net deposition current as they continue on to strike the collection screen. This behavior is verified by the data in Fig. 39. For spacings less than 10 mm, the droplet impact on the electrodes increases significantly as *y_s* increases where the power supply current drawn increases accordingly. The optimum electrode spacing in the real situation is actually around 10 mm, as seen in Fig. 38 and 39. In these figures, the sharp decrease in deposition current is seen for the 5 mm spacing as the electrodes are moved from 30 to 40 mm in the vertical direction. At this location the spray sheet begins its transformation to droplets (see Fig. 40) and the number of drops in the region becomes much greater, along with the probability of an electrode impact. Thus, the hydrodynamics of the spray clearly arise as a key factor not addressed by the model.

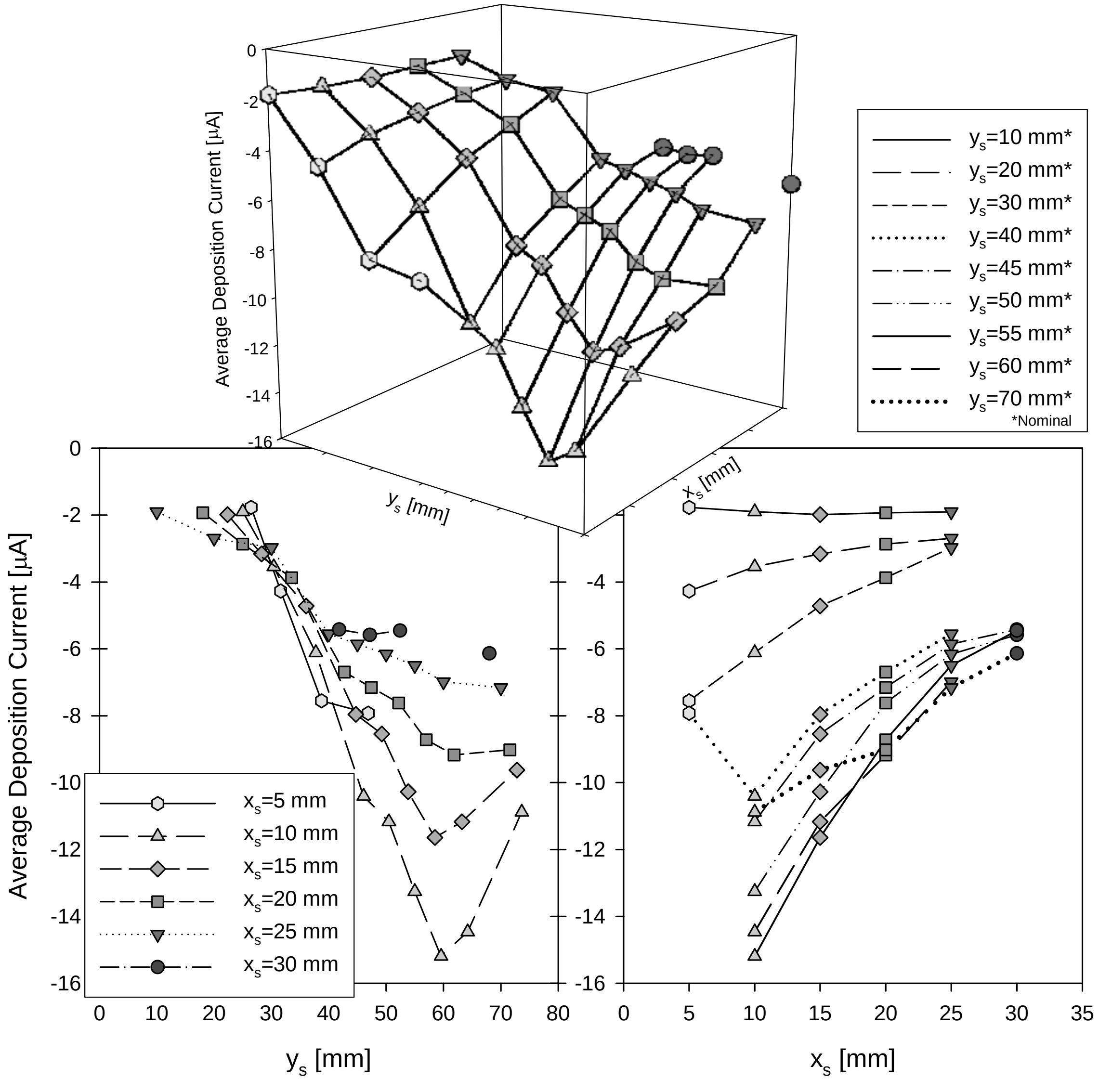

Figure 38 Deposition current averaged over 3 trials (for most points) for indicated electrode placements. Raw data and relevant uncertainties may be found in the appendix. The 3-D plot has been decomposed into orthogonal views (below) for more precise visualization. Note that the lines are only included for ease of visualization and identification only (no trend or curve fit is applied).

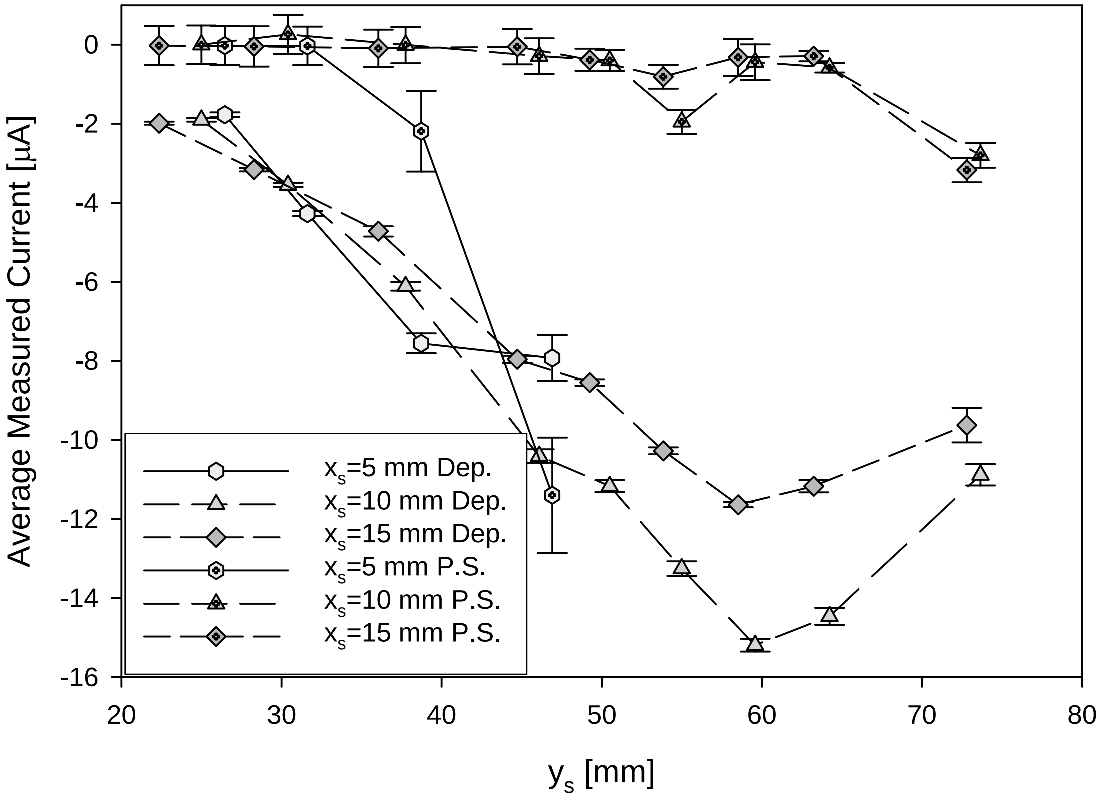

Figure 39 The measured deposition current (Dep.) and negative power supply current (P.S.) demonstrating how droplet impact is detected by measurement uncertainty and power supply current drawn.

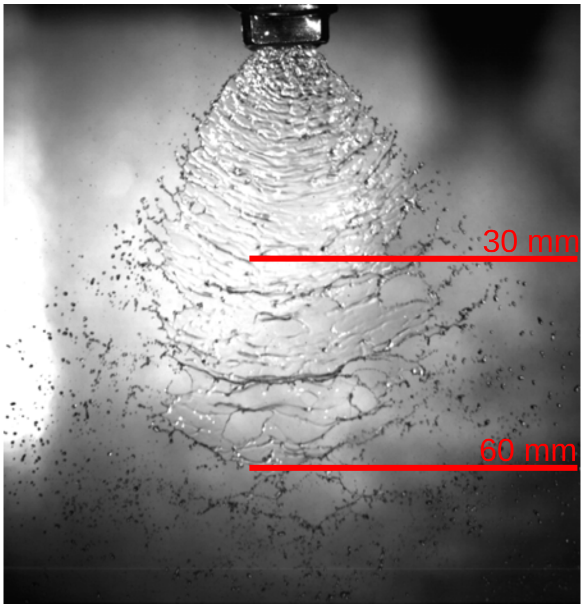

Figure 40 Enhanced high speed photograph indicating the scale of the spray sheet.

The characteristic dip, or increase, for the deposition current as a function of the y-position as seen in Fig. 37 is also seen in Fig. 38. This valley may be loosely considered to correspond to a kind of coherent length for the real sheet spray, as it induces the maximum deposition current, regardless of the x-spacing. More importantly, this dip indicates the optimum electrode position for this nozzle. It is interesting to note the increase in leakage, or power supply current drawn, both before and after this location is reached. A high speed camera (Fig. 40) gives insight into the spray breakup phenomena which gives some explanation for the location of this optimum y-position. Figure 40 shows a conduction path that extends into the range of 60 mm, and at this location large ligaments of the spray sheet finally become completely detached from the coherent sheet.

Note that the electrodes had to be lowered beyond what was originally intended in order to find this maximum deposition current. The original electrode length was selected such that it matched the spray width when the electrode holders were at maximum extension. The electrode holders were quickly modified to allow farther extensions (y_s spacings), but as a result, the spray was then wider than the electrodes were long. It was felt that any end effects related to the electrodes may cause some unpredicted anomaly. Thus, a pair of electrodes was made approximately 1.7 times longer than the original pair and the tests re-run around this optimum area as a check.

The results of the long electrode tests (Fig. 41) are interesting as they not only confirm what the original short electrodes found (an optimum y-spacing of around 60 mm), but also support another hypothesis regarding the effect of the size of the electrodes. Note that the electrodes were the same diameter, but the long electrodes were 66% longer (12.7 cm vs. the original 7.62 cm), and thus had 66% more capacitance. According to the model, these long electrodes should therefore have imparted around two thirds more deposition current. The fact is that the long electrodes did not perform as well as their shorter counterparts as they were struck by many more drops, negating the total cloud charge. This effect can be seen through examination of the raw data as having a larger spread, or deviation from the average deposition current, a behavioral pattern demonstrated by even the short electrodes when held closer to the spray (i.e. when they were hit by more drops).

Another common metric used to quantify spray charging effects is the charge-to-mass ratio of the individual drops. One method to estimate the average charge-to-mass ratio is [34]

$$\frac{q_d}{m_d} = \frac{i_c}{\dot{m}_{spray}}. \tag{35}$$

Dividing the maximum measured deposition current (-15.2 μA) by the flow rate (0.022 kg/s) yields an average charge-to-mass ratio magnitude of 6.9×10^{-4} C/kg. The Rayleigh limit provides a sense of scale for this measurement, and for an assumed average drop size of 500 μm diameter drop, that limit can be calculated [34]

$$q_R = \pi\sqrt{8\varepsilon_o \sigma\, d_d^3} = 7.97\times10^{-11}\ \mathrm{C}\,. \tag{36}$$

Dividing by the mass of a 500 µm drop (specified by the nozzle manufacturer) gives the limiting charge-to-mass ratio of the drop as 1.2×10^{-3} C/kg. Thus, in the optimum position, the average spray drop is being charged to almost 57% of its theoretical limit.

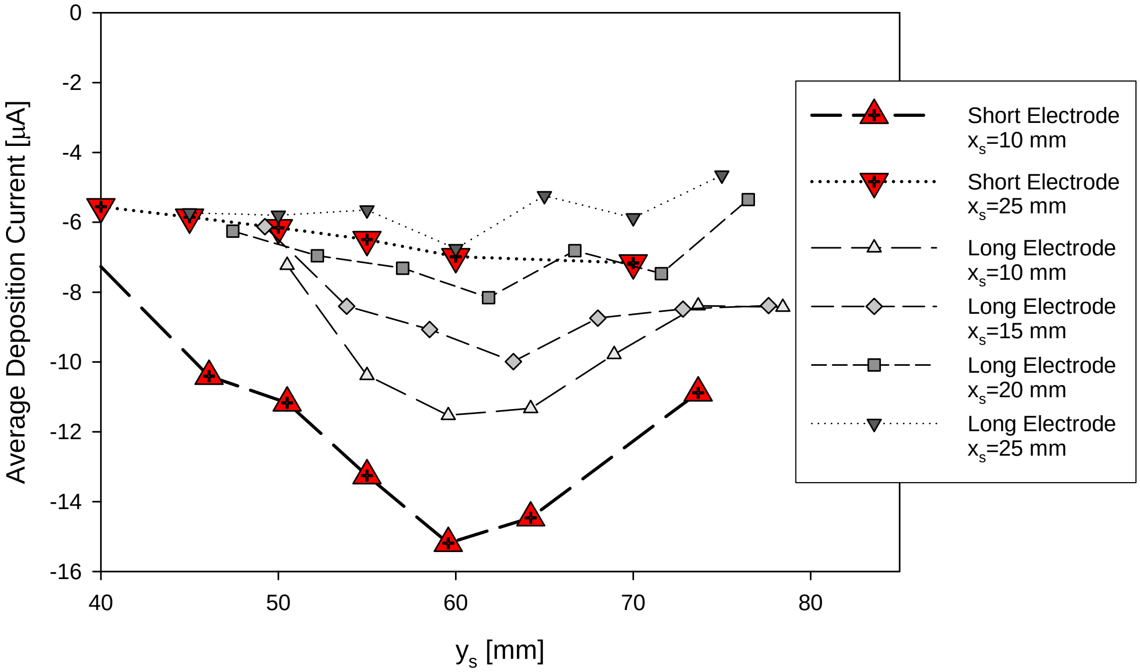

Figure 41 The average measured deposition current induced with the long electrodes. The large data points represent the original deposition current obtained with the short electrodes. The raw data and uncertainties may be found in the appendix.

5.1.3 Conclusions from Spray Charging

A simple induction charging nozzle has been developed for use with a fully hydraulic, flat fan, water spray. Charging is achieved by passing the sheet portion of the spray between two, relatively small diameter, parallel electrodes whose position can be changed to find the optimum electrode location. The optimum location deemed that which results with the maximum deposition current on a collection screen. A simple, analytic model was first derived to gain fundamental knowledge about the relationships between the variables that determine the deposition current (*x* and *y* electrode position, power supply voltage, and nozzle pressure), and to aid in the prediction of the optimum electrode location.

The nozzle was then tested to verify the trends indicated by the model and understand the effects of spray hydrodynamics on drop charging relative to electrode spacing. The model and experimental data agreed on the linear relationship between the applied voltage and the deposition current, and a nonlinear relationship between the nozzle operating pressure and deposition current which is modeled well as a quadratic function within the ranges investigated. It was hypothesized that the relatively small electrodes would perform well as their small size, and resulting small capacitance/charge, would diminish the Coulombic forces that attract the oppositely charged spray drops towards the electrodes, and that if the drops were attracted to the electrodes, the electrodes would be such a small target that the probability of impact would be reduced. Further, if an impact did result and water were to accumulate on the electrodes, the size and shape of the electrode would not support the formation of a drop large enough to form into an injection site. A second set of longer electrodes (having more capacitance) were used and found to be not as effective in generating as much deposition current as the shorter electrodes. Data indicated that many more droplets were striking the larger electrodes, diminishing the otherwise larger charging effect. As also indicated by the model, experiments showed that decreasing the x-spacing between the electrodes and the spray resulted in an increase in deposition current, however, in the experimental case, droplet impact issues were revealed as the x-spacing became very small. Finally, the optimum electrode location in the y-direction was found.

The next steps in this research could be to use high speed imaging to see how the drops flight paths deviate as the voltage is applied to long and short electrodes. This may allow the conclusions regarding droplet impact to be more firmly reinforced if the differences between electrodes can be quantified. Other areas of research may center on reshaping the electrodes to compliment the shape of the sheet region of the spray. This would allow the reduction of applied voltage as the field can be applied more precisely. Also, coatings for the electrodes may be considered. For example, droplets will be even less likely to form into injection sites if a hydrophobic coating is applied to the electrodes as the drops will be blown off the electrodes in the turbulent region near the spray.

5.2 Spray Collection

Upon review of the high speed imaging data, it was decided that quantifying the droplet rebound would be virtually impossible (see Fig. 42). Fortunately, upon further viewing in a simultaneous fashion, the differences in the number and strength of the rebounded drops were easily seen with the naked eye. It was readily apparent that the two piece concept produced the fewest number of rebounded drops, and most of those drops were concentrated in the lower part of the 'V' where they would not impact the walls anyway.

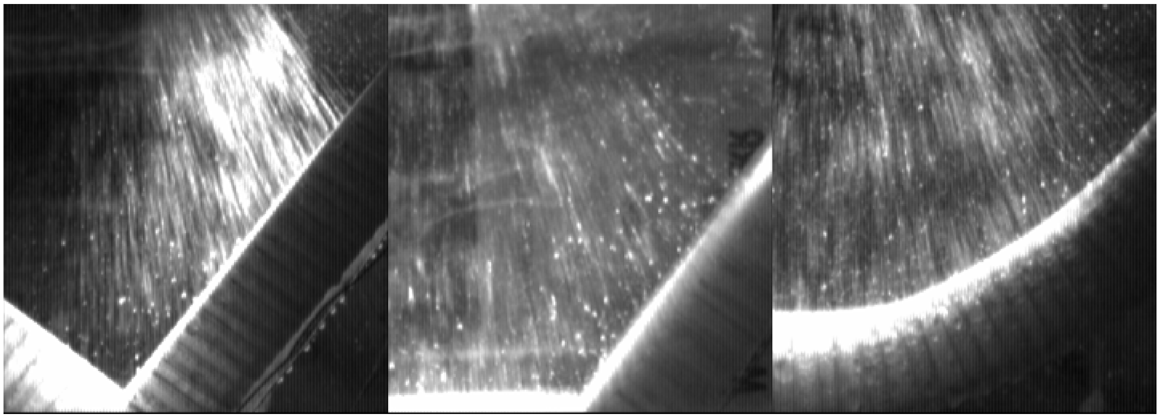

Figure 42 Selected frames from high speed video for the three false wall geometries tested. Compare with Fig. 8 for reference

In the process though, it was also discovered that the honeycomb itself, was creating problems. Even if the cells were aligned with the spray, the edges of the cells still existed as target areas which, when hit by a drop, would cause the drops to break apart and rebound chaotically. Thus, an alternate collection scheme was employed by modifying the two-piece trap. This new scheme was created by removing a two inch wide section of the honeycomb material which was directly below the spray. Thus a majority of the spray passed, unobstructed, to the collection tray resulting in virtually no rebounded drops. A high speed still is shown in Fig. 43 which looks from the top of the spray downward (note the bare section where honeycomb has been removed is clearly visible).

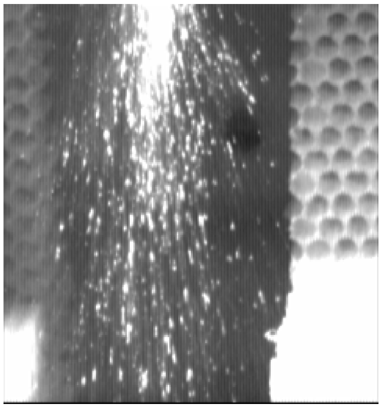

Figure 43 A single frame from the high speed video showing the final false wall concept from above.

The removal of the section of honeycomb material did raise a question regarding the airflow quality. Note that the concept of using the cells was that it prevented air from entering the collection tray. Now, without the small cells with flush openings, there was some debate concerning how much air would circulate into the collection tray. Thus, Fluent was used to check for airflow disruption with the removed honeycomb section. The test section to be modeled is shown in Fig. 44, and some selected Fluent results are shown in Figs. 45 and 46.

Observe that separators were added to the collection tray to prevent bulk fluid motion which could mix with the airstream. Further, the honeycomb cells have been represented by a lattice type structure (Figs. 45 and 46 show this feature) so that a reasonable mesh can be obtained in the model.

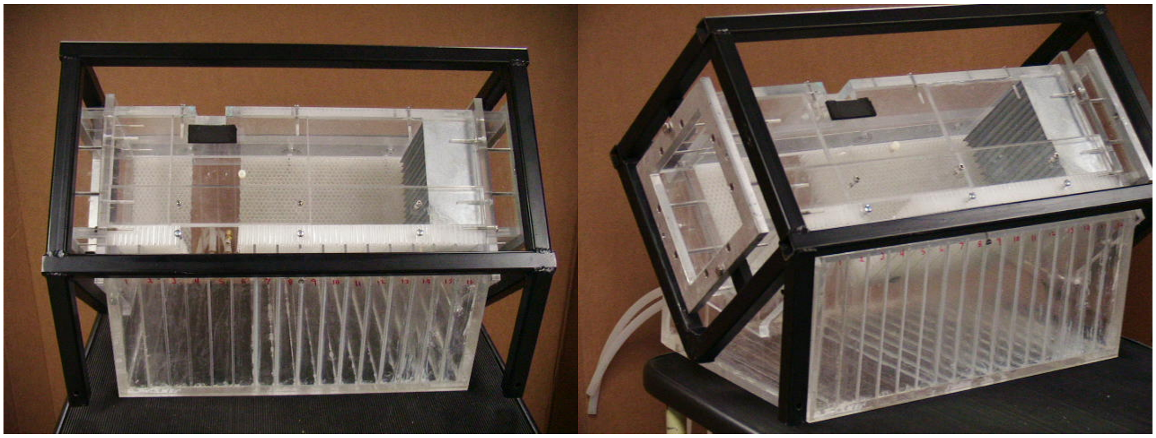

Figure 44 Final test section design. Note the section of honecomb material removed and the addition of a drift eliminator at the exit of the test section (air flows from left to right).

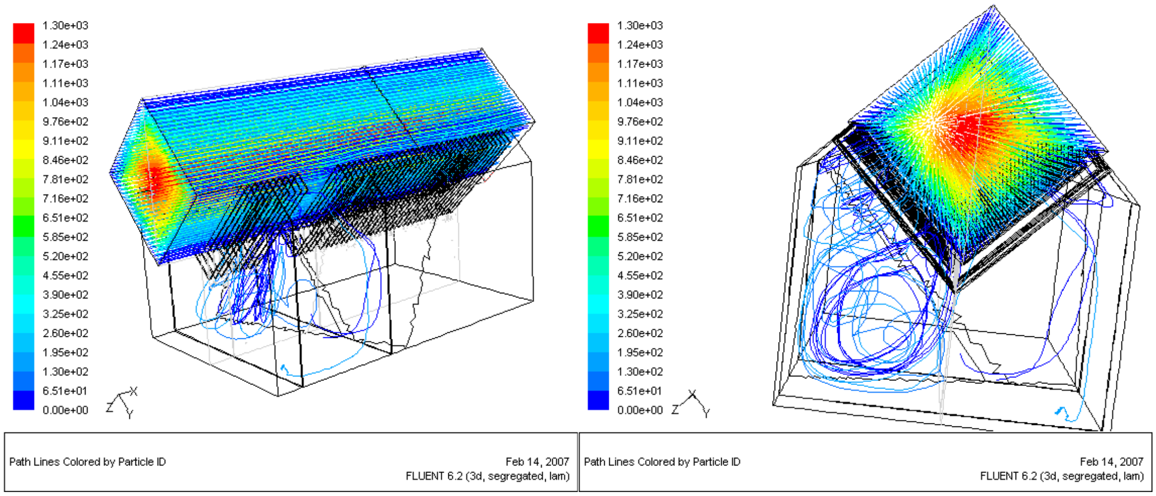

Figure 45 Fluent simulation checking for air flow irregularities on final test section design for 1 m/s face velocity. Only the two key tray separators have been included for sake of computational efficiency.

Figure 45 shows that the bulk of the air flows though the test section with very little disturbance. Figure 46 shows that what air does flow into the trap has a very low velocity, which means that only a small amount of air mass is actually passing into the collection tray. What is not evident from the Fluent simulations is the effect of the spray entering the air stream. In any case, this final scheme was then built into the test section to be used in the subsequent heat and mass transfer studies.

For sake of completeness, it should be mentioned that another alternative was tested. It was reasoned that the high momentum of the drops caused the violent splatter upon impact. Thus, an alternate strategy was to lower the false wall so that the drops would have more time to slow (due to drag forces) before striking the cell edges and walls. The test section incorporated the three piece design and is seen in Fig. 47. It was suspected that the lowered wall would significantly impact the flow characteristics, so a Fluent simulation was performed as a check. The results show (Figs. 48 and 49) that the flow was altered, but upon closer inspection, the flow entering the collection tray was of a very low velocity. This concept was run during shakedown testing and found to be no better than the previous, flush wall concept (shown in Fig. 50) in terms of rebounded droplets collecting on the ceiling of the test section and in the exiting runner. The final test section to be used in heat and mass transfer experiments is, again, found in Fig. 44. The final point to mention was that a drift eliminator was designed, built, and installed in the test section. To this point, a simple mesh screen was sandwiched between the face plates at the exit of the test section and the entrance of the instrumentation section. The geometry of the screen allowed a tremendous amount of moisture to accumulate and stay on the screen wires. In the cases of higher air flow, the wires would become covered with entrained drops not normally present in the lower air velocity cases. It was felt that this was simply part of the system and is accordingly accounted for in the measurements. However, it was also felt that this extra moisture might muddle the effects caused by more subtle changes in variables like the water flow rate or temperature. Because of this ambiguity, a drift eliminator was designed and implemented.

The drift eliminator can be seen in Fig. 44 at the exit of the test section. It consists of a series of plates that diverts the air flow so that the moisture impacts and adheres to the plates. As the moisture accumulates, gravity strips the moisture from the plates. This method is more effective than the screen, and also, because of boundary layer development, shields a bulk of the air from the collected moisture on the surface of the plates. Fluent simulations were performed at various face velocities to test the design before construction. The results are shown as Figs. 51 and 52. Testing has confirmed the successful performance of the drift eliminator.

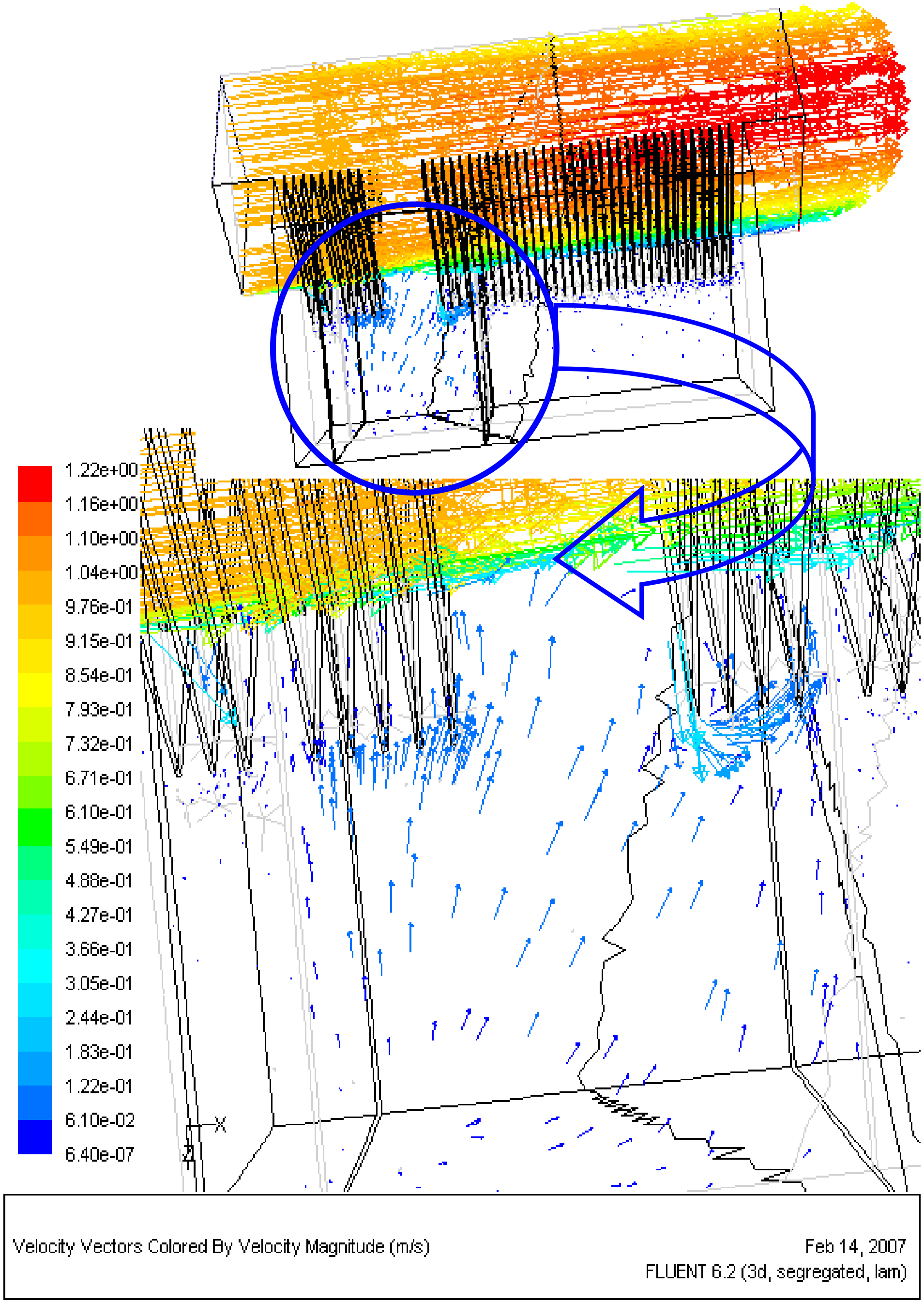

Figure 46 Fluent simulation checking for airflow irregularities on final test section design for 1 m/s face velocity. The magnitude of the velocity vectors approaches zero.

Figure 47 Test section incorporating the lowered wall concept with the three piece wall design.

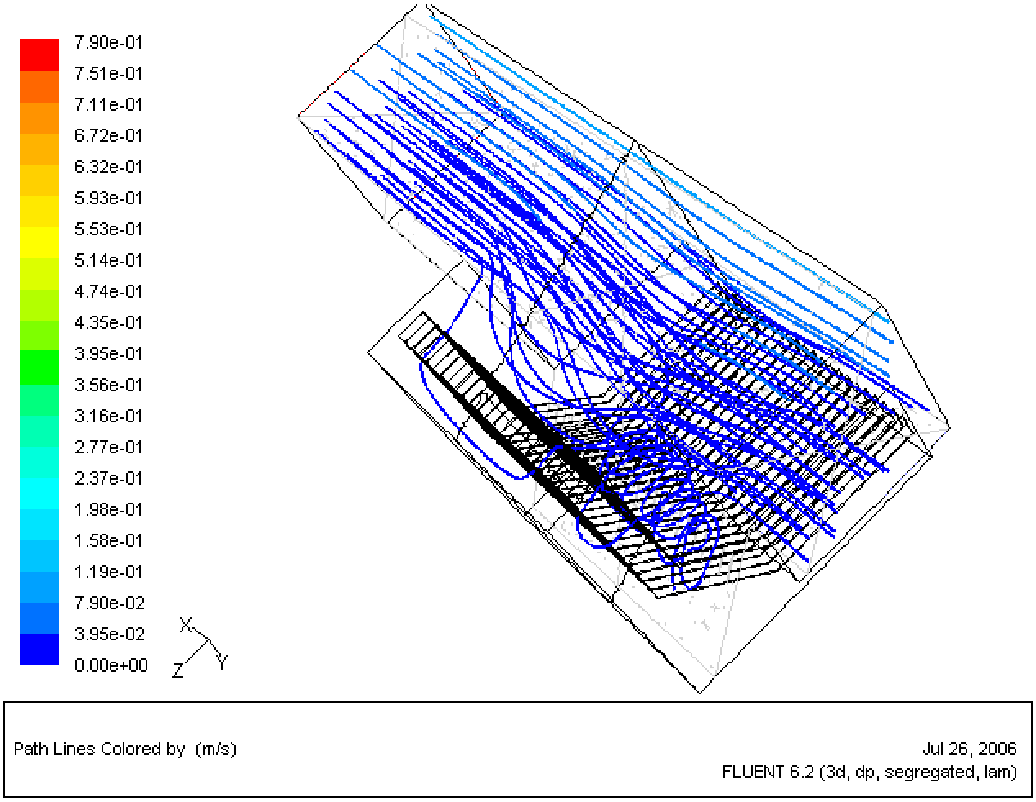

Figure 48 Fluent simulation showing path lines for lowered wall concept.

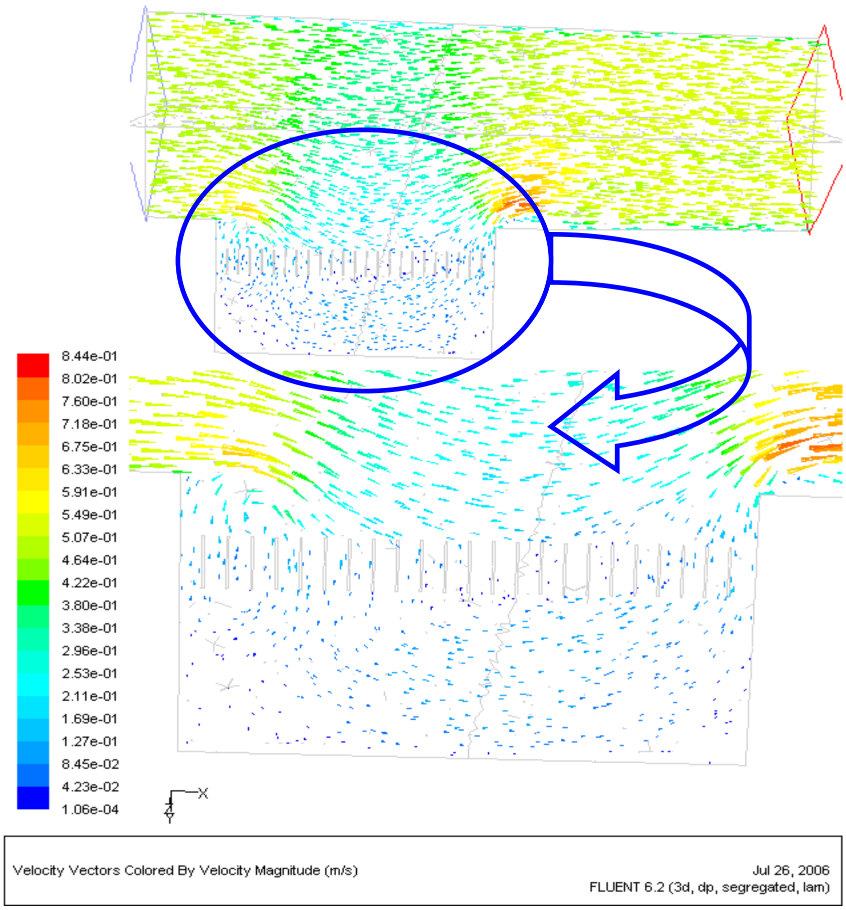

Figure 49 Fluent simulation showing velocity vectors for lowered wall concept.

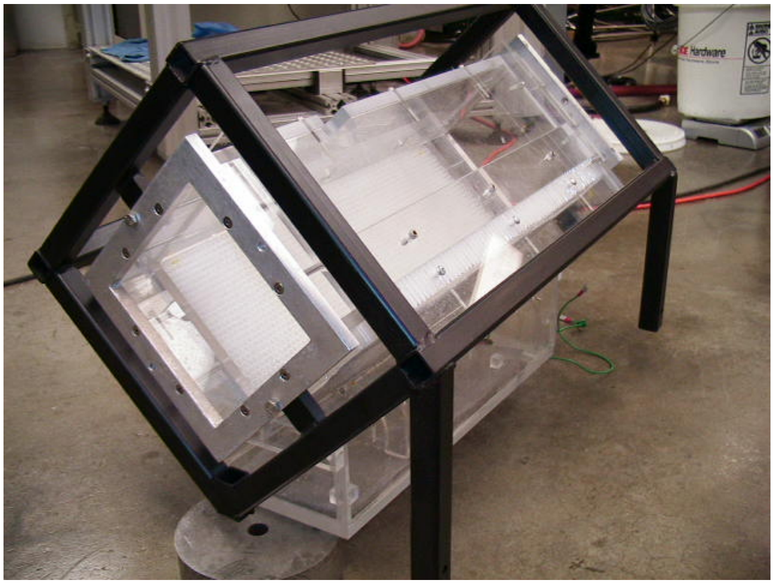

Figure 50 Old test section used in preliminary investigations. Note that no section of the false wall has been removed and the collection tray does not have separators.

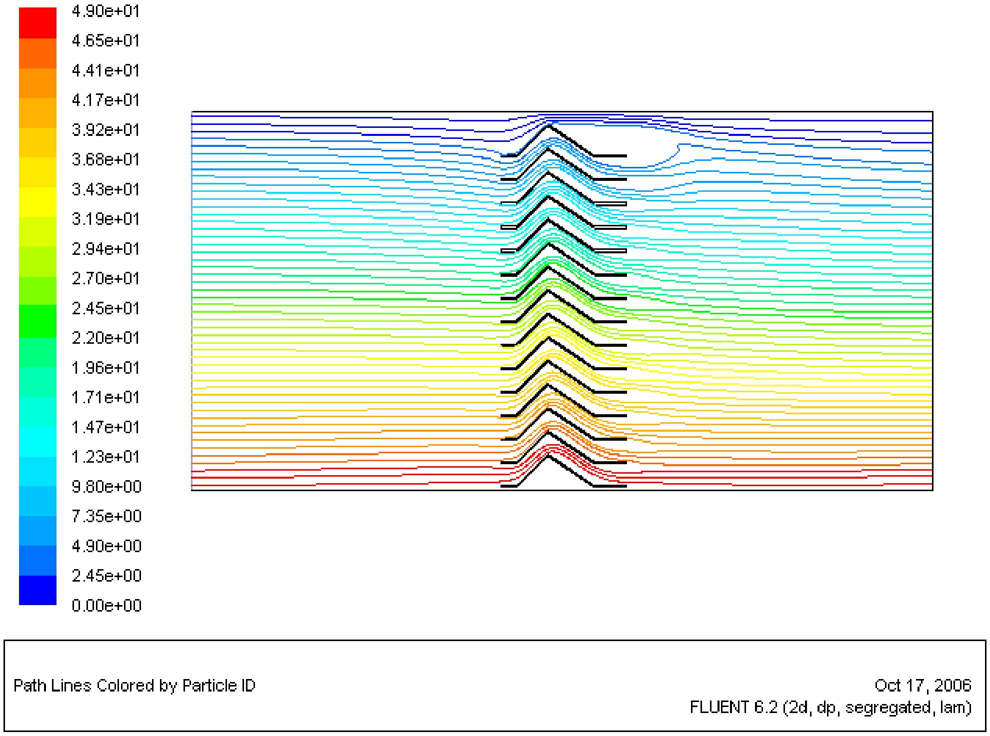

Figure 51 Fluent simulation of drift eliminator.

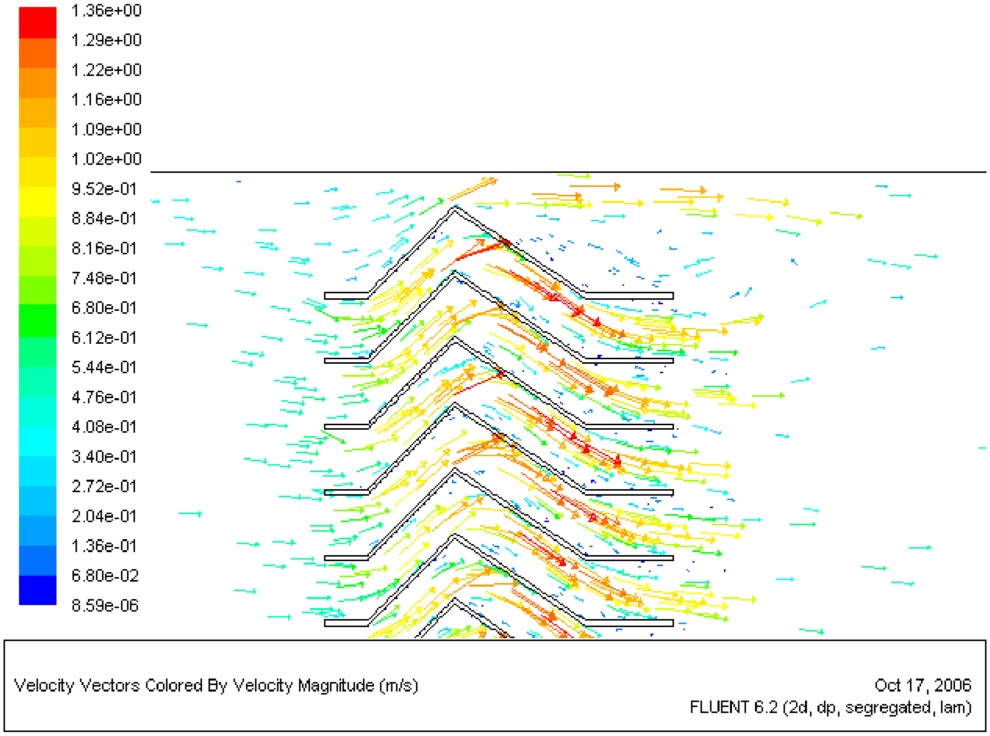

Figure 52 Fluent simulation of drift eliminator. Note how the flow is accelerated into the wall of the second bend.

5.3 Heat and Mass Transfer

5.3.1 Experimental Results

Given the volume of the experimental results, only selected results are shown in the body of the text, while a comprehensive list is provided in the Appendix, section 8.6. The results presented here will be briefly introduced to indicate the general behavior of the system, with a more thorough analysis in the following section.

The first point to mention involves the discrepancies found in the energy balances. Note that a mass balance (which would involve measuring the amount of water collected) is not possible in such experiments. However, a sensible energy balance between the water and air was attempted. This involved measurement of the water's exit temperature. As mentioned before, there was some speculation as to if this measurement was accurate enough, relative to the other measurements. In studying this energy balance information, it is clear that this exiting water temperature measurement was not accurate enough. The probe used to measure the exiting water temperature could not be placed in a position that provided reliable measurements. If it was raised into the spray field, it was more likely to read the air temperature. If it was lowered it would be submerged in the collection tray, which was not insulated. What is of real interest, however, is the change in the air's temperature and moisture content, not just the sensible energy. With this point being acknowledged, the discussion can move forward where the experimental results, which focus on the airside thermal performance, will be highlighted.

Figures 53-56 provide an example of the results included in the Appendix (section 8.6). Figure 53 shows the total airside heat transfer for the conditions listed in the legend. The test conditions listed in the legend are: the incoming air dry-bulb temperature, the face velocity, the incoming water temperature, and finally the incoming relative humidity, respectively. Inspection of the figure reveals that more heat is removed from the air as the water flow rate is increased. Further, heat transfer increases as relative humidity increases, and the smaller nozzle (producing more, finer drops) generally allows for more heat transfer. However, it is important to compare Fig. 53 with Fig. 54, which shows the sensible heat transfer as a function of water flow rate for each nozzle.

Contrasting these figures, it is generally the case that there is greater sensible heat transfer for a given flow rate in the lower relative humidity cases. This conclusion is logical for two reasons. Firstly, humid air has a greater total enthalpy which must be reduced by dehumidification (latent cooling), as seen in Fig. 55. Secondly, there is more evaporative cooling taking place as the relative humidity decreases. Though it will be discussed in detail later, the evaporative cooling that takes place in the experiments will be briefly discussed.

The incoming water temperature in these selected experiments was 10 ºC. Note that the humidity ratio at 10 ºC saturation is approximately 8 g/kg, which is slightly above the humidity ratio of the 32% *RH* tests. If no extra evaporative cooling were taking place, the 32% *RH* exit state points would not breach this 8 g/kg limit (i.e. no extra moisture would be added). However, this is clearly not the case. This addition of extra moisture is an indicator that evaporative cooling has occurred. Also, for the cases of higher initial relative humidities, the inlet and exit process points do not align to indicate a process that ultimately drives to the 10 ºC, 100% *RH* limit. In each of these cases, the process' direction leads toward some higher saturation temperature. The larger temperature indicates that either not enough moisture has been removed and/or extra sensible cooling (via an evaporative cooling process) has occurred, both of which are signs that moisture has been added.

Further comparison of the figures reveals that the behavior seen on the psychrometric chart (Fig. 55) is reflected in the total and sensible heat transfer plots. For example, there is only a small amount of total heat transferred in the 32% *RH* case, and this is seen by the fact that the change in enthalpy (see Fig. 55) is quite small relative to the 56% and 68% *RH* cases. Likewise, the reverse is also true, i.e. greater enthalpy changes in the 68% *RH* data in Fig. 55 are seen as greater total heat transfers in Fig. 53.

In general, however, the conclusion to be drawn from these results is reasonable: as the humidity increases, moisture is more likely to be removed; as humidity decreases, moisture is likely to be added. It is also concluded that the test section design is not performing flawlessly as some undesired moisture addition is taking place. Note that this moisture addition was not a complete surprise as the new test section design was not perfect, even though it was the best to date.

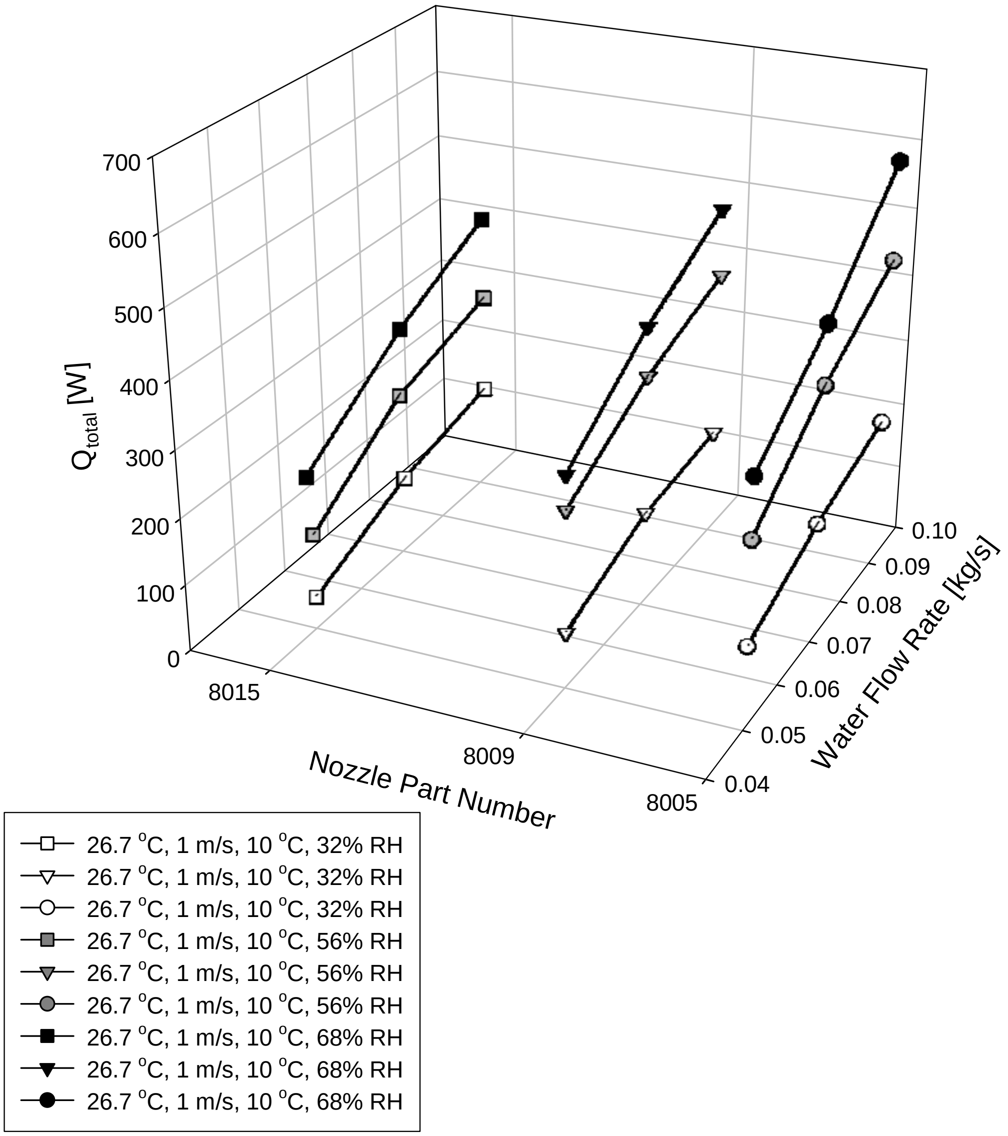

Figure 53 Total heat transfer as a function of water flow rate for the three nozzles used.

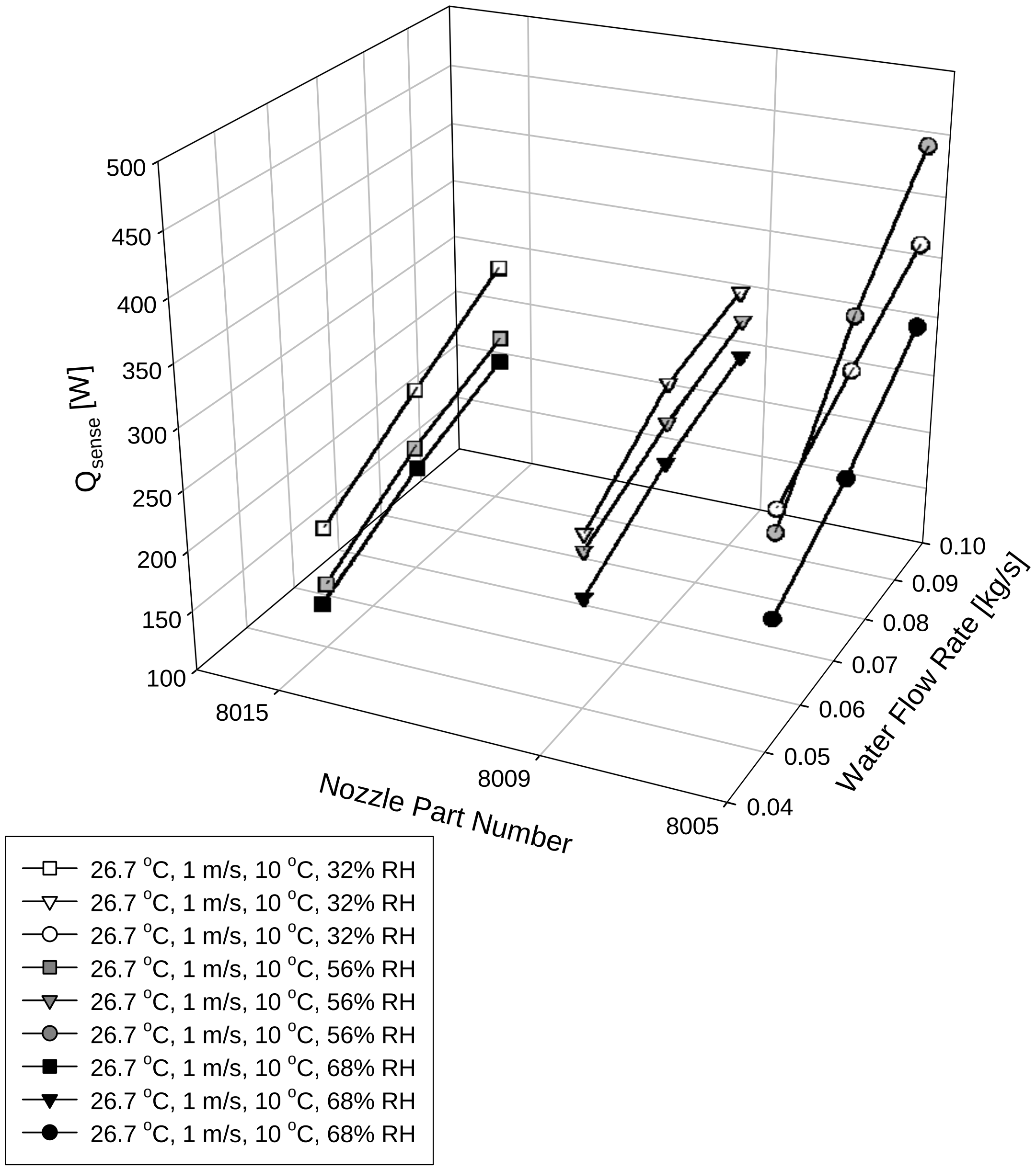

Figure 54 Sensible heat transfer as a function of water flow rate for the three nozzles used.

The last results graphed are the performance factors, F_p, for the sprays as defined by ASHRAE [28]. This factor has been developed specifically for direct contact systems used for cooling and dehumidification of moist air, which does account for the energy associated with moisture transfer [28]:

$$F_p = \frac{h_{a,in} - h_{a,out}}{h_{a,in} - h^*_{a,out}} \quad . \tag{37}$$

In this case the calculated enthalpies of the air are used, where $h^*_{a,out}$ is the enthalpy of the exiting air calculated using the exit air's dry bulb temperature and the exiting water temperature as the wet bulb temperature. If the exiting air wet bulb and water temperature are the same, then the air washer is said to be operating at its theoretical limit. The example results of this performance factor are shown in Fig. 56.

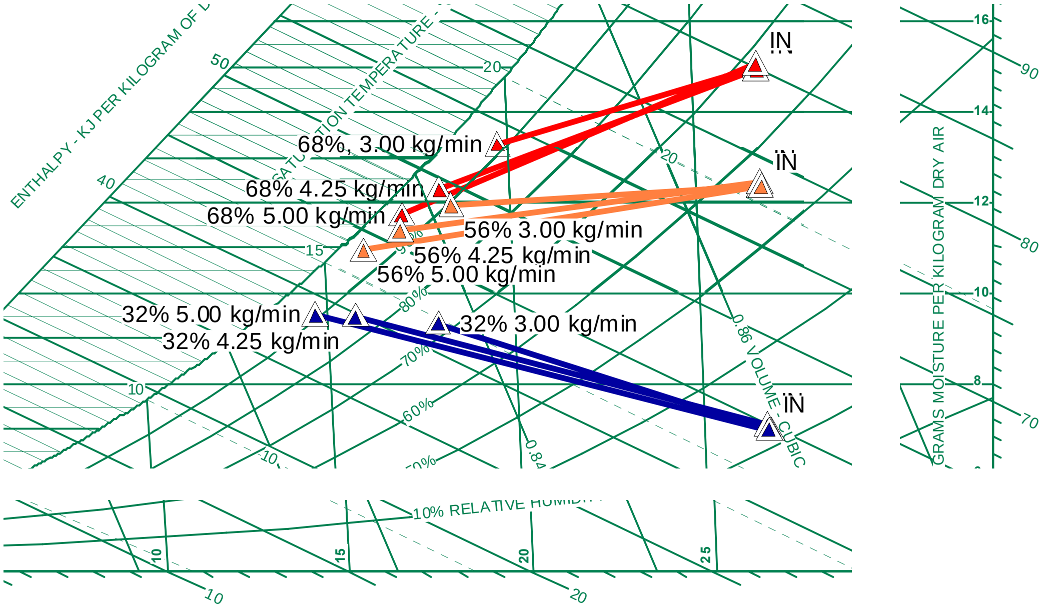

Figure 55 Sensible heat transfer as a function of water flow rate for the three nozzles used.

It is difficult to draw accurate general conclusions about this metric. It could be said that the smaller nozzles (producing greater spray surface areas) are more likely to create a condition which will reach saturation (i.e. they have a higher performance factor), however, it must be realized that the exiting water temperature is used in the calculation of this measure, and recall that there is some question to regarding the accuracy of that measurement. Further, cases of spray accumulation may act to skew the actual performance factor value. Unfortunately, after referencing all of the data, the effect of moisture accumulation within the test section and changes in relative humidity is not discernable. Again, the dependence on the exit water temperature (unfortunately) detracts from the value of this metric. This information is included for sake of completeness and also to highlight the fact that it could be of value in future research, provided the exiting water temperature can be measured with greater confidence.

5.3.2 Correlation Development

As discussed in section 3.4, the dependant variable investigated here is the overall heat transfer coefficient, *UA*. This metric is chosen for a two key reasons. The *UA* metric has some fundamental basis, as it is simply the thermal resistance of the system multiplied by the effective area of the system, or heat exchanger working surface. Thus, an estimate of *UA* should be derivable from first principles and appropriate approximations. The other metrics mentioned in the Appendix (section 8.5) are not derivable from the same kind of first principles as they are based purely on measurement differences. Secondly, a metric like *UA* would allow for direct comparison to other more common heat exchangers, whereas a metric like the performance factor, F_p, would only be applicable when comparing this system to other direct contact systems.

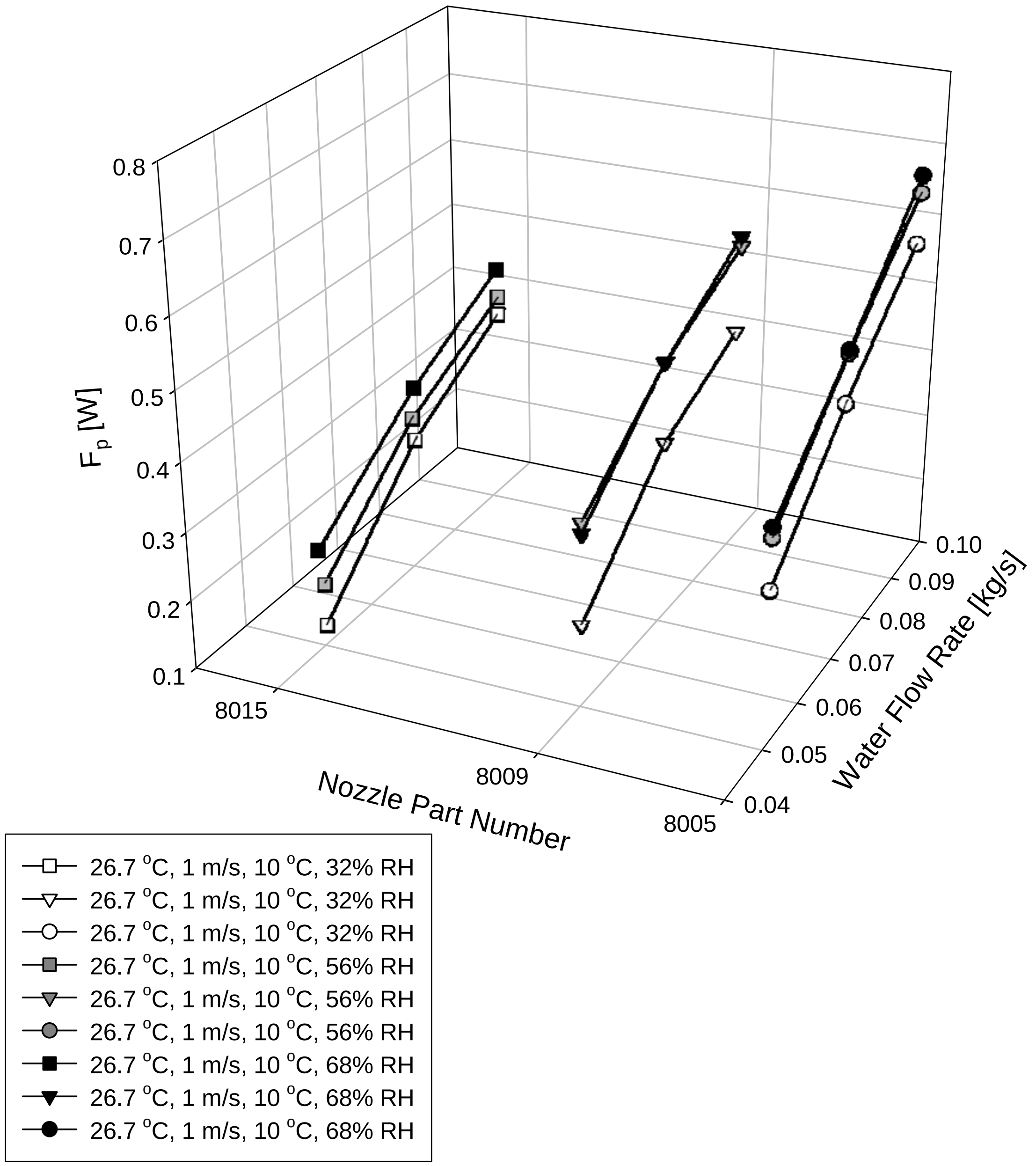

Figure 56 The direct contact heat exchanger performance factor as a function of water flow rate for the three nozzles tested.

It is known that the moisture content of the air affects the amount of sensible heat transfer, so this information must be incorporated to this sensible heat transfer metric. Further, by studying the conclusions found in [8], it is clear that the dominant independent variables to be included in the formulation should be the relative humidity and drop size.

The equation development begins by understanding the thermal resistance network. As assumed in previous work [8], a simple lumped capacitance model will be used to describe the transient behavior of the drop. Accordingly, the external forced convection is the only thermal resistance:

$$UA = h_{sphere} A_{spray} = \frac{q_{sens}}{\Delta T_{lm}} . \tag{38}$$

The form of the Ranz-Marshall relation [41] will be used as the starting point for the correlation as it is a widely used form, and it is the same correlation used in the MatLab algorithm which models the full spray (section 5.4):

$$UA = \frac{\overline{\mathrm{Nu}}_D k_a}{2r_d} A_{spray} = \frac{k_a}{2r_d}\left(C1 + C2\,\mathrm{Re}^{M1}\,\mathrm{Pr}^{0.3}\right) A_{spray} . \tag{39}$$

The coefficients *C1*, *C2*, and *M1* are found by curve fitting the experimental data. Further, these coefficients can be made to be a function of the relative humidity and drop size so that they bring that information into the total *UA* calculation.

As described below, the area of the spray over which the heat and moisture is transferred is estimated based on the estimated mean drop size, the nozzle orifice area, and the spray chamber size. The total area is taken as the number of drops in the test section at a given time times the surface area of those drops:

$$A_{spray} = N_{drops} A_{drop} = 4\pi r_d^2 N_{drops} \tag{40}$$

where the number of drops can be made as a function of the volume of the spray:

$$N_{drops} = \frac{V_{spray}}{V_{drop}} = \frac{\left(\frac{\dot{m}_w}{\rho_w}\right) t_f}{\frac{4}{3}\pi r_d^3} \tag{41}$$

where t_f is the average flight time of the drops. The flight time of the drops is a function of the speed of the drop and the distance the drop must travel in the spray chamber:

$$t_f = \frac{L_{avg}}{v_s} = \frac{L_{avg}}{\frac{\dot{m}_w}{\rho_w A_{orif}}} \tag{42}$$

where L_{avg} is the average droplet path length and A_o is the nozzle orifice area. Combining these equations reveals that the average spray surface area is calculated by

$$A_{spray} = \frac{3 L_{avg} A_{orif}}{r_d} . \tag{43}$$

Combining Eq. (39) and (43) reveals the final form of the *UA* correlation:

$$UA = \frac{3}{2}\frac{k_a L_{avg} A_{orif}}{r_d^2}\left(C1 + C2\,\mathrm{Re}^{M1}\,\mathrm{Pr}^{0.3}\right). \tag{44}$$

The drop Reynolds number in Eq. (44) is calculated according to

$$\mathrm{Re} = \frac{2r_d}{\mu_a}\sqrt{\left(\frac{\dot{m}_w}{A_{orif}}\right)^2 + \left(\rho_a U_{\inf}\right)^2}\ . \tag{45}$$

Numerous curve fitting approaches were taken, but the most satisfactory solutions were obtained by using Excel's built in solver to minimize the following equation

$$Error^2 = \left\{UA_{measured} - \frac{3}{2}\frac{k_a L_{avg} A_{orif}}{r_d^2}\left[C1 + C2\left(\frac{2r_d}{\mu_a}\sqrt{\left(\frac{\dot{m}_w}{A_{orif}}\right)^2 + \left(\rho_a U_{\inf}\right)^2}\right)^{M1} \mathrm{Pr}^{0.3}\right]\right\}^2 \tag{46}$$

by altering *C1*, *C2*, and *M1*. Thus, a set of coefficients were obtained for each experimental run. First, the data was broken into two major classes – experiments carried out with 26.7 °C air (dry bulb) and 33.0 °C air. Then, within these two major groups, these coefficients were then grouped by thermal loading settings (RH, T_{wi}, U_∞ note there are 12 possible combinations) leaving each set to consist of three runs having a different water flow rate setting. These coefficients in each three run set were averaged, thus removing the effects of the water flow rate. Then, the remaining averages were organized by nozzle, creating three sets (corresponding to the three nozzles) of 12 averaged values for *C1*, *C2*, and *M1*.

For each nozzle, the 12 coefficients were plotted in groups according to the test conditions to look for trends within the 12 runs. An example of this plotting is seen in Fig. 57, which shows the coefficients *C1* and *C2* for the largest nozzle (8015).

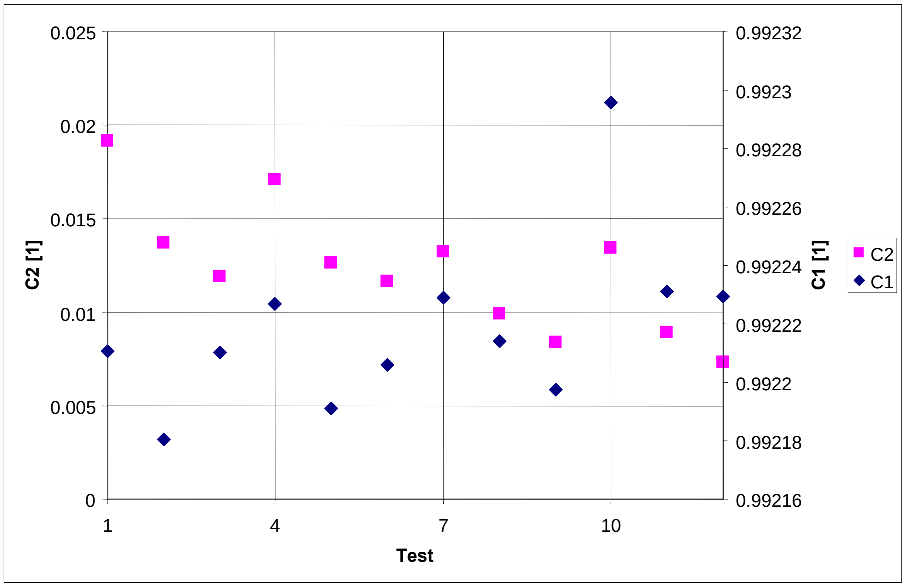

Test	RH	Uinf	Twi
1	32	3	10
2	56	3	10
3	68	3	10
4	32	3	5
5	56	3	5
6	68	3	5
7	32	1	10
8	56	1	10
9	68	1	10
10	32	1	5
11	56	1	5
12	68	1	5

Figure 57 Trending of coefficients with test conditions.

Figure 57 shows how *C2* is clearly a function of the relative humidity, whereas *C1* has no consistent trending with relative humidity. One could also argue that *C2* is a function of the free stream velocity as *C2* is typically greater when the face velocity is higher, however, this effect is not as strong as the effect of relative humidity. In the case of *C1*, there is no consistent grouping with respect to any of the three remaining variables. Further, closer inspection of the actual magnitude of *C1* shows that there is little change in its value relative to that of *C2*. In light of these facts combined with similar behavior for the other two nozzles, *C1* is taken as a constant value, but *C2* and *M1* are made to be a function of the relative humidity and average drop size.

It will be seen later that the free stream velocity, which was initially assumed to not play as dominant a role (based on prior work [8] which did not identify it as a statistically significant variable), may, in fact, be worth incorporating into the *C2* coefficient. However, in this initial development *C2* and *M1* were only considered to be driven by the drop size and relative humidity.

Because *C2* and *M1* are then functions of only two variables, they may be fitted to simple surfaces. The coefficients were then averaged for a given relative humidity. The result was a set of nine coefficients that corresponded to a combination of the three relative humidities and three mean drop sizes.

The nine coefficients were then entered into a commercial curve fitting software package, TableCurve 3D (version 4.0), to be fitted to surfaces. Note that this was performed for both the 26.7 °C and 33.0 °C data. Many factors were accounted for in the selection of the proper surface equation for *C2* and *M1*. For example, the computational efficiency was taken into account with other factors like the fit error and r^2 measures. Further, the general shape of the surface and form of the equation were accounted for. For example, equations with terms that took the form of $1/r_d$ were avoided. Even though the final correlation will only be valid over the range of variables tested, it was not considered wise to incorporate the possibility of a singularity in the equation. The final forms for *C2* and *M1* are then

$$C2 = \frac{a + b(RH) + c(RH^2) + d(r_d)}{1 + e(RH) + f(RH^2) + g(r_d) + h(r_d^2)} \tag{47}$$

a	0.009673
b	-0.00027
c	2.33E-06
d	-2.2061
e	-0.01612
f	0.00015
g	-2655.88
h	3.48E+06

$$M1 = a + b(RH) + c(r_d) + d(RH^2) + e(r_d^2) + f(RHr_d) \tag{48}$$

a	0.659543
b	-3.24E-05
c	78.21746
d	1.48E-07
e	-106497
f	-0.07243

These coefficients provided satisfactory results for both the 26.7 °C and 33.0 °C data. The value of *C1* was averaged to be 0.99157 for all cases.

The uncertainty of the new correlation was determined with an error propagation analysis. The total uncertainty for *UA* was then

$$\begin{aligned} u_{UA} = & \sqrt{\left(\frac{\partial UA}{\partial C1}u_{C1}\right)^2 + \left(\frac{\partial UA}{\partial C2}u_{C2}\right)^2 + \left(\frac{\partial UA}{\partial M1}u_{M1}\right)^2 +} \\ & \sqrt{\left(\frac{\partial UA}{\partial \dot{m}_w}u_{\dot{m}_w}\right)^2 + \left(\frac{\partial UA}{\partial U_{\inf}}u_{U_{\inf}}\right)^2 +} \\ & \sqrt{\left(\frac{\partial UA}{\partial r_d}u_{r_d}\right)^2 + \left(\frac{\partial UA}{\partial L_{avg}}u_{L_{avg}}\right)^2 +} \\ & \sqrt{\left(\frac{\partial UA}{\partial k_a}u_{k_a}\right)^2 + \left(\frac{\partial UA}{\partial \mu_a}u_{\mu_a}\right)^2 + \left(\frac{\partial UA}{\partial \Pr}u_{\Pr}\right)^2} \end{aligned} \tag{49}$$

Note that the uncertainties in Eq. (49) are organized by: uncertainty in curve fitting, uncertainty in measurement, uncertainty in estimated values, and uncertainty in thermal properties.

It was found that when all terms are included in the analysis, the uncertainty is unacceptably large, with the dominating term being the uncertainty in the free stream viscosity, μ_a, being four to five orders of magnitude larger than uncertainties from the other terms. This was because when *UA* is differentiated with respect to this variable which is located in the denominator, the variable, which is a relatively small number to begin with, is squared. Initially, the uncertainty of the fluid properties is taken as the difference in these property values over the largest air temperature swing through experimentation. This method proved too gross, therefore, this and the other material property uncertainty terms are dropped from this analysis as focused is placed on the error in curve fitting and measurements.

Once the thermal property uncertainties were removed, the uncertainty of the curve fitting on *C2* was the dominant uncertainty, being approximately one to two orders of magnitude larger than the other uncertainties, depending on the test conditions.

The measurement uncertainty is obtained from the experimental uncertainty analysis discussed in sections 4.3.4, and 8.3. The curve fitting uncertainty follows from another error propagation analysis. The curve fitting software provided a standard error associated with each coefficient. These values were then multiplied by 1.96 to achieve the 95% confidence limits and taken as the new uncertainties used in the analysis. An example calculation follows for *M1*:

$$\begin{aligned} u_{M1} &= \sqrt{\left(\frac{\partial M1}{\partial a}u_a\right)^2 + \left(\frac{\partial M1}{\partial b}u_b\right)^2 + \left(\frac{\partial M1}{\partial c}u_c\right)^2 + \left(\frac{\partial M1}{\partial d}u_d\right)^2 + \left(\frac{\partial M1}{\partial e}u_e\right)^2 + \left(\frac{\partial M1}{\partial f}u_f\right)^2} \\ &= \sqrt{(u_a)^2 + (RHu_b)^2 + (r_d u_c)^2 + (RH^2 u_d)^2 + (r_d^2 u_c)^2 + (RHr_d u_f)^2} \end{aligned} \tag{50}$$

Note that in the process of curve fitting using regression methods, it is assumed that the independent variables are error free. Figure 58a shows the predicted *UA* values and the experimental values as a function of water flow rate for the 26.7 ºC data, while Fig. 58b shows the same information for the 33.0 ºC data. Note that the incoming air temperature does not appear in the formulation of the *UA* correlation, and judging from the similarity of the plots in Figs. 58a and 58b, it should not.

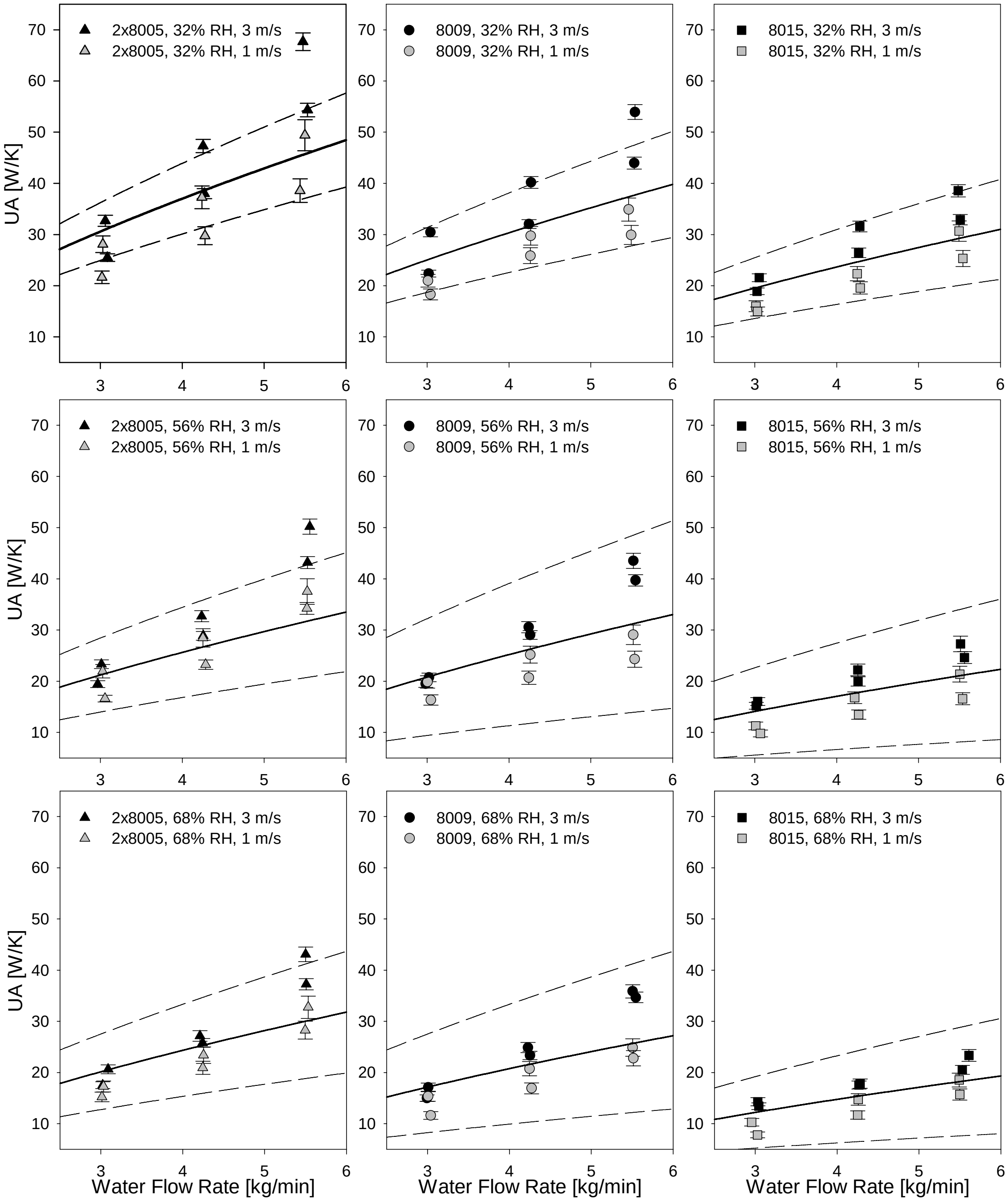

Figure 58a *UA* values as a function of water flow rate for the 26.7 ºC data. The predicted value is the solid black line, and the broken lines outline the 95% confidence range.

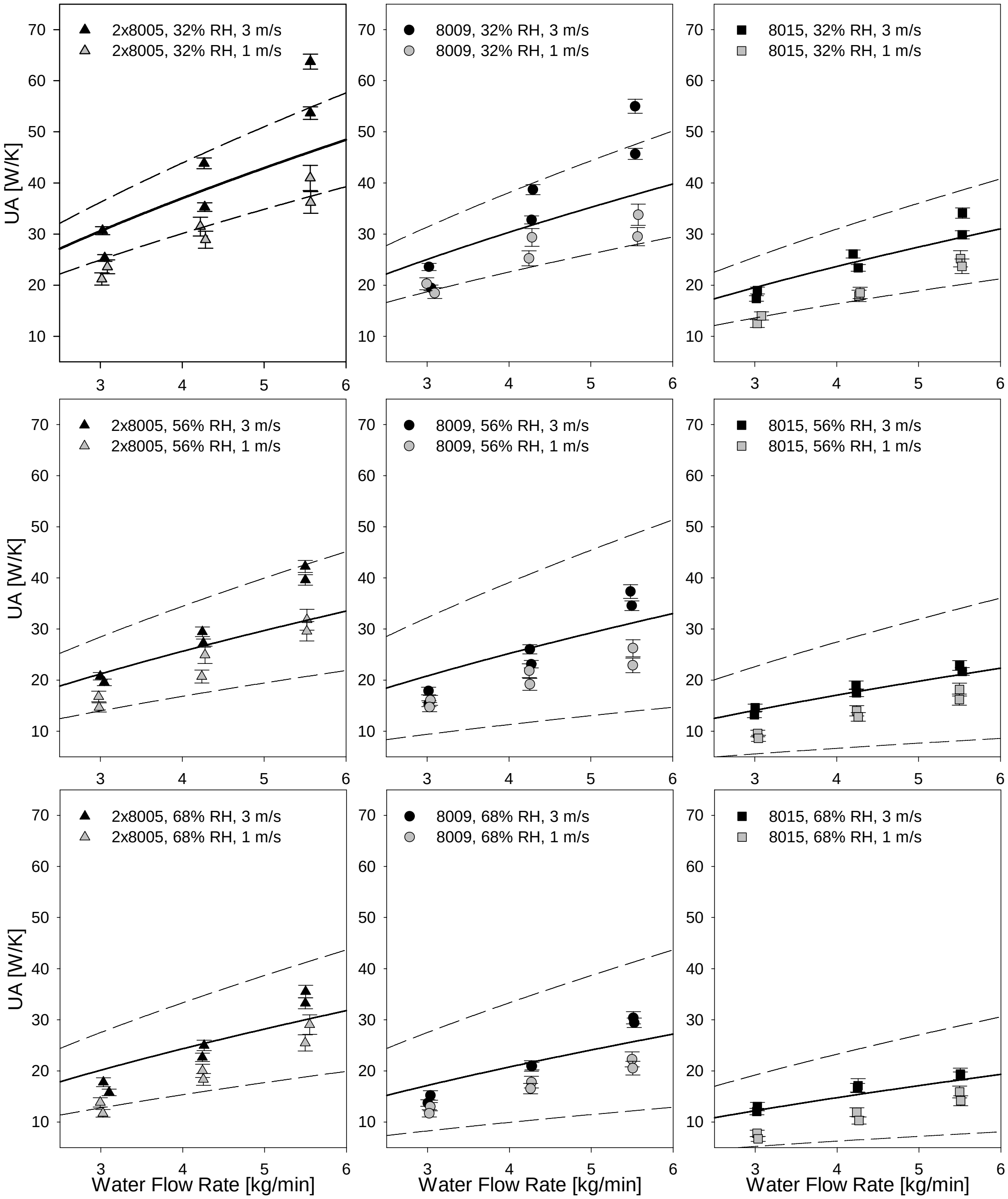

Figure 58b *UA* values as a function of water flow rate for 33.0 ºC data. The predicted value is the solid black line, and the broken lines outline the 95% confidence range.

Figures 58a and 58b show how the water flow rate affects the overall heat transfer. Increasing the water flow rate effectively increases the spray area by producing more drops. A pressure differential drives the water flow, thus increasing the nozzle pressure increases the flow rate; however, increasing the nozzle pressure changes the droplet size distribution slightly. Due to the fact that this change is slight (according to the nozzle manufacturer [40]) and the fact that this change was not measured, for the sake of this analysis, this effect is noted, but ignored as a constant mean drop size is assumed over all operating pressures. Regardless, the fact that increasing the water flow rate increases the spray area is not diminished.

Another point seen in the figures is that decreasing the mean drop size also increases the overall heat transfer. Again, this is attributed to the increase in spray surface area (as the spray volume is consistent). According to Eq. (38), this, and the previous claim about nozzle flow rate, is justified.

Increasing the relative humidity tends to suppress heat transfer, seen by an associated decreasing of *UA*. However, as Eq. (38) shows, the heat transfer being suppressed is actually the sensible heat transfer. Therefore, perhaps a better way to note this behavior is to say that the lower relative humidities boosts heat transfer (and *UA*), aided by the evaporative cooling phenomenon.

Further, inspection of the figures reveals that, in general, the higher face velocities yield a higher experimental *UA* value due to a greater associated heat transfer. Though the face velocity is included in the formation of the analytic expression of *UA* in a fundamentally meaningful term (the Reynolds number, see Eq. (44) and (45)), it does not have a strong enough effect in this location so as to significantly alter the predicted *UA* value over the range of face velocities of interest. Upon viewing the data in this form, it is evident that the face velocity, which was intentionally neglected in the first formulation of this correlation (see discussion around Fig. 57), could be included to provide a more precise estimate of the expected *UA*. Nevertheless, it will be noted that the spread of face velocities generally lies within the confidence range.

For the purposes of this exercise, it will be argued that the inclusion of the face velocity information in this first formulation would not have been in keeping with the facts found in previous research [8] (i.e. the statistical significance of the variables). Further, this initial attempt was focused on creating a correlation in the must fundamental form possible. This fundamental form must ideally operate on the minimum number of coefficients, and similarly, those coefficients should be as simple as possible (thus, they were only made a function of the most statistically significant variables, one of which was not the face velocity). However, in retrospect, the role of the face velocity is discernable, and if another attempt to develop a correlation were made, it is recommended that the face velocity be included. Also, because the face velocity was not expected to play such a strong role, it was only investigated at two levels. To create a more accurate correlation, this variable should be tested at three levels (like the drop size and relative humidity). Further, at this time it can only be recommended that the velocity information be included in the *C2* coefficient due to what is hypothesized to be the occurrence of experimental anomalies that give rise to uncharacteristically high *UA* values at the high face velocity and higher flow rates. The details of this point follow.

The free stream velocity again causes inaccuracies with the *UA* expression as seen by the experimental data points created with the small nozzles running at the 5.50 kg/min flow rates and 3 m/s face velocities. Note that a nearly linear relationship between *UA* and water flow rate is expected (aside from the prediction plots in Figs. 58a and 58b, a small discussion of this linear behavior is also found in section 8.5.2). However, in these cases, the experimental *UA* values are typically noticeably greater than what is predicted. It is hypothesized that this higher value results from droplet rebound, which leads to extra, or 'adjacent,' cooling. Significant pressures are required (O~80-100 psi [550-690 kPa]) to generate the 5.50 kg/min water flow rates with the small nozzles. These pressures translate to greater droplet momentum, which, in turn, translates to greater amounts of droplet rebound. This rebound exacerbates the problem of droplet collection on the test section ceiling and entrainment, especially at the higher face velocity where drag forces become more significant. Entrained drops, even if they fall out of the air stream, have a longer residence time than what the *UA* expression predicts. With this extra time (which is essentially impossible to quantify) comes extra sensible and latent heat transfer. In the case that the droplets do not fall out of the air stream, the drift eliminator will remove them. The drift eliminator, being cooled by the droplets it removes, acts as an extended surface, providing even further cooling and perhaps even moisture addition as well assuming the droplets do not drip from the eliminator in a timely enough manner. This claim is further justified by the fact that this sharp increase in *UA* is more pronounced at the lower relative humidites where evaporative cooling can play a more significant role.

It is for the above-mentioned reason that it is recommended that the face velocity information should appear in the *C2* coefficient only. As mentioned before, a nearly linear response with respect to the water flow rate is expected. No doubt, the inclusion of this information in *M1* could create a more nonlinear prediction with respect to the water flow rate; however, this would not be fundamentally meaningful as it would not fit with the near-linear expectation. Basically, by fitting the coefficients perfectly to the data, one would essentially be introducing information about undesired phenomenon which might not be present in, say, a larger test section. Indeed, the *C2* coefficient acts as a kind of slope (see Eq. (44) and (45)), and if it were made to have a positive relation to the face velocity as well as the drop size and relative humidity, it is clear that it would increase, essentially creating a larger slope, as the face velocity increases.

These points emphasize the balance of understanding for application of the analytic *UA* expression. The expression is only intended to be applicable over the ranges of the variables of interest, and applications beyond these ranges must be made judiciously or not at all (especially regarding the drop size and relative humidity as these equations have been fitted to surfaces that may not behave predictably far beyond the ranges investigated). Further, it is understood that this expression applies to a test section and spray of similar geometry, i.e. a diamond shaped cross section in conjunction with a flat fan spray. Inasmuch as these parameters are accounted for, factors like entrained droplets and adjacent cooling due to moisture collection on the test section ceiling and drift eliminator as well as the drift eliminator itself, are not accounted for, as they could not practically be accounted for. These variables, though not quantifiable, must be kept in mind while using the expression as a ‘first order’ design tool, e.g. one must realize that droplet entrainment might result in an increase in overall heat transfer or loss of humidity control, especially at higher face velocities.

5.4 Full Spray Model

5.4.1 Model Description

The full spray model simulates the heat and mass transfer for a spray by first calculating the heat and mass transfer from many single drops, and then summing that information. The single drop simulation is based on an energy balance between the drop and a finite volume of moist air surrounding the drop, as defined by a radius *b*. Review of the adapted model in the Master’s thesis [8] has shown some inaccuracies, thus the model has been re-derived, and that derivation can be found in the Appendix, section 8.1.1, while the code can be found in the Appendix, section 8.7. The governing differential equations are then:

$$\frac{dT_d}{dt} = \frac{3}{2r_d^2 \rho_w c_{p,w}} \left[k_a Nu\left(T_\infty - T_d\right) - \left(u_{lv}\left(T_d\right) + RT_d\right) D_v Sh\left(c_s - c\right) \right] \tag{51}$$

$$\frac{dT_\infty}{dt} = \frac{3r_d}{2\left(b^3 - r_{d,o}^3\right)\left(\rho_a c_{v,a} + c c_{v,v}\right)} \left[-k_a Nu\left(T_\infty - T_d\right) + \left(c_{v,v}\left(T_d - T_\infty\right) + RT_d\right) D_v Sh\left(c_s - c\right) \right] \tag{52}$$

$$\frac{dr_d}{dt} = \frac{-D_v Sh\left(c_s - c\right)}{2\rho_w r_d} \tag{53}$$

$$\frac{dc}{dt} = \frac{3r_d}{2\left(b^3 - r_{d,o}^3\right)} D_v Sh\left(c_s - c\right) \tag{54}$$

$$\frac{d^2 x}{dt^2} = \frac{\left(\frac{1}{2}\rho_a C_d \left(\pi r_d^2\right)\left(U_{\text{inf}} - \frac{dx}{dt}\right)\left|U_{\text{inf}} - \frac{dx}{dt}\right|\right)}{m_d} \tag{55}$$

$$\frac{d^2 y}{dt^2} = -g + \frac{\left(-\frac{1}{2}\rho_a C_d \left(\pi r_d^2\right)\left(\frac{dy}{dt}\right)\left|\frac{dy}{dt}\right|\right)}{m_d} \tag{56}$$

$$\frac{d^2 z}{dt^2} = \frac{\left(-\frac{1}{2}\rho_a C_d \left(\pi r_d^2\right)\left(\frac{dz}{dt}\right)\left|\frac{dz}{dt}\right|\right)}{m_d} \tag{57}$$

MatLab’s built in ordinary differential equation solver, “ode45,” solves these highly coupled equations. Examples of the graphical output showing the unbounded spray and the ‘trimmed’ spray in the test section are shown in Figs. 59-62. The effect of the free stream drag on the drops is seen in Figs. 59 and 60. Figures 61 and 62 show the portion of the spray in the test section, and it is this portion of the spray that is of interest for heat and mass transfer calculations.

The simulation is composed of two function files: `MCdrops.m`, which is the base function file, handling the pre- and post-processing, and `MCdropeqns3D.m`, which is the core of the program called by the differential equation solver. The user supplies the initial conditions. The program then builds the random variable matrices with this information as described in section 3.5. The differential equation solver is then called in a loop, being supplied with a new set of initial conditions pulled from the random variable matrices. The results are stored in a three dimensional matrix, with each layer of the matrix containing the transient information (solution to the governing equations) for a given drop.

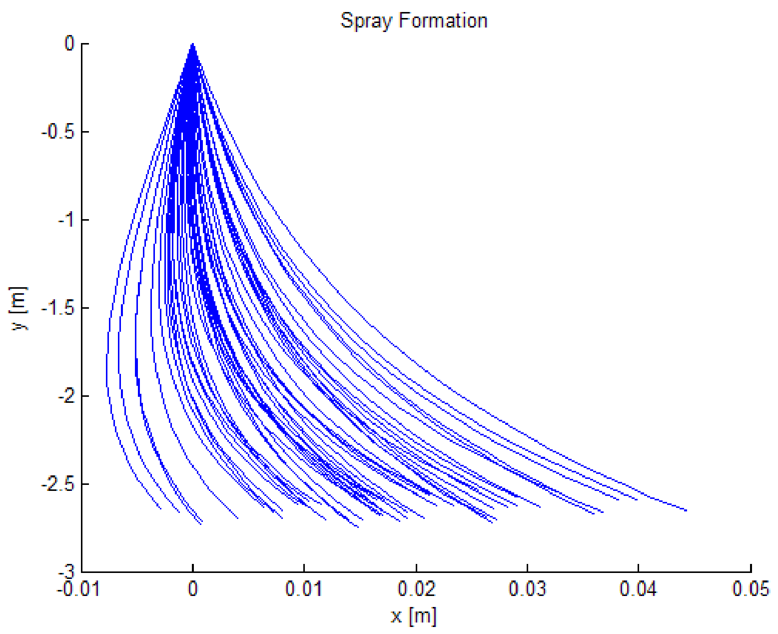

Figure 59 MatLab `MCdrops.m` output of "Figure No. 30" showing unbounded spray formation from the side. Note that the airflow is in the positive x-direction.

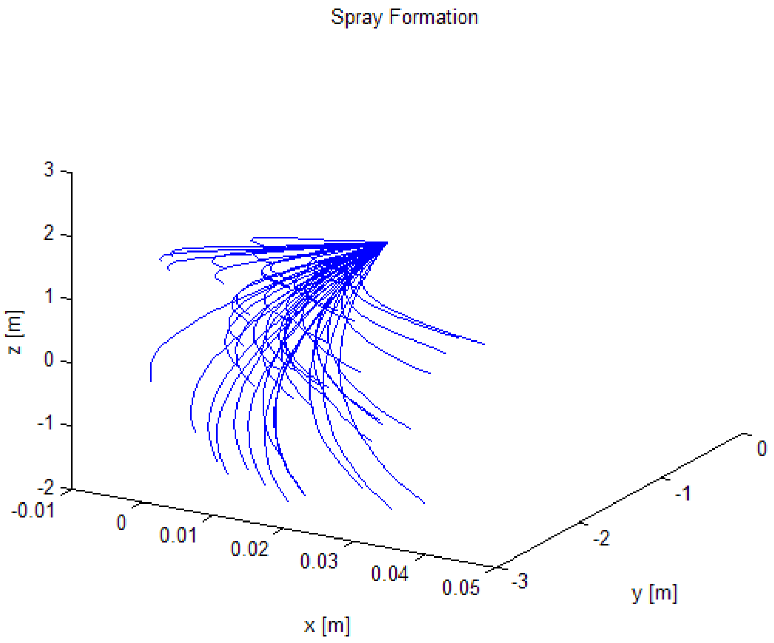

Figure 60 MatLab `MCdrops.m` output of "Figure No. 30" showing unbounded spray formation from an oblique angle showing the spray fanning in the z-direction. Note that the airflow is in the positive x-direction.

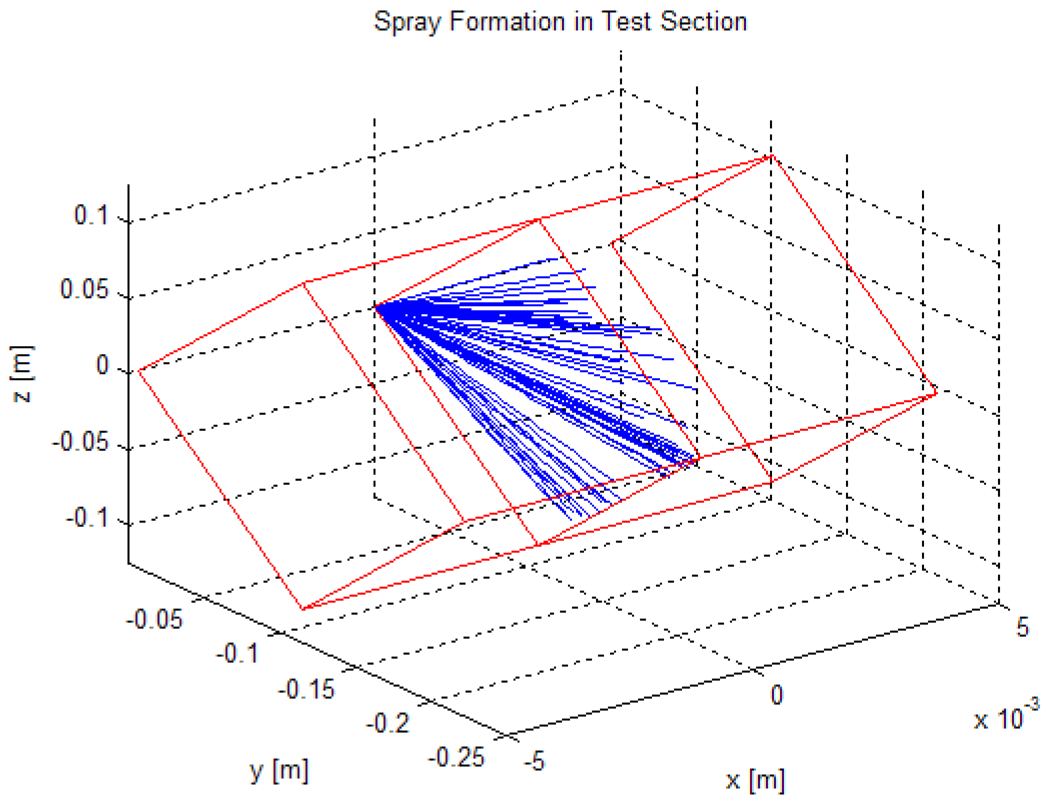

Figure 61 MatLab `MCdrops.m` output of "Figure No. 31" showing bounded spray formation. Note that the red lines represent the perimeter of the test section. The airflow is in the positive x-direction.

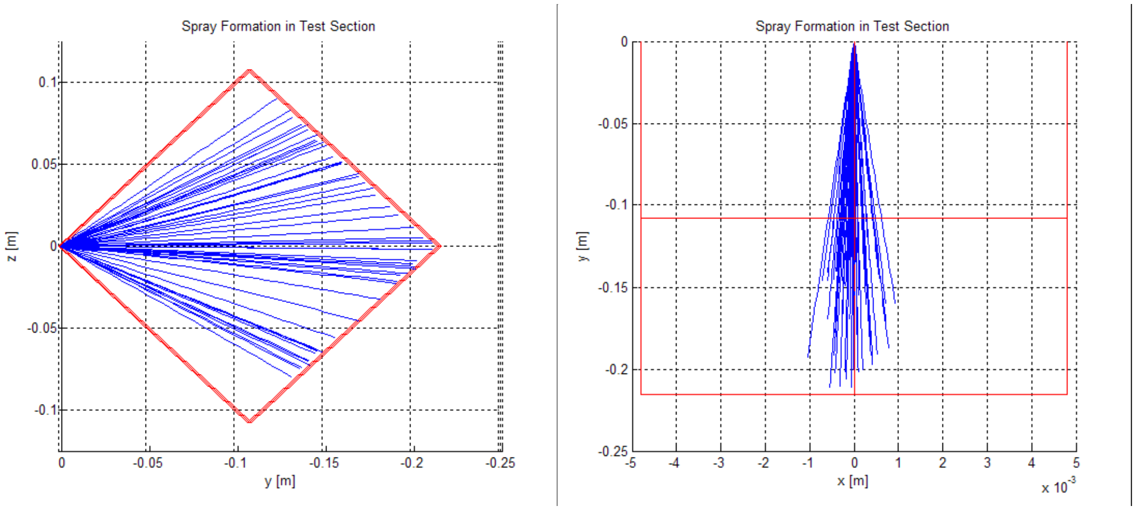

Figure 62 MatLab `MCdrops.m` output of "Figure No. 31" showing bounded spray formation looking directly down the test section (left figure) and a directly normal side view (right figure). Note that the red lines represent the perimeter of the test section. The airflow is in the positive x-direction.

Post processing begins by trimming the three dimensional matrix. The goal is to compute the heat and mass transfer to/from the drops when they are in the test section (as shown in Figs.

61 and 62). Thus, the drop position information is used to identify when the drop is in the test section. If it is in the section, then the drop and air information in that layer is written to a second matrix used for further post processing.

As mentioned before, the goal is to find the heat and mass transferred in the simulation. Because the energy balance exists, the averaged heat and mass transfer for the simulation can be calculated using the drop side information. The heat and mass transfer for each drop is then calculated, and those values are summed for every drop. As the state of the drop is known at the beginning and end of the flight, that information is used to calculate the average sensible and total heat transfer, and mass transfer, respectively:

$$\begin{gathered} \dot{Q}_{sens} = m_d \frac{du_l}{dt} - \dot{m}_v \left(u_{fg}\left(T_d\right) + RT_d\right) \Rightarrow \\ \overline{\dot{Q}}_{sens} = \frac{4}{3}\pi\rho_w \left\{c_{pw}\left(T_{d,f} r_{d,f}^3 - T_{d,i} r_{d,i}^3\right) - \left(r_{d,f}^3 - r_{d,i}^3\right)\left[3146235 + \left(R - 2822\right)\left(T_{d,f} - T_{d,i}\right)\right]\right\}\frac{1}{t_f} \end{gathered} \tag{58}$$

$$\begin{gathered} \dot{Q}_{tot} = \dot{Q}_{sens} + \dot{m}_v \left(u_{fg} + RT_d\right) = m_d \frac{du_l}{dt} \Rightarrow \\ \overline{\dot{Q}}_{tot} = \frac{4}{3}\pi\rho_w \left[c_{pw}\left(T_{d,f} r_{d,f}^3 - T_{d,i} r_{d,i}^3\right)\right]\frac{1}{t_f} \end{gathered} \tag{59}$$

$$\Delta c = \frac{4}{3}\pi\left(b^3 - r_{d,o}^3\right)\left(c_f - c_i\right) \tag{60}$$

5.4.2 Model Calibration

Before application, the model must be calibrated by adjusting the variable *b* that defines the volume of air that surrounds the drop. It was initially reasoned that the volume of air could simply be adjusted until the simulation results matched the experimental results. This method of finding an "effective *b*" did not provide realistic results. However, it is included for sake of completeness and the analysis is included in the Appendix, section 8.8. The second option for finding *b*, being based on a more fundamental analysis of the system, follows. In this method, the volume of air being treated is uniformly divided amongst the drops.

The solution of *b* begins by finding the volume of air that enters and leaves the test section in the simulation time (i.e. the volume of air to be treated in the amount of time the drops are in the air stream). This volume is found using simple geometry and the information in Eq. (42):

$$V_{flow} = U_{\inf} A_{x\sec t} t_f = U_{\inf} A_{x\sec t} \frac{L_{avg}}{\left(\dfrac{\dot{m}_w}{\rho_w A_{orif}}\right)} \tag{61}$$

From this formulation, it is clear that increasing the free stream velocity, $U_{\inf}$, or the size of the test section (the cross sectional area, A_{xsect}, and/or the average flight length, L_{avg}) will increase the amount of air to be treated. Likewise, decreasing the amount of spray will also effectively increase the amount of air to be treated.

The volume of air per drop is then evenly divided, again with the use of an earlier equation, Eq. (41):

$$V_{air} = \frac{V_{flow}}{N_{drops}} = \frac{V_{flow} V_{drop}}{V_{spray}} = \frac{V_{flow} \frac{4}{3} \pi r_{d,o}^3}{\left(\frac{\dot{m}_w}{\rho_w} \right) t_f} \tag{62}$$

Substituting in the flight time information (Eq. (42)) and Eq. (61), the volume of air is found:

$$V_{air} = \frac{4 \pi r_{d,o}^3 \rho_w U_{\inf} A_{x\sec t}}{3 \dot{m}_w} \tag{63}$$

The value of *b* then simply comes from the basic geometry of a sphere, accounting for the volume of the drop:

$$b = \left[r_{d,o}^3 \left(1 + \frac{\rho_w U_{\inf} A_{x\sec t}}{\dot{m}_w} \right) \right]^{\frac{1}{3}} \tag{64}$$

In its final form, it is clear that *b* is still proportional to the free stream speed and the cross section of the test section, and inversely proportional to the water flow rate. Also, note that this form highlights how *b* is actually directly proportional to the initial mean drop size.

5.4.3 Simulation Results

The total and sensible heat transfer results for a series of simulations are shown in this section. A detailed discussion comparing these simulated results to their experimental counterparts follows in the subsequent section.

The total heat transfer is presented first in Fig. 63. The results indicate that increasing water flow rate will increase total heat transfer. Further, decreasing drop size (increasing spray area) will also increase total heat transfer. Note that this information agrees with not only common logic, but also the experimental results presented in section 5.3.1.

The sensible heat transfer also increases with water flow rate and reduction in mean droplet diameter, as shown in Fig. 64. This pattern is also in agreement with the experimental results. However, it will be noted that the response to relative humidity is the reverse of what is seen in the experimental results. This and other differences and similarities are discussed more thoroughly in the next section.

5.5 Experimental and Simulated Results Comparison

5.5.1 Results Comparison

By comparing the experimental and simulated results, the model reveals its value as a powerful design tool – highlighting not just fundamental thermodynamic information, but by providing a kind of gage by which the experimental performance can be judged in terms of quality and theoretical potential.

Figures 65 and 66 show the experimental and numerical results for total heat transfer together for easier comparison.

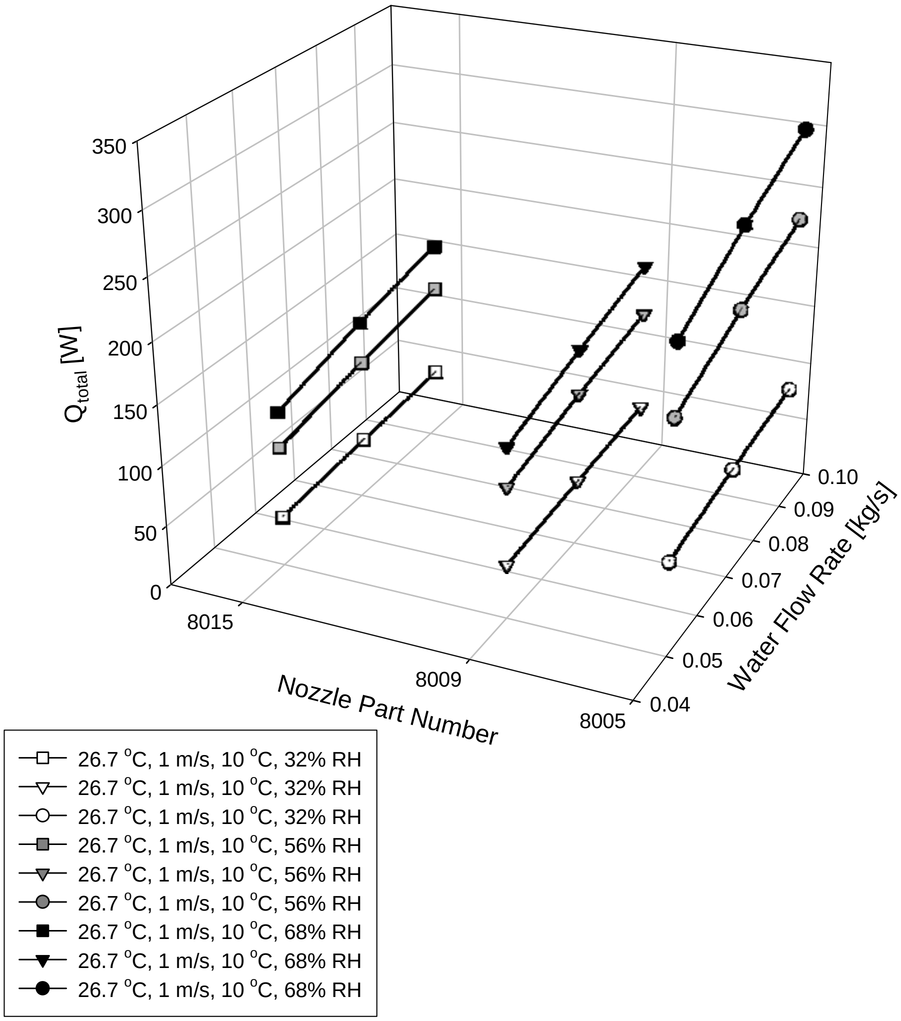

Figure 63 Simulated total heat transfer for the thermal loading conditions listed in the legend.

Comparison of the graphs in Fig. 65 and Fig. 66 reveals that the simulation tends to under-predict the total heat transfer. The amount of under-prediction ranges from 15% to 65%, with an average difference of 50%, which corresponds to actual difference measures ranging from 8 W to 314 W, with an average difference of 147 W (this point will be addressed in detail later), however, the result *trends* are remarkably similar. As mentioned before, both results show that increasing water flow rate and decreasing the average drop size increases total heat transfer. Beyond this, more subtle similarities can be found. For example, note how the difference in results between the 56% and 68% relative humidity runs is smaller than the difference between the 32% and 56% relative humidity runs in both the experimental and simulation results. In addition, the decrease in heat transfer (most distinct in the 68% relative humidity tests) is greater between the 8005 and 8009 nozzle than between the 8009 and 8015 nozzles in both the experimental and numerical results. Yet another similarity in this case is the sensitivity to the relative humidity. The total heat transfer is not as sensitive to nozzle selection at lower humidity levels, but at high humidity levels, there is significantly more cooling with decreasing drop (nozzle) size.

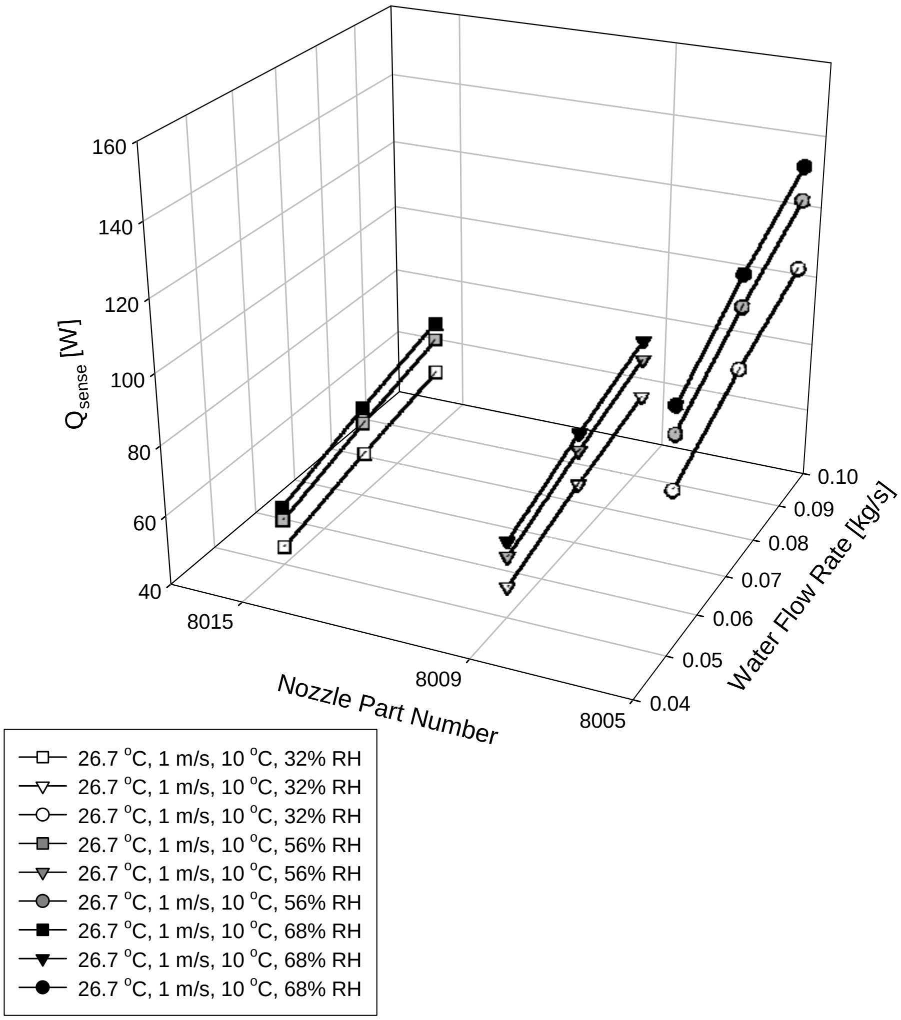

Figure 64 Simulated sensible heat transfer for the thermal loading conditions listed in the legend.

The sensible heat transfer comparison, shown in Figs. 67 and 68 also exhibits similar trends mentioned before: increasing water flow rate and decreasing drop size increases heat transfer. The sensible heat transfer in the experimental tests was greater than that in the simulation (similar to the total heat transfer). The differences in this case range from 48% to 81%, with an average difference of 69%, corresponding to values of 83 W to 273 W, with and average deviation of 177 W. But, it is immediately apparent the data behaves in a uniquely different manner with respect to the relative humidity. Note how the most amount of sensible heat is transferred in the experiments when the relative humidity was low, yet the opposite is true for the numerical simulations which transfer the most amount of heat with high relative humidity. This brings to light the first key difference between the model and the experiments, as the droplet control issue is immediately apparent.

The differences between these and other results are most easily explained with a psychrometric chart, as shown in Fig. 69. Figure 69 shows the experimental process (denoted by 'E') and the simulation process (denoted by 'S') for the thermal loading conditions in Figs. 65-68, i.e. 26.7 ºC air, 10 ºC water, 1 m/s face velocity, and either 32%, 56%, or 68% relative humidity, while only the 5.5 kg/min water flow rate in the 8015 nozzle is shown.

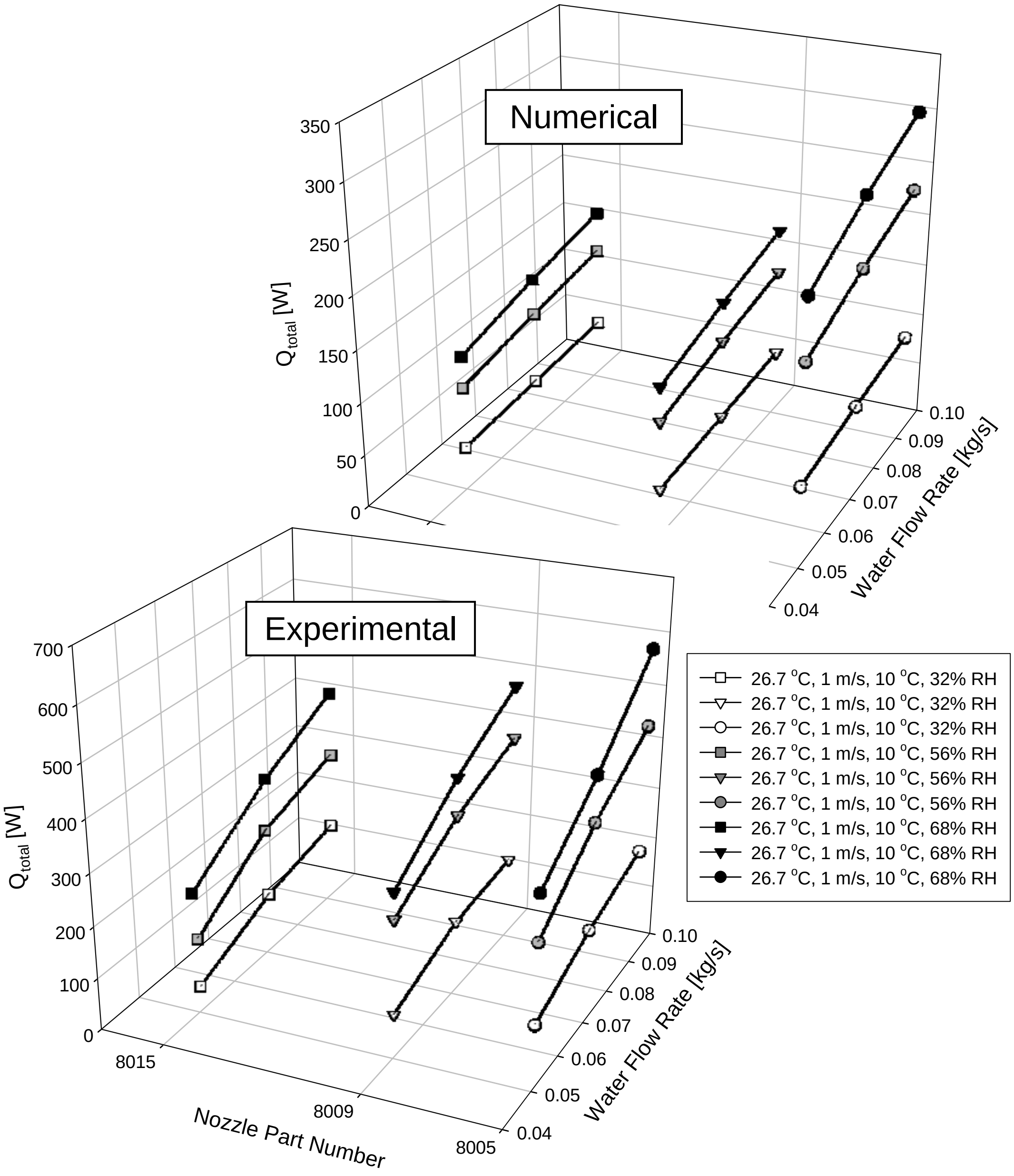

Figure 65 Experimental and simulation results for the thermal loading conditions listed in the legend.

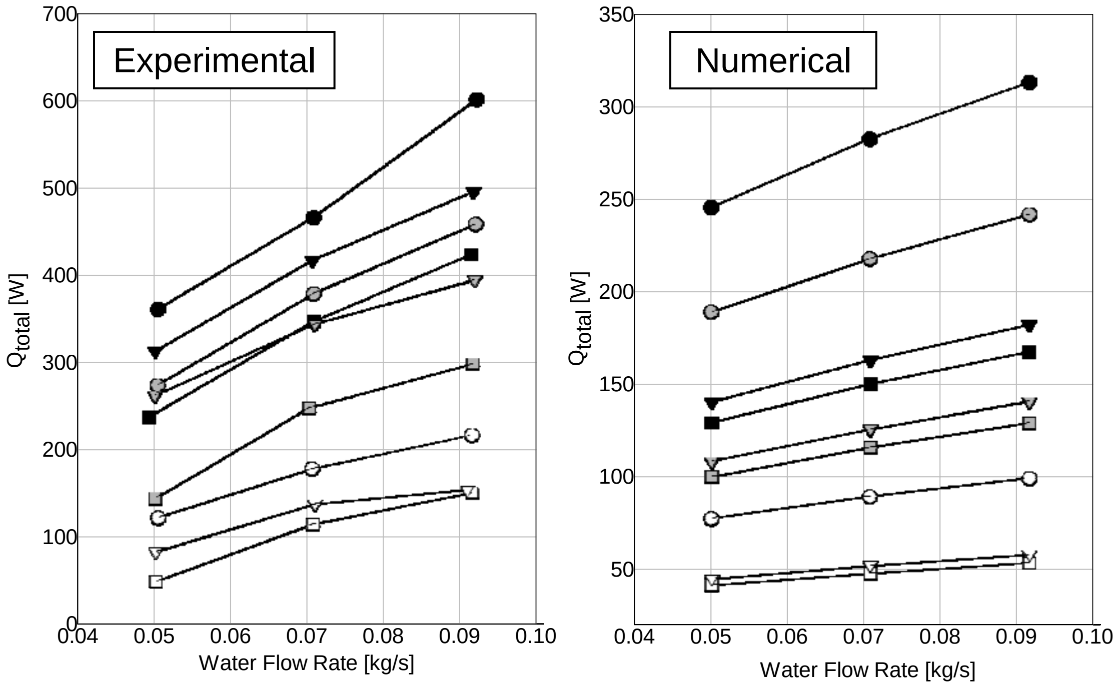

Figure 66 Experimental and simulation results for the thermal loading conditions listed in the legend in Fig. 65.

The first thing noted is that the exit air temperatures are not as cold in the simulations. This is reasonable in light of the above figures that showed that less heat was transferred in the simulations. Beyond this though, the simulation is seen to behave in a more idealistic manner as in every case less moisture is added as compared to the experiments. Note that this is considered more 'idealistic' because the basic understanding of the problem is to transfer heat with the minimum amount of droplet rebound and inadvertent moisture addition, and in the model, there is absolutely no provision for droplet rebound or droplet entrainment. With regard to the experiments though, droplet rebound and the presence of other moisture sources (e.g. the collection tray itself, as well as droplets adhered to the ceiling, honeycomb, etc.) act to add moisture. This extra moisture causes the reversal of the relative humidity response.

The extra moisture in the experimental test section is more likely to provide a source of evaporative cooling – especially at the lower relative humidities. Thus, the air is sensibly cooled to a greater extent, especially at the lower relative humidites, in this direct contact process. Remembering back to Fig. 55 which showed the experimental responses on a psychrometric chart, this additional moisture increase was seen.

These results are interesting from an application standpoint. One could compare these results and conclude that the test section is performing relatively well in low relative humidity situations, evident by the fact that the design allows for 'free' evaporative cooling. However, it could also be argued that this test section could stand further refinement, because in the higher relative humidities, when dehumidification is also an important objective, there appears to be potential to remove even more moisture.

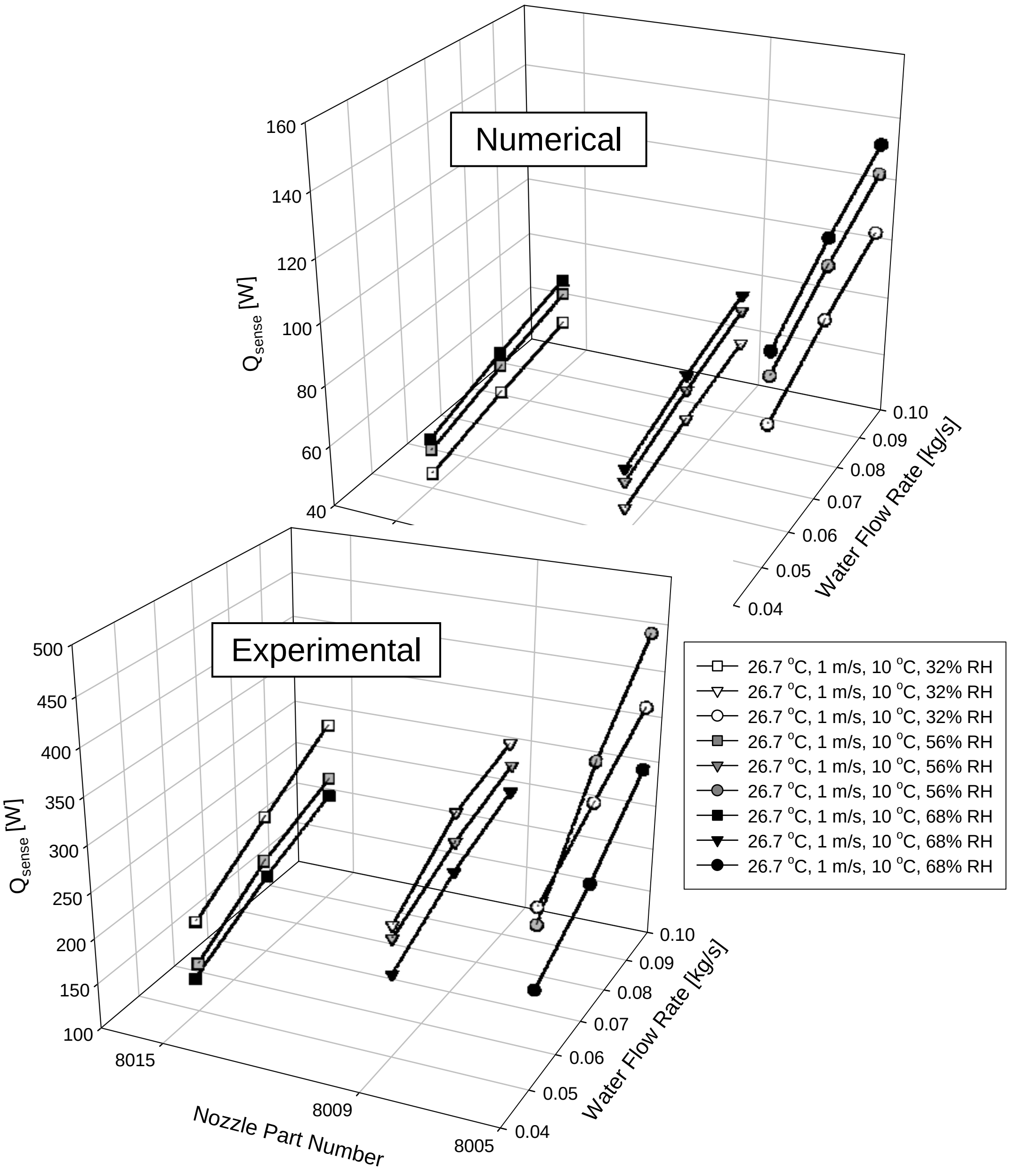

Figure 67 Experimental and simulation results for the thermal loading conditions listed in the legend.

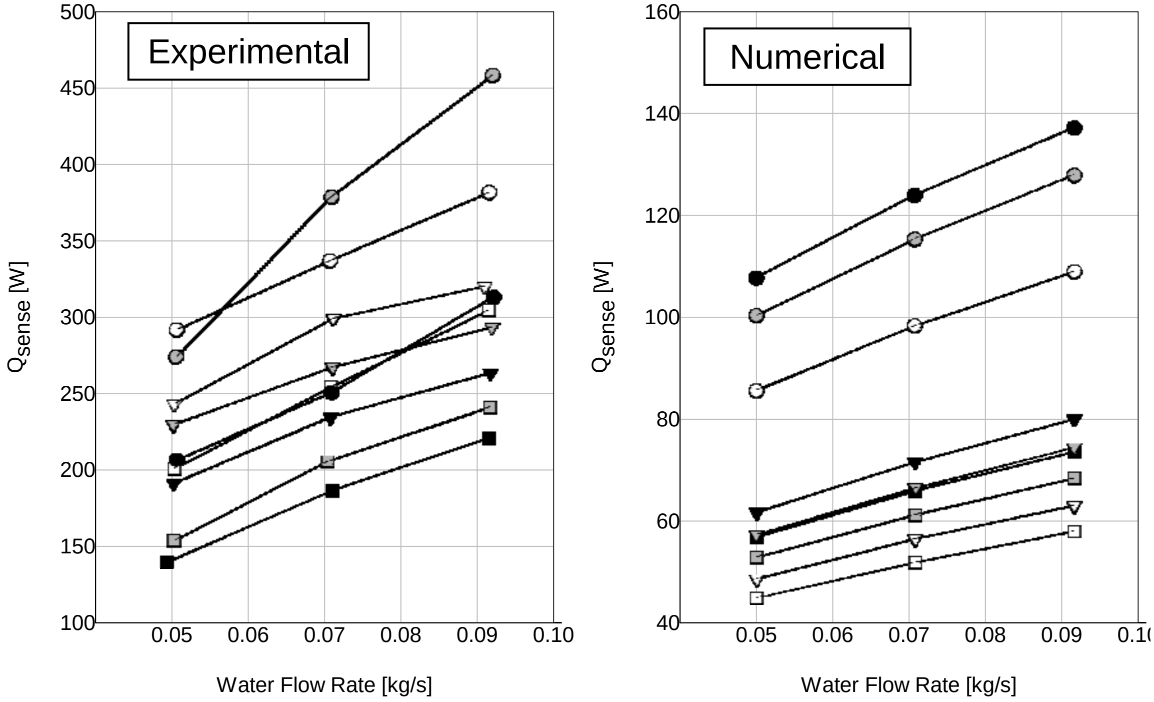

Figure 68 Experimental and simulation results for the thermal loading conditions listed in the legend in Fig. 67.

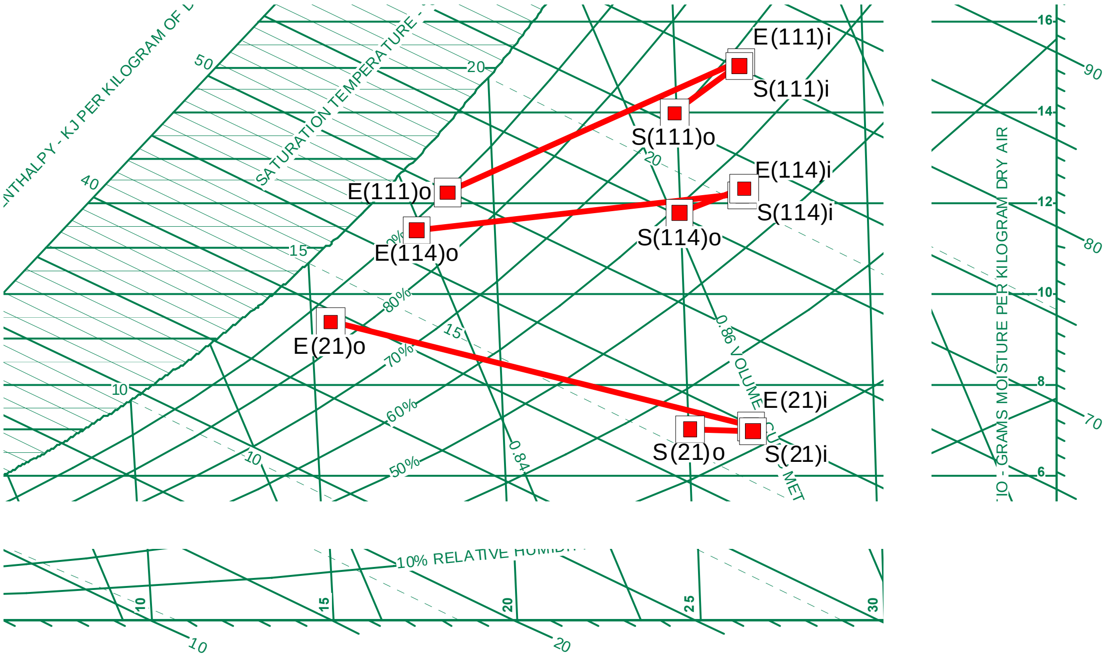

Figure 69 Psychrometric chart comparing the experimental and simulation results for 5.5 kg/min water flow rate with the 8015 nozzle.

5.5.2 Discussion and Validation

The above comments beg certain questions concerning the performance of the test section as well as other issues like 'what are the differences between the model and the prototype test section?', which can only be answered by carefully analyzing the two systems and then quantifying their differences. These quantities may then be held against the results to see if they can actually account for the discrepancies.

The model is the simpler of the two systems having no allowance for the extra cooling modes as described above, and accordingly, it is reasonable to see that the simulated heat transfer should be less. The task then is to quantify how much less. Ten key differences between the model and the experiments exist. Four of these differences will be quantified, but first, the remaining six differences will be addressed for sake of completeness, even though it can be reasoned that these differences can either counteract one another, or possibly even act to diminish the differences in results. In any case, it should be mentioned that in the cases where the differences could cause a significant change in the thermal performance, it is essentially impossible to quantify their effect.

The first point that must always be mentioned involves the so called 'second order effects' such as temperature dependant properties. Note that the model does have some temperature dependant properties where it was felt necessary (the vapor diffusion coefficient and the internal energy of the vapor), however, the air density, conduction coefficients, and specific heats are considered constant. Other second order differences might include the effects of droplet surface contamination, a topic addressed in previous work [8] where it was pointed out that surfactants were found to, in some cases, significantly alter droplet evaporation [42]. In the experiments, the air supplied to the test section was filtered as well as the water, however, the ultra fine particles that would eventually become dissolved in the water could, in theory, alter the latent heat transfer characteristics. Yet another second order effect would be the presence of temperature and moisture gradients within the spray field. In the model, the moist air around the drop is simply assumed to be well mixed. The last point in this group worth mentioning is the potential for the droplets' deformation from a spherical shape. Though typically not an issue for droplets less than 1000 μm in diameter [42], it could be a factor in light of the high-speed imaging collected in the spray charging study. Figure 40 provides an example of how, in the early spray formation, ligaments and coalesced or ruptured droplets can initially be non-spherical, if even for a short time. This is, of course, a deviation from the Nusselt and Sherwood correlations used, which, themselves have associated inaccuracies, which will be addressed in more detail later.

The topic of spray characteristics leads to the second key difference: the difference in the drop size distribution. The actual spray distribution information is not available, and thus estimates have been made for the simulations. Of course, these estimates could be seen to have a negligible effect just as easily as they have a considerable effect. For example, if the distribution is underestimated, then the argument is made that the many smaller drops (which, according to the nozzle comparisons, can have significantly more heat transfer) and their associated larger heat transfer is unaccounted for. Conversely, a larger distribution also means that larger drops will be formed as well, which could counteract the argument that the heat transfer is under predicted by failure to account for the smaller drops. Further, in a real flat fan spray, a sheet region exists (again, see Fig. 40) which is not accounted for in the model. In this case, though, this effect could be seen to actually help the model transfer more heat than the real spray as the surface area to volume ratio of the sheet is smaller than that of a spray. However, it is appropriately reasoned that this sheet effect is negligible considering the fact that the simulations still under predict the heat transfer.

The third major difference ties to the spray and its relation to the test section geometry, as some spray inevitably strikes the edges of the honeycomb false wall causing primary droplet rebound. These rebounded drops, rebounding back into the bulk air stream, then have the opportunity to transfer more heat and mass. Additionally, these drops can strike other droplets to compound the aforementioned droplet coalescence and rupture issues that change the drop size distribution.

Following the droplet rebound issue, the fourth key difference between the model and experiments is the fact that the rebounded drops can accumulate on the ceiling of the test section as well as other surfaces, like the honeycomb cells adjacent to the spray area and the drift eliminator (note that the slower moving, rebounded drops are more likely to be entrained and carried to the drift eliminator). This accumulated moisture acts as a sink, as the droplets are still below the saturation temperature of the air. Initially, this could be thought to actually increase moisture removal, however, it must be realized that under steady state operation, this moisture is simply accumulating on the walls until it reaches the saturation temperature of the air. At this point, the moisture removal must stop and this effect is negligible. Another way to think about this is to realize that the moisture is only removed when it actually leaves the air stream, i.e. if it condenses on a drop or conglomerates into a large enough mass on the ceiling, for example, such that the gravity effects dominate over the surface tension effects, and the droplet falls to the collection tray.

The fifth and sixth key issues, like the fourth, center on the possibility for extra convection off cooled surfaces, namely the water surface in the collection tray and the chilled walls of the test section. The pool of collected water, leaving the test section under the force of gravity, does have the potential to interact with the air stream as the spray itself can act as a kind of wall, deflecting a portion of the air stream down into the collection tray. Further, the spray drops themselves also induce air motion into the collection tray. In either case, the portion of air circulated into the tray will be well mixed, and yet to be conditioned (not having passed through the spray). Both of these criteria increase the potential for heat transfer. Also, the spray directly impacts the sides of the collection tray, and to some extent, the ceiling of the test section. Though these walls are constructed of cast acrylic, their surfaces do chill, and thus serve as another surface to be counted for additional heat transfer.

It is difficult to tally the potential heat transfer from the six key differences listed thus far. However, the final four differences will be quantified to some extent. The four remaining differences are the measurement error, the error associated with the Nusselt and Sherwood numbers, the additional droplet hang time, and heat transfer off the drift eliminator.

The experimental uncertainty, addressed in section 4.3.4, shows that the values in Figs. 65-68 could be off by an average of 8% (roughly 30 W for the average experiment though it could be higher or lower in extreme cases). This alone cannot account for the discrepancies, however, it must be reiterated to put the problem in perspective. The experiments, though accurate, should not be held as the absolute standard against which the model is checked. It is the agreement in the trending behavior that is most important as this indicates that the fundamental behavior has been captured.

In the simulation, the spray passes through the air only one time, and the simulation ends as soon as the drop exits the cross section of the simulated test section. In the experiments, the droplets pass through the free stream, however, they still have the potential to interact with the air once out of the general free stream. As mentioned before, in the real situation, the spray sheet, as well as the drag from the droplets, will direct some airflow into the collection tray. In this process, the droplets are exposed to the air for an additional 4 to 7 cm, which is actually a considerable amount considering the average length of flight in the test section is 18 cm. Therefore, this configuration can actually increase the effective drop flight or life by 20% to 40%. Considering the fact that the droplets typically have not warmed more than 1 ºC at this point, it is not unreasonable, then, to assume that this discrepancy could account for an additional amount of cooling in the experiments that is not accounted for in the model.

Unfortunately, it is difficult to quantify this discrepancy, and the problem must be approached with some logical reasoning. As the experimental test section cannot be made in such a way so as to prevent this extra cooling, the model side will be investigated. To try to quantify this extra heat transfer, the code is modified such that the effective area of the simulated test section is larger. This gives rise to more droplets and gives those droplets a longer flight time. For the results that follow, the test section is increased in size from 0.1524 m x 0.1524 m to 0.1981 m x 0.1981 m – a 69% increase in area, equating to an increase in average flight length from 18.395 cm to 23.9152 cm (a difference of 5.52 cm, or a 30% increase).

The face velocity was kept constant, therefore the volume of air being treated increases. In much the same way that the heat transfer increases with increasing velocity (due to more air being treated) increasing this air volume will also increase heat transfer. Initially, however, one might think that this would null the comparison between the model and experiments. By the formulation of the model, this is not the case. Remembering that the model actually sums the heat and mass transfer from a single drop and moist air volume, increasing that moist air volume is precisely equivalent to increasing the droplet flight path (in which it would, indeed, be exposed to more air). The results comparisons are shown in Figs. 70 and 71, and are virtually identical, except for the magnitude of heat transferred (note the y-axes).

The larger test section does provide more heat transfer, as expected. For these simulations, the total heat transfer increased by 24% ±0.6% (corresponding to approximately 50 W, depending on the conditions, with a maximum increase of 100 W). The sensible heat transfer, too, increased by 24% ±0.6% (corresponding to an increase from 20 W to 40 W, depending on the flow rate and humidity).

While discussing the variability of the model, it is pertinent to address another key point of possible error, which is the accuracies of the Nusselt and Sherwood numbers. The Ranz-Marshall equations for the Nusselt and Sherwood numbers were developed from empirical data collected from monitoring the cooling and evaporation of free falling liquid spheres with Reynolds numbers less than 200 [41]. The Reynolds numbers for the drops in this research range from 300 to 1100. The validity of applying Ranz-Marshall correlations in this range of Reynolds numbers was addressed in detail in previous work [8] and found to be satisfactory; however, there is still some associated uncertainty with the correlation. The uncertainty found in the Ranz-Marshall paper [41] was listed as a maximum of 10% uncertainty (though they note that it was usually less than this). This maximum error will be used to investigate the uncertainty as it relates to the simulated heat transfer.

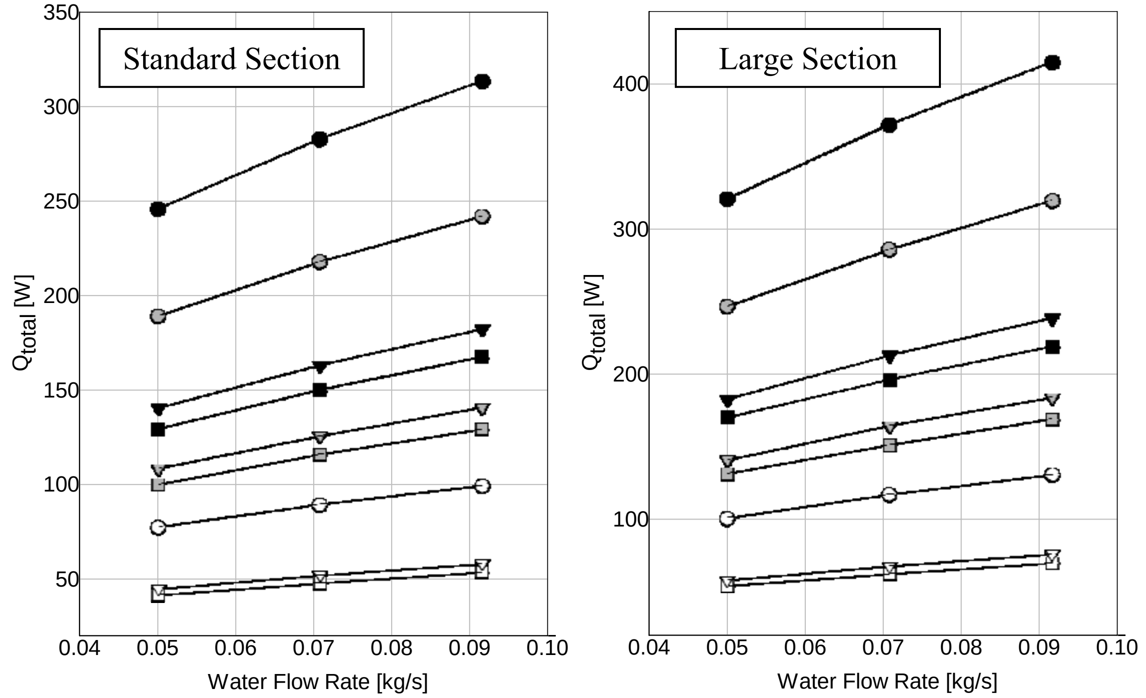

Figure 70 Comparison of total heat transfer between the standard 0.1524 m square section and 0.1981 m square section simulations. The test conditions are the same as those in Fig. 67.

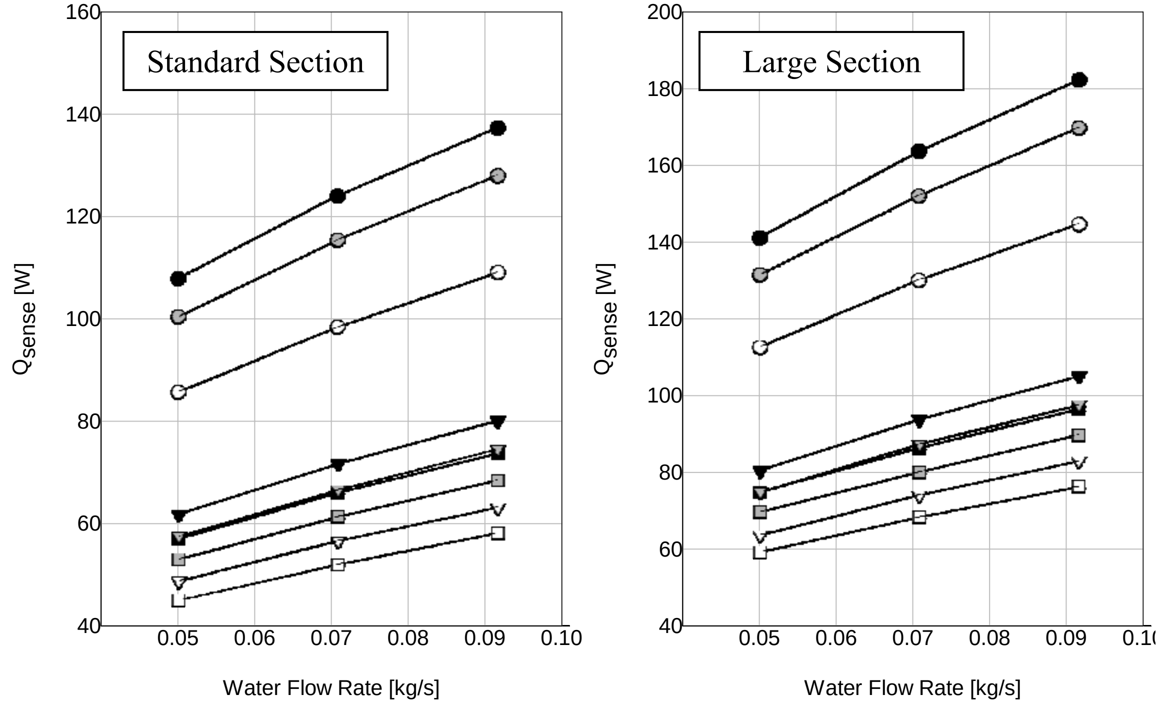

Figure 71 Comparison of sensible heat transfer between the standard 0.1524 m square section and 0.1981 m square section simulations. The test conditions are the same as those in Fig. 67.

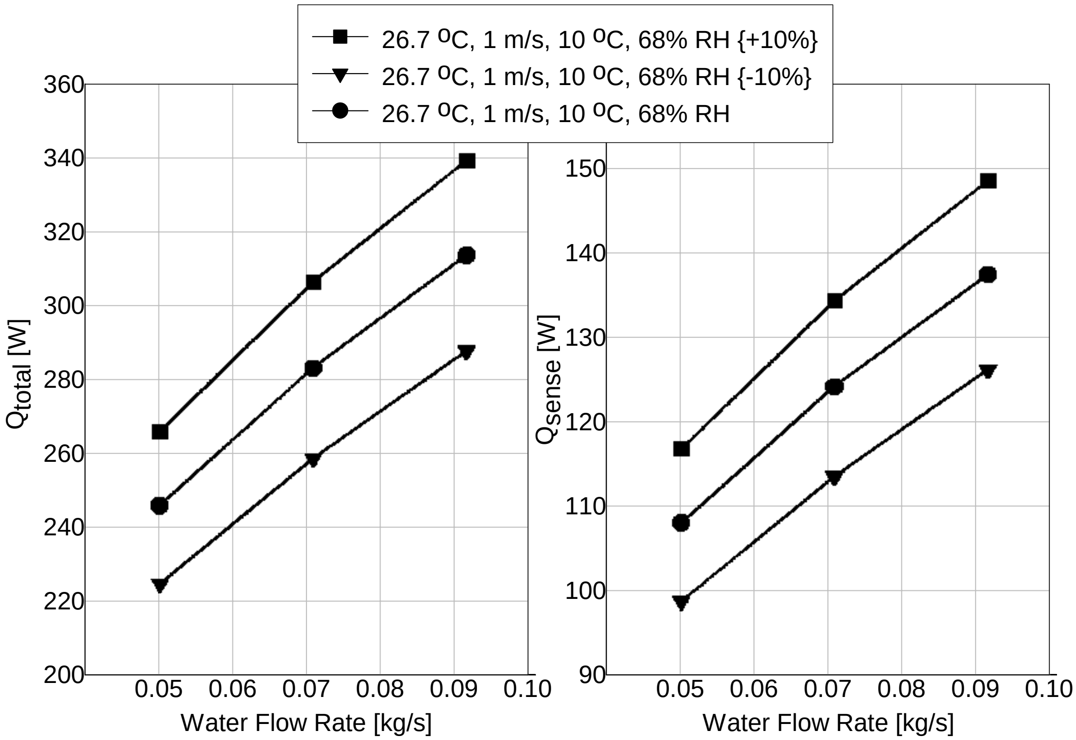

Figure 72 Change in total and sensible heat transfer as Nusselt and Sherwood numbers are increased and decreased by 10% for the 8005 nozzle at the test conditions shown in the legend.

As the most amount of heat was transferred with the smallest ‘8005’ nozzles (at 68% *RH*), they are simulated so as to provide the largest response, and corresponding resolution in post processing of differences as described below. For this investigation, the code was simply modified such that the Nusselt and Sherwood numbers were multiplied by either 1.1 or 0.9, corresponding to a 10% increase or decrease in the calculated values. The results are shown in Fig. 72. There is a corresponding change of plus or minus 8.3% ±0.3% in the total and sensible heat transfer.

The final key discrepancy between the model and the experiments centers on the drift eliminator. The purpose of the drift eliminator, as the name implies, is to remove entrained moisture (i.e. droplets) from the air stream. The water droplets collected on the drift eliminator, like those collecting on other surfaces in the test section, are still well below the dry bulb and dew point temperature of the air (except in the case of 32% *RH*). These drops chill the steel drift eliminator, turning it into a series of cold fins. The eliminator can then act to sensibly cool the air, or even remove moisture if the inlet relative humidity is high enough.

To investigate the impact of the drift eliminator on heat transfer, Fluent simulations were ran as no known correlations exist describing heat transfer off of such a surface. Figure 72 shows the temperature contours resulting from the 2-D solution. Note that the inlet air temperature was taken as 18 ºC. This value was assumed as an approximate average of the exiting air temperatures (i.e. after the spray, but before the drift eliminator) from the experiments. The true inlet temperature will vary depending on the exact test conditions, but this value of 18 ºC was used to quantify the order of magnitude of heat transfer in question. The wall sides of the test section are considered insulated, while the drift eliminators themselves are set at

11 ºC (corresponding to an initial 10 ºC water temperature) for the test shown in Fig. 71. The entrance air velocity was 1 m/s.

Note that heat transfer with dry air is simulated, so the results are for sensible heat transfer only. The heat transfer was figured by using the inlet and exit air temperature reported by the area-weighted average in hand calculations, and by using the built in simulation reports for the area-weighted average total surface heat flux to the fins. These two methods revealed that for the test conditions in question, the sensible heat transfer to the drift eliminator was 79 W. Of course, if the latent component were added, the total heat transfer could be well over this value in the high humidity case where dehumidification can still occur. It is difficult to try to put this value in terms of a percentage of the total heat transfer, however, as it can range anywhere from 19% to 192% of the simulated heat transfer. It will be mentioned that another simulation was ran with the drift eliminator set to 6 ºC (to simulate a 5 ºC water spray), and approximately 100 W of sensible heat transfer was achieved at 1 m/s face velocity, and approximately 200 W were transferred when the 6 ºC fins were used with a 3 m/s face velocity. The results of this Fluent analysis highlight the impact that the drift eliminator may have in future applications of a direct contact system.

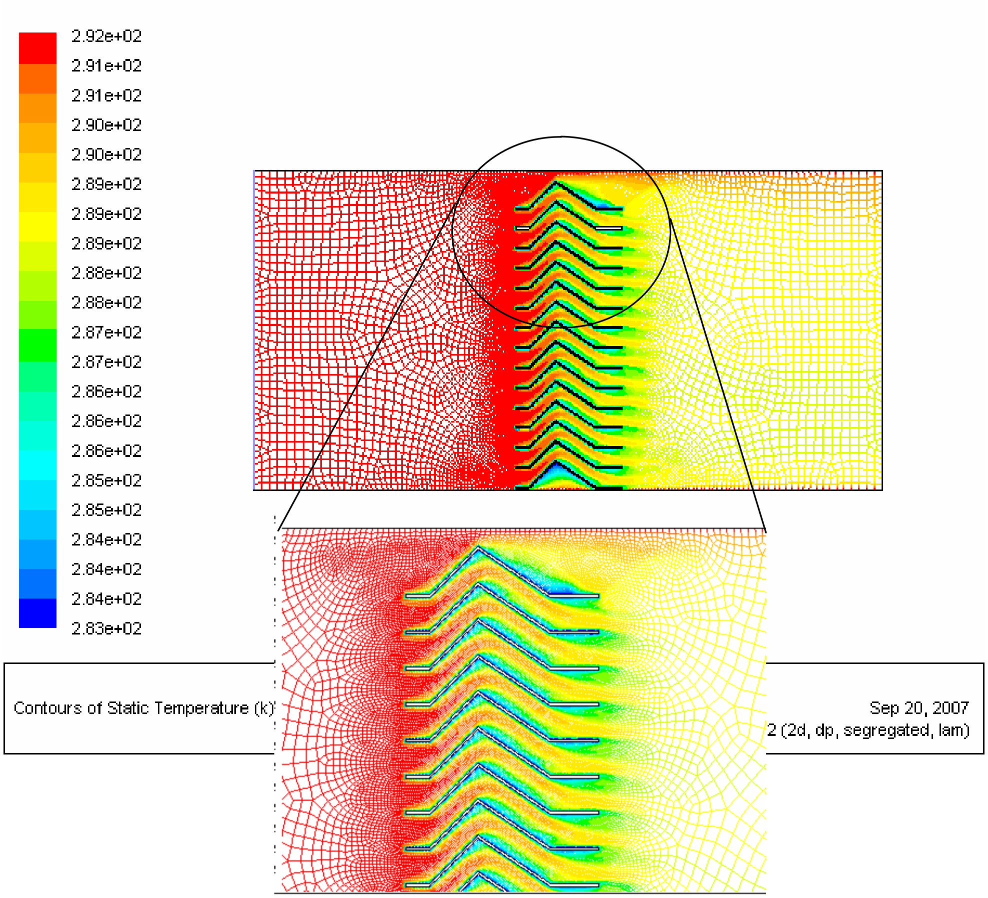

Figure 73 Static temperature contours from a Fluent simulation investigating heat transfer from the drift eliminator.

Table 4 Uncertainty in simulation/experimentation.

Factor	**% Difference**	**Value [W]**
Experimental Uncertainty	±8%	30*
Extended Flight Time	24%	50*
Correlation Uncertainty	±8%	15*
Drift Eliminator	19%-190%	79*
Total	8%-40%**	174
Qtotal	15%-65%	8-314
Qtotal Average	50%	147
Qsense	48%-81%	83-273
Qsense Average	69%	177

*Average value for the results presented.
**Not including percent error from the drift eliminator.

The uncertainties or discrepancies quantified in this study are listed in Table 4. After reviewing these differences, it is unlikely that any single factor or discrepancy accounts for the difference in heat transfer between the model and the experimental tests. Further, it would be difficult to the point of impossible to try to identify for every test, which combination of discrepancies come together, and in what magnitude, to create or eliminate the inconsistency. Nonetheless, this exercise is successful in the fact that it is evident that even just the final four differences can come together to eliminate the difference in results.

Again though, just because the differences can be accounted for does not eliminate the fact that the model still under-predicts the energy exchange by its formulation. There are a few options to consider, and the ultimate choice depends on how one intends to use the model. For example, one might argue that the model could/should be expanded, perhaps in another project, to account for the inconsistencies. In that project, the experimental data could be used to incorporate a semi-empirical factor that accounts for the probability of droplet entrainment based, namely, on the conditions like calculated droplet speed and face velocity. This probability factor could then be applied in another kind of Monte-Carlo simulation to create additional heat and mass transfer that would be associated with the droplet entrainment. Further, the drift eliminator heat transfer could be accounted for. This heat transfer could be ‘activated’ by the probability of droplet entrainment. Although this would eventually come together to be an impressive model, the task is easier said than done. The single greatest challenge would lie with quantifying the actual heat and mass transfer from the entrained drops and drift eliminator. Practically speaking, this feat is nothing short of impossible.

In light of such difficulty, the question of expanding the model is then revisited. In reality, it could be said that refining the model to account for these ‘test section specific’ issues actually detracts from its value as a more universal design tool. This argument follows in much the same way as that for the correlation. In its current form, backed by the conclusions of this investigation, the model is known to behave in much the same way as the experimental tests (for the range of conditions investigated), and that it uniformly under-predicts the heat and mass transfer as compared to the experiments run in the prototype test section developed, being of similar geometry and function.

6.0 CONCLUSIONS

The spray charging study showed that the novel nozzle design was effective in charging flat fan water sprays, however, charging the spray did not help to collect droplets. The collection study revealed that any object in the spray path is likely to cause droplet rebound, and therefore the best method to minimize droplet rebound was to remove a section of the false wall separating the collection tray from the air stream.

The wind tunnel performed well, though testing was limited to days which had naturally drier air. The test section developed for the heat and mass transfer experiments, being the rotated square shape with a section of the false wall removed, was the best to date. The exiting water temperature measurements were not as accurate as desired, and unfortunately, it was concluded that little could be done to alleviate this problem.

The heat and mass transfer experiments, though tedious, provided an ample amount of data, which was used to develop a *UA* correlation that was a function of the mean drop size, the free stream relative humidity, and the water flow rate – the three key driving variables for the system performance. It was later concluded that inclusion of the free stream velocity could make for a more precise prediction; however, if this were to be done, more experimental testing at a third face velocity is recommended.

The correlation was derived from a fundamental analysis of the system, the heart of which centers on forced convection on a single drop. Though the overall heat transfer coefficient, *UA*, is normally used for sensible heat transfer calculations, the coefficients were made to be a function of the relative humidity and drop size, the key factors that affect sensible heat transfer. The uncertainty for the *UA* correlations was also developed with the key uncertainty being that which results from the curve fitting of the coefficient *C2*.

A full spray model was developed. The model was found to underestimate the experimental results as it did not account for extra sources of cooling specific to the experimental test section such as extended drop lifetimes and convection off a chilled drift eliminator. However, the model was found to follow the response trends seen in the experimental data.

In retrospect, three key products resulted from this research: the experimental data, the correlation, and the model. Taken individually, and under the strictest scrutiny, one could argue that these items are not as valuable as they could be, as they all have inherent flaws that stem from uncertainty, e.g. poor exit water temperature or air speed measurements (experiments), lack of incorporation of certain data upon formulation (correlation), or lack of incorporation of experimental variables like adjacent cooling (model and correlation). However, taken as a whole, it is argued that these three items work together to create a system of tools, each of which covering the shortcomings of the others.

The experimental data is for discrete points of interest over a certain range of conditions, thus, there are gaps in the information. The correlation, which has some, but not all, of the experimental phenomenon incorporated, lends itself to bridge some of the gaps between the experimental data points. The analytic correlation further lends itself to be manipulated algebraically so that independent variable ranges may be identified for a desired overall heat transfer coefficient. Of course, this overall heat transfer does not fully identify the exit state of the air, so the model then becomes useful as it more precisely defines the details of the heat transfer problem. The model does not lend itself as an initial investigation tool given the associated computational intensity; however, the correlation can be rapidly applied for a first order analysis. The results of the correlation and models are, as highlighted, not absolutely precise. But, having identified the shortcomings of each tool, some engineering judgment can be applied to guide initial prototype design, for example.

7.0 REFERENCES

[1] Zhang, H., 2004, “Numeric Rresearch on a Vaporizing Fuel Droplet in a Forced Convective Environment,” *Int. Journal of Multiphase Flow*, **30**, p. 181-198.

[2] Roth, K.W., Westphalen, D., Dieckmann, J., Hamilton, S.D., and Goetzler, W., 2002, "Energy Consumption Characteristics of Commercial Building HVAC Systems -Volume III: Energy Savings Potential", available at: http://wwvv.eren.doe.gov/building/documents

[3] Watt, J.R., and Brown, W.K., 1997, *Evaporative Air-conditioning Handbook*, Fairmont Press, Lilburn, GA.

[4] Hensley, J., 2003 “Development of a modular wind tunnel and experimental process for use in the investigation of electrohydrodynamically enhanced spray cooling” Honors Thesis, University of Missouri - Columbia.

[5] Hensley, J., Lynch, J., Hawn, C., Siegel, S., 2004 “Feasibility Study of a Direct Contact Heat Transfer Heat Exchanger for Use in a Residential HVAC System,” final report submitted to DEED for 2003 Senior Technical Design Project.

[6] El-Morsi, M., Klein, S.A., and Reindl, D.T., 2003, “Air Washers – A New Look at a Vintage Technology,” *ASHRAE Journal*, October 2003, pp. 32-36.

[7] El-Morsi, M.S., 2002, “Optimization of Direct Contact Spray Coolers,” Ph.D. thesis, University of Wisconsin-Madison, Madison, WI.

[8] Hensley, J. 2005, “A Practical Model for Investigating Heat and Mass Transfer in a Direct Contact Heat Exchanger,” Master’s thesis, University of Missouri – Columbia.

[9] Jacobs, H.R., 1988, “Direct-Contact Heat Transfer for Process Technologies,” *Journal of Heat Transfer*, **110**, pp.1259-1270.

[10] Letan, R., 1981, “A Parametric Study of a Particulate Direct Contact Heat Exchanger,” *Transactions of the ASME*, **103**, August 1981, pp. 586-590.

[11] Sideman, S., Moalem-Maron, D., 1982, “Direct Contact Condensation,” *Advances in Heat Transfer*, **15**, pp. 227-281.

[12] Tadrist, L., Seguin, P., Santini, R., Pantaloni, J., 1985, “Experimental and Numerical Study of Direct Contact Heat Exchangers,” *International Journal of Heat and Mass Transfer*, **28**, 6, pp.1215-1227.

[13] Yoo S.Y., Kwon, H.K., 2004, “An Experimental Study on the Performance of Air/Water Direct Contact Air Conditioning System,” *KSME International Journal*, **18**, 6, pp. 1002-1009.

[14] Brucker, A.P., Mattick, A.T., 1984, “High Effectiveness Liquid Droplet/Gas Heat Exchanger for Space Power Applications,” *Acta Astronautica*, **11,** 7-8, pp. 519-526.

[15] Chen., K.H., Trezek, G.J., 1977, “The Effect of Heat Transfer Coefficient, Local Wet Bulb Temperature and Drop Size Distrubution Function of the Thermal Performance of Sprays,” *Journal of Heat Transfer*, **99**, pp. 381-385.

[16] Kachhwaha, S.S., Dhar, P.L., Kale, S.R., 1997, “Experimental studies and numerical simulation of evaporative cooling if air with a water spray – I. Horizontal parallel flow,” *International Journal of Heat and Mass Transfer*, **41**, 2, pp. 447-464.

[17] Kachhwaha, S.S., Dhar, P.L., Kale, S.R., 1997, “Experimental studies and numerical simulation of evaporative cooling if air with a water spray – II. Horizontal counter flow,” *International Journal of Heat and Mass Transfer*, **41**, 2, pp. 465-474.

[18] Bo, N., 2001, “Numerical Simulation and Experimental Studies of Air Treatment Process with Water Sprays of One Row Counter Flow,” *Journal of Dong Hua University (Eng. Ed.)*, **18**, 3, pp. 14-19.

[19] Ni Bo, 1999, “Numerical Method for Heat and Mass Transfer in Air Washer – 1. Mathematical Solution for a Droplet Evaporating in a Finite Surrounding Airstream,” *Journal of China Textile University (Eng. Ed.)*, **16**, 4, pp.101-103.

[20] Ni Bo, 2000, “Numerical Method for Heat and Mass Transfer in Air Washer – 2. Spray Drop Trajectories of Horizontal Parallel Flow,” *Journal of China Textile University (Eng. Ed.)*, **17**, 1 pp.68-71.

[21] Bailey, A.G., 1988*, Electrostatic Spraying of Liquids*, John Wiley & Sons Inc. New York, NY.

[22] Law, S.E., Bowen, H.D., 1966, “Charging Liquid Spray by Electrostatic Induction,” *Trans. of ASAE*, **9** (4), pp. 501-506.

[23] Law, S.E., 1978, “Embedded-Electrode Electrostatic-Induction Spray-Charging Nozzle: Theoretical and Engineering Design,” *Trans. of ASAE*, **21**, pp. 1096-1104.

[24] Beckwith, T.G., Marangoni, R.D., Lienhard, J.H., 1993, *Mechanical Measurements, 5th Ed.*, Addison-Wesley Publishing Company, Inc., Reading, MA.

[25] ANSI/ASHRAE. 2000. Standard 33-2000: Method of Testing Forced Circulation Air Cooling and Air Heating Coils. Atlanta: American Society of Heating and Refrigerating and Air-Conditioning Engineers, Inc.

[26] ANSI/ASHRAE. 1987. Standard 41.2-1987: Standard Method for Libratory Airflow Measurement. Atlanta: American Society of Heating and Refrigerating and Air-Conditioning Engineers, Inc.

[27] *Laminar Flow Elements: Installation and Operation Instructions.* File No. 501:440-10. http://www.meriam.com/downloads/pdf/Manuals/lfe_manual.pdf. (8/31/2005)

[28] ASHRAE, 2001, *2001 ASHRAE Handbook-Fundamentals*, Atlanta: American Society of Heating and Refrigerating and Air-Conditioning Engineers, Inc.

[29] Incropera, F.P., Dewitt, D.P., 2002, Introduction to Heat Transfer, 4th Ed., John Wiley & Sons, Inc., USA.

[30] Staed, S.C., 2007, "Creation of "Unit Cell" Concept for Air-to-Liquid Heat Exchanger Research and Development," Master's thesis, University of Missouri – Columbia.

[31] Carrier Corporation, 2000, "Product Data, 38AK007-012, 38AKS008-044 with40RM007-034 and 28CB, LA088, 012 Commercial Air Cooled, Split Systems – 6 to 40 Nominal Tons," Syracuse, NY.

[32] Jones, T.B., 1995, Electromechanics of Particles, Cambridge University Press, New York, NY.

[33] Law, S.E., 2001, "Agricultural Electrostatic Spray Application: A Review of Significant Research and Development during the 20th Century," *J. of Electrostatics*, **51-52**, pp. 25-42.

[34] Gemci, T., Hitron, R., Chigier, N., 2002, "Measuring Charge-To-Mass Ratio of Individual Droplets Using Phase Doppler Interferometery," *ILASS Americas, 15th Annual Conference on Liquid Atomization and Spray Systems, Madison, WI, May 2002.*

[35] ASHRAE, 1996, *1996 ASHRAE Handbook-HVAC Systems and Equipment*, Atlanta: American Society of Heating and Refrigerating and Air-Conditioning Engineers, Inc.

[36] Moran, M.J., Shapiro, H.N., 2000, *Fundamentals of Engineering Thermodynamics, 4th Ed.*, John Wiley & Sons, Inc., USA.

[37] Bejan, 1997, *Advanced Engineering Thermodynamics, 2nd Ed.*, John Wiley & Sons, Inc., New York.

[38] Marchant, J.A., Dix, A.J., Wilson, J.M., 1985, "The Electrostatic Charging of Spray Produced by Hydraulic Nozzles, Part I. Theoretical Analysis," *J. Agric. Eng. Res.*, **31**, pp. 329-344.

[39] Giancoli, D.C., 1984, General Physics, Prentice-Hall, Inc., Englewood Cliffs, New Jersey.

[40] Spraying Systems Co., 2002, *Industrial Spray Products,* Catalog 60B.

[41] Ranz, W.E., Marshall, W.R., 1952, "Evaporation from Drops – Part 2," *Chemical Engineering Progress*, **48**, 3&4, pp. 173-180.

[42] Clift, R., Grace, J.R., and Weber, M.E., 1978, *Bubbles, Drops, and Particles*, Academic Press, New York, NY.

[43] Kestin, J., J.H. Whitelaw, 1964, “The viscosity of dry and humid air,” *International Journal of Heat and Mass Transfer*, **7**, pp.1245-1255.

8.0 APPENDIX

8.1 Derivations

8.1.1 Droplet Heat and Mass Transfer Model Development

The full spray model operates by summing the individual contributions from the many drops in the spray. Thus, a series of ordinary differential equations are used to describe the heat and mass transfer between a single drop and a volume of air surrounding that drop. The drop and the salient forces for the problem are shown in Fig. A1.

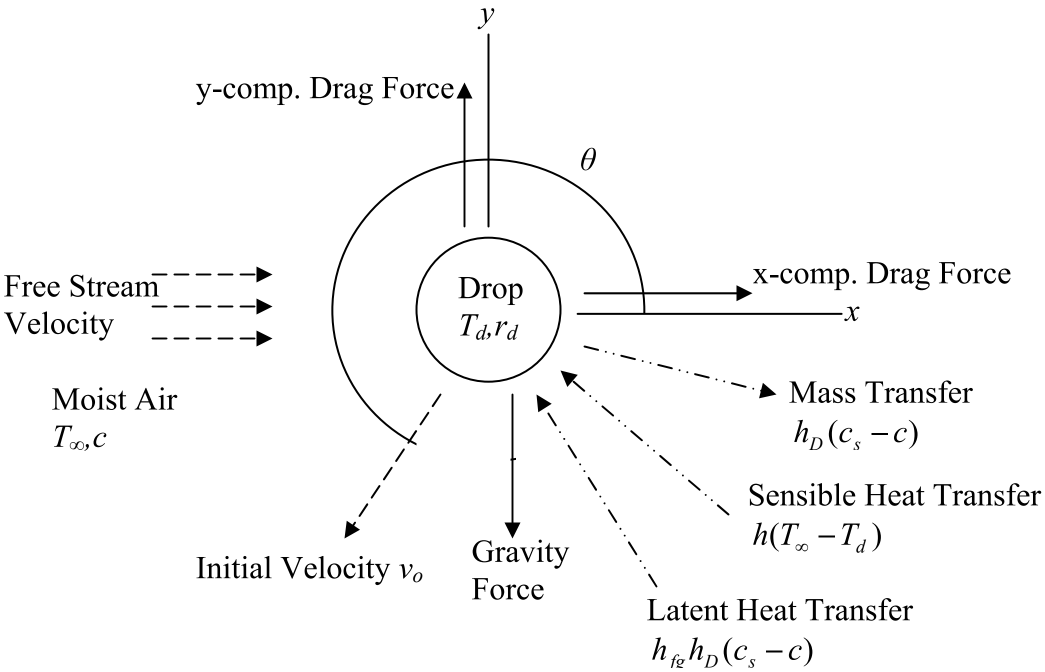

Figure A1 The forces and heat and mass transfer of drop in moist air stream.

Note that forced convection is the only mode for sensible heat transfer, yet the energy balance considers the interaction between a spherical drop and a spherical, finite volume of air in which the drop is centered. In the real situation, the drop could be thought of to interact with a column of air (following the drop's path), however, this spherical approximation is made to account for the fact that in the real situation of a full spray, neighboring drops and their heat and mass transfer act to diminish the driving gradients for the system. By fixing a finite volume of air, this diminishing of the driving forces due to a kind of cloud effect can be approximated. The problem, then, would appear to lie with the determination of the volume of air around the drop.

In the drop/air system shown in Fig. A2, the energy for the closed system must be conserved (note that the system is considered well insulated). Thus, the value of *b* used to define the moist air volume does not matter for purposes of the energy balance, however, the value of *b* will determine the total amount of energy that can be transferred, and thus, determines the final component temperatures, moisture concentration, and drop size.

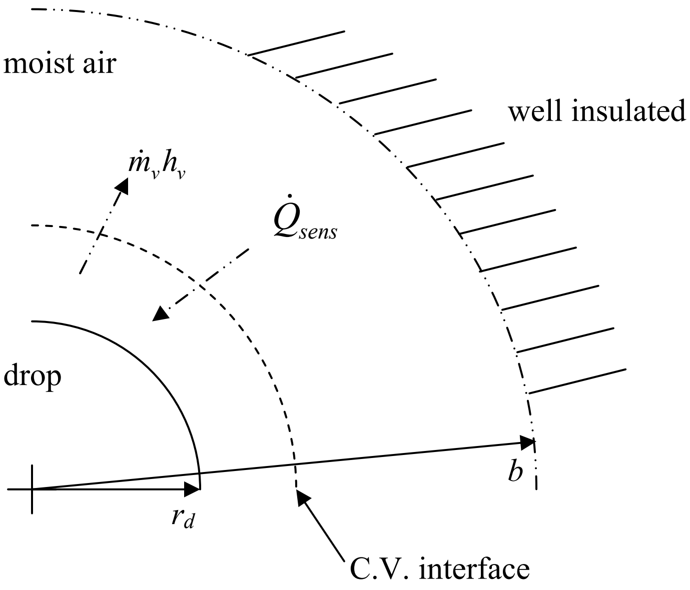

Figure A2 Quarter view of drop/moist air system showing the control volume interface beyond the surface of the drop.

Note that in Fig. A2 there is a thin layer of moist air and vapor in the drop's control volume. With this assumption, it is known that the phase change takes place in the drop system, and thus, as noted in the figure, the mass that crosses the boundary is in vapor form. In this derivation the amount of air in this layer will be assumed negligible, and the layer will be driven to the limiting case of being negligibly thin such that the change in internal energy of the vapor need not be considered. Beginning with a First Law energy balance on the drop and the thin layer of vapor, assuming that the change in kinetic and potential energy for the drop is zero, that the deformation of the control volume is small (no work term), and neglecting kinetic and potential energy effects of the mass leaving the control volume, the First Law reduces to:

$$\frac{dE_{C.V.,drop}}{dt}=\frac{dU_{drop}}{dt}=\frac{d}{dt}\left[m_d u_l(T_d)\right]=u_l(T_d)\frac{dm_d}{dt}+m_d\frac{du_l}{dt}=\dot{Q}_{sens}-\dot{m}_v h_v(T_d) \quad \text{(A1)}$$

For the airside of the derivation, with negligible work contribution and negligible changes in kinetic and potential energy assumptions, the First Law reduces to:

$$\frac{dE_{C.V.,air}}{dt}=\frac{dU_{air}}{dt}=\frac{d}{dt}\left[m_a u_a(T_\infty)+m_v u_v(T_\infty)\right]=m_a\frac{du_a}{dt}+m_v\frac{du_v}{dt}+u_v\frac{dm_v}{dt}=-\dot{Q}_{sens}+\dot{m}_v h_v(T_d) \quad \text{(A2)}$$

The change in mass of the drop must equal the change in mass of the vapor in the air volume, and these must also equal the mass flow rate of vapor found on the right side of Eqs. (A1) and (A2). By substituting specific heat properties (assuming a constant volume process) and rearranging terms, Eqs. (A1) and (A2) reduce to Eqs. (A3) and (A4), respectively:

$$m_d\frac{du_l}{dt}=m_d c_{p,w}\frac{dT_d}{dt}=\dot{Q}_{sens}-\dot{m}_v\left[h_v(T_d)-u_l(T_d)\right] \quad \text{(A3)}$$

$$m_a \frac{du_a}{dt} + m_v \frac{du_v}{dt} = m_a c_{v,a} \frac{dT_\infty}{dt} + m_v c_{v,v} \frac{dT_\infty}{dt} = -\dot{Q}_{sens} + \dot{m}_v \left[h_v(T_d) - u_v(T_\infty) \right] \quad \text{(A4)}$$

Application of ideal gas relations helps simplify the system farther. The following relation is utilized [36]:

$$h_v = u_v + pv = u_v + RT \quad \text{(A5)}$$

Application to the vapor flow rate terms in Eqs. (A3) and (A4) yields, respectively:

$$h_v(T_d) - u_l(T_d) = u_v(T_d) - u_l(T_d) + RT_d = u_{lv}(T_d) + RT_d \quad \text{(A6)}$$

$$h_v(T_d) - u_v(T_\infty) = u_v(T_d) - u_v(T_\infty) + RT_d = c_{v,v}(T_d - T_\infty) + RT_d \quad \text{(A7)}$$

The relationship describing the difference in internal energy between the liquid and vapor is found by curve fitting thermodynamic tables [36]:

$$u_{lv}(T) = 3146235 - 2822T \quad \text{(A8)}$$

For purposes of the computation, the amount of vapor in the moist air system is tracked with the vapor concentration, c, in units of kilograms of water per cubic meter of dry air. Combining all this information reveals the final form of the energy equations:

$$\frac{dT_d}{dt} = \frac{3}{4\pi r_d^3 \rho_w c_{p,w}} \left[\dot{Q}_{sens} - \dot{m}_v (u_{lv} + RT_d) \right] \quad \text{(A9)}$$

$$\frac{dT_\infty}{dt} = \frac{3}{4\pi (b^3 - r_{d,o}^3)(\rho_a c_{v,a} + c c_{v,v})} \left[-\dot{Q}_{sens} + \dot{m}_v (RT_d) \right] \quad \text{(A10)}$$

In Eq. (A10), the initial drop radius, $r_{d,o}$, is used as this is a constant volume process. This initial droplet radius is not to be confused with the time varying drop radius (described below).

The sensible heat transfer is due to forced convection, and is calculated according to [29]:

$$\dot{Q}_{sens} = (4\pi r_d^2) \frac{k_a Nu}{2r_d} (T_\infty - T_d) = 2\pi r_d k_a Nu (T_\infty - T_d). \quad \text{(A11)}$$

The mass flow rate of vapor is found with application of Fick's law of vapor diffusion. Note that there is some discussion on the subject of mass transfer in [8], the conclusions of which indicate that this law is applicable under the conditions of the model. Thus, the mass transfer follows:

$$\dot{m}_v = (4\pi r_d^2) \frac{D_v Sh}{2r_d} (c_s - c) = 2\pi r_d D_v Sh (c_s - c) \quad \text{(A12)}$$

Substitution of Eqs. (A11) and (A12) into (A9) and (A10) gives the final form of the differential equations describing the drop and air temperature as a function of time:

$$\frac{dT_d}{dt}=\frac{3}{2r_d^2\rho_w c_{p,w}}\left[k_a Nu\left(T_\infty - T_d\right)-\left(u_{lv}\left(T_d\right)+RT_d\right)D_v Sh\left(c_s - c\right)\right] \tag{A13}$$

$$\frac{dT_\infty}{dt}=\frac{3r_d}{2\left(b^3 - r_{d,o}^3\right)\left(\rho_a c_{v,a}+cc_{v,v}\right)}\left[-k_a Nu\left(T_\infty - T_d\right)+\left(c_{v,v}\left(T_d - T_\infty\right)+RT_d\right)D_v Sh\left(c_s - c\right)\right] \tag{A14}$$

The mass transfer follows from a simple mass balance. On the drop side, the change in drop mass must equal the mass flow rate of vapor as defined by Eq. (A12):

$$\frac{dm_d}{dt}=-\dot{m}_v=\frac{d}{dt}\left(\frac{4}{3}\pi r_d^3\rho_w\right)=\frac{4}{3}\pi\rho_w\left(3r_d^2\right)\frac{dr_d}{dt}=-2\pi r_d D_v Sh\left(c_s - c\right) \tag{A15}$$

Simplifying Eq. (A15) gives the final form of the differential equation used:

$$\frac{dr_d}{dt}=\frac{-D_v Sh\left(c_s - c\right)}{2\rho_w r_d} \tag{A16}$$

On the air side, the increase in the mass must equal the mass flow rate of the vapor again, while the change in actual air mass (nitrogen, oxygen, etc.) does not change. Noting that the density is assumed constant, the air volume then does not change, and thus the air volume is defined with the initial drop radius:

$$\frac{dm_a}{dt}=\dot{m}_v=\frac{d}{dt}\left(m_a + m_v\right)=\frac{d}{dt}\left(V_a c\right)=V_a\frac{dc}{dt}=\frac{4}{3}\pi\left(b^3 - r_{d,o}^3\right)\frac{dc}{dt}=2\pi r_d D_v Sh\left(c_s - c\right) \tag{A17}$$

Using the information from Eq. (A12), Eq. (A17) reduces to the final form used in the model:

$$\frac{dc}{dt}=\frac{3r_d}{2\left(b^3 - r_{d,o}^3\right)}D_v Sh\left(c_s - c\right) \tag{A18}$$

The dynamic side of the model has been detailed in [8], so the governing equations will only be listed here. Note, however, that the forces due to an electric field (present in the original model) have been omitted, and a third dimensional acceleration term has been added:

$$\frac{d^2x}{dt^2}=\frac{\left(\frac{1}{2}\rho_a C_d\left(\pi r_d^2\right)\left(U_{\text{inf}} - \frac{dx}{dt}\right)\left|U_{\text{inf}} - \frac{dx}{dt}\right|\right)}{m_d} \tag{A18}$$

$$\frac{d^2y}{dt^2}=-g+\frac{\left(-\frac{1}{2}\rho_a C_d\left(\pi r_d^2\right)\left(\frac{dy}{dt}\right)\left|\frac{dy}{dt}\right|\right)}{m_d} \tag{A19}$$

$$\frac{d^2 z}{dt^2} = \frac{\left(-\frac{1}{2}\rho_a C_d \left(\pi r_d^2\right)\left(\frac{dz}{dt}\right)\left|\frac{dz}{dt}\right|\right)}{m_d} \tag{A20}$$

The nondimensional numbers used in the computation, again, were developed in [8], and are listed here for sake of completeness:

$$\mathrm{Re} = \frac{\rho_a u d}{\mu_a} = \frac{\rho_a \sqrt{\left(U_{\inf} - \frac{dx}{dt}\right)^2 + \left(\frac{dy}{dt}\right)^2 + \left(\frac{dz}{dt}\right)^2}\, 2r_d}{\mu_a} \tag{A21}$$

$$\mathrm{Sh} = 2.0 + 0.6\,\mathrm{Re}^{1/2}\,\mathrm{Sc}^{1/3} \tag{A22}$$

$$\mathrm{Sc} = \frac{\mu_{\mathrm{a}}}{\rho_{\mathrm{a}} D_v} \tag{A23}$$

$$\mathrm{Nu} = 2.0 + 0.6\,\mathrm{Re}^{1/2}\,\mathrm{Pr}^{1/3} \tag{A24}$$

$$C_d = \frac{24}{\mathrm{Re}}\left(1 + \frac{1}{6}\mathrm{Re}^{2/3}\right) \tag{A25}$$

Note that the vapor diffusivity, D_v, was found to be the most significant temperature sensitive property used in the computation, and thus this value is computed inside of the algorithm according to [16]:

$$D_v = 2.495 \times 10^{-5}\left(\frac{T_\infty}{292.88}\right)^{2.334}. \tag{A26}$$

The vapor concentration at the surface of the drop, c_s, is calculated inside the algorithm as well as it is a function of the drop temperature. The relation is calculated according to:

$$c_s = \left(\frac{A + C T_d^{1/2} + E T_d}{1 + B T_d^{1/2} + D T_d}\right)\rho_a \tag{A27}$$

A	0.1170816400
B	-0.0951059000
C	-0.0143272280
D	0.0022436935
E	0.0004388500

8.1.2 Spray Charging Model Development

Law [23] points out that for induction charging to be effective, the fluid must be sufficiently conductive to allow for proper charge movement in the time frame of droplet formation. Quantitatively, the charge relaxation time of the fluid, τ, must be much smaller than the formation time of the droplet, t_f. According to Jones [32] the charge relaxation time for water in air is given by

$$\tau = \frac{\varepsilon_{water} + 2\varepsilon_{air}}{\sigma_{water} - \sigma_{air}} \approx 7.5\times10^{-6}\ \text{s}\,. \tag{B1}$$

Law [23] estimates a droplet formation time as the length of the free jet, or sheet in this instance, divided by the velocity of the jet. An empirical correlation for flat fan sprays proposed by Marchant et al. [38] shows that the sheet velocity for the nozzle of interest is on the order of 20 m/s. Marchant et al. [38] also discuss the issue of the actual sheet length, which they call the coherent length, L_c. This length is physically measured to be the distance from the nozzle to the point where the sheet breaks up on a real spray (more on this point later). For the flat fan nozzle of interest, the average droplet formation time is on the order of $8\text{x}10^{-4}$ s, two full orders of magnitude longer than the charge relaxation time. Thus, water can be inductively charged.

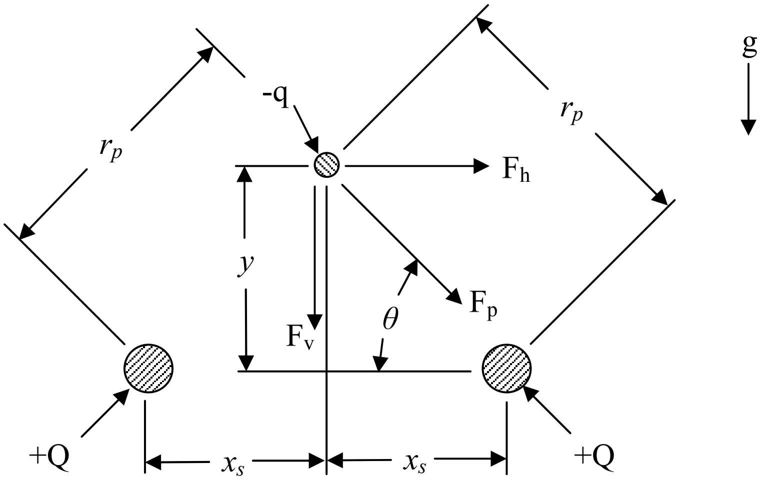

Figure B1 Geometry and decomposition of forces on the test charge, -q, moving downwards past the charged electrode, +Q.

Theory states, the maximum charge will be imparted on the drops if they form in the region of highest field intensity [23]. In order to find this location, a simple model is created wherein a test charge is moved through a simplified electrode geometry (see Fig. B1). The resulting Coulombic force is calculated as a function of position, revealing the location of maximum intensity.

When the electrodes are charged to the same potential, the field is symmetric, and the resulting horizontal forces on the test charge cancel one another. However, in the real situation with the presence of a grounded spray, the electric field in the horizontal direction will exist, and it is this field, normal to the spray sheet, that is of interest Starting with the Coulombic force, $\mathrm{F_{p,}}$ defined as [39]

$$\mathrm{F_p} = \frac{1}{4\pi\varepsilon_o}\frac{|\mathrm{q}||\mathrm{Q}|}{r_p^2}, \tag{B2}$$

where r_p can be defined as

$$r_p = \sqrt{x_s^2 + y^2} \ . \tag{B3}$$

The horizontal force, $\mathrm{F_h}$, on the test charge from one electrode can be resolved as

$$\mathrm{F_h} = \mathrm{F_p}\cos\theta = \frac{\mathrm{qQ}}{4\pi\varepsilon_o}\frac{x_s}{\left(x_s^2 + y^2\right)^{3/2}}. \tag{B4}$$

Dividing this force by the test charge will give the electric field magnitude in the horizontal direction (i.e. normal to the spray surface):

$$\mathrm{E_h} = \frac{dV}{dx} = \frac{\mathrm{F_h}}{\mathrm{q}} = \frac{\mathrm{Q}}{4\pi\varepsilon_o}\frac{x_s}{\left(x_s^2 + y^2\right)^{3/2}} \ . \tag{B5}$$

Ultimately, one would like to know the electric field strength as a function of the applied power supply voltage, V_{ps}, the electrode spacing, x_s, and the vertical position, y. The spacing of the electrodes is measured easily enough, and the charge on the electrodes may be approximated using Gauss's law on a cylinder. Assuming a long cylinder model and that the potential is zero at the surface of the grounded spray, Eq. (B5) becomes

$$\mathrm{E_h} = \frac{V_{ps} l_e}{2\ln\left(\frac{x_s}{r_e}\right)}\frac{x_s}{\left(x_s^2 + y^2\right)^{3/2}}. \tag{B6}$$

It will now be assumed that Eq. (B6) approximates the field on the surface of the spray sheet. According to Gauss's law, the free surface charge, ρ_s, on the sheet may be described as [39]

$$\rho_s = \varepsilon_o \mathrm{E_h}. \tag{B7}$$

Equation (B7) is valuable as it allows some prediction of the spray cloud current, i_c.

Before continuing this derivation, it necessary to understand the actual geometry of the spray/sheet. As mentioned before, Marchant et al. [38] describe a coherent length of the spray sheet, and note that this is actually difficult to quantify as the sheet actually has an irregular shape (see Fig. B2). Nonetheless, for this first order model, the sheet will be approximated by a simple isosceles triangle as depicted with the dimensions shown in Fig. B2.

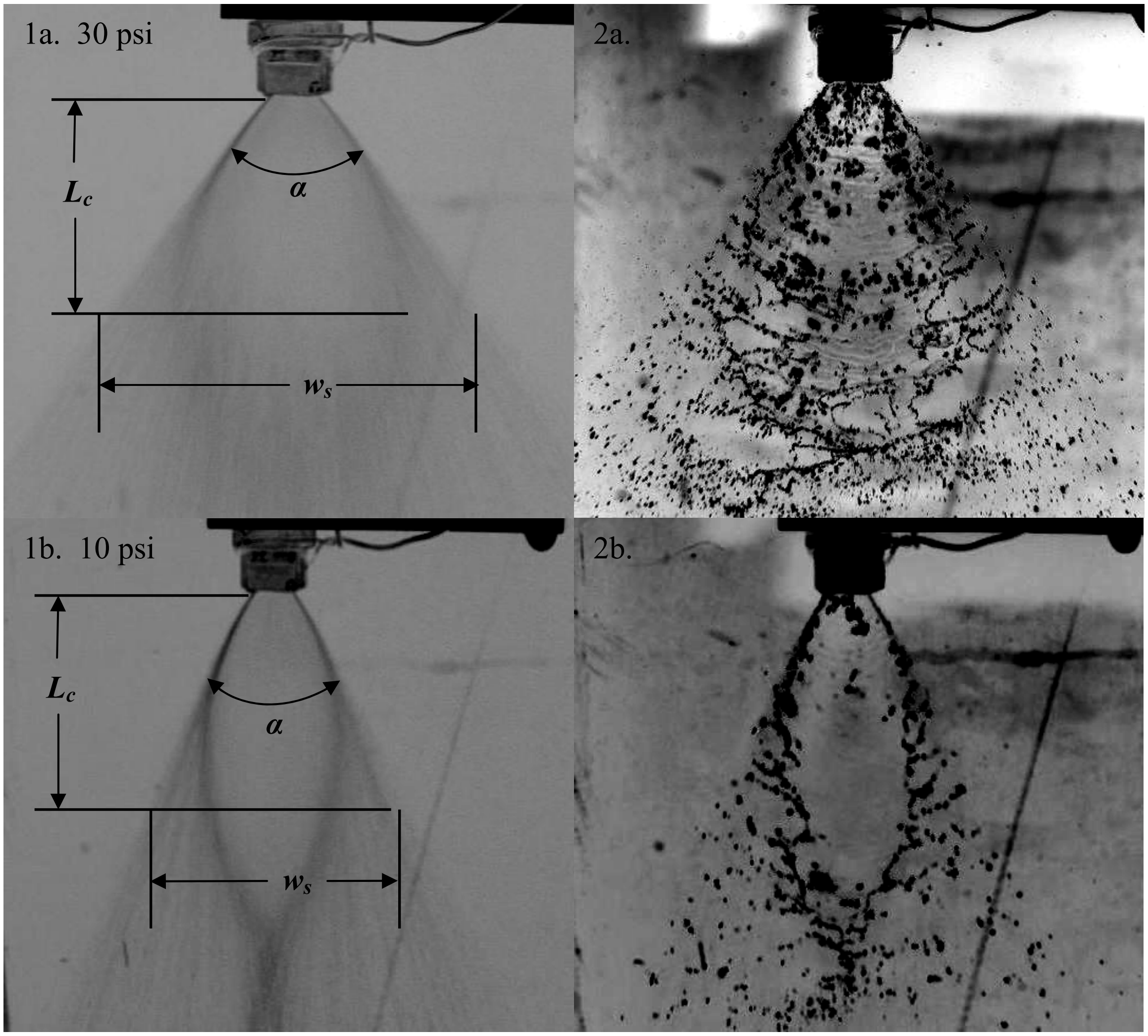

Figure B2 Photos showing the sheet region of two sprays: case a. at 30 psi, case b. at 10 psi. The second photos are taken with a flash and capture the individual droplets in more detail.

Assuming a thin sheet, the spray current can be approximated as

$$i_c = \rho_s 2 w_s v_s \tag{B8}$$

where w_s is the width of the sheet and v_s is the velocity of the sheet. The factor of two is added to account for the fact that the sheet actually has finite thickness and that both sides of the spray are being charged. It would be convenient to denote the spray cloud current as a function of the operational parameters like the voltage and nozzle pressure. Fortunately, w_s and v_s are directly related to the nozzle pressure. The three measurements in Fig. B2 are related by

$$\tan\left(\frac{\alpha}{2}\right) = \frac{w_s}{2L_c}. \tag{B9}$$

Tabulated data is available from the manufacturer of the nozzle being tested [40] to which simple curves are fitted with surprising accuracy to reveal the volumetric flow rate, $\dot{V}_s$, and spray angle, α, as a function of pressure. These parameters were found to follow the relations

$$\alpha = \frac{1}{a_1 + \frac{b_1}{p}} \tag{B10}$$

and

$$\dot{V}_s = a_2 + b_2 p^{1/2} \tag{B11}$$

where p is the pressure in kPa, α is in degrees, and $\dot{V}_s$ is in units of m^3/s, and the coefficients a_x and b_x are a characteristic of the nozzle. The volumetric flow rate is divided by the nozzle orifice area, A_{orif}, to find the velocity of the sheet/spray for Eq. (B8). The coherent length is estimated as indicated by Fig. B2, where an area of the sheet region has been truncated to account for the fact that an approximately equal area of the sheet is already forming into droplets above the coherent length. This method of measurement was used to develop the following relation for the nozzle of interest

$$L_c \approx \frac{1}{3\sqrt{p}} \tag{B12}$$

It is felt that this method is sufficient for this first order analysis (as will be seen in the following section).

Simple substitution will reveal the expected spray current as a function of easily measured independent variables:

$$i_c = \frac{\varepsilon_o V_{ps} l_e}{3\ln\left(\frac{x_s}{r_e}\right)} \frac{x_s}{\left(x_s^2 + y^2\right)^{3/2}} \left(\frac{a_2 + b_2\sqrt{p}}{A_{orif}\sqrt{p}}\right) \tan\left(\frac{1}{2\left(a_1 + \frac{b_1}{p}\right)}\right). \tag{B13}$$

8.1.3 Exergy Destruction in a DCHX

Solving for the exergy destroyed in the fluid flow problem of the DCHX begins by assuming steady state conditions, therefore [36][37]:

$$\mathrm{E}_{\mathrm{xd}} = T_o \dot{S}_{gen} = \frac{d\mathrm{E}_{\mathrm{x}}}{dt} = 0 = \sum_j \left(1 - \frac{T_o}{T_j}\right)\dot{Q} - \left(\dot{W}_{CV} - P_o \frac{dV_{CV}}{dt}\right) + \sum_i \dot{m}\mathbf{e}_f - \sum_e \dot{m}\mathbf{e}_f \tag{C1}$$

where the summations over, and subscripts, i and e denote inlet and exit, respectively, and $\mathbf{e}_f$ denotes flow exergy. Assuming a well insulated system (no heat transfer crossing the boundary), and a fixed control volume (no work produced by the system), Eq. (C1) becomes:

$$\mathrm{E}_{\mathrm{xd}} = \sum_i \dot{m}\mathbf{e}_f - \sum_e \dot{m}\mathbf{e}_f$$

$$\mathrm{E}_{\mathrm{xd}} = \sum_i \dot{m}\left[\left(u + \frac{V^2}{2} + gz - u_o\right) + \left(pv - p_o v_o\right) - T_o\left(s - s_o\right)\right] - \sum_e \dot{m}\mathbf{e}_f \tag{C2}$$

$$\mathrm{E}_{\mathrm{xd}} = \sum_i \dot{m}\left[\left(h - h_o\right) - T_o\left(s - s_o\right) + \left(\frac{V^2}{2} + gz\right)\right] - \sum_e \dot{m}\mathbf{e}_f$$

Expanding Eq. (C2) while assuming negligible air side pressure drop (constant air velocity relative to the water velocity change), negligible velocity of the water leaving the test section, and negligible gravity effects reveals

$$\begin{gathered}\mathrm{E}_{\mathrm{xd}} = \dot{m}_a\left[\left(h_{ai} - h_o\right) - T_o\left(s_{ai} - s_o\right)\right] + \dot{m}_w\left[\left(h_{wi} - h_o\right) - T_o\left(s_{wi} - s_o\right) + \left(\frac{V^2}{2}\right)\right] - \\ \dot{m}_a\left[\left(h_{ae} - h_o\right) - T_o\left(s_{ae} - s_o\right)\right] - \dot{m}_w\left[\left(h_{we} - h_o\right) - T_o\left(s_{we} - s_o\right)\right]\end{gathered} . \tag{C3}$$

Assuming negligible mass exchange in a mass balance, Eq. (C3) reduces to

$$\mathrm{E}_{\mathrm{xd}} = \dot{m}_a\left[\left(h_{ai} - h_{ae}\right) - T_o\left(s_{ai} - s_{ae}\right)\right] + \dot{m}_w\left[\left(u_{wi} - u_{we}\right) + \left(p_{wi}v_{wi} - p_{we}v_{we}\right) - T_o\left(s_{wi} - s_{we}\right) + \left(\frac{V_{wi}^2}{2}\right)\right] \tag{C4}$$

A further assumption of a negligible change in specific volume on the water side and thermodynamic property substitutions can be applied to Eq. (C4). When these modifications are made with the addition of Eq. (C5) (the velocity of the water coming into the test section through the nozzle orifice area, A_{orif}) will yield Eq. (C6) which is precisely that shown as Eq. (F7) in section 8.5.

$$V_{wi} = \frac{\dot{m}_w}{\rho_w A_{orif}} \tag{C5}$$

$$\begin{gathered}\mathrm{E}_{\mathrm{xd}} = \dot{m}_a\left[h_{ai} - h_{ae} - T_o c_{p,avg,a}\ln\left(\frac{T_{ae}}{T_{ai}}\right)\right] + \dot{m}_w\left[h_f\left(T_{wi}\right) + v_f\left(T_{wi}\right)\times\left(p_{wi} - p_{sat,w}\left(T_{wi}\right)\right)\right] \\ - \dot{m}_w\left[h_f\left(T_{we}\right) - v_f\left(T_{we}\right)\times\left(p_{we} - p_{sat,w}\left(T_{we}\right)\right)\right] - \dot{m}_w\left[T_o c_{p,avg,w}\ln\left(\frac{T_{we}}{T_{wi}}\right) + \frac{1}{2}\left(\frac{\dot{m}_w}{\rho_w A_{orif}}\right)^2\right]\end{gathered} \tag{C6}$$

This exergy destruction is located in the denominator of the proposed DCHX efficiency metric, so some might question what happens when the exergy destruction limits to zero. Thus, the following equation is used to test the metric:

$$\lim_{E_{xd}\to 0}\eta_{pDCHX} = \lim_{E_{xd}\to 0}\frac{q_{useful}}{\mathrm{E}_{\mathrm{xd}}} = \lim_{E_{xd}\to 0}\frac{\dot{m}_{air}\left(h_{air,out} - h_{air,in}\right)}{\mathrm{E}_{\mathrm{xd}}} . \tag{C7}$$

To begin this solution one must look at the limiting case of

$$\lim_{E_{xd}\to 0}\mathrm{E}_{\mathrm{xd}}=0\,. \tag{C8}$$

But, Eq. (C8) is a trivial solution in-and-of itself. To find the conditions that make Eq. (C8) true requires a start with the 1$^{\mathrm{st}}$ Law of Thermodynamics for the DCHX assuming steady state operation,

$$\frac{dE}{dt}=0=\sum\dot{Q}-\sum\dot{W}+\sum_{i}\dot{m}\left(h+\frac{V^{2}}{2}+gz\right)-\sum_{e}\dot{m}\left(h+\frac{V^{2}}{2}+gz\right). \tag{C9}$$

Again, the same assumptions are applied as in the exergy destruction derivation: well insulated and rigid control volume with negligible mass exchange, height change, air side pressure drop, change in specific volume of the water, and water exit velocity. With these assumptions and the application of basic thermodynamic principles, Eq. (C9) can be solved for the temperature of the water exiting the DCHX, T_{we}:

$$T_{we}=T_{wi}+\frac{\dot{m}_{a}c_{p,a}}{\dot{m}_{w}c_{p,w}}\left(T_{ai}-T_{ae}\right)+\frac{v_{w}}{c_{p,w}}\left(p_{wi}-p_{we}\right)+\frac{V_{wi}^{2}}{2c_{p,w}}\,. \tag{C10}$$

Now, Eq. (C10) can be substituted into Eq. (C6) to yield

$$\mathrm{E}_{\mathrm{xd}}=\dot{m}_{a}c_{p,a}T_{o}\ln\left(\frac{T_{ai}}{T_{ae}}\right)-\dot{m}_{w}c_{p,w}T_{o}\ln\left\{1+\frac{1}{T_{wi}}\left[\frac{\dot{m}_{a}c_{p,a}}{\dot{m}_{w}c_{p,w}}\left(T_{ai}-T_{ae}\right)+\frac{v_{w}}{c_{p,w}}\left(p_{wi}-p_{we}\right)+\frac{V_{wi}^{2}}{2c_{p,w}}\right]\right\} \tag{C11}$$

For the exergy destruction to approach zero, the exiting air temperature, T_{ae}, must be approaching the inlet air temperature, T_{ai}. Thus, Eq. (C8) can be rewritten in the form:

$$\lim_{T_{ae}\to T_{ai}}\mathrm{E}_{\mathrm{xd}}=-\dot{m}_{w}c_{p,w}T_{o}\ln\left\{1+\frac{1}{T_{wi}}\left[\frac{v_{w}}{c_{p,w}}\left(p_{wi}-p_{we}\right)+\frac{V_{wi}^{2}}{2c_{p,w}}\right]\right\}. \tag{C12}$$

In this form, the limit exists in theory, but in practice for the exiting air temperature to be unchanged, the mass flow rate (and thus Δp across the nozzle and V_{wi}) must be zero (as can be shown with an energy balance). Thus, the limit does approach zero, and taking the limit as T_{ae} approaches T_{ai} is valid.

Of course, as T_{ae} approaches T_{ai}, q_{useful} must also approach zero. Therefore, the limit in Eq. (C7) is indeterminate. The limit is then found with the application of l'Hopital's rule which, in its general form says:

$$\lim_{x\to a}\frac{f(x)}{g(x)}=\lim_{x\to a}\frac{f'(x)}{g'(x)} \tag{C13}$$

Differentiating q_{useful} and E_{xd} with respect to T_{ae} while assuming constant properties yields

$$\frac{dq_{useful}}{dT_{ae}} = \frac{d}{dT_{ae}}\left[\dot{m}_a c_{p,a}\left(T_{ae} - T_{ai}\right)\right] = \dot{m}_a c_{p,a} \tag{C14}$$

and

$$\frac{d\mathrm{E}_{\mathrm{xd}}}{dT_{ae}} = \dot{m}_a c_{p,a} T_o \left[\frac{1}{T_{wi} + \frac{\dot{m}_a c_{p,a}}{\dot{m}_w c_{p,w}}\left(T_{ai} - T_{ae}\right) + \frac{v_w}{c_{p,w}}\left(p_{wi} - p_{we}\right) + \frac{V_{wi}^2}{2c_{p,w}}} - \frac{1}{T_{ae}}\right], \tag{C15}$$

respectively. Taking the limits of these two equations then yields

$$\lim_{T_{ae} \to T_{ai}} \frac{dq_{useful}}{dT_{ae}} = \dot{m}_a c_{p,a} \tag{C16}$$

and

$$\lim_{T_{ae} \to T_{ai}} \frac{d\mathrm{E}_{\mathrm{xd}}}{dT_{ae}} = \dot{m}_a c_{p,a} T_o \left[\frac{1}{T_{wi} + \frac{v_w}{c_{p,w}}\left(p_{wi} - p_{we}\right) + \frac{V_{wi}^2}{2c_{p,w}}} - \frac{1}{T_{ai}}\right]. \tag{C17}$$

Thus,

$$\lim_{E_{xd} \to 0} \eta_{pDCHX} = \lim_{E_{xd} \to 0} \frac{q_{useful}}{\mathrm{E}_{\mathrm{xd}}} = \lim_{T_{ae} \to T_{ai}} \frac{\frac{dq_{useful}}{dT_{ae}}}{\frac{d\mathrm{E}_{\mathrm{xd}}}{dT_{ae}}} = \frac{1}{T_o \left[\frac{1}{T_{wi} + \frac{v_w}{c_{p,w}}\left(p_{wi} - p_{we}\right) + \frac{V_{wi}^2}{2c_{p,w}}} - \frac{1}{T_{ai}}\right]}. \tag{C18}$$

But, remembering that in the real case, for T_{ae} to approach T_{ai}, the mass flow of water must approach zero, as argued before. Thus, Eq. (A18) can be rewritten as

$$\lim_{E_{xd} \to 0} \eta_{pDCHX} = \lim_{E_{xd} \to 0} \frac{q_{useful}}{\mathrm{E}_{\mathrm{xd}}} = \lim_{T_{ae} \to T_{ai}} \frac{\frac{dq_{useful}}{dT_{ae}}}{\frac{d\mathrm{E}_{\mathrm{xd}}}{dT_{ae}}} = \frac{1}{T_o \left[\frac{1}{T_{wi}} - \frac{1}{T_{ai}}\right]}. \tag{C19}$$

Thus the limit exists only if the inlet water and air temperatures differ. If there is no temperature difference, there is no entropy generation or exergy destruction in the heat exchange process because, essentially, there is no process. Thus, the metric is valid from a theoretical standpoint.

8.2 Calibration Information

8.2.1 Calibration Procedures

8.2.1.1 Thermistor Calibration

The procedure for each pressure transducer calibration is described below.

1) Ensure that the wind tunnel Model 7708 card is inserted in card slot #2. Power up the DAQ. The DAQ needs to be on for at least four hours to achieve thermal equilibrium before use.
2) Power up the computer and open *TunnelSystem 3.4.xls*. This spreadsheet was developed with ExcelLink capabilities to perform the data collection. During calibration only the **DMM Scan** page is needed.
3) Submerge the thermistor probe tips into a temperature controlled water bath. For this system the Neslab RTE-111 was used as the temperature bath.
4) Next set up the Kaye® Model M2801 Intelligent reference RTD so that the tip of the sensor is completely submerged into the bath.
5) Set the bath to the desired starting temperature.
6) Use the DMM to record at a total 35 of readings for each thermistor at the given temperature.
7) Record the IRTD reference temperature in a .txt file to as it changes with time. The variation in the water temperature is typically less than 0.01˚C at each temperature interval.
8) Average the DMM resistance readings for each thermistor and reference them to the average IRTD temperature.
9) Complete up and down the temperature scale, and then take random points to have a full scale temperature range. For standard calibration the water temperature was varied from 1.5 to 95 ˚C (limits of water bath) at increments of 5 ˚C.
10) Using 2-D Table Curve Software, curve fit each thermistor's resistance with the IRTD temperature measurement in the form of,

$$T = a + bR_x + c\ln(R_x)^2 + dR_x^{1/2} + \frac{e}{R_x^{1/2}}, [°\mathrm{C}]$$

    where where T is the tempeature, R_x is the measures resistance, and a, b, c, d, and e are constants.

11) Calculate the calibration constants and standard fit error, for use in data reduction and uncertainty measurements.

Figure C1 Calibration of Thermistors using Kaye Intelligent RTD Temperature Probe.

8.2.1.2 Pressure Transducer Calibration

The procedure for each pressure transducer calibration is described below.

1) Ensure that the wind tunnel Model 7708 card is inserted in card slot #2. Power up the DAQ. The DAQ needs to be on for at least four hours to achieve thermal equilibrium before use.
2) Power up the computer and open *TunnelSystem 3.4.xls*. This spreadsheet was developed with ExcelLink capabilities to perform the data collection. During calibration only the **DMM Scan** page is needed.
3) The high side of the transducer is connected to the high side of the monometer with rubber tubing, while the low side of the transducer and monometer left open to the ambient air. For the low pressure transducer the high side was connected to a 0-2" scale monometer, Fig. B2a. For the high pressure and LFE transducer the high side was connected to a 0-5" scale monometer, Fig B2b.
4) At zero pressure the bypass valve was opened and the zero potentiometer was adjusted to a DMM reading of ±0.01Vdc by turning the demodulator potentiometer clockwise for an increase in output and counter-clockwise for a decrease.
5) Once the DMM reading reads nominally zero, pressure was increased to the full scale pressure by slowly applying pressure with a syringe to the opening low side of the transducer.
6) The bypass valve is quickly closed to maintain pressure on the high side of the transducer and the syringe is removed, opening the low side to ambient.
7) The span potentiometer on the demodulator is adjusted to 10±0.01Vdc.

8) Steps 4-7 repeated until there is no interaction between the adjustments.
9) Again pressurize the system recording the transducer voltage for 35 measurements. Line up your eye with the reflective strip in the Heise gauge and record the current pressure manually into excel.
10) Complete up and down the temperature scale, and then take random points to have a full scale pressure range. The pressure transducer output voltage is averaged and referenced to the manual monometer reading.
11) Using 2-D Table Curve Software, curve fit the transducer's resistance with the monometer pressure measurement in the form of,

$$\Delta P = a + bV_x, \left[\text{inches of H}_2\text{O}\right]$$

where ΔP is the pressure difference of the transducer, V_x is the transducer output voltage and a and b are constants.

12) Calculate the calibration constants and standard fit error, for use in data reduction and uncertainty measurements.
13) Repeat this process for all three transducers.

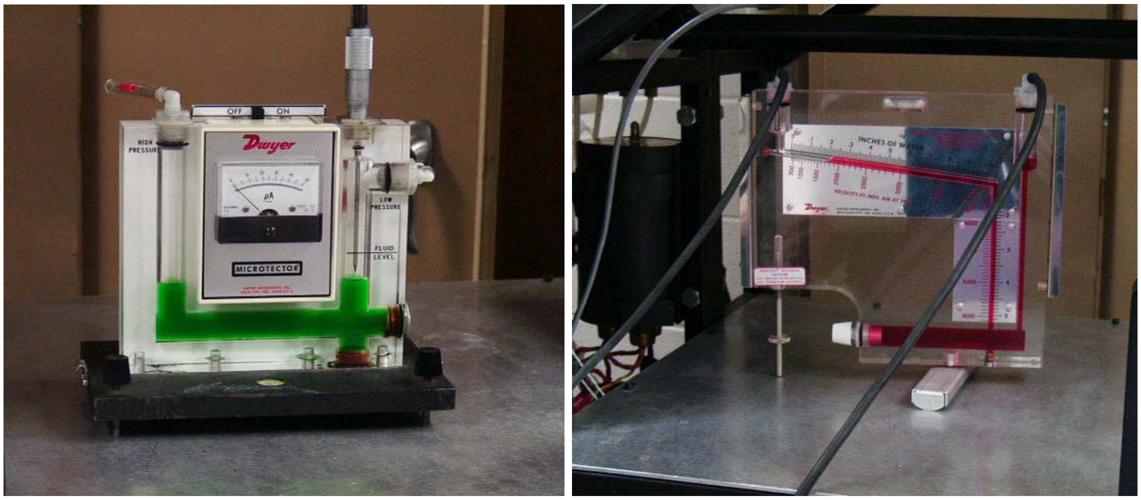

(a) **(b)**

Figure C2 Monometers used for transducer calibration. (a) Dwyer Microtector Monometer Model 1430. (b) Dwyer Inclined Monometer Model 421-5.

8.2.2 Calibration Curves

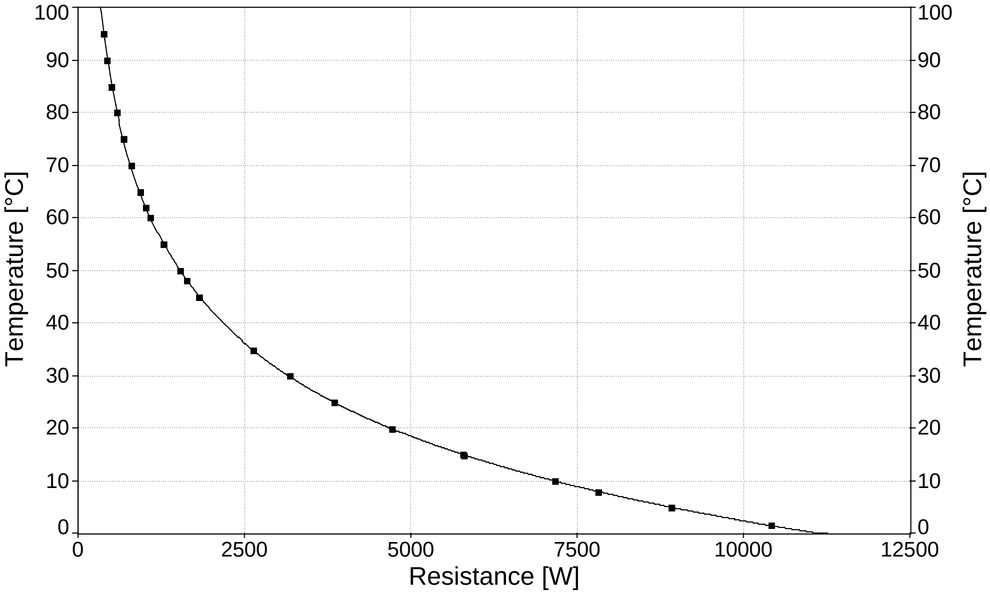

Figure D1 Calibration curve for thermistor liquid temperature measurement at inlet of unit cell coil, Thermistor 03.

Curve fit results:

$$\begin{aligned} T_{H_2O,in} &= 113.71108 - 0.00071546492 R_x - 1.8597361 \ln(R_x)^2 \\ &\quad + 0.46008194 R_x^{1/2} + \frac{763.80718}{R_x^{1/2}}, [°\mathrm{C}] \end{aligned} \tag{D1}$$

$r^2 = 0.99999943$, Fit Error = ±0.023139307 °C

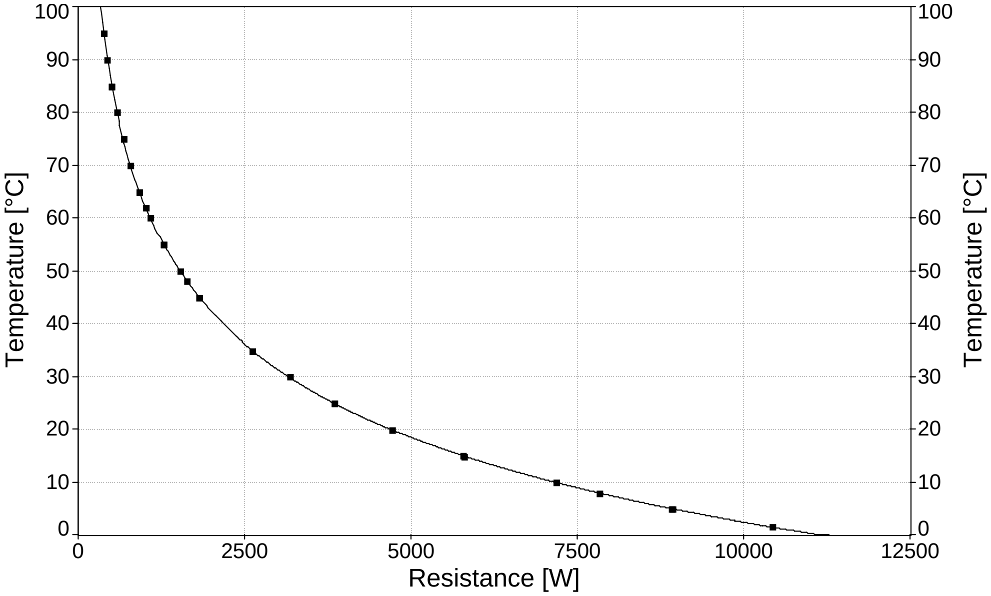

Figure D2 Calibration curve for thermistor liquid temperature measurement at outlet of unit cell coil, Thermistor 02.

Curve fit results:

$$T_{H_2O,out} = 113.47824 - 0.00069285596R_x - 1.8502718\ln(R_x)^2 + 0.4528775{R_x}^{1/2} + \frac{759.64283}{{R_x}^{1/2}}, [°\mathrm{C}] \qquad \text{(D2)}$$

$r^2 = 0.99999931$, Fit Error = ±0.024140901°C

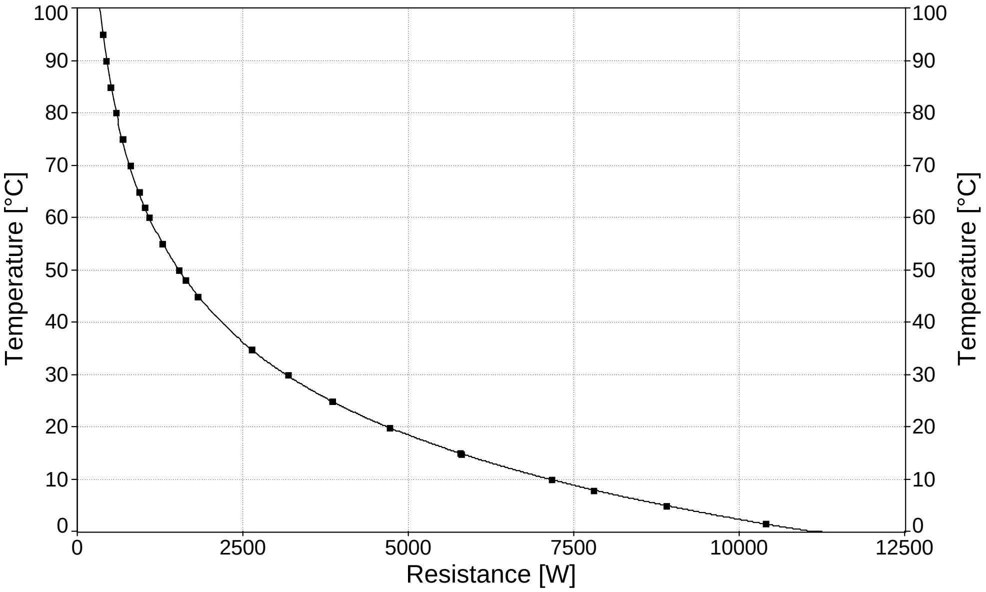

Figure D3 Calibration curve for thermistor dry bulb temperature measurement at entrance of unit cell coil, Thermistor 05.

Curve fit results:

$$T_{db,in} = 113.58891 - 0.00072555816 R_x - 1.8607934 \ln(R_x)^2 + 0.46242089 R_x^{1/2} + \frac{767.83469}{R_x^{1/2}}, [°\text{C}] \quad \text{(D3)}$$

$r^2 = 0.99999959$, Fit Error = ±0.019533228°C

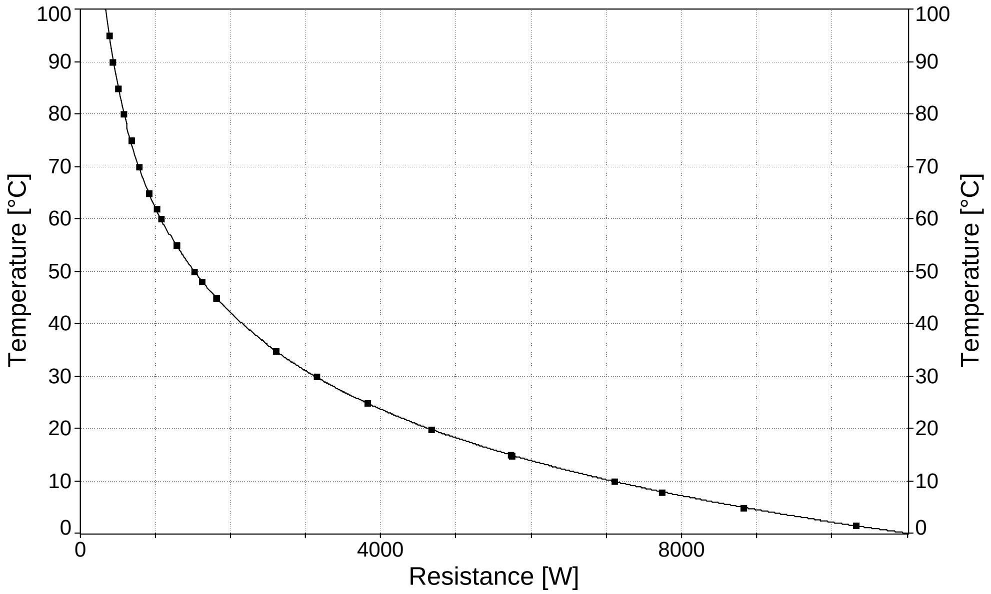

Figure D4 Calibration curve for thermistor wet bulb temperature measurement at entrance of unit cell coil, Thermistor 13.

Curve fit results:

$$T_{wb,in} = 114.55212 - 0.00077249748 R_x - 1.8881801 \ln\left(R_x\right)^2 + 0.48083624 R_x^{1/2} + \frac{746.67237}{R_x^{1/2}}, \left[°\mathrm{C}\right] \tag{D4}$$

$$r^2 = 0.99999946, \qquad \text{Fit Error} = \pm 0.02243783°\mathrm{C}$$

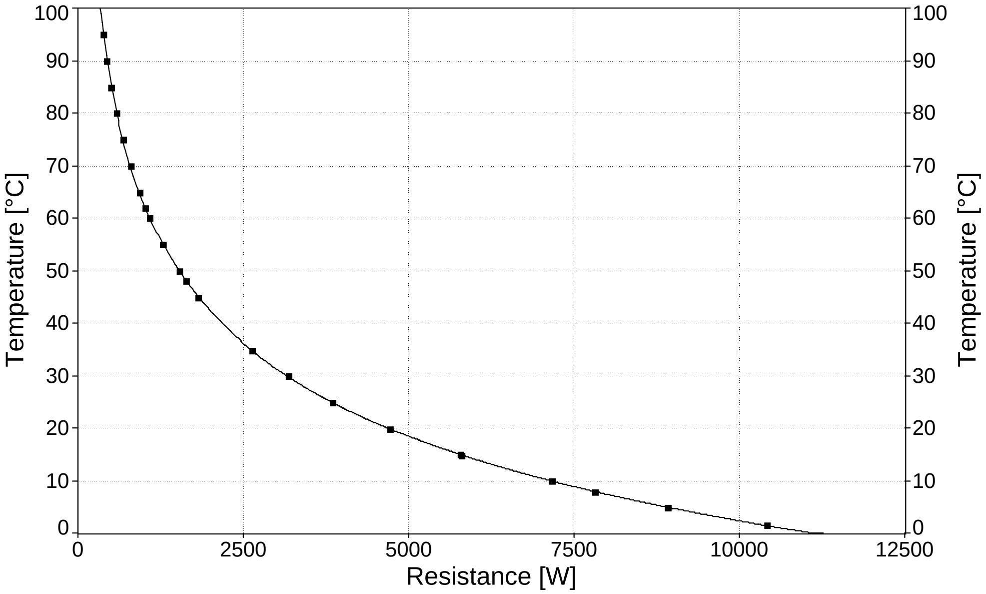

Figure D5 Calibration curve for thermistor dry bulb temperature measurement at exit of unit cell coil, Thermistor 12.

Curve fit results:

$$T_{db,out} = 113.77966 - 0.00072733091 R_x - 1.863571 \ln(R_x)^2 + 0.46384128 R_x^{1/2} + \frac{763.83747}{R_x^{1/2}}, [°\mathrm{C}] \quad \text{(D5)}$$

$r^2 = 0.99999951$, Fit Error = ±0.021404824°C

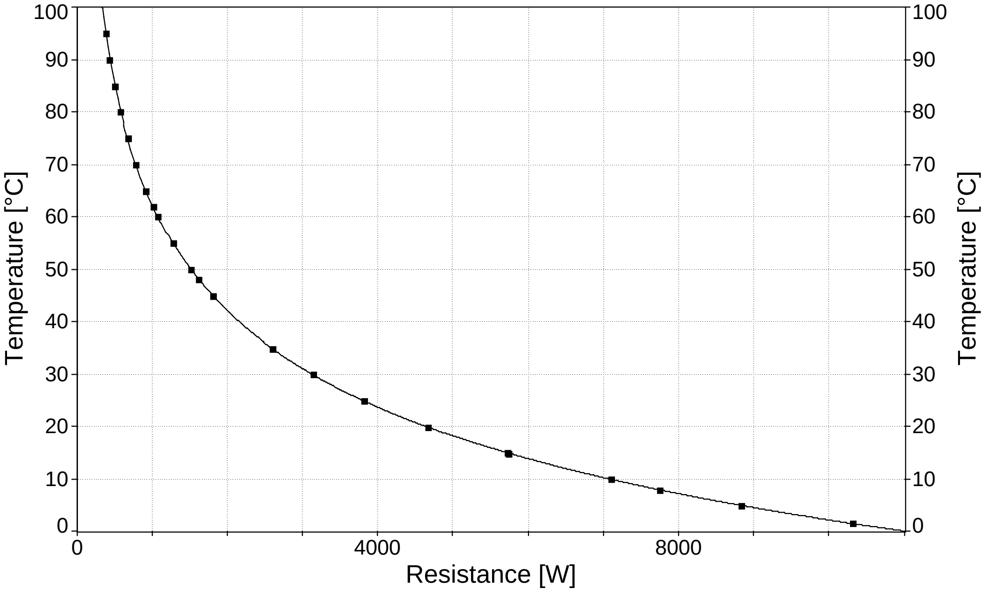

Figure D6 Calibration curve for thermistor wet bulb temperature measurement at exit of unit cell coil, Thermistor 11.

Curve fit results:

$$T_{wb,out} = 111.54607 - 0.000631955 R_x - 1.8094344 \ln(R_x)^2 + 0.42788409 {R_x}^{1/2} + \frac{771.02275}{{R_x}^{1/2}}, [°\mathrm{C}] \tag{D6}$$

$r^2 = 0.99999964$, Fit Error = ±0.018255735°C

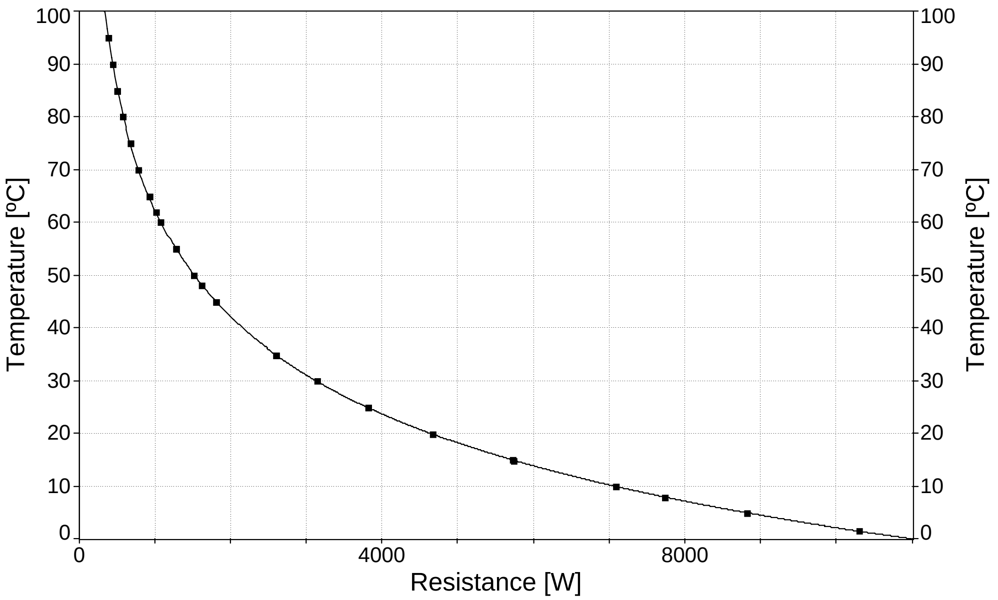

Figure D7 Calibration curve for thermistor dry bulb temperature measurement at exit of LFE, Thermistor 07.

Curve fit results:

$$
\begin{aligned}
T_{db,LFE} &= 114.66075 - 0.00077512961 R_x - 1.8919729 \ln(R_x)^2 \\
&\quad + 0.48273276 R_x^{\ 1/2} + \frac{749.59643}{R_x^{\ 1/2}}, [^\circ\mathrm{C}]
\end{aligned}
\qquad \text{(D7)}
$$

$r^2 = 0.99999953$, Fit Error $= \pm 0.020964312^\circ\mathrm{C}$

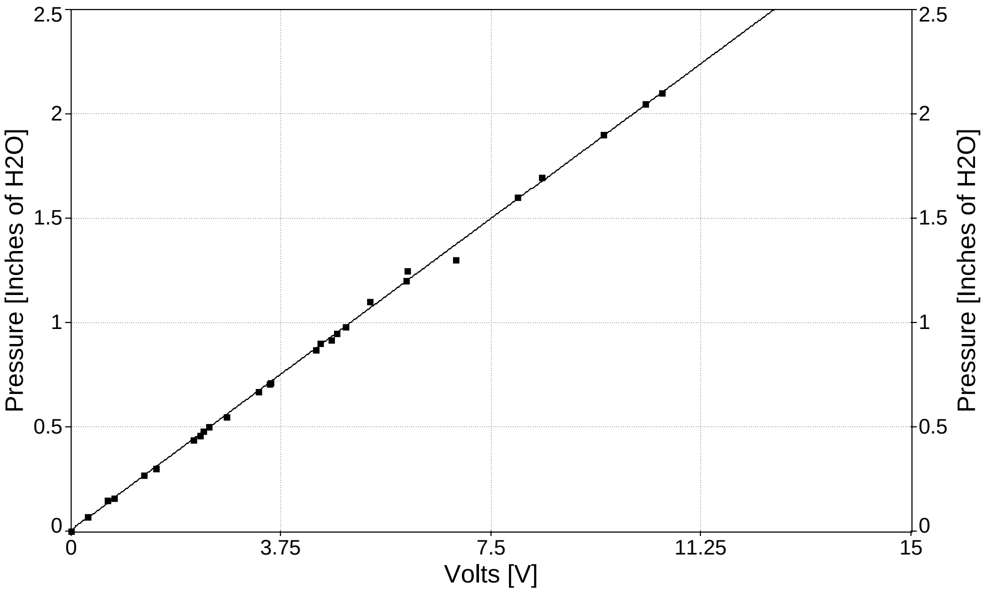

Figure D8 Calibration curve for high pressure transducer across unit cell coil.

Curve fit results:

$$\Delta P_{high} = 0.0067979735 + 0.1987901 V_x, \left[\text{inches of } H_2O\right] \qquad \text{(D8)}$$

$$r^2 = 0.9991105, \qquad \text{Fit Error} = \pm 0.018731318 \text{ inches of } H_2O$$

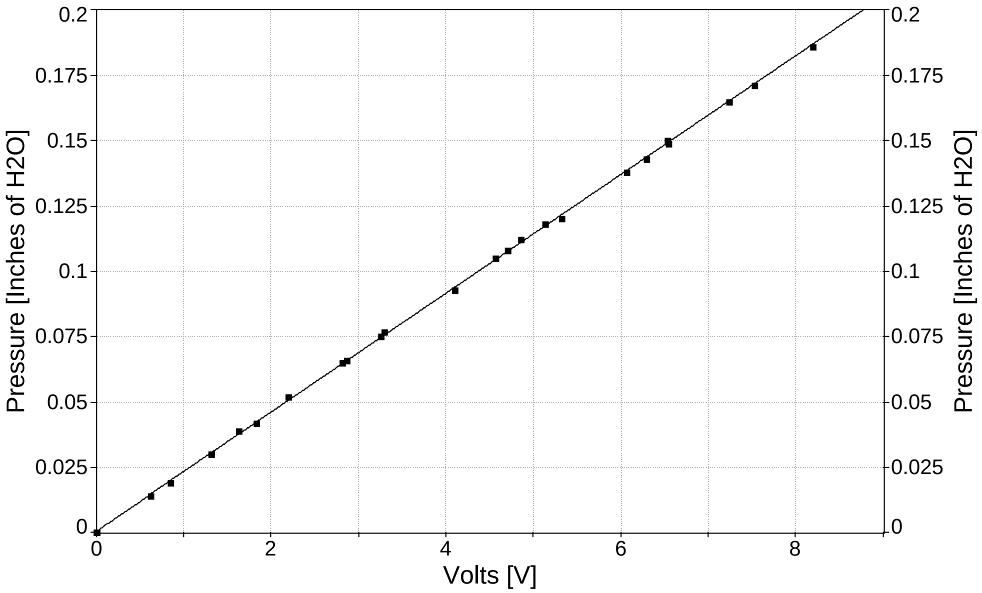

Figure D9 Calibration curve for low pressure transducer across unit cell coil.

Curve fit results:

$$\Delta P_{low} = 0.00060798952 + 0.022712102 V_x, \left[\text{inches of } \mathrm{H_2O}\right] \qquad \text{(D9)}$$

$$r^2 = 0.99978336, \qquad \text{Fit Error} = \pm 0.00086336154 \text{ inches of } \mathrm{H_2O}$$

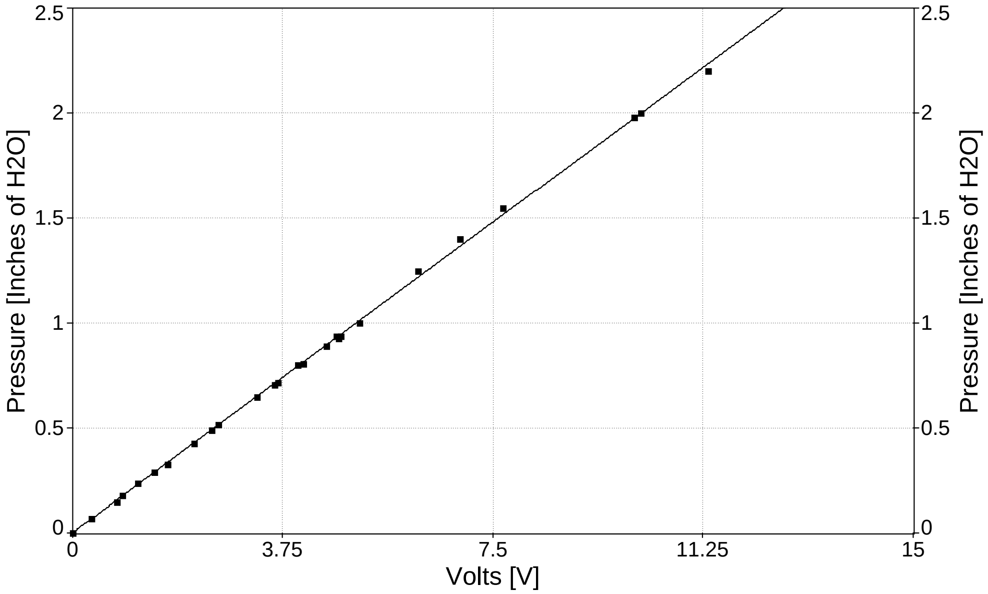

Figure D10 Calibration curve for pressure transducer across the LFE.

Curve fit results:

$$\Delta P_{LFE} = 0.002012748 + 0.19710571 V_x, \left[\text{inches of } H_2O\right] \qquad \text{(D10)}$$

$$r^2 = 0.99946949, \qquad \text{Fit Error} = \pm 0.01456268 \text{ inches of } H_2O$$

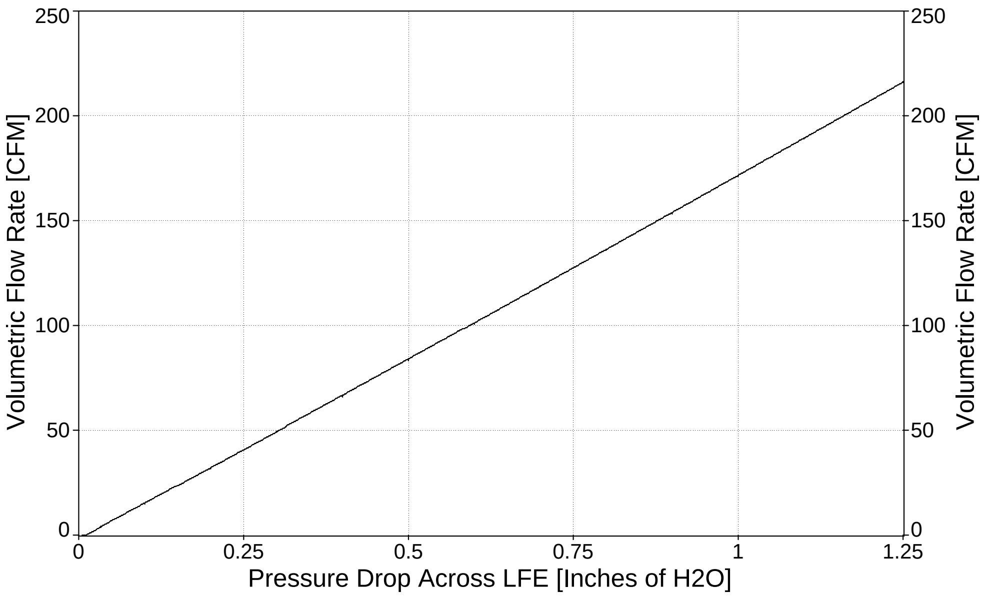

Figure D11 Calibration curve for LFE with respect to pressure drop.

Curve fit results:

$$\begin{aligned}\dot{V}_{uncorrected} &= -1.605079 + 168.6945\Delta P_{LFE} + 5.7677054\Delta P_{LFE}^{\ 2} \\ &\quad - 0.9937183\Delta P_{LFE}^{\ 3}, \left[\mathrm{m^3/s}\right]\end{aligned} \tag{D11}$$

$$\text{Instrument Bias} = \pm 0.0086 \times \dot{V}_{uncorrected}\ \mathrm{m^3/s}$$

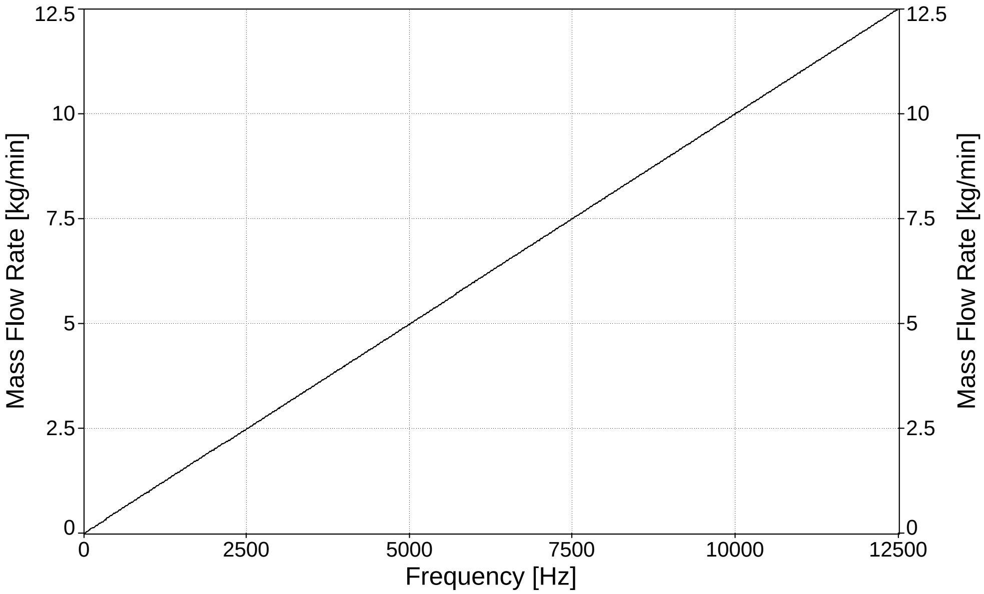

Figure D12 Calibration curve for Micromotion flowmeter with respect to frequency.

Curve fit results:

$$\dot{m}_{H_2O} = 0.01\omega, \left[\text{kg/min}\right] \tag{D12}$$

$$\text{Instrument Bias} = \pm 0.0023 \times \dot{m}_{H_2O} \text{ kg/min}$$

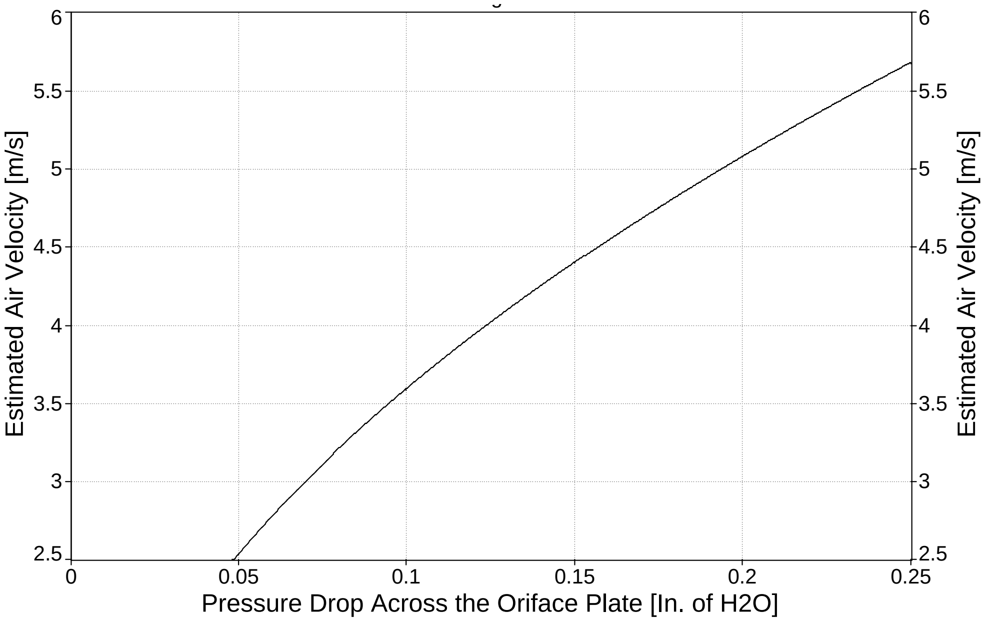

Figure D13 Calibration curve for air regualtion oriface plates with respect to pressure drop.

Curve fit results:

$$\vec{v} = 11.3655 \Delta P^{0.4998}, \left[\mathrm{m}^3/\mathrm{s}\right] \quad \text{(D13)}$$

8.3 Uncertainty Calculations

The following is a sample uncertainty calculation for the dry-bulb air temperature change across the DCHX. The conditions for this test have moist air flowing with an actual face velocity of 1.0 m/s and an inlet air temperature of $T_{db,in}$=26.7 °C and $T_{in,wet}$=16.1 °C. Water flows at 4.25 kg/min with an inlet temperature of 10 °C.

To find the overall uncertainty for the inlet dry bulb temperature, the uncertainty in the thermistor resistance measurements from the DMM first must be calculated. Because the instrumentation was calibrated in place, there is no bias limit associated with the Keithley DMM in the readings, therefore only the precision limits are important. The precision limits associated with the DMM are calculated using the standard deviation of the reading and confidence interval of 95%. A total of 99 resistance measurements give an average of 3602.398 Ω and standard a standard deviation of 2.492 Ω. Therefore the precision limit can be calculated by [24],

$$P_{\text{DMM}} = \frac{\sigma_{\text{std}}}{\sqrt{n}} t_{v,95} = \frac{2.492}{\sqrt{99}}(1.96) = 0.491\,\Omega \tag{E1}$$

where n is the number of samples, σ_{std} is the measurement standard deviation, and $t_{v,95}$ is the t-distribution value at a 95% confidence interval. The degrees of freedom, v, for the t-distribution are calculated by

$$v = n - 1. \tag{E2}$$

Common t-distribution tables provide, $t_{v,95} = 1.96$. Thus the total uncertainty concerned with the DMM in the calculation of the resistance of the dry bulb thermistor is

$$u_{\text{DMM}} = \sqrt{P_{\text{DMM}}{}^2 + B_{\text{DMM}}{}^2} = \sqrt{(0.491)^2 + (0)^2} = \pm 0.491\,\Omega. \tag{E3}$$

There are two forms of bias associated with the temperature measurement, the bias in the thermistors and the bias of the calibration instrument. For the inlet dry bulb temperature measurement these two biased limits are,

$$B_{\text{Instrument}} = 0.025°\text{C} \text{ and } B_{\text{Calibration}} = 0.0005°\text{C}. \tag{E4}$$

The two precision limits for the temperature uncertainty are the precision of the resistance measurement and the precision of the calibration curve. The precision in the resistance measurement can be calculated by,

$$P_{\text{Metric}} = \frac{\partial T_{db,in}}{\partial R_x} u_{\text{DMM}} = -0.007(0.491) = -0.001°\text{C} \tag{E5}$$

where $\frac{\partial T_{db,in}}{\partial R_x}$ is the partial derivative of Eq. (D3) with respect to resistance. The precision of the calibration curve is based upon the Standard Fit Error of the calibration curve, which is $\delta_{\text{STD Fit}} = \pm 0.019533228°\text{C}$ for the dry-bulb thermistor. Since 32 samples were taken during the calibration process the v for the calibration precision is 31. The overall calibration precision can be calculated by,

$$P_{\text{Calibration}} = \delta_{\text{STD Fit}}\left(t_{v,95}\right) = 0.0195(1.96) = 0.038\,^\circ\text{C}. \tag{E6}$$

Finally the overall uncertainty for the inlet dry bulb temperature is

$$u_{\text{T}_{\text{db,in}}} = \sqrt{B_{\text{Instrument}}{}^2 + B_{\text{Calibration}}{}^2 + P_{\text{Calibration}}{}^2 + P_{\text{Metric}}{}^2} = \pm 0.046\,^\circ\text{C}. \tag{E7}$$

The following is a sample calculation for the total air side heat transfer under the same test conditions as described above. The total air side heat transfer can be calculated using

$$Q_{air} = \dot{m}_{air}\left(h_{out} - h_{in}\right). \tag{E8}$$

Assuming that the uncertainties for the measured quantities were calculated as described above the mass flow rate and enthalpies can be calculated as

$$\begin{aligned} \dot{m}_{air} &= 0.027 \pm 0.003 \text{ kg/s} \\ h_{in} &= 45.016 \pm 0.147 \text{ kJ/kg} \\ h_{out} &= 39.889 \pm 0.115 \text{ kJ/kg.} \end{aligned} \tag{E9}$$

Thus the air side energy transfer is

$$Q_{air} = \dot{m}_{air}\left(h_{out} - h_{in}\right) = 0.027(39.889 - 45.016) = -138.429 \text{ W}. \tag{E10}$$

Error propagation is accounted for with the sensitivity equation:

$$u_{Q_{air}} = \sqrt{\left[\left(\frac{\partial Q_{air}}{\partial \dot{m}_{air}}\right)u_{\dot{m}_{air}}\right]^2 + \left[\left(\frac{\partial Q_{air}}{\partial h_{out}}\right)u_{h_{out}}\right]^2 + \left[\left(\frac{\partial Q_{air}}{\partial h_{in}}\right)u_{h_{in}}\right]^2}. \tag{E11}$$

where u_x represents the uncertainty of each measurement and the partial derivative of each is calculated

$$\frac{\partial Q_{air}}{\partial \dot{m}_{air}} = h_{out} - h_{in} = \text{-5127.0 J/kg}, \tag{E12}$$

$$\frac{\partial Q_{air}}{\partial h_{out}} = \dot{m}_{air} = 0.027 \text{ kg/s}, \tag{E13}$$

and

$$\frac{\partial Q_{air}}{\partial h_{in}} = -\dot{m}_{air} = -0.027 \text{ kg/s}. \tag{E14}$$

Thus the total uncertainty of the air side energy transfer is calculated by,

$$u_{Q_{air}} = \sqrt{\left[(-5127.0)0.003\right]^2 + \left[(0.027)147.0\right]^2 + \left[(-0.027)115.0\right]^2} \; . \qquad \text{(E15)}$$
$$= \pm 16.185 \text{ W}$$

8.4 Experimental Data

8.4.1 Spray Charging Study

The following tables contain the data used in generating the plots in section 4.1.

Table F5 Measured data for short (7.62 cm) electrodes

x_s ± 0.5 mm	y_s ± 0.5 mm	Avg. Deposition Current [μA]	Dep. Current Uncertainty [μA]	Avg. Power Supply Current [μA]	P. S. Current Uncertainty [μA]
5.0	26.5	-1.77	0.059	0.02	0.50
5.0	31.6	-4.27	0.063	0.03	0.49
5.0	38.7	-7.55	0.250	2.19	1.02
5.0	46.9	-7.93	0.580	11.40	1.46
10.0	25.0	-1.90	0.045	0.00	0.49
10.0	30.4	-3.55	0.055	-0.26	0.49
10.0	37.7	-6.11	0.107	0.01	0.46
10.0	46.1	-10.41	0.170	0.29	0.45
10.0	50.5	-11.17	0.149	0.40	0.27
10.0	55.0	-13.25	0.185	1.95	0.30
10.0	59.6	-15.19	0.160	0.44	0.45
10.0	64.2	-14.46	0.213	0.58	0.12
10.0	73.7	-10.88	0.270	2.80	0.31
15.0	22.4	-1.98	0.039	0.02	0.50
15.0	28.3	-3.16	0.042	0.04	0.51
15.0	36.1	-4.72	0.127	0.09	0.47
15.0	44.7	-7.96	0.092	0.05	0.45
15.0	49.2	-8.55	0.081	0.38	0.28
15.0	53.9	-10.27	0.087	0.81	0.30
15.0	58.5	-11.64	0.066	0.32	0.47
15.0	63.2	-11.17	0.155	0.29	0.13
15.0	72.8	-9.62	0.437	3.17	0.31
20.0	18.0	-1.93	0.036	0.01	0.49
20.0	25.0	-2.87	0.059	-0.08	0.50
20.0	33.5	-3.87	0.053	-0.16	0.45
20.0	42.7	-6.69	0.068	0.01	0.46
20.0	47.4	-7.16	0.060	0.19	0.28
20.0	52.2	-7.62	0.068	0.59	0.29
20.0	57.0	-8.72	0.065	0.49	0.30
20.0	61.8	-9.17	0.068	0.14	0.11
20.0	71.6	-9.02	0.095	2.44	0.24
25.0	10.0	-1.90	0.032	0.00	0.50
25.0	20.0	-2.69	0.035	-0.07	0.49
25.0	30.0	-2.98	0.063	0.21	0.47
25.0	40.0	-5.56	0.059	-0.03	0.46
25.0	45.0	-5.86	0.044	0.17	0.28
25.0	50.0	-6.16	0.061	0.36	0.12
25.0	55.0	-6.50	0.068	0.45	0.46
25.0	60.0	-6.99	0.096	0.05	0.12
25.0	70.0	-7.17	0.044	1.12	0.58
30.0	41.8	-5.42	0.039	-0.02	0.42
30.0	47.2	-5.59	0.050	0.52	0.43
30.0	52.4	-5.45	0.078	0.72	0.45

Table F6 Measured data for long (12.7 cm) electrodes.

x_s ± 0.5 mm	y_s ± 0.5 mm	Avg. Deposition Current [μA]	Dep. Current Uncertainty [μA]
10.0	50.5	-7.23	0.17
10.0	55.0	-10.38	0.17
10.0	59.6	-11.53	0.13
10.0	64.2	-11.33	0.26
10.0	68.9	-9.79	0.25
10.0	73.7	-8.39	0.21
10.0	78.4	-8.43	0.22
15.0	49.2	-6.13	0.13
15.0	53.9	-8.40	0.08
15.0	58.5	-9.07	0.08
15.0	63.2	-9.99	0.11
15.0	68.0	-8.75	0.11
15.0	72.8	-8.49	0.11
15.0	77.6	-8.39	0.03
20.0	47.4	-6.25	0.08
20.0	52.2	-6.96	0.08
20.0	57.0	-7.32	0.08
20.0	61.8	-8.16	0.09
20.0	66.7	-6.81	0.06
20.0	71.6	-7.47	0.11
20.0	76.5	-5.35	0.16
25.0	45.0	-5.74	0.05
25.0	50.0	-5.80	0.04
25.0	55.0	-5.65	0.08
25.0	60.0	-6.76	0.08
25.0	65.0	-5.24	0.05
25.0	70.0	-5.88	0.10
25.0	75.0	-4.65	0.15

8.5 Evaluation Methods and Metric Options

8.5.1 Evaluation Methods - Metric Options

As in any engineering problem, an optimum DCHX system configuration is sought, e.g. there should be an optimum drop size for a given spray chamber size and heat load. This kind of optimization is only possible if there is a clear performance metric which can be either maximized or minimized. However, for the direct contact system, there are three key facets to inspect with respect to performance: sensible heat transfer, latent heat transfer, and energy consumed in operation. At this time, it is not known if an all encompassing metric exists in a widely recognized form, thus efforts are made here to highlight or develop some possible measurement parameters.

It would be beneficial if the metric is nondimensional, like the common heat exchanger effectiveness which focuses on sensible heat transfer [7][13][29]:

$$\varepsilon = \frac{q}{q_{\max}} = \frac{\dot{m}_a c_{p,a}\left(T_{a,in} - T_{a,out}\right)}{\left(\dot{m}c_p\right)_{\min}\left(\Delta T\right)_{\max}} \tag{F1}$$

where $c_{p,a}$ is taken to be the specific heat of dry air only. However, for this application, this effectiveness is not altogether satisfactory as it does not account for the mass transfer – a key feature of the direct contact system. Yoo and Kwon [13] used a slightly different effectiveness metric in their experiments which attempted to capture the latent portion of the process:

$$\varepsilon = \frac{q}{q_{\max}} = \frac{\dot{m}_a\left(h_{a,in} - h_{a,out}\right)}{\left(\dot{m}c_p\right)_{\min}\left(\Delta T\right)_{\max}}\,. \tag{F2}$$

The sensible heat ratio is an indicator of the dehumidification effectiveness according to ASHRAE [28], where a lower ratio is indicative of more dehumidification:

$$SHR = \frac{q_{sens}}{q_{total}} = \frac{\dot{m}_a c_{p,a}\left(T_{a,in} - T_{a,out}\right)}{\dot{m}_a\left(h_{a,in} - h_{a,out}\right)}\,. \tag{F3}$$

But, this process measure does not relate the performance to a theoretical maximum for a given system, i.e. it indicates relative, not absolute, dehumidification efficiency.

ASHRAE does list a performance factor, F_p, which has been developed specifically for direct contact systems used for cooling and dehumidification of moist air which does account for the energy associated with moisture transfer [28]:

$$F_p = \frac{h_{a,in} - h_{a,out}}{h_{a,in} - h^*_{a,out}}\ . \tag{F4}$$

In this case the measured enthalpies of the air are used, and $h^*_{a,out}$ is the enthalpy of the exiting air calculated using the exit air's dry bulb temperature and the exiting water temperature as the wet bulb temperature. If the exiting air wet bulb and water temperature are the same, then the air washer is said to be operating at its theoretical limit. This is a good metric as it accounts for the real limit of operation. However, it does not clearly reveal whether the heat transfer is primarily sensible or latent. Also, one foreseen problem with this metric is that it relies on the exiting water temperature measurement. There is some debate as to how accurate this measurement is on the current experimental system (see section 4.3.2.2.4).

Still, another type of metric, like a system COP or EER value, is sought. Figure F1 demonstrates the rationale as it is clear from some selected experimental results[1] that the total transfer measures alone do not provide all pertinent information about the systems *overall* efficiency. Figure F1 shows how increasing flow rates will simply increase the total transfer, and essentially the effectiveness. What is not shown by these measures are the costs associated with those transfers. For example, with a COP measure, the useful energy transfer is divided by the energy required to get that transfer [36]:

$$\mathrm{COP} = \frac{Q_{useful}}{W_{cycle}}. \tag{F5}$$

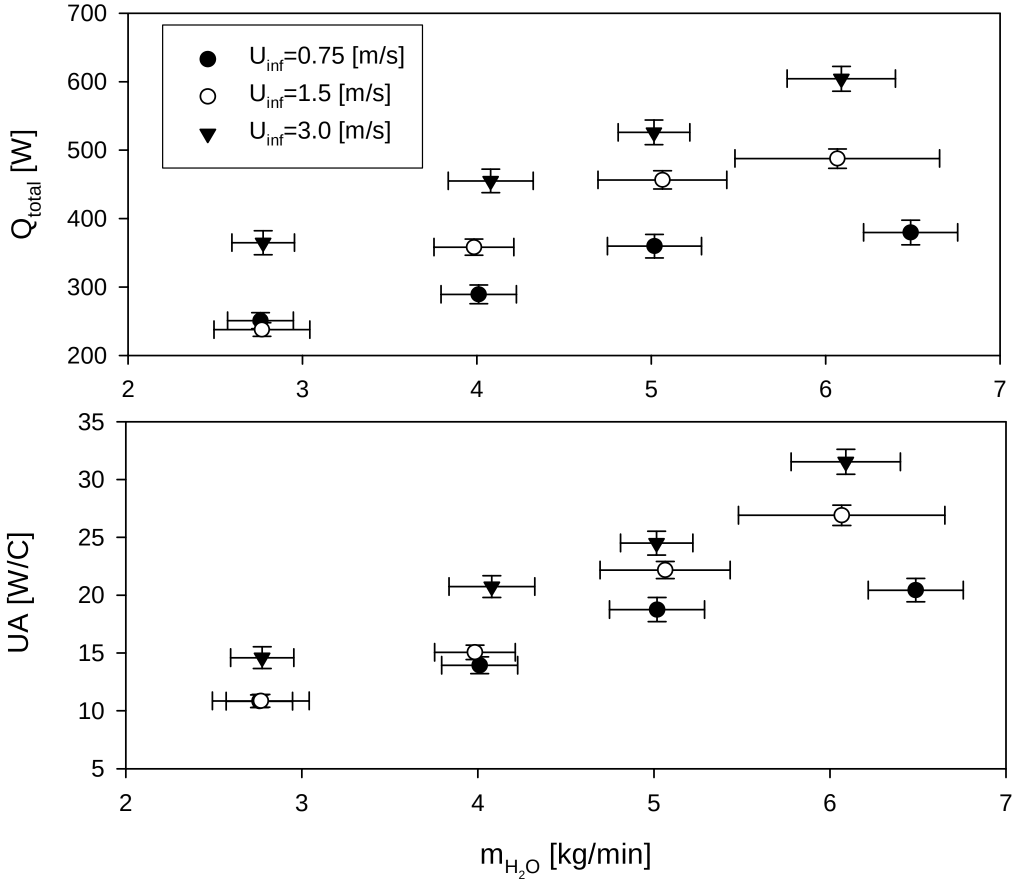

Figure F1 Thermal performance of the third generation test section (lowered wall). The effect of the variation of the mass flow rate of water is shown (8015 nozzle).

---

[1] Data was collected in the shakedown testing of the third generation prototype (lowered wall, 3-piece false wall design seen in Fig. 46). In this study, the effects of the ratio of mass flow rates were investigated. It will be argued that the droplet control in this test section was not as good as in the current section (with section of false wall removed), however the data still indicates that trends can be extracted, even from rough testing. The data from only one nozzle (nozzle 8015) is presented, thus the effects of the drop size, or spray area, are not evident.

Of course, it is not practical to define/measure the consumed energy on the experimental system. The key is to find a metric like the COP which divides the useful heat transfer by the cost required to get that heat flow. As the actual cost is difficult to measure, it is proposed that the exergy destruction rate, E_{d}, be used. This accounts for the change in not only the pressure from the nozzle to the atmosphere (flow work), but also the change in enthalpy of the system. This new metric is tentatively referred to as the prototype direct contact heat exchanger efficiency, η_{pDCHX}, for lack of research for a better or more common term. Thus, η_{pDCHX} is defined as:

$$\eta_{pDCHX} = \frac{q_{useful}}{\mathrm{E}_{\mathrm{xd}}} = \frac{\dot{m}_a \left(h_{a,out} - h_{a,in} \right)}{\mathrm{E}_{\mathrm{xd}}}. \tag{F6}$$

The exergy destruction rate [36] is then defined for the direct contact problem as:

$$\begin{aligned} \mathrm{E}_{\mathrm{xd}} &= \dot{m}_a \left[h_{a,in} - h_{a,out} - T_o c_{p,avg,a} \ln\left(\frac{T_{a,out}}{T_{a,in}} \right) \right] + \dot{m}_w \left[h_f \left(T_{w,in} \right) + v_f \left(T_{w,in} \right) \times \left(p_{w,in} - p_{sat,w} \left(T_{w,in} \right) \right) \right] \\ &- \dot{m}_w \left[h_f \left(T_{w,out} \right) - v_f \left(T_{w,out} \right) \times \left(p_{w,out} - p_{sat,w} \left(T_{w,out} \right) \right) \right] - \dot{m}_w \left[T_o c_{p,avg,w} \ln\left(\frac{T_{w,out}}{T_{w,in}} \right) + \frac{1}{2} \left(\frac{\dot{m}_w}{\rho_w A_o} \right)^2 \right] \end{aligned} \tag{F7}$$

In deriving Eq. (F7) (derivation and discussion found in Appendix, section 8.1.3), it is assumed that the change in mass flow rates of air and water from inlets to exits is negligible, and that the changes in potential energy are also negligible for both fluids. Further, the change in kinetic energy for the air is assumed negligible and the velocity of the water leaving the test section is taken to be zero for calculation purposes; however, the velocity of the water entering the test section is accounted for by the last term in Eq. (F7) where the mass flow rate of the water is divided by the water density and the nozzle orifice area, A_o. The final assumption is that the system is well insulated, thus no heat crosses the control volume boundary.

8.5.2 Preliminary Results and Exergy Destruction Discussion

The difficulties in measuring the exiting water temperature in the final test section (used to collect the data in section 5.3) did not allow for a reliable investigation into the exergy destruction. However, the potential significance and novelty as well as the effort invested in developing this metric combines to warrant further discussion on this subject. To begin the discussion that highlights the significance of the metric, a small set of experimental data will be analyzed by conventional means to contrast the logic in analyzing the results.

Data was collected in the shakedown testing of the third generation prototype (lowered wall, 3-piece false wall design seen in Fig. 46). In this study, the effects of the ratio of mass flow rates were investigated. It will be argued that the droplet control in this test section was not as good as in the current section (with section of false wall removed), however the data still indicates that trends can be extracted, even from rough testing. The data from only one nozzle (nozzle 8015) is presented, thus the effects of the drop size, or spray area, are not evident.

All tests were run at an inlet dry and wet bulb air temperature of 26.7 ± 0.1 °C, and 19.3 ± 0.2 °C, respectively. The water temperature for all tests was maintained at 4.9 ± 0.1 °C. The mass flow rate of air was set at 1.20, 2.40, and 4.80 (± 0.06) kg/min (corresponding to free stream air face velocities of 0.7, 1.5, and 3.0 m/s). The water mass flow rate settings were 2.7, 4.0, 5.0, and 6.2 (± 0.2) kg/min.

The results in Fig. F2 show the effect of the variation of the water and air mass flow rates. Inspection shows that increasing the water flow rate produces a decrease in the exiting air temperature, while increasing the air flow rate produces an increase in the exiting air temperature. It is reasonable to expect that the exiting air temperature drops as the mass flow of water increases. Note that, in general, the drop size does not change appreciably over this flow regime, however, the total number of drops, and hence, the total surface area of the spray increases, increasing the potential for convection.

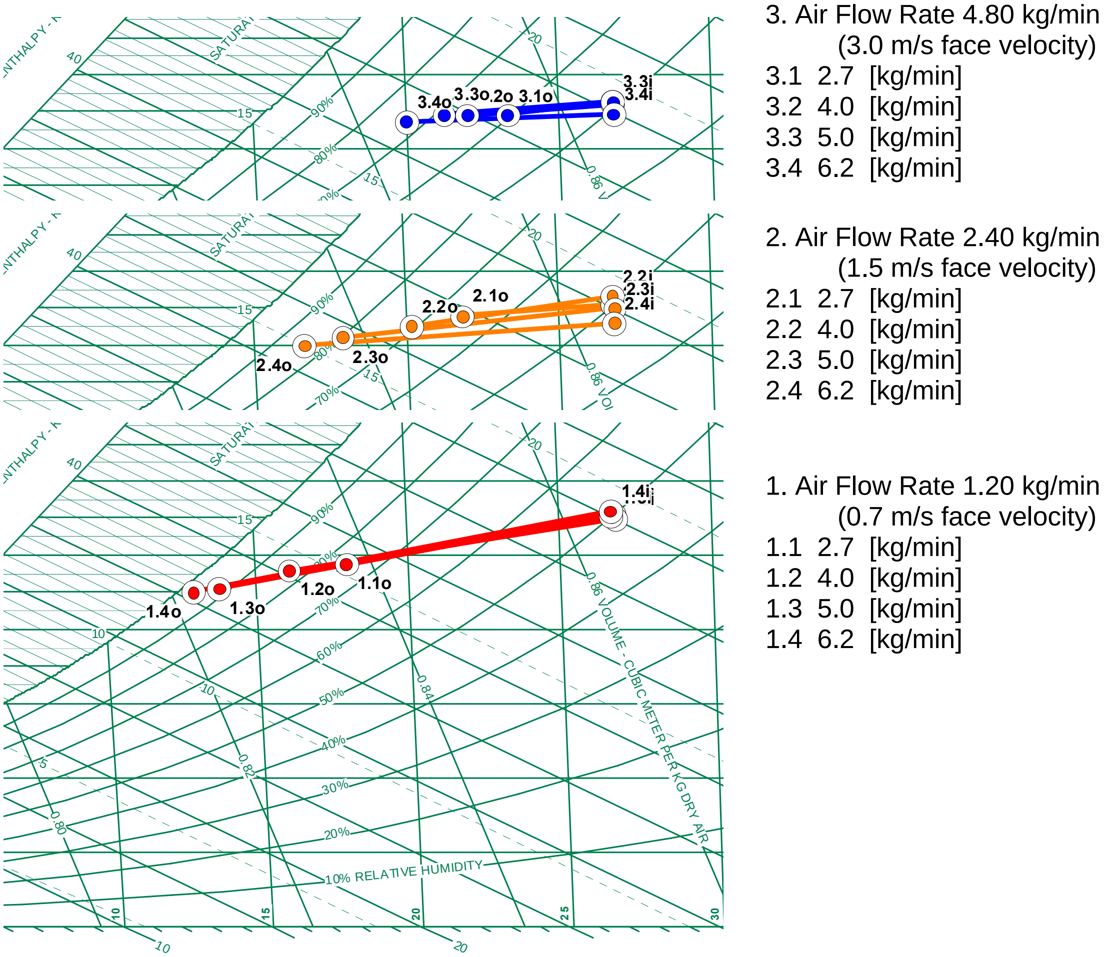

Figure F2 Thermal performance of the third generation test section (lowered wall) showing the effect of the variation of the mass flow rate of water and air.

What is not shown in Fig. F2 is the total heat transfer. Figure F3 reveals that the total heat transferred is greater for the larger air flow rates.

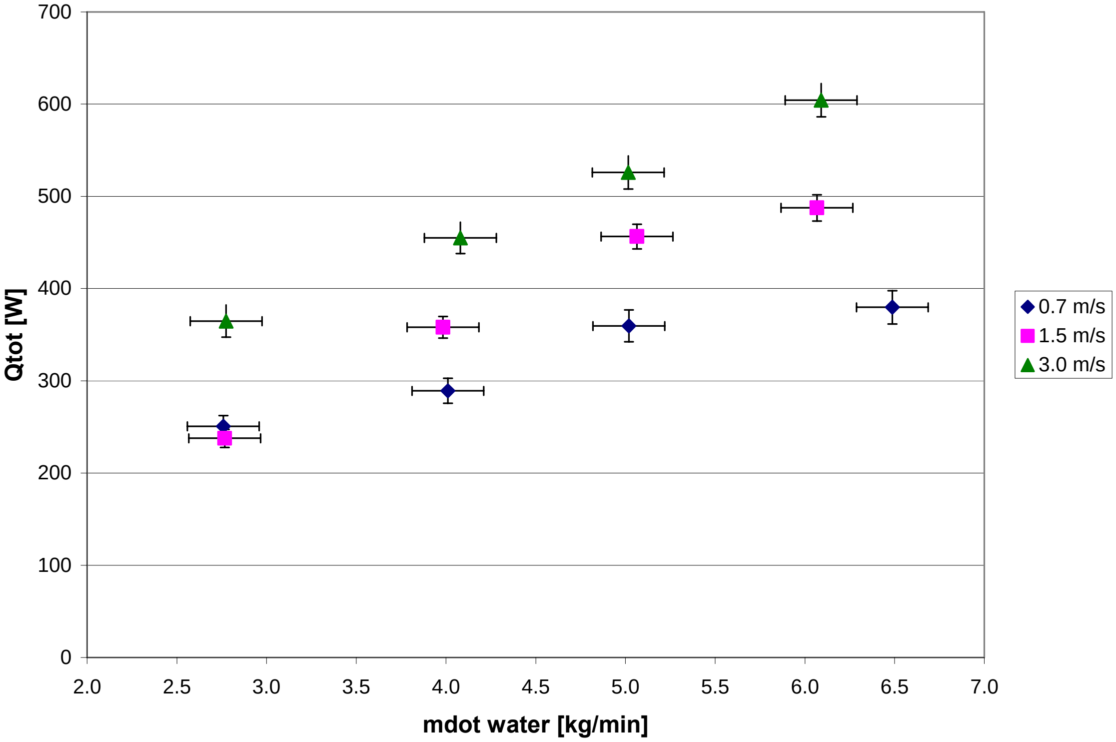

Figure F3 Variation of total heat transfer with change in mass flow rate of air and water in the third generation test section.

These results follow with conventional heat exchanger theory, i.e. for a given temperature differential, increasing the surface area in a crossflow heat exchanger (equivalently, increasing mass flow rate in a DCHX) will produce an approximately linear response according to [29]:

$$q = \dot{m}c_p \Delta T = UAF\Delta T_{lm,CF} = UAF\left[\frac{(T_{ae} - T_{wi}) - (T_{ai} - T_{we})}{\ln\left(\dfrac{T_{ae} - T_{wi}}{T_{ai} - T_{we}}\right)}\right]. \qquad \text{(F8)}$$

This statement assumes that the temperature variation on the water side is small (which it is in this case), and the air temperature is well above the water temperature. Inspection of the temperature changes in Fig. F2 justifies this assumption more for the 1.5 and 3.0 m/s face velocities, but it does not hold as well for the 0.7 m/s case which has a larger corresponding temperature change. Further, as T_{ae} in Eq. (F8) increases, so does q, approximately linearly, provided T_{ae} is above T_{wi}, as seen in Fig. F4. Again, this agrees with Fig. F2 where the exiting air temperature is increasing with air flow rate. Figure F5 shows the approximate linear behavior as the face velocity is increased too. This is equivalent to increasing the '*U'* in '*UAF'*, as convection is increased.

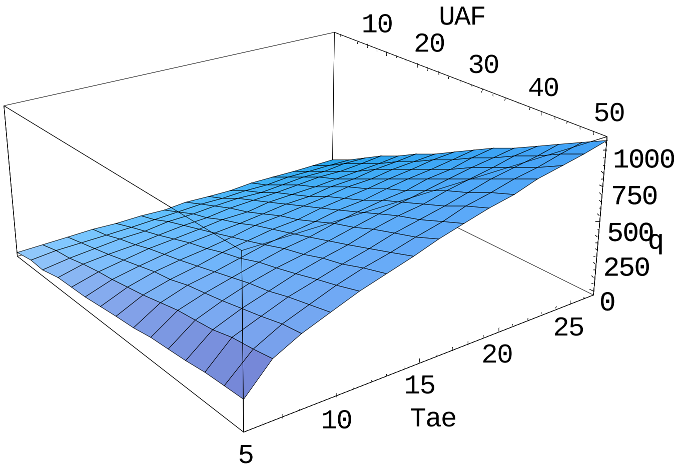

Figure F4 Analytical solution to Eq. (40) for test conditions: T_{ai}=26.7, T_{wi} =4.9, T_{we}=5.7. Though we do not yet know the value of *UAF*, these values are arbitrarily chosen just to show the linear behavior.

It is interesting to see, in Fig. F3, the condition of 0.7 m/s face velocity with 6.2 kg/min water flow rate in comparison to the 5.0 kg/min flow rate. Trusting the data, the effect of increasing the water flow rate appears to diminish (note that the temperature difference in these settings is also not as large). At this time, there is some question as to if this is due to a kind of saturation effect. This point is readdressed later.

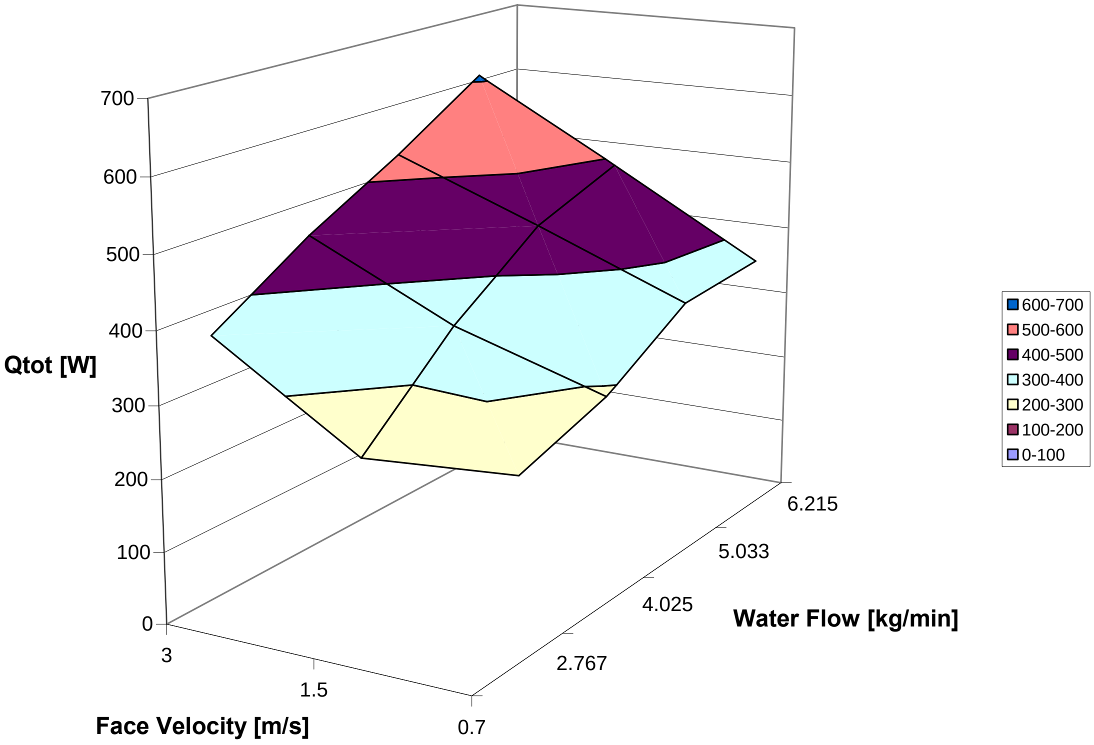

Figure F5 Total heat transfer in the third generation test section.

Continuing with the data set, it is interesting to study the latent heat transfer. This data, in Fig. F6, shows the importance of droplet control. Note that the latent heat is *removed* from the air (note Fig. F2 shows dehumidification is taking place). In the cases where more water is sprayed into the air (more drops are present with higher velocity creating more rebound issues), it can be seen that the higher air velocity has the effect of entraining the drops, as seen by the decrease in effective dehumidification. However, this effect is not quantifiable, and neither are the other more subtle effects relating to the changing spray characteristics with nozzle pressure (water flow rate). Note though that the increasing spray surface area in the case of a low face velocity (which is less likely to entrain the rebounded drops) increases the moisture removed.

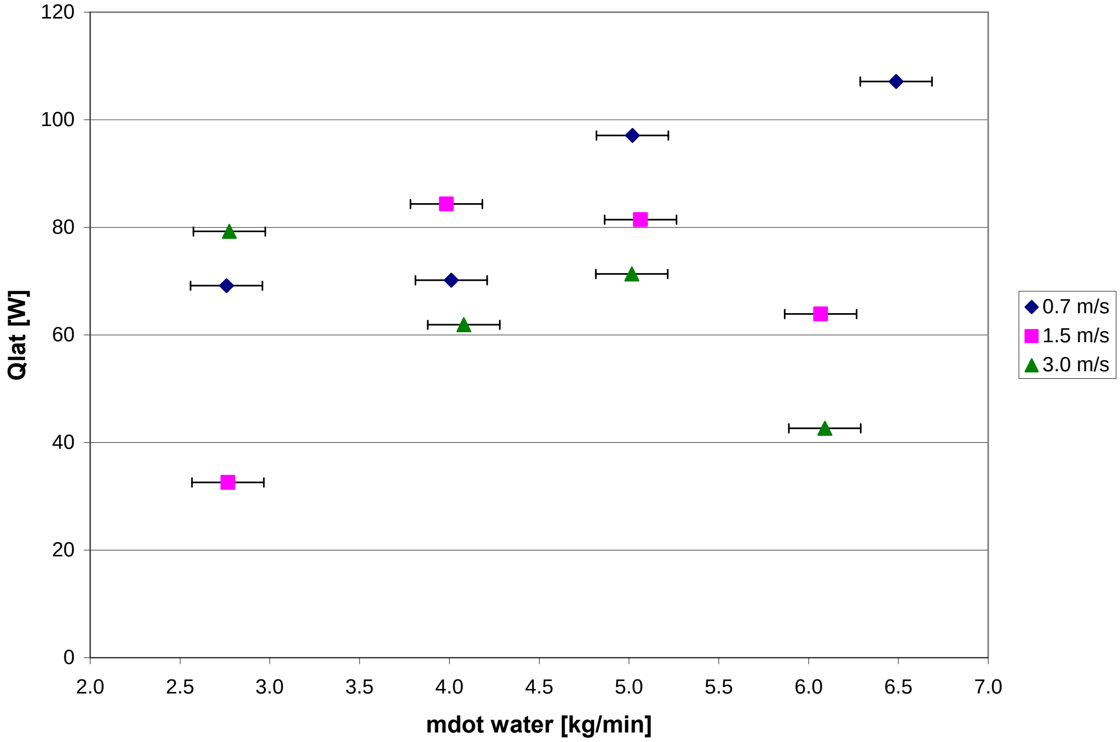

Figure F6 Latent heat transfer in the third generation test section.

It is also interesting to look at a couple of the performance metrics discussed in section 8.5.1. For example, ε, the heat exchanger effectiveness, as calculated by Eq. (F2), is shown in Fig. F7.

The results of Fig. 58 are not surprising. The maximum heat transfer, q_{max} in Eq. (F2), does not vary much as $\left(\dot{m}c_p\right)_{\min}$ does not vary much, being a function of the air mass flow rate. Thus, the increase in effectiveness response to increasing the water flow rate is reasonable (remembering that a decrease in exiting air temperature also followed the increasing water flow rate). The increase in effectiveness with the decreasing of face velocity is also reasonable as the mass flow in the denominator of Eq. (F2) is decreasing at the same rate as that in the numerator (canceling the effect), while the temperature response (in the numerator) increases, as seen in Fig. F2.

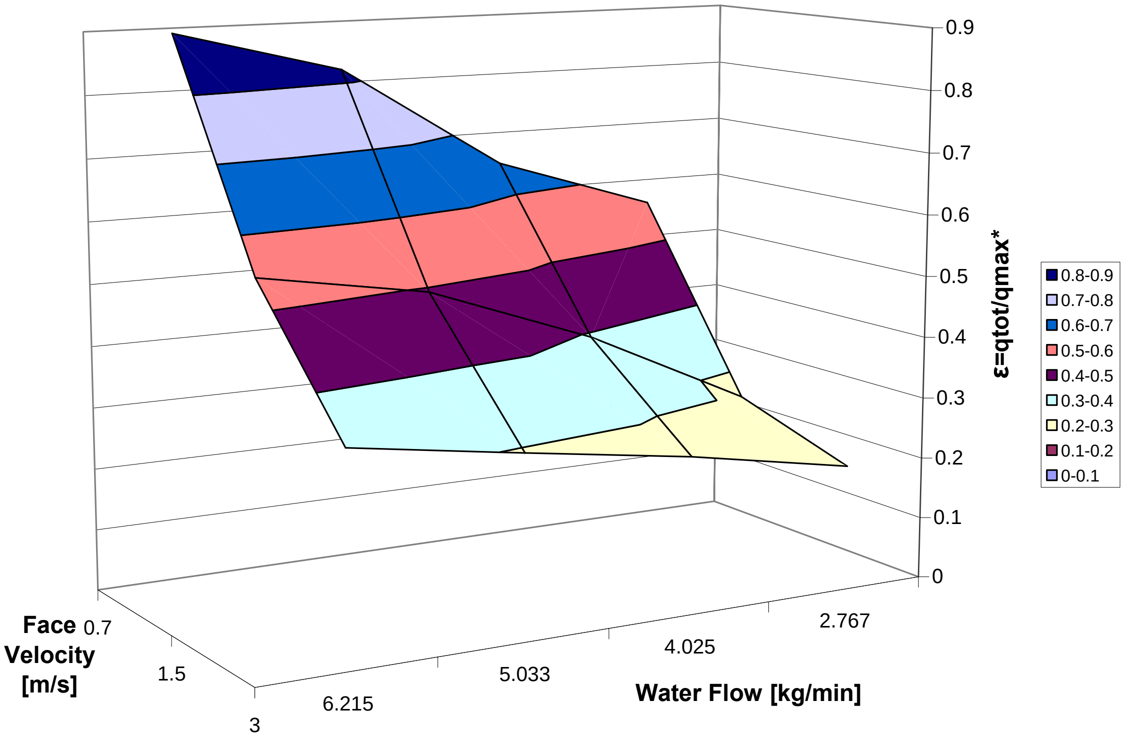

Figure F7 Heat exchanger efficiency calculated with q_{total}.

Another interesting point to mention is the almost 90% effectiveness at the low air and high water flow rate. In referencing to Fig. F3 (the 'saturation effect'), things begin to clarify. The heat transfer did not continue to increase as the system was reaching its physical limit, according to Fig. F7. Again, the mechanism for this limit has yet to be addressed, though.

The prototype DCHX efficiency, η_{pDCHX}, results (as calculated by Eq. (F6)) are shown in Fig. F8. Figure F8 shows that the low air flow performance is substantially better than the high air flow configuration. Initially, one might guess that this results from the additional air side flow work. However, in the derivation of this metric, that flow work was considered negligible relative to that on the water side, and was thus dropped. So these results appear to arrive from some other process. To address this, it helps to look at just the exergy destruction as calculated by Eq. (F7) (see Fig. F9).

The results of Fig. F9 are interesting; in the case of the low face velocity, showing a clear optimum system configuration. Further, note that this does not strictly agree with the common heat exchanger effectiveness (Fig. F7). The decrease in η_{pDCHX} with the last increase in water flow rate strikes at the heart of the purpose of this metric. This response captures the additional exergy that is required and destroyed (in the form of flow work) to achieve the last few Watts of heat transfer.

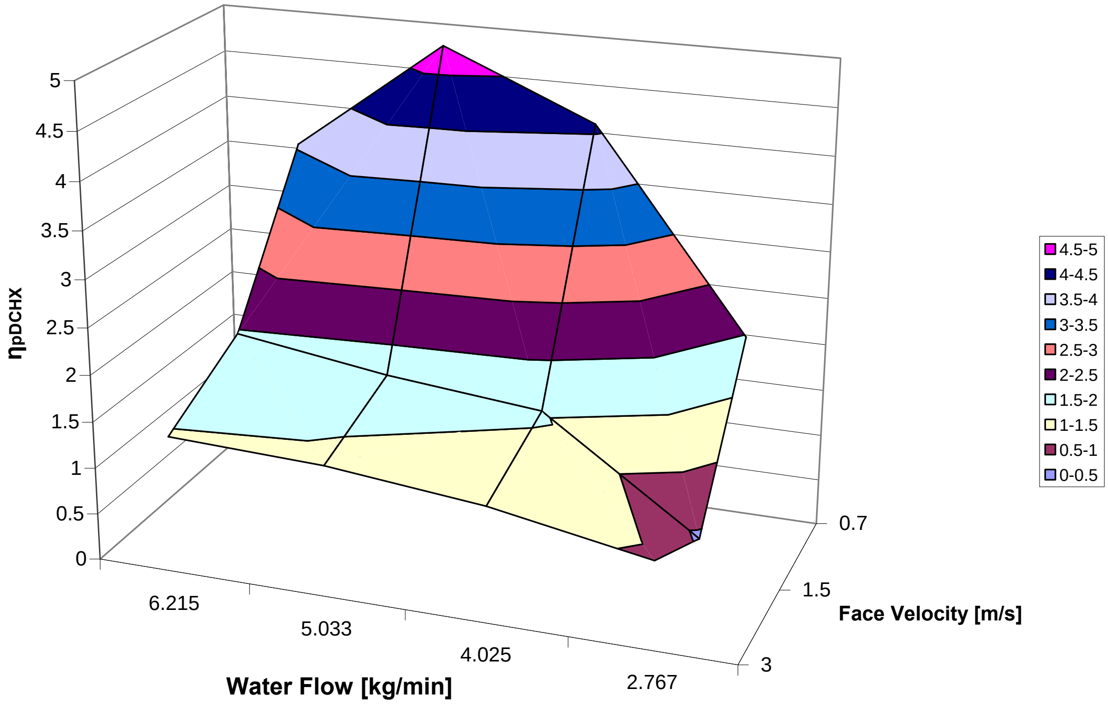

Figure F8 The prototype DCHX efficiency metric results for the third generation test section.

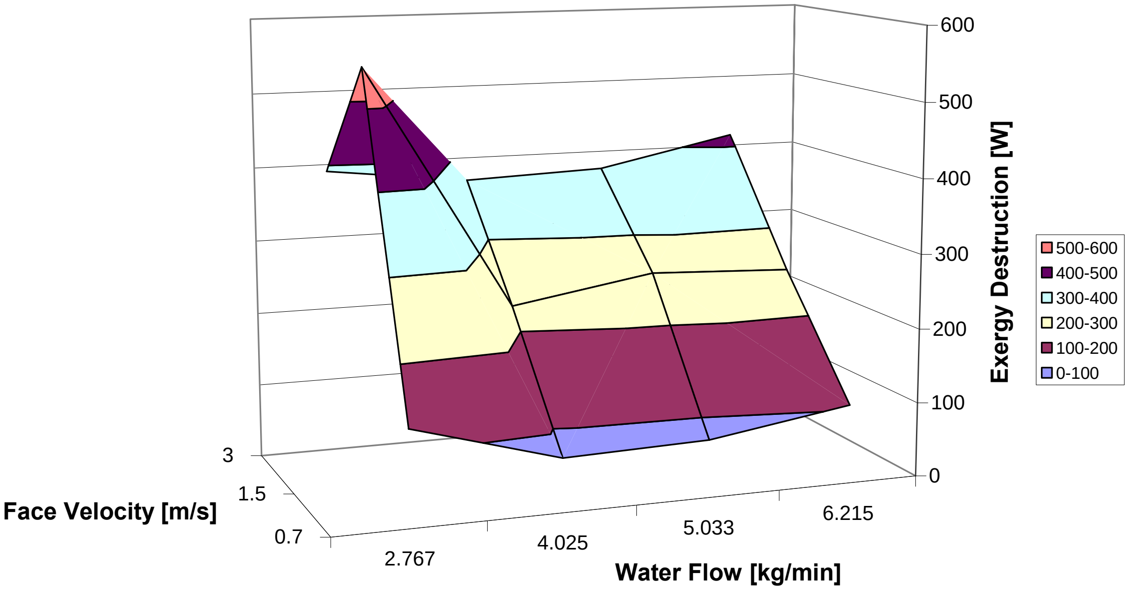

Figure F9 The exergy destruction in the third generation test section.

Excluding the outlying point (1.5 m/s and 2.7 kg/min), there appears to be a consistent trough formed, with the minimum corresponding to 4.0 kg/min of water flow, regardless of face velocity. It is clear that the exergy destruction in the low air flow case is approximately 300 W less than in the highest air flow case, but in comparing to Fig. F5, the amount of heat transfer is only around 100 to 200 W less for the low air flow rates. This indicates that the low air flow rates somehow make better use of the prototype heat exchanger geometry or spray conditions.

To help begin to understand this problem, it helps to look at a modified exergy wheel, as introduced by Bejan [37], shown in Fig. F10.

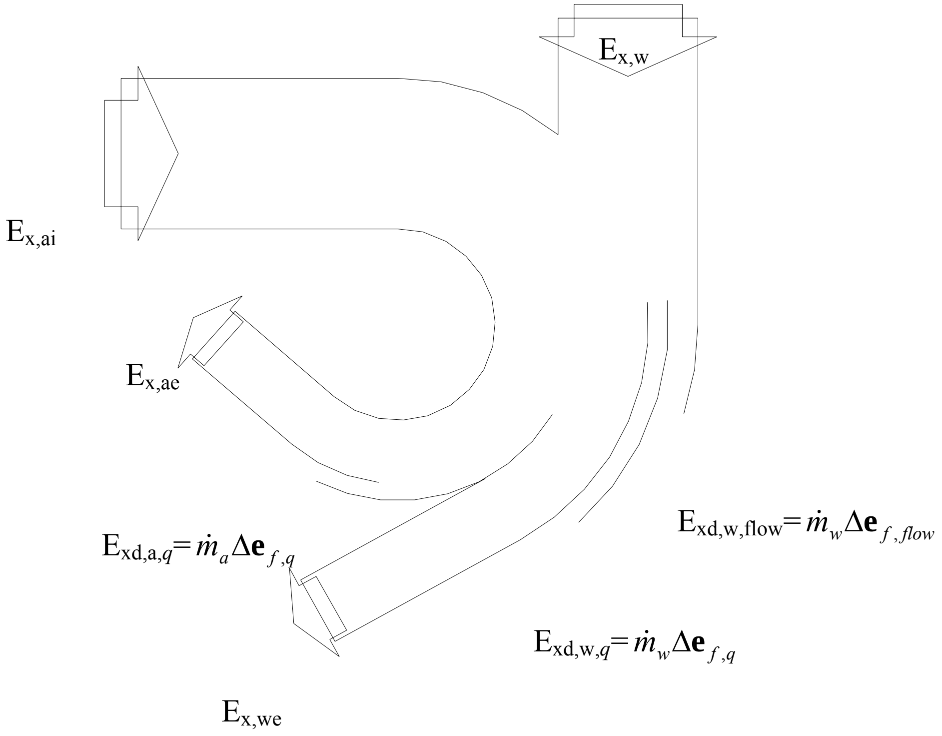

Figure F10 A modified exergy wheel for the pDCHX. Note that the wheel is generally use to describe a closed loop cycle, and is therefore a true wheel. In this open loop analysis, the 'wheel' is not closed.

The first thing to notice in Fig. F10 is that the exergy destruction due to air side flow work is not present, as assumed in the derivation. However, this flow work destruction is noted on the water side as $E_{xd,\ w,\ flow}$. The efficiency metric, η_{pDCHX} is only concerned with the exergy destruction terms: $E_{xd,\ w,\ flow}$, $E_{xd,\ w,\ q}$, and $E_{xd,\ a,\ q}$. In the case of the low air velocity, the exergy destruction due to heat transfer, $E_{xd,\ a,\ q}$, is not as large simply due to the fact that not as much heat is transferred. One could also make the same argument for the water side exergy destruction due to heat transfer, $E_{xd,\ w,\ q}$. This is the reason that the destruction plotted in Fig. F9 for the low air flow is not as great.

In light of this discussion, one must be careful with the application of any metric being a function of exergy. In optimizing with respect to exergy, one must be careful in identifying the variables considered 'variable.' In this case, it would be argued that the mass air flow is not necessarily something that can be readily changed in a design situation (though the face may be, unfortunately the test section does not have these capabilities). However, the water flow rate can be changed. Fortunately, a local minimum is seen as this variable is changed.

Bearing this in mind, one could study Fig. F8 and say that for the 0.7 m/s face velocity, the spray volume should be approximately 5.0 kg/min. The addition of any more water flow will not be utilized by the water spray, i.e. more energy will be destroyed in flow work than is transferred in the form of heat. If the system is run at a face velocity of 3.0 m/s, however, the system can apparently handle more than 6.2 kg/min, i.e. the air has more capacity to make use of the additional water flow, thus more heat energy will be transferred than the amount of energy destroyed in the flow process.

8.6 Experimental Results

The following graphs are grouped by series. The 216 experiments fall into one of eight series, four for 26.7 °C tests and four for the 33.0 °C tests. Within these two major categories, the series are grouped according to the free stream velocity and water temperature. This grouping highlights the effects of water flow rate and relative humidity within a thermal loading condition.

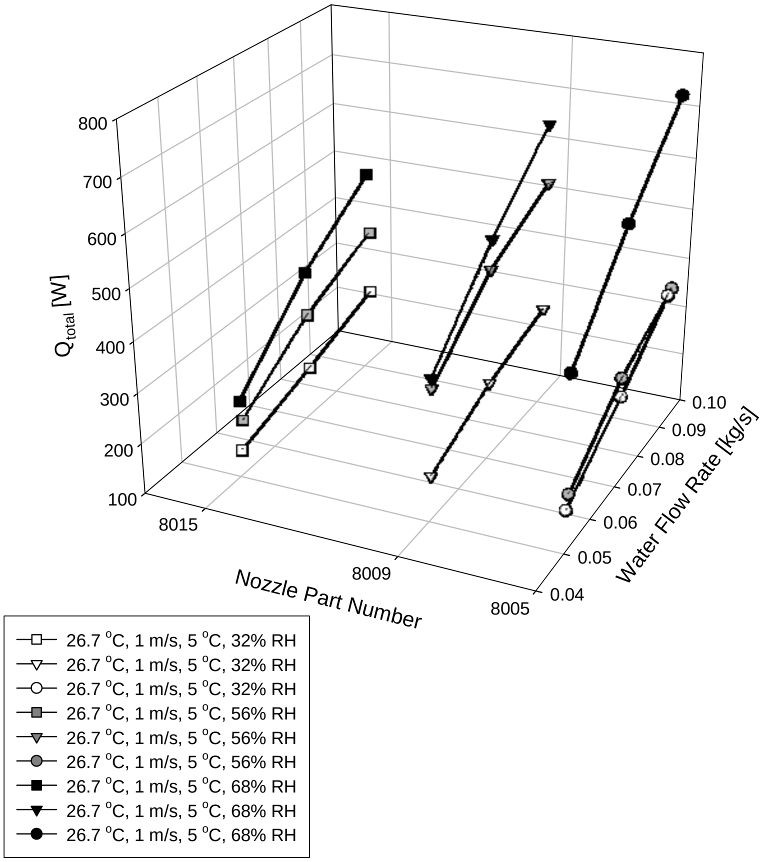
Q_total [W]
800
700
600
500
400
300
200
100
8015
8009
8005
Nozzle Part Number
0.04
0.05
0.06
0.07
0.08
0.09
0.10
Water Flow Rate [kg/s]
26.7 °C, 1 m/s, 5 °C, 32% RH
26.7 °C, 1 m/s, 5 °C, 32% RH
26.7 °C, 1 m/s, 5 °C, 32% RH
26.7 °C, 1 m/s, 5 °C, 56% RH
26.7 °C, 1 m/s, 5 °C, 56% RH
26.7 °C, 1 m/s, 5 °C, 56% RH
26.7 °C, 1 m/s, 5 °C, 68% RH
26.7 °C, 1 m/s, 5 °C, 68% RH
26.7 °C, 1 m/s, 5 °C, 68% RH

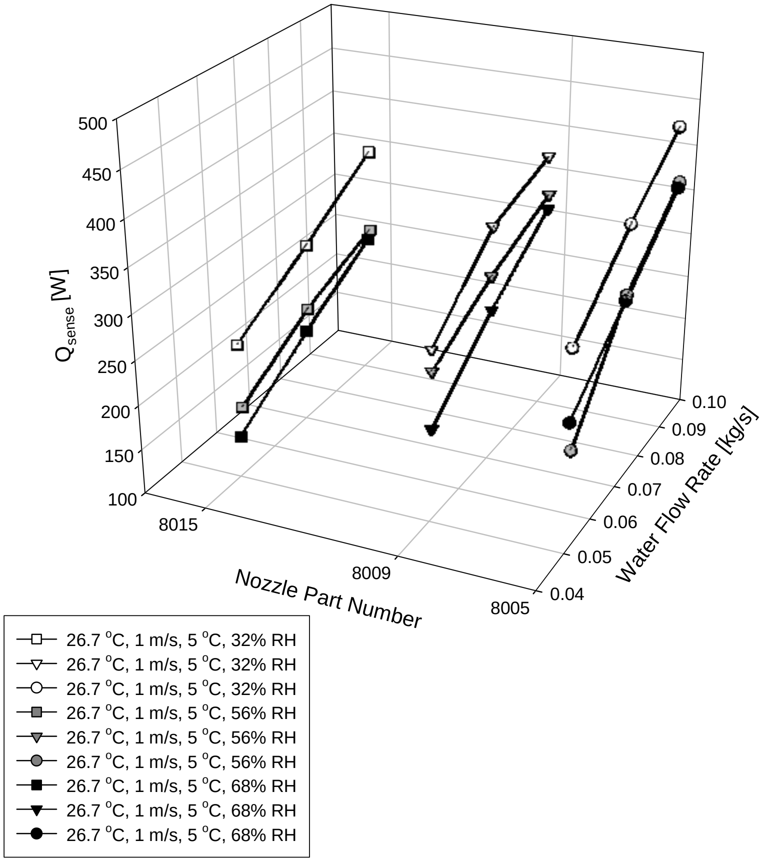
Q_sense [W]
500
450
400
350
300
250
200
150
100
8015
8009
8005
Nozzle Part Number
0.04
0.05
0.06
0.07
0.08
0.09
0.10
Water Flow Rate [kg/s]
26.7 °C, 1 m/s, 5 °C, 32% RH
26.7 °C, 1 m/s, 5 °C, 32% RH
26.7 °C, 1 m/s, 5 °C, 32% RH
26.7 °C, 1 m/s, 5 °C, 56% RH
26.7 °C, 1 m/s, 5 °C, 56% RH
26.7 °C, 1 m/s, 5 °C, 56% RH
26.7 °C, 1 m/s, 5 °C, 68% RH
26.7 °C, 1 m/s, 5 °C, 68% RH
26.7 °C, 1 m/s, 5 °C, 68% RH

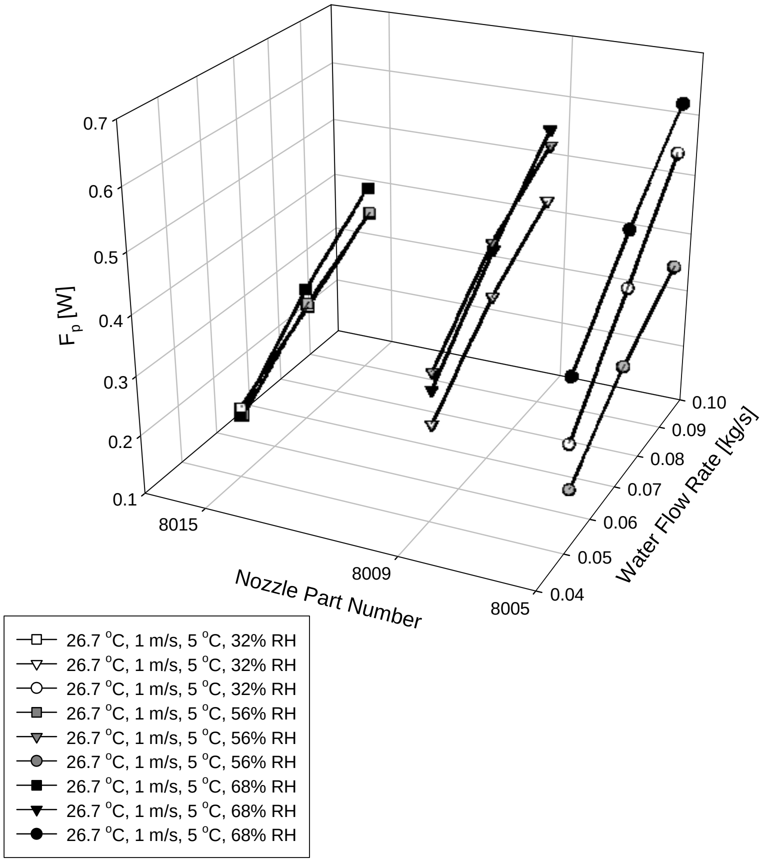
F_p [W]
0.7
0.6
0.5
0.4
0.3
0.2
0.1
8015
8009
8005
Nozzle Part Number
0.04
0.05
0.06
0.07
0.08
0.09
0.10
Water Flow Rate [kg/s]
26.7 °C, 1 m/s, 5 °C, 32% RH
26.7 °C, 1 m/s, 5 °C, 32% RH
26.7 °C, 1 m/s, 5 °C, 32% RH
26.7 °C, 1 m/s, 5 °C, 56% RH
26.7 °C, 1 m/s, 5 °C, 56% RH
26.7 °C, 1 m/s, 5 °C, 56% RH
26.7 °C, 1 m/s, 5 °C, 68% RH
26.7 °C, 1 m/s, 5 °C, 68% RH
26.7 °C, 1 m/s, 5 °C, 68% RH

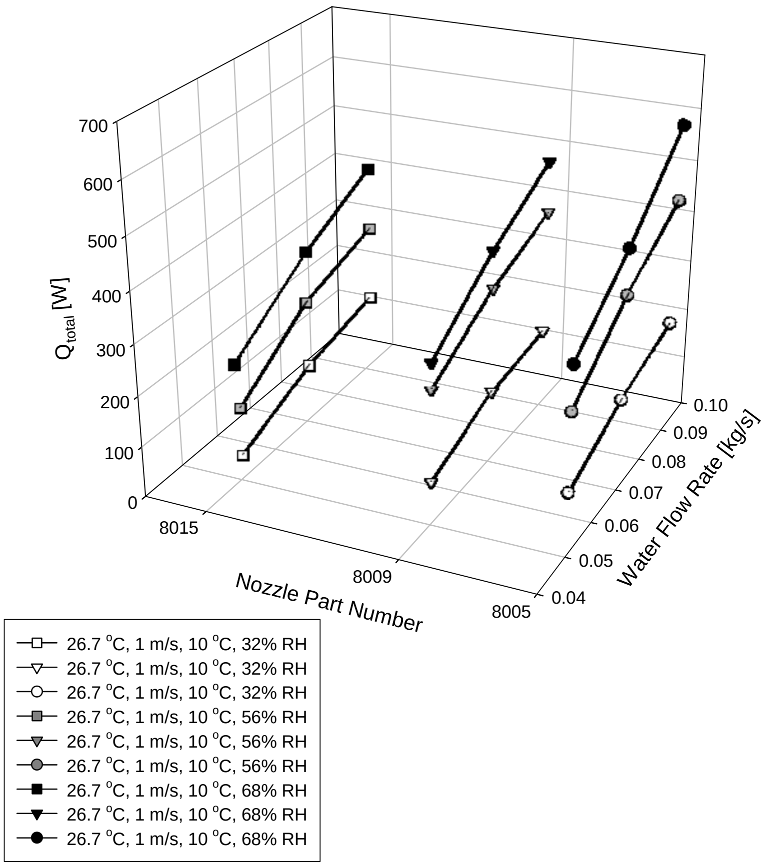
Q_{total} [W]
0
100
200
300
400
500
600
700
8015
8009
8005
Nozzle Part Number
0.04
0.05
0.06
0.07
0.08
0.09
0.10
Water Flow Rate [kg/s]
26.7 °C, 1 m/s, 10 °C, 32% RH
26.7 °C, 1 m/s, 10 °C, 32% RH
26.7 °C, 1 m/s, 10 °C, 32% RH
26.7 °C, 1 m/s, 10 °C, 56% RH
26.7 °C, 1 m/s, 10 °C, 56% RH
26.7 °C, 1 m/s, 10 °C, 56% RH
26.7 °C, 1 m/s, 10 °C, 68% RH
26.7 °C, 1 m/s, 10 °C, 68% RH
26.7 °C, 1 m/s, 10 °C, 68% RH

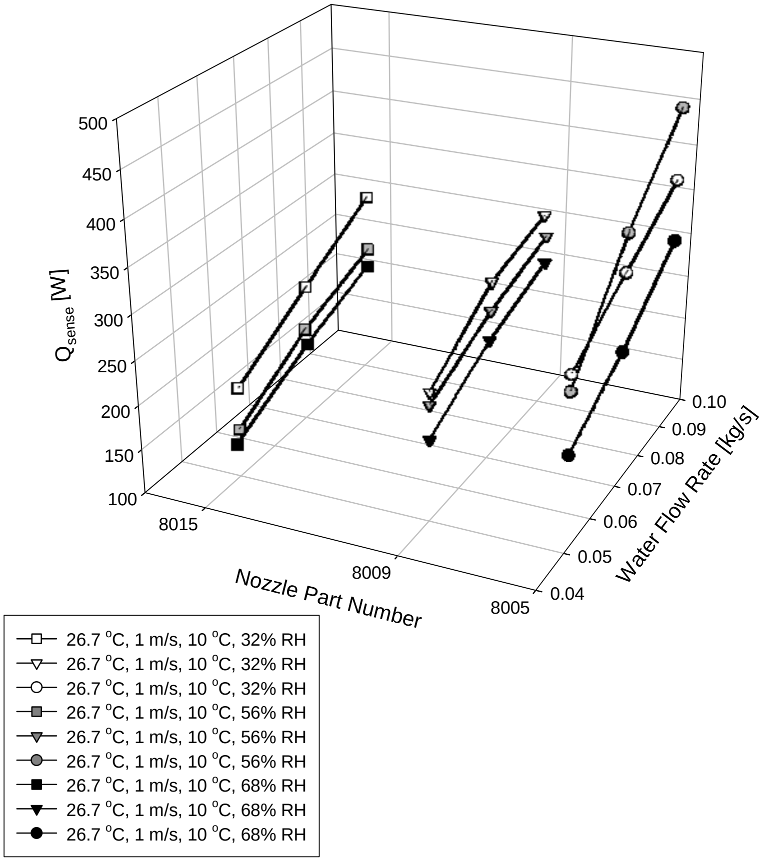
Q_{sense} [W]
100
150
200
250
300
350
400
450
500
8015
8009
8005
Nozzle Part Number
0.04
0.05
0.06
0.07
0.08
0.09
0.10
Water Flow Rate [kg/s]
26.7 °C, 1 m/s, 10 °C, 32% RH
26.7 °C, 1 m/s, 10 °C, 32% RH
26.7 °C, 1 m/s, 10 °C, 32% RH
26.7 °C, 1 m/s, 10 °C, 56% RH
26.7 °C, 1 m/s, 10 °C, 56% RH
26.7 °C, 1 m/s, 10 °C, 56% RH
26.7 °C, 1 m/s, 10 °C, 68% RH
26.7 °C, 1 m/s, 10 °C, 68% RH
26.7 °C, 1 m/s, 10 °C, 68% RH

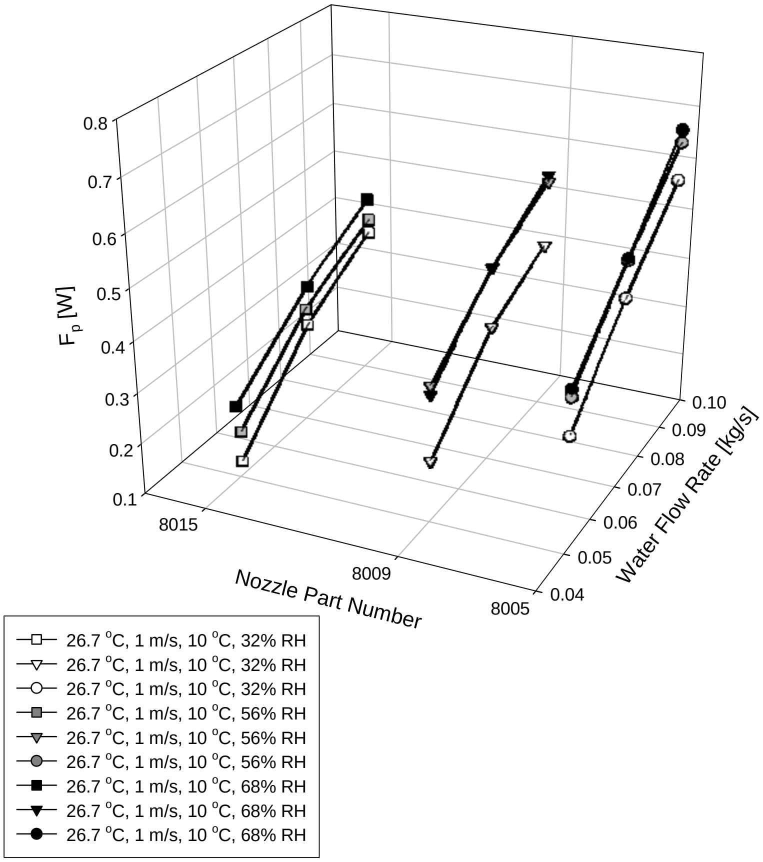

0.8
0.7
0.6
0.5
0.4
0.3
0.2
0.1
F_p [W]
8015
8009
8005
Nozzle Part Number
0.04
0.05
0.06
0.07
0.08
0.09
0.10
Water Flow Rate [kg/s]
26.7 °C, 1 m/s, 10 °C, 32% RH
26.7 °C, 1 m/s, 10 °C, 32% RH
26.7 °C, 1 m/s, 10 °C, 32% RH
26.7 °C, 1 m/s, 10 °C, 56% RH
26.7 °C, 1 m/s, 10 °C, 56% RH
26.7 °C, 1 m/s, 10 °C, 56% RH
26.7 °C, 1 m/s, 10 °C, 68% RH
26.7 °C, 1 m/s, 10 °C, 68% RH
26.7 °C, 1 m/s, 10 °C, 68% RH

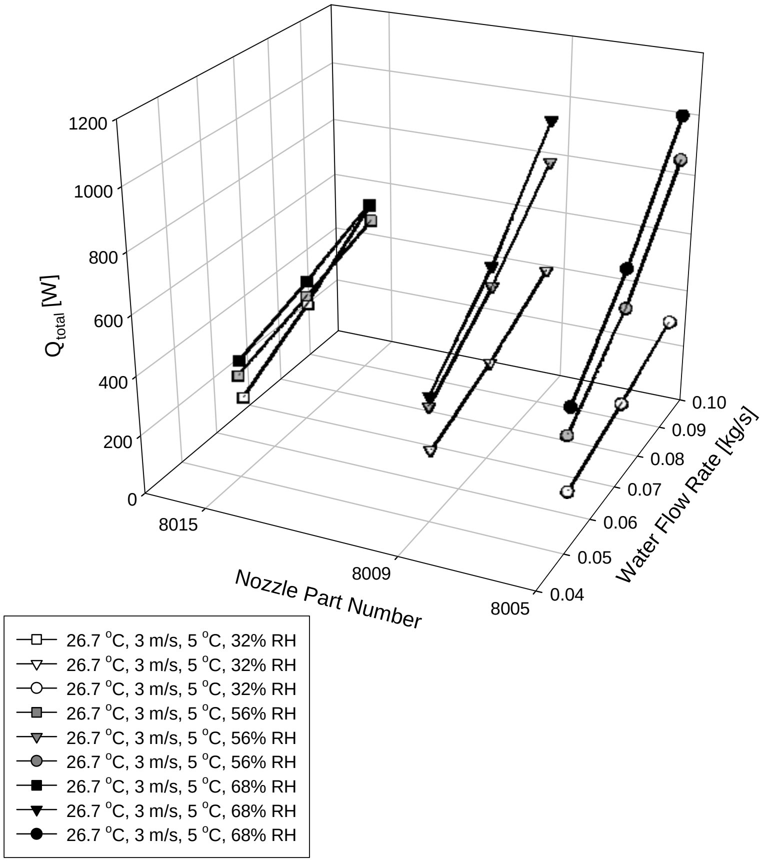

Q_total [W]
0
200
400
600
800
1000
1200
Nozzle Part Number
8015
8009
8005
Water Flow Rate [kg/s]
0.04
0.05
0.06
0.07
0.08
0.09
0.10
□ 26.7 °C, 3 m/s, 5 °C, 32% RH
▽ 26.7 °C, 3 m/s, 5 °C, 32% RH
○ 26.7 °C, 3 m/s, 5 °C, 32% RH
▨ 26.7 °C, 3 m/s, 5 °C, 56% RH
▽ 26.7 °C, 3 m/s, 5 °C, 56% RH
● 26.7 °C, 3 m/s, 5 °C, 56% RH
■ 26.7 °C, 3 m/s, 5 °C, 68% RH
▼ 26.7 °C, 3 m/s, 5 °C, 68% RH
● 26.7 °C, 3 m/s, 5 °C, 68% RH

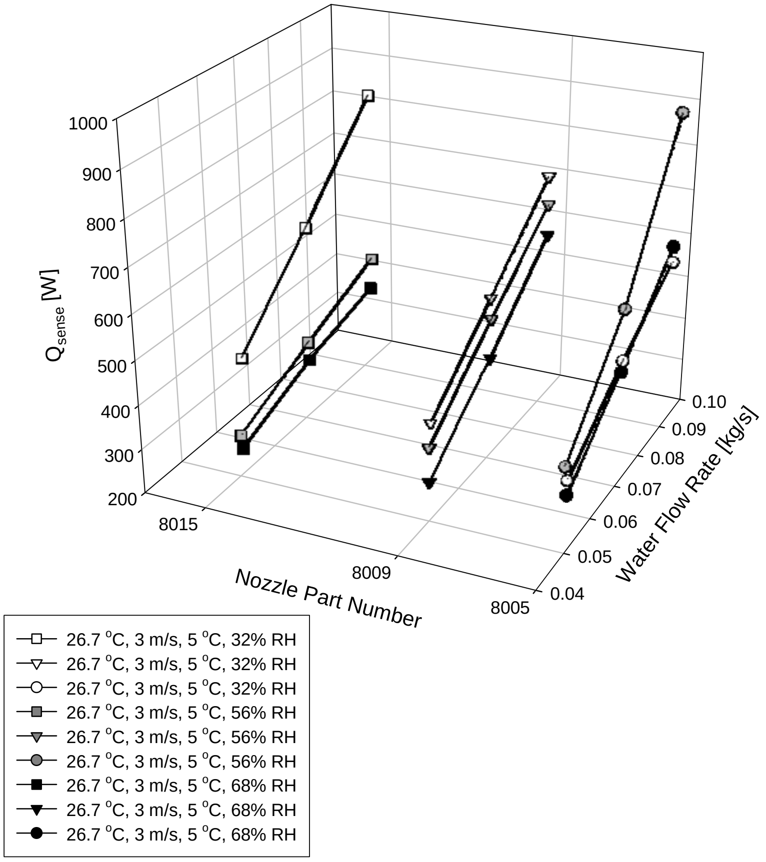

Q_sense [W]
200
300
400
500
600
700
800
900
1000
Nozzle Part Number
8015
8009
8005
Water Flow Rate [kg/s]
0.04
0.05
0.06
0.07
0.08
0.09
0.10
□ 26.7 °C, 3 m/s, 5 °C, 32% RH
▽ 26.7 °C, 3 m/s, 5 °C, 32% RH
○ 26.7 °C, 3 m/s, 5 °C, 32% RH
▨ 26.7 °C, 3 m/s, 5 °C, 56% RH
▽ 26.7 °C, 3 m/s, 5 °C, 56% RH
● 26.7 °C, 3 m/s, 5 °C, 56% RH
■ 26.7 °C, 3 m/s, 5 °C, 68% RH
▼ 26.7 °C, 3 m/s, 5 °C, 68% RH
● 26.7 °C, 3 m/s, 5 °C, 68% RH

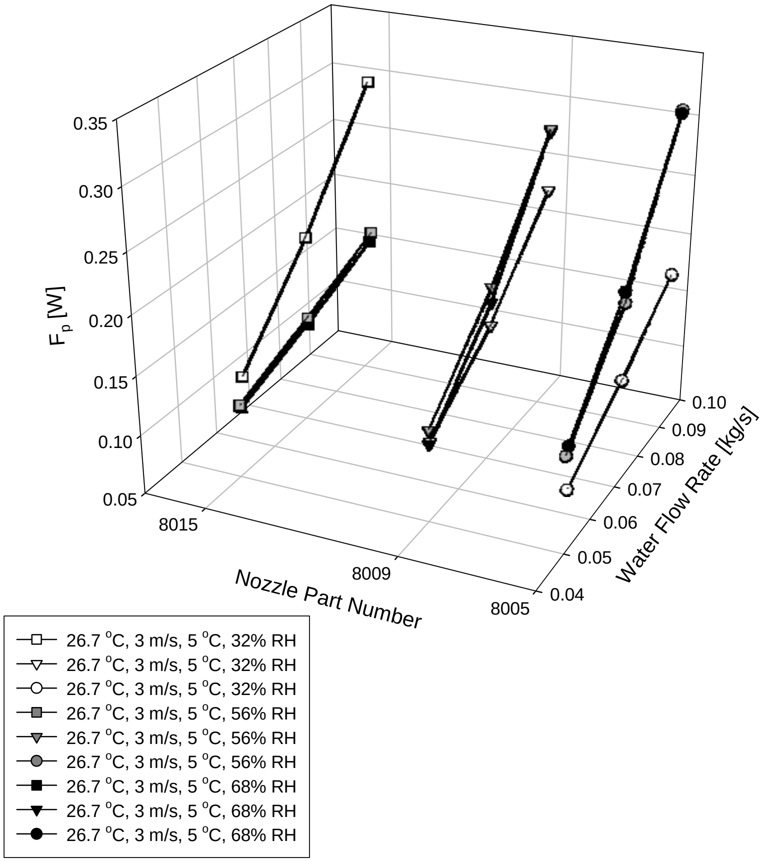
F_p [W]
0.35
0.30
0.25
0.20
0.15
0.10
0.05
Nozzle Part Number
8015
8009
8005
Water Flow Rate [kg/s]
0.10
0.09
0.08
0.07
0.06
0.05
0.04
□ 26.7 °C, 3 m/s, 5 °C, 32% RH
▽ 26.7 °C, 3 m/s, 5 °C, 32% RH
○ 26.7 °C, 3 m/s, 5 °C, 32% RH
▨ 26.7 °C, 3 m/s, 5 °C, 56% RH
▽ 26.7 °C, 3 m/s, 5 °C, 56% RH
● 26.7 °C, 3 m/s, 5 °C, 56% RH
■ 26.7 °C, 3 m/s, 5 °C, 68% RH
▼ 26.7 °C, 3 m/s, 5 °C, 68% RH
● 26.7 °C, 3 m/s, 5 °C, 68% RH

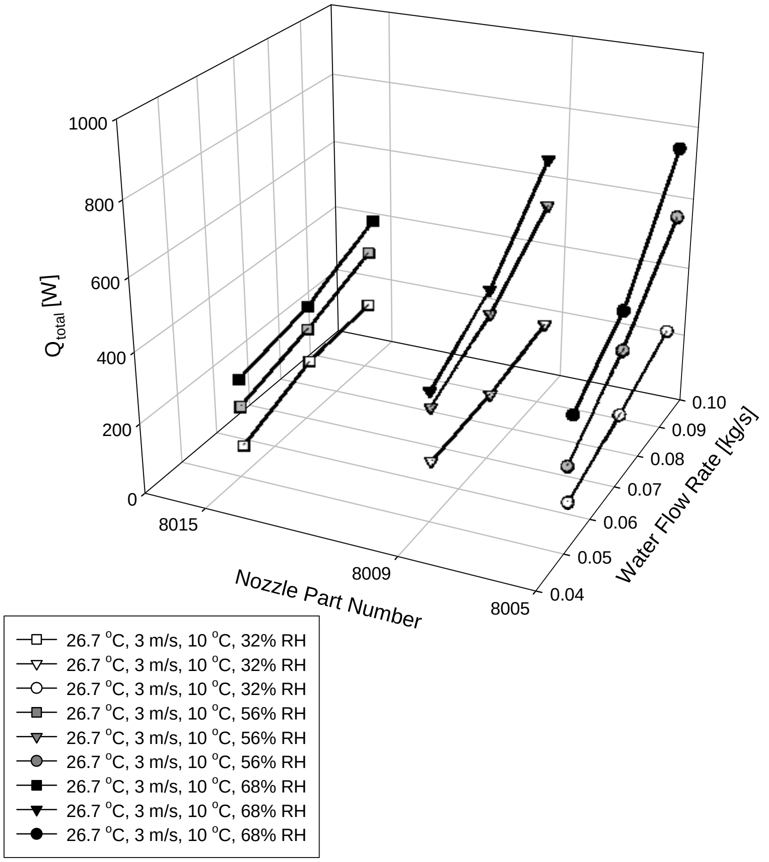

Q_{total} [W]
0
200
400
600
800
1000
8015
8009
8005
Nozzle Part Number
0.04
0.05
0.06
0.07
0.08
0.09
0.10
Water Flow Rate [kg/s]
26.7 °C, 3 m/s, 10 °C, 32% RH
26.7 °C, 3 m/s, 10 °C, 32% RH
26.7 °C, 3 m/s, 10 °C, 32% RH
26.7 °C, 3 m/s, 10 °C, 56% RH
26.7 °C, 3 m/s, 10 °C, 56% RH
26.7 °C, 3 m/s, 10 °C, 56% RH
26.7 °C, 3 m/s, 10 °C, 68% RH
26.7 °C, 3 m/s, 10 °C, 68% RH
26.7 °C, 3 m/s, 10 °C, 68% RH

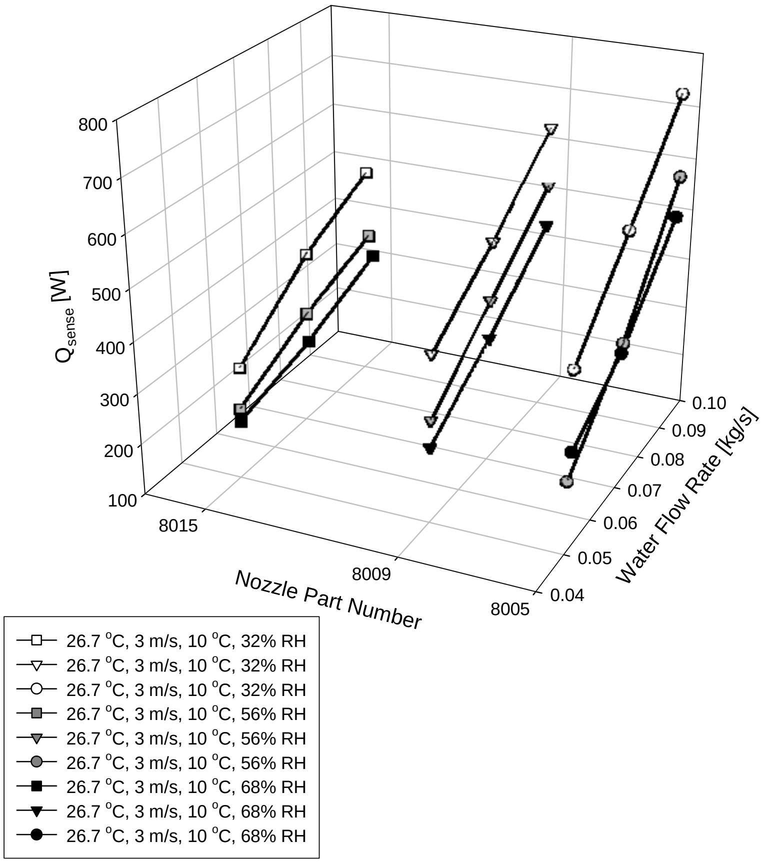

Q_{sense} [W]
100
200
300
400
500
600
700
800
8015
8009
8005
Nozzle Part Number
0.04
0.05
0.06
0.07
0.08
0.09
0.10
Water Flow Rate [kg/s]
26.7 °C, 3 m/s, 10 °C, 32% RH
26.7 °C, 3 m/s, 10 °C, 32% RH
26.7 °C, 3 m/s, 10 °C, 32% RH
26.7 °C, 3 m/s, 10 °C, 56% RH
26.7 °C, 3 m/s, 10 °C, 56% RH
26.7 °C, 3 m/s, 10 °C, 56% RH
26.7 °C, 3 m/s, 10 °C, 68% RH
26.7 °C, 3 m/s, 10 °C, 68% RH
26.7 °C, 3 m/s, 10 °C, 68% RH

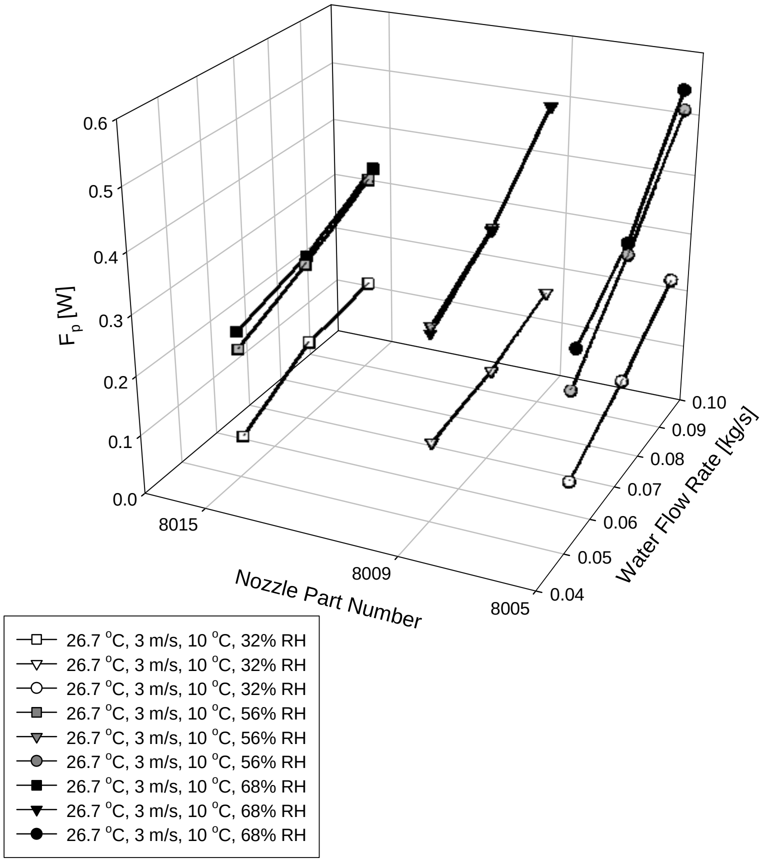
0.6
0.5
0.4
0.3
0.2
0.1
0.0
F_p [W]
8015
8009
8005
Nozzle Part Number
0.10
0.09
0.08
0.07
0.06
0.05
0.04
Water Flow Rate [kg/s]
□ 26.7 °C, 3 m/s, 10 °C, 32% RH
▽ 26.7 °C, 3 m/s, 10 °C, 32% RH
○ 26.7 °C, 3 m/s, 10 °C, 32% RH
▨ 26.7 °C, 3 m/s, 10 °C, 56% RH
▽ 26.7 °C, 3 m/s, 10 °C, 56% RH
● 26.7 °C, 3 m/s, 10 °C, 56% RH
■ 26.7 °C, 3 m/s, 10 °C, 68% RH
▼ 26.7 °C, 3 m/s, 10 °C, 68% RH
● 26.7 °C, 3 m/s, 10 °C, 68% RH

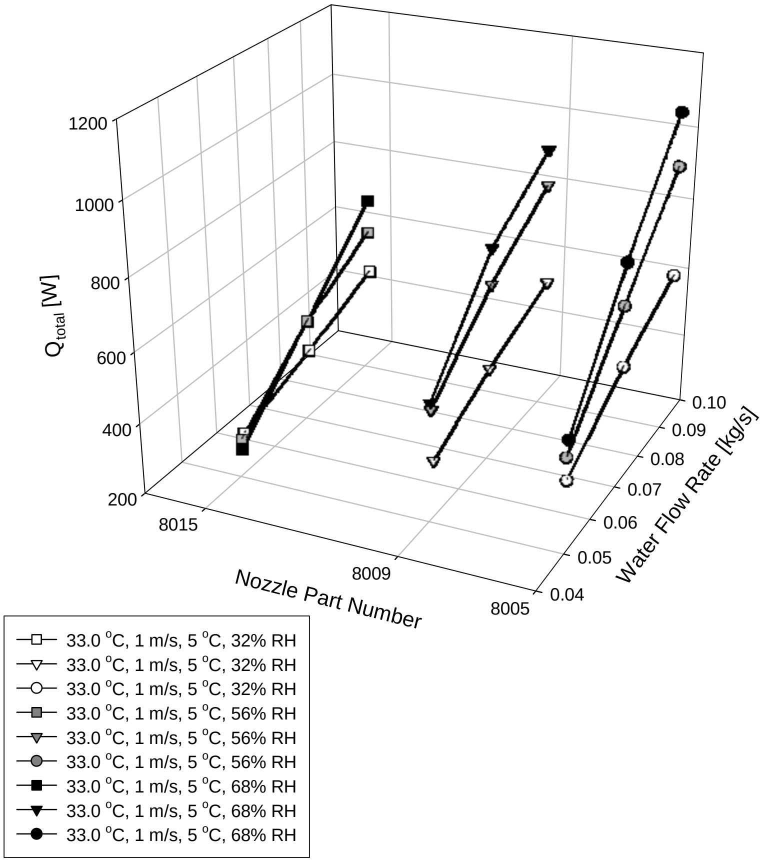
1200
1000
800
600
400
200
Q_total [W]
8015
8009
8005
Nozzle Part Number
0.04
0.05
0.06
0.07
0.08
0.09
0.10
Water Flow Rate [kg/s]
□ 33.0 °C, 1 m/s, 5 °C, 32% RH
▽ 33.0 °C, 1 m/s, 5 °C, 32% RH
○ 33.0 °C, 1 m/s, 5 °C, 32% RH
■ 33.0 °C, 1 m/s, 5 °C, 56% RH
▼ 33.0 °C, 1 m/s, 5 °C, 56% RH
● 33.0 °C, 1 m/s, 5 °C, 56% RH
■ 33.0 °C, 1 m/s, 5 °C, 68% RH
▼ 33.0 °C, 1 m/s, 5 °C, 68% RH
● 33.0 °C, 1 m/s, 5 °C, 68% RH

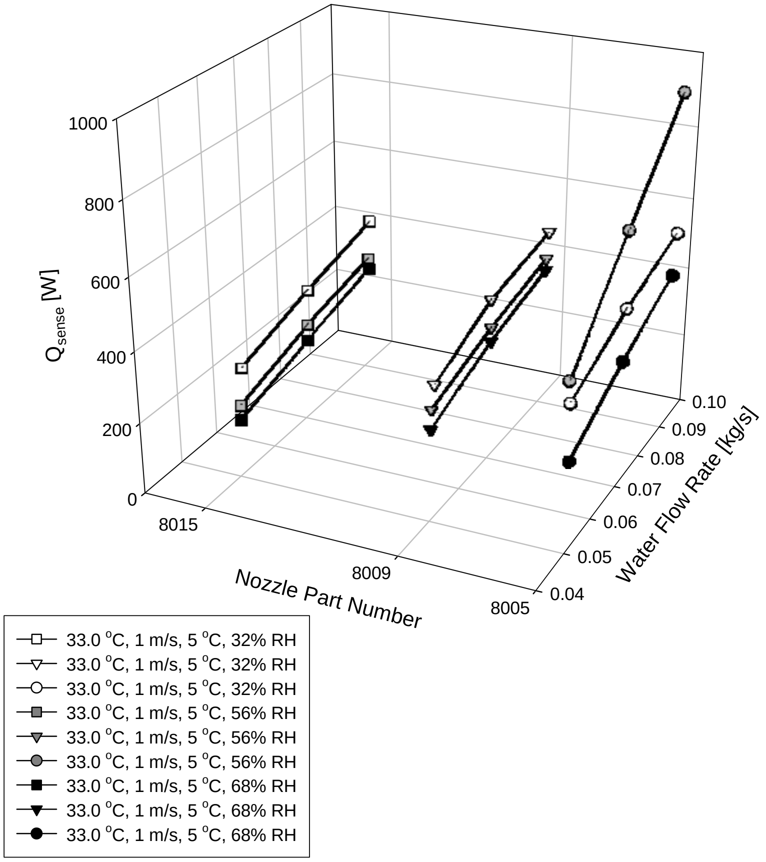
1000
800
600
400
200
0
Q_sense [W]
8015
8009
8005
Nozzle Part Number
0.04
0.05
0.06
0.07
0.08
0.09
0.10
Water Flow Rate [kg/s]
□ 33.0 °C, 1 m/s, 5 °C, 32% RH
▽ 33.0 °C, 1 m/s, 5 °C, 32% RH
○ 33.0 °C, 1 m/s, 5 °C, 32% RH
■ 33.0 °C, 1 m/s, 5 °C, 56% RH
▼ 33.0 °C, 1 m/s, 5 °C, 56% RH
● 33.0 °C, 1 m/s, 5 °C, 56% RH
■ 33.0 °C, 1 m/s, 5 °C, 68% RH
▼ 33.0 °C, 1 m/s, 5 °C, 68% RH
● 33.0 °C, 1 m/s, 5 °C, 68% RH

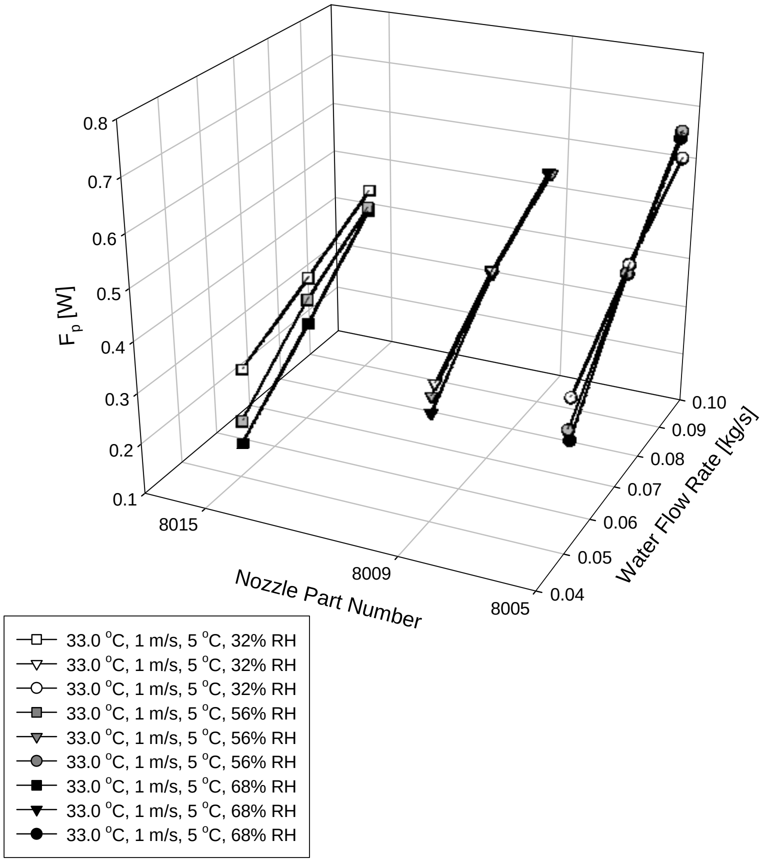
F$_p$ [W]
0.8
0.7
0.6
0.5
0.4
0.3
0.2
0.1
8015
8009
8005
Nozzle Part Number
0.04
0.05
0.06
0.07
0.08
0.09
0.10
Water Flow Rate [kg/s]
□ 33.0 ^{o}C, 1 m/s, 5 ^{o}C, 32% RH
▽ 33.0 ^{o}C, 1 m/s, 5 ^{o}C, 32% RH
○ 33.0 ^{o}C, 1 m/s, 5 ^{o}C, 32% RH
▨ 33.0 ^{o}C, 1 m/s, 5 ^{o}C, 56% RH
▼ 33.0 ^{o}C, 1 m/s, 5 ^{o}C, 56% RH
● 33.0 ^{o}C, 1 m/s, 5 ^{o}C, 56% RH
■ 33.0 ^{o}C, 1 m/s, 5 ^{o}C, 68% RH
▼ 33.0 ^{o}C, 1 m/s, 5 ^{o}C, 68% RH
● 33.0 ^{o}C, 1 m/s, 5 ^{o}C, 68% RH

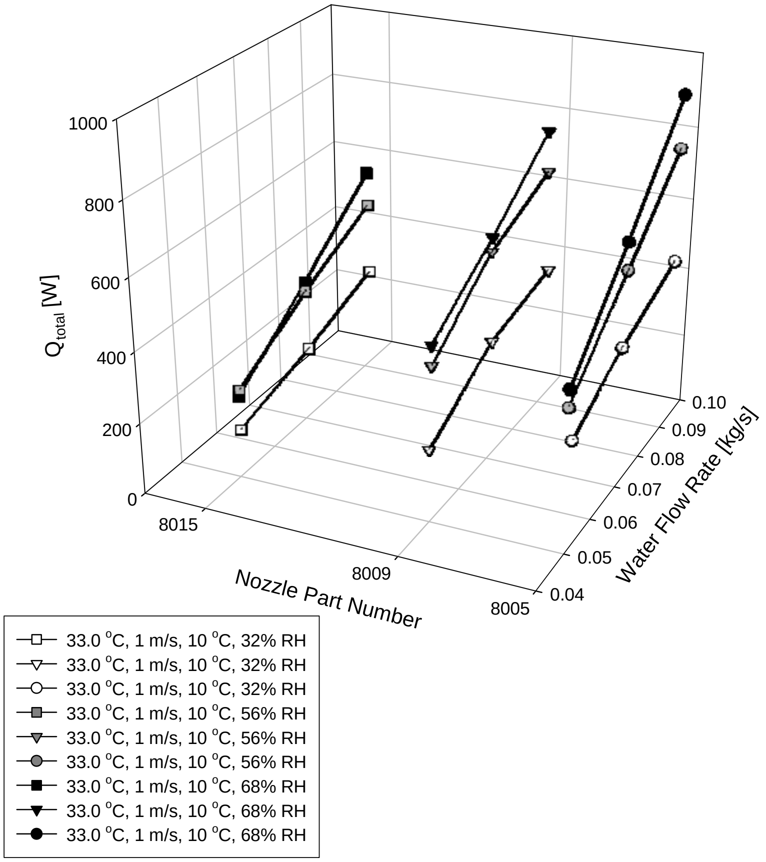
1000
800
600
400
200
0
Q$_{total}$ [W]
8015
8009
8005
Nozzle Part Number
0.10
0.09
0.08
0.07
0.06
0.05
0.04
Water Flow Rate [kg/s]
□ 33.0 °C, 1 m/s, 10 °C, 32% RH
▽ 33.0 °C, 1 m/s, 10 °C, 32% RH
○ 33.0 °C, 1 m/s, 10 °C, 32% RH
■ 33.0 °C, 1 m/s, 10 °C, 56% RH
▼ 33.0 °C, 1 m/s, 10 °C, 56% RH
● 33.0 °C, 1 m/s, 10 °C, 56% RH
■ 33.0 °C, 1 m/s, 10 °C, 68% RH
▼ 33.0 °C, 1 m/s, 10 °C, 68% RH
● 33.0 °C, 1 m/s, 10 °C, 68% RH

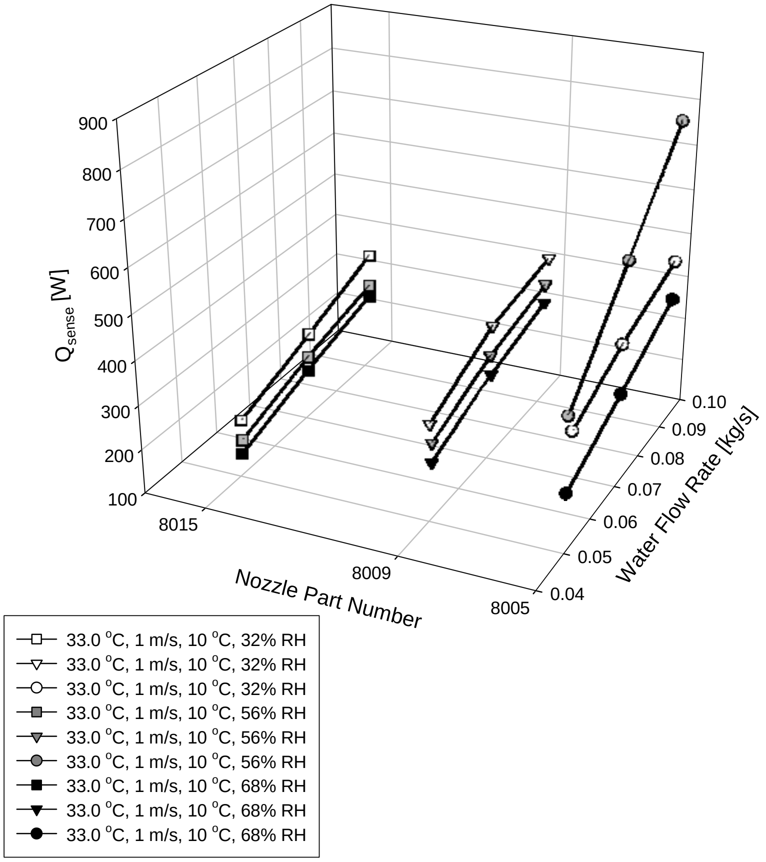
900
800
700
600
500
400
300
200
100
Q$_{sense}$ [W]
8015
8009
8005
Nozzle Part Number
0.10
0.09
0.08
0.07
0.06
0.05
0.04
Water Flow Rate [kg/s]
□ 33.0 °C, 1 m/s, 10 °C, 32% RH
▽ 33.0 °C, 1 m/s, 10 °C, 32% RH
○ 33.0 °C, 1 m/s, 10 °C, 32% RH
■ 33.0 °C, 1 m/s, 10 °C, 56% RH
▼ 33.0 °C, 1 m/s, 10 °C, 56% RH
● 33.0 °C, 1 m/s, 10 °C, 56% RH
■ 33.0 °C, 1 m/s, 10 °C, 68% RH
▼ 33.0 °C, 1 m/s, 10 °C, 68% RH
● 33.0 °C, 1 m/s, 10 °C, 68% RH

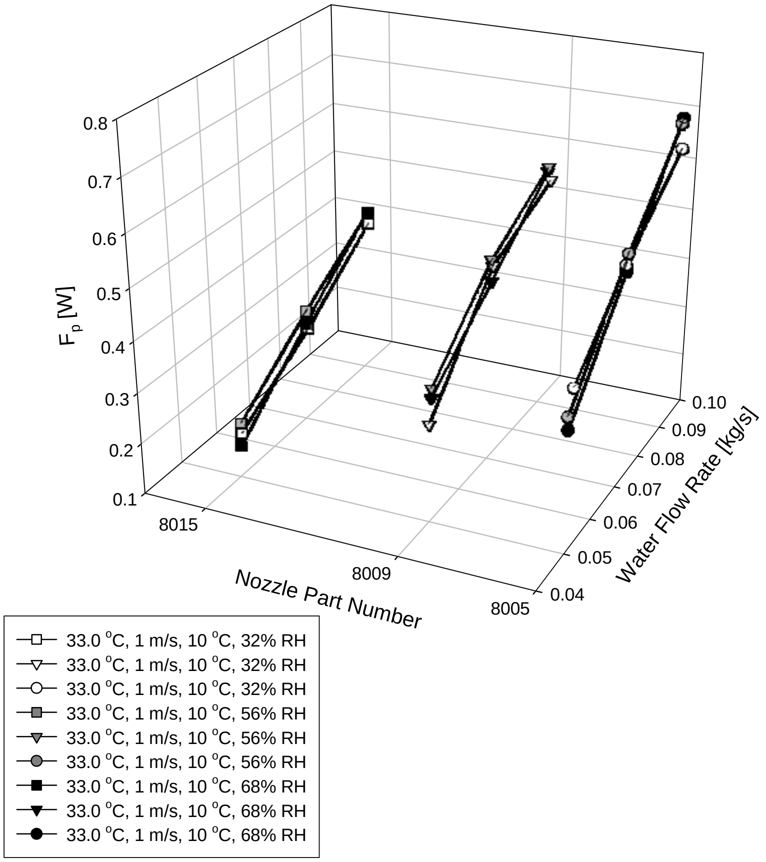
F_p [W]
0.8
0.7
0.6
0.5
0.4
0.3
0.2
0.1
8015
8009
8005
Nozzle Part Number
0.10
0.09
0.08
0.07
0.06
0.05
0.04
Water Flow Rate [kg/s]
33.0 °C, 1 m/s, 10 °C, 32% RH
33.0 °C, 1 m/s, 10 °C, 32% RH
33.0 °C, 1 m/s, 10 °C, 32% RH
33.0 °C, 1 m/s, 10 °C, 56% RH
33.0 °C, 1 m/s, 10 °C, 56% RH
33.0 °C, 1 m/s, 10 °C, 56% RH
33.0 °C, 1 m/s, 10 °C, 68% RH
33.0 °C, 1 m/s, 10 °C, 68% RH
33.0 °C, 1 m/s, 10 °C, 68% RH

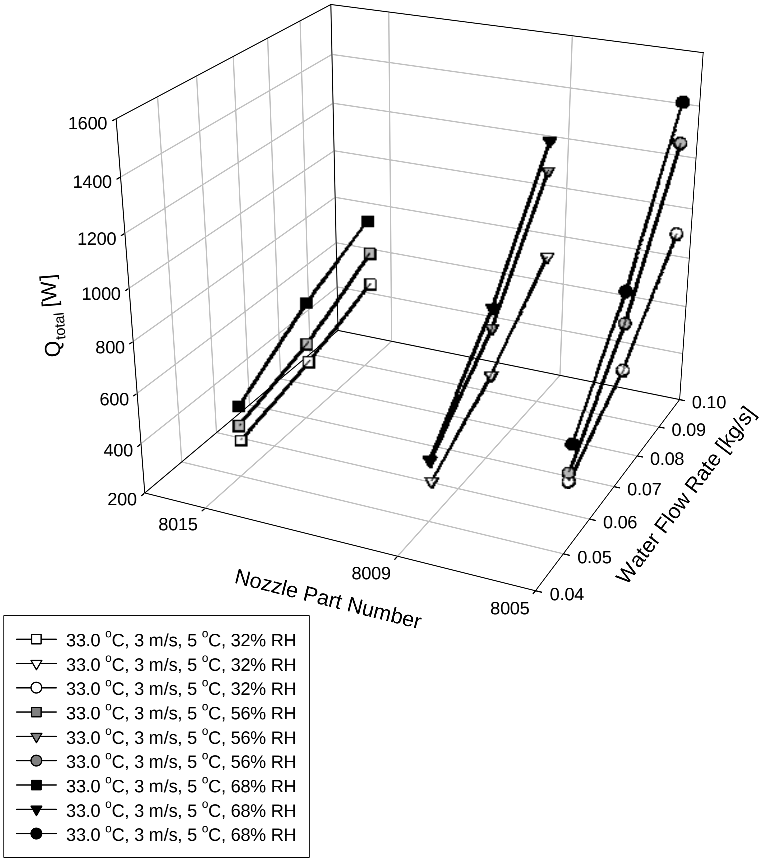
1600
1400
1200
1000
800
600
400
200
Q_{total} [W]
8015
8009
8005
Nozzle Part Number
0.10
0.09
0.08
0.07
0.06
0.05
0.04
Water Flow Rate [kg/s]
□ 33.0 °C, 3 m/s, 5 °C, 32% RH
▽ 33.0 °C, 3 m/s, 5 °C, 32% RH
○ 33.0 °C, 3 m/s, 5 °C, 32% RH
▨ 33.0 °C, 3 m/s, 5 °C, 56% RH
▼ 33.0 °C, 3 m/s, 5 °C, 56% RH
● 33.0 °C, 3 m/s, 5 °C, 56% RH
■ 33.0 °C, 3 m/s, 5 °C, 68% RH
▼ 33.0 °C, 3 m/s, 5 °C, 68% RH
● 33.0 °C, 3 m/s, 5 °C, 68% RH

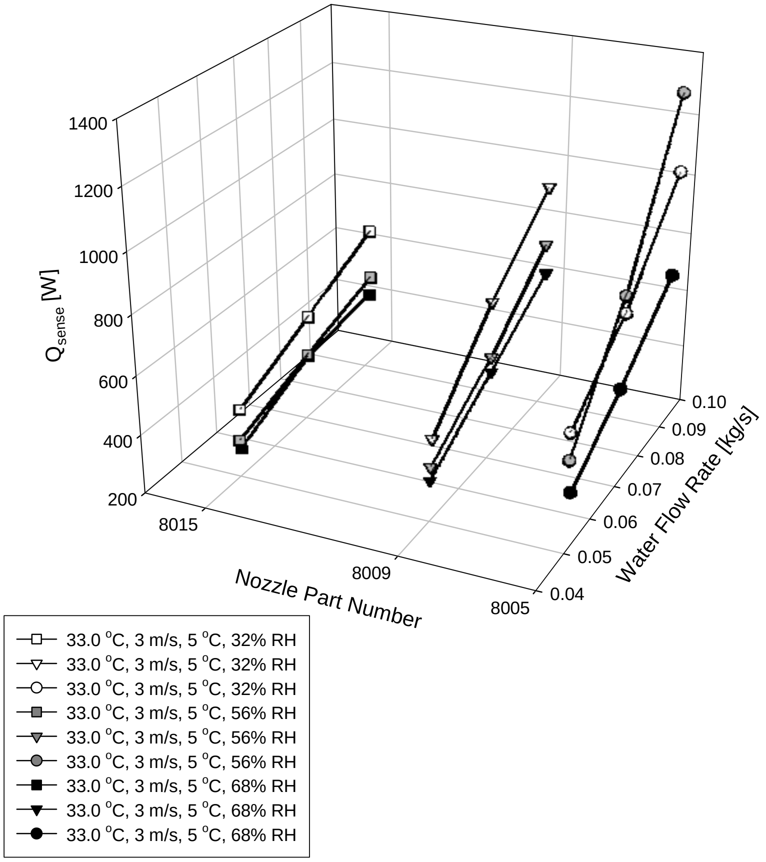
1400
1200
1000
800
600
400
200
Q_{sense} [W]
8015
8009
8005
Nozzle Part Number
0.10
0.09
0.08
0.07
0.06
0.05
0.04
Water Flow Rate [kg/s]
□ 33.0 °C, 3 m/s, 5 °C, 32% RH
▽ 33.0 °C, 3 m/s, 5 °C, 32% RH
○ 33.0 °C, 3 m/s, 5 °C, 32% RH
▨ 33.0 °C, 3 m/s, 5 °C, 56% RH
▼ 33.0 °C, 3 m/s, 5 °C, 56% RH
● 33.0 °C, 3 m/s, 5 °C, 56% RH
■ 33.0 °C, 3 m/s, 5 °C, 68% RH
▼ 33.0 °C, 3 m/s, 5 °C, 68% RH
● 33.0 °C, 3 m/s, 5 °C, 68% RH

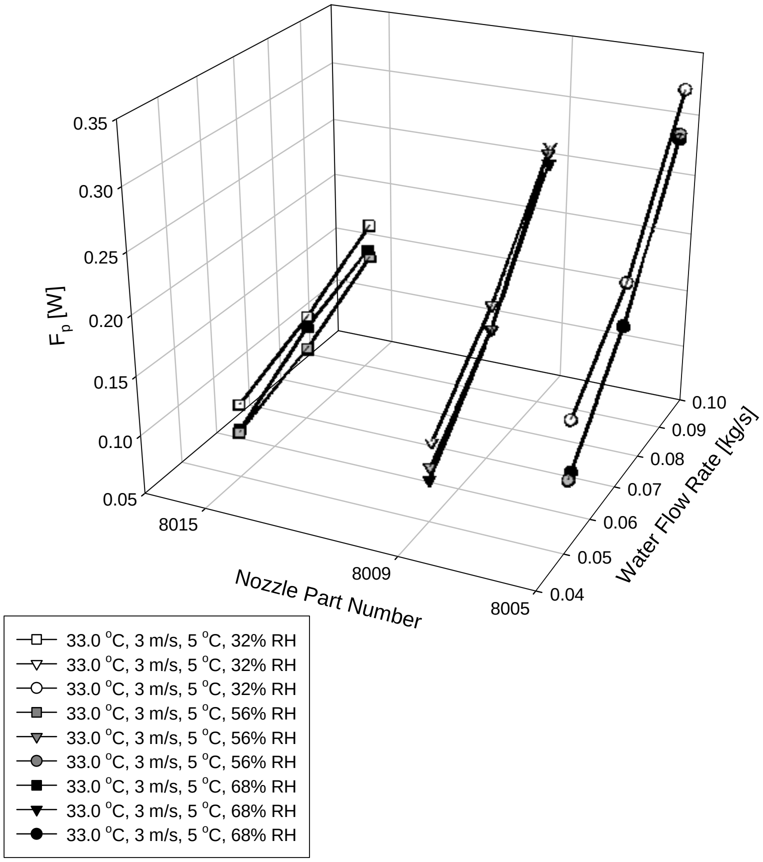

F$_p$ [W]
0.35
0.30
0.25
0.20
0.15
0.10
0.05
Nozzle Part Number
8015
8009
8005
Water Flow Rate [kg/s]
0.10
0.09
0.08
0.07
0.06
0.05
0.04
33.0 °C, 3 m/s, 5 °C, 32% RH
33.0 °C, 3 m/s, 5 °C, 32% RH
33.0 °C, 3 m/s, 5 °C, 32% RH
33.0 °C, 3 m/s, 5 °C, 56% RH
33.0 °C, 3 m/s, 5 °C, 56% RH
33.0 °C, 3 m/s, 5 °C, 56% RH
33.0 °C, 3 m/s, 5 °C, 68% RH
33.0 °C, 3 m/s, 5 °C, 68% RH
33.0 °C, 3 m/s, 5 °C, 68% RH

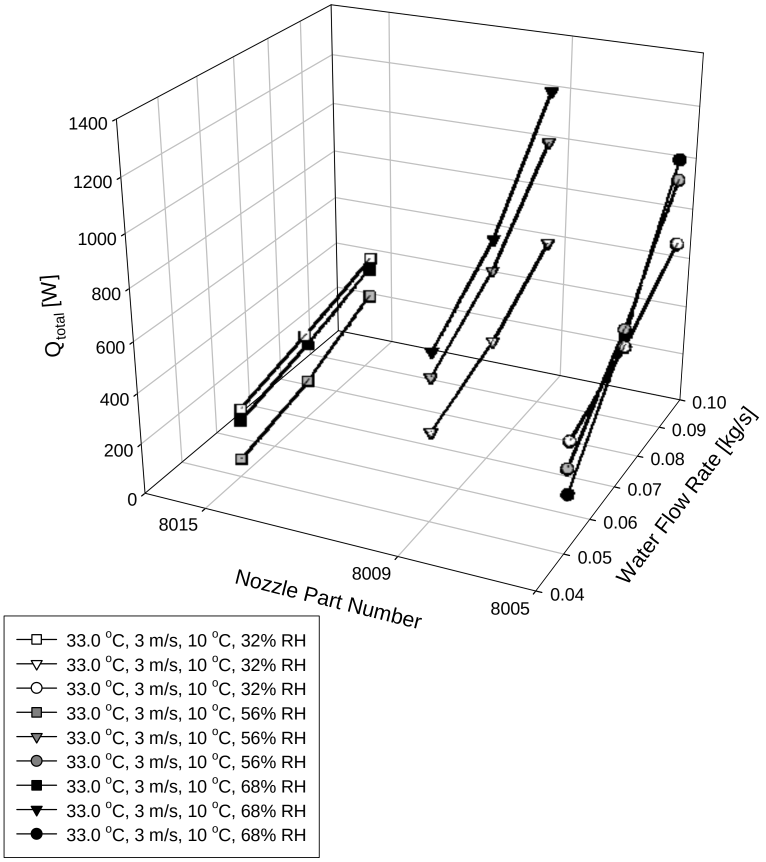

Q_total [W]
0
200
400
600
800
1000
1200
1400
8015
8009
8005
Nozzle Part Number
0.04
0.05
0.06
0.07
0.08
0.09
0.10
Water Flow Rate [kg/s]
33.0 °C, 3 m/s, 10 °C, 32% RH
33.0 °C, 3 m/s, 10 °C, 32% RH
33.0 °C, 3 m/s, 10 °C, 32% RH
33.0 °C, 3 m/s, 10 °C, 56% RH
33.0 °C, 3 m/s, 10 °C, 56% RH
33.0 °C, 3 m/s, 10 °C, 56% RH
33.0 °C, 3 m/s, 10 °C, 68% RH
33.0 °C, 3 m/s, 10 °C, 68% RH
33.0 °C, 3 m/s, 10 °C, 68% RH

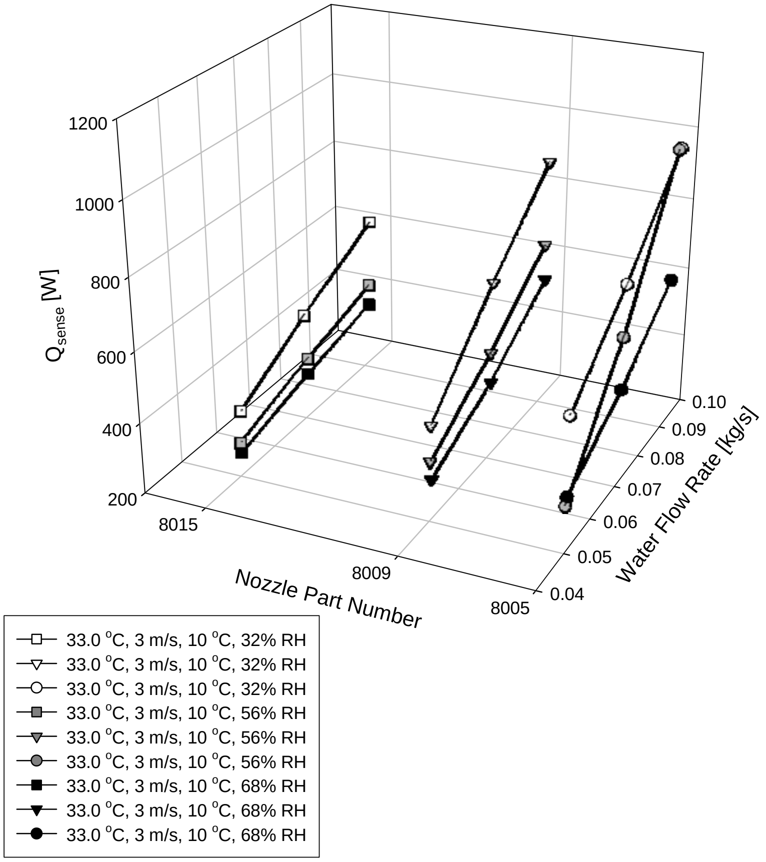

Q_sense [W]
200
400
600
800
1000
1200
8015
8009
8005
Nozzle Part Number
0.04
0.05
0.06
0.07
0.08
0.09
0.10
Water Flow Rate [kg/s]
33.0 °C, 3 m/s, 10 °C, 32% RH
33.0 °C, 3 m/s, 10 °C, 32% RH
33.0 °C, 3 m/s, 10 °C, 32% RH
33.0 °C, 3 m/s, 10 °C, 56% RH
33.0 °C, 3 m/s, 10 °C, 56% RH
33.0 °C, 3 m/s, 10 °C, 56% RH
33.0 °C, 3 m/s, 10 °C, 68% RH
33.0 °C, 3 m/s, 10 °C, 68% RH
33.0 °C, 3 m/s, 10 °C, 68% RH

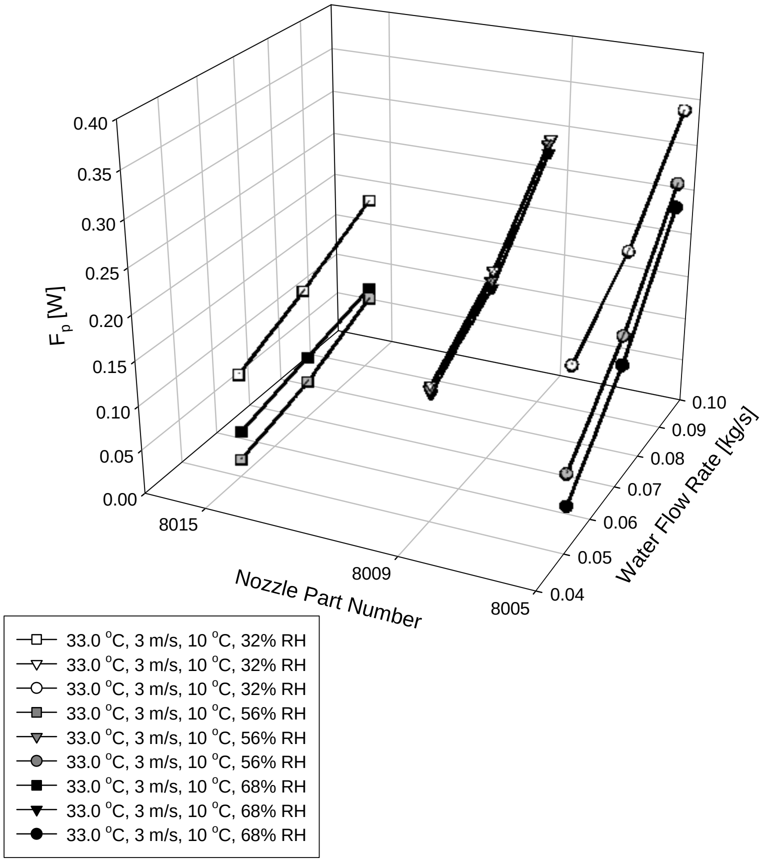
F_p [W]
0.00
0.05
0.10
0.15
0.20
0.25
0.30
0.35
0.40
Nozzle Part Number
8015
8009
8005
Water Flow Rate [kg/s]
0.04
0.05
0.06
0.07
0.08
0.09
0.10
□ 33.0 °C, 3 m/s, 10 °C, 32% RH
▽ 33.0 °C, 3 m/s, 10 °C, 32% RH
○ 33.0 °C, 3 m/s, 10 °C, 32% RH
▨ 33.0 °C, 3 m/s, 10 °C, 56% RH
▼ 33.0 °C, 3 m/s, 10 °C, 56% RH
● 33.0 °C, 3 m/s, 10 °C, 56% RH
■ 33.0 °C, 3 m/s, 10 °C, 68% RH
▼ 33.0 °C, 3 m/s, 10 °C, 68% RH
● 33.0 °C, 3 m/s, 10 °C, 68% RH

Test Information												
Date Tested:	1/14/07		1/14/07		1/14/07		1/14/07		1/14/07		1/14/07	
Nozzle:	8015		8015		8015		8009		8009		8009	
Nozzle Area [m2]	4.48E-06		4.48E-06		4.48E-06		2.85E-06		2.85E-06		2.85E-06	
Nozzle Pressure [psi][Pa]	10.5	72395.0	10.5	72395.0	10.5	72395.0	30.0	206842.7	62.0	427475.0	105.0	723949.5
Measurements	Value	Error	Value	Error	Value	Error	Value	Error	Value	Error	Value	Error
Barometric Pressure [pa]	100664.3	1.3	100664.3	1.3	100664.3	1.3	100664.3	1.3	100664.3	1.3	100664.3	1.3
Air Face Velocity [m/s]	3.08	0.11	3.04	0.11	3.04	0.11	3.07	0.11	3.03	0.11	2.98	0.11
Front Tdb [C]	26.74	0.05	26.77	0.05	26.76	0.05	26.69	0.05	26.72	0.05	26.73	0.05
Front Twb [C]	16.12	0.05	16.08	0.07	16.08	0.05	16.16	0.05	16.10	0.06	16.09	0.05
Wfront [g/kg]	7.14	0.05	7.08	0.06	7.08	0.05	7.21	0.05	7.12	0.05	7.11	0.05
Back Tdb [C] Zeroed	23.04	0.05	21.60	0.05	20.70	0.05	21.73	0.05	20.46	0.05	18.88	0.05
Back Twb [C] Zeroed	15.75	0.05	15.36	0.05	15.26	0.04	15.44	0.05	15.29	0.05	15.08	0.04
Wback [g/kg]	8.23	0.04	8.39	0.05	8.65	0.04	8.42	0.04	8.78	0.05	9.20	0.04
Water Flow Rate [kg/s]	0.051	0.000	0.071	0.000	0.091	0.000	0.051	0.000	0.071	0.000	0.092	0.000
Water Inlet [C]	10.02	0.05	10.03	0.05	10.04	0.05	10.02	0.05	10.00	0.05	10.01	0.05
Water Outlet [C]	10.43	0.05	10.49	0.05	10.50	0.05	10.45	0.05	10.54	0.05	10.69	0.05
Calculated Measurements	Value	Error	Value	Error	Value	Error	Value	Error	Value	Error	Value	Error
Air Mass Flow Rate [kg/s]	0.083	0.003	0.083	0.003	0.083	0.003	0.083	0.003	0.083	0.003	0.082	0.003
Air Side Heat Transfer [W]	82.3	15.1	160.5	18.0	182.0	16.0	164.1	15.9	178.9	17.1	219.3	16.7
Air Side Sensible Heat Transfer [W]	314.7	19.1	435.4	24.4	511.1	24.1	421.7	21.7	526.9	25.6	652.8	28.7
Water Side Heat Transfer [W]	88.3	11.1	136.3	15.6	176.2	19.9	90.9	11.1	161.0	15.6	260.3	20.3
% difference	-6.8		17.8		3.3		80.6		11.1		-15.7	
Sensible UA Value CF [W/C]	21.6	0.8	31.6	1.1	38.5	1.2	30.4	0.9	40.2	1.1	53.9	1.5
LTMD [C]	14.60	0.05	13.79	0.05	13.26	0.05	13.85	0.05	13.11	0.05	12.10	0.05
Epsilon	0.059		0.116		0.131		0.118		0.129		0.160	
Fp	0.066		0.133		0.151		0.131		0.149		0.190	
Epsilon (sensible)	0.225		0.314		0.368		0.302		0.381		0.477	
Enthalpy In [kJ/kg]	45.09	0.13	44.99	0.16	44.97	0.13	45.22	0.13	45.04	0.15	45.01	0.13
Enthalpy Out [kJ/kg]	44.11	0.12	43.05	0.13	42.77	0.12	43.26	0.12	42.88	0.13	42.32	0.12
Air Specific Volume [m3/kg]	0.8581	0.0002	0.8544	0.0002	0.8525	0.0002	0.8550	0.0002	0.8519	0.0002	0.8480	0.0002

Test Information												
Date Tested:	1/14/07		1/14/07		1/14/07		1/14/07		1/14/07		1/14/07	
Nozzle:	2x 8005		2x 8005		2x 8005		2x8005		2x8005		2x8005	
Nozzle Area [m2]	3.18E-06		3.18E-06		3.18E-06		3.18E-06		3.18E-06		3.18E-06	
Nozzle Pressure [psi][Pa]	24.0	165474.2	49.0	337843.1	85.0	586054.4	24.0	165474.2	49.0	337843.1	85.0	586054.4
Measurements	Value	Error	Value	Error	Value	Error	Value	Error	Value	Error	Value	Error
Barometric Pressure [pa]	100664.3	1.3	100664.3	1.3	100664.3	1.3	100664.3	1.3	100664.3	1.3	100664.3	1.3
Air Face Velocity [m/s]	3.08	0.11	3.04	0.11	3.00	0.11	3.06	0.11	3.03	0.11	3.00	0.11
Front Tdb [C]	26.73	0.05	26.74	0.05	26.74	0.05	26.74	0.05	26.72	0.05	26.72	0.05
Front Twb [C]	16.18	0.08	16.07	0.06	16.05	0.06	16.07	0.06	16.04	0.06	16.02	0.06
Wfront [g/kg]	7.20	0.07	7.07	0.06	7.05	0.05	7.08	0.05	7.06	0.05	7.04	0.05
Back Tdb [C] Zeroed	21.53	0.06	19.73	0.05	17.73	0.05	21.27	0.05	19.09	0.05	16.70	0.05
Back Twb [C] Zeroed	15.57	0.06	15.16	0.05	14.78	0.05	14.92	0.05	14.26	0.05	13.42	0.04
Wback [g/kg]	8.66	0.06	8.94	0.05	9.34	0.04	8.03	0.04	8.21	0.04	8.31	0.04
Water Flow Rate [kg/s]	0.051	0.000	0.071	0.000	0.091	0.000	0.051	0.000	0.071	0.000	0.092	0.000
Water Inlet [C]	10.01	0.05	9.98	0.05	10.09	0.05	5.07	0.05	5.04	0.05	4.97	0.05
Water Outlet [C]	10.88	0.05	10.91	0.05	11.05	0.05	6.36	0.05	6.47	0.05	6.58	0.05
Calculated Measurements	Value	Error	Value	Error	Value	Error	Value	Error	Value	Error	Value	Error
Air Mass Flow Rate [kg/s]	0.084	0.003	0.083	0.003	0.083	0.003	0.083	0.003	0.083	0.003	0.083	0.003
Air Side Heat Transfer [W]	135.0	20.7	200.3	18.6	278.9	18.5	263.0	18.2	402.6	21.5	578.5	25.9
Air Side Sensible Heat Transfer [W]	443.5	26.9	593.3	28.2	757.4	32.6	464.2	23.7	644.5	29.1	845.1	35.1
Water Side Heat Transfer [W]	186.8	11.6	278.6	15.6	367.9	20.1	279.9	11.4	428.6	15.7	625.9	20.7
% difference	-27.7		-28.1		-24.2		-6.0		-6.1		-7.6	
Sensible UA Value CF [W/C]	32.7	1.1	47.3	1.3	67.7	1.7	25.5	0.7	38.0	1.0	54.3	1.3
LTMD [C]	13.57	0.05	12.54	0.05	11.19	0.05	18.21	0.05	16.96	0.05	15.56	0.05
Epsilon	0.096		0.144		0.202		0.145		0.223		0.320	
Fp	0.116		0.178		0.258		0.133		0.208		0.303	
Epsilon (sensible)	0.316		0.425		0.549		0.256		0.357		0.468	
Enthalpy In [kJ/kg]	45.26	0.18	44.94	0.15	44.89	0.14	44.95	0.14	44.88	0.15	44.81	0.14
Enthalpy Out [kJ/kg]	43.65	0.16	42.52	0.14	41.51	0.12	41.80	0.12	40.03	0.12	37.83	0.11
Air Specific Volume [m3/kg]	0.8547	0.0002	0.8501	0.0002	0.8451	0.0002	0.8529	0.0002	0.8473	0.0002	0.8408	0.0001

Test Information												
Date Tested:	1/15/07		1/15/07		1/15/07		1/15/07		1/15/07		1/15/07	
Nozzle:	8009		8009		8009		8015		8015		8015	
Nozzle Area [m2]	2.85E-06		2.85E-06		2.85E-06		4.48E-06		4.48E-06		4.48E-06	
Nozzle Pressure [psi][Pa]	30.0	206842.7	62.0	427475.0	105.0	723949.5	10.5	72395.0	22.0	151684.7	38.0	262000.8
Measurements	Value	Error	Value	Error	Value	Error	Value	Error	Value	Error	Value	Error
Barometric Pressure [pa]	100664.3	1.3	100664.3	1.3	100664.3	1.3	100664.3	1.3	100664.3	1.3	100664.3	1.3
Air Face Velocity [m/s]	3.06	0.11	3.02	0.11	2.99	0.11	3.07	0.11	3.05	0.11	3.02	0.11
Front Tdb [C]	26.71	0.05	26.72	0.05	26.70	0.05	26.71	0.05	26.75	0.05	26.74	0.05
Front Twb [C]	16.01	0.06	16.09	0.06	16.03	0.06	15.98	0.06	15.99	0.09	15.97	0.07
Wfront [g/kg]	7.03	0.05	7.11	0.05	7.05	0.06	6.99	0.06	6.98	0.08	6.96	0.07
Back Tdb [C] Zeroed	21.75	0.05	19.99	0.05	18.04	0.05	22.48	0.05	21.07	0.05	19.85	0.05
Back Twb [C] Zeroed	14.96	0.05	14.63	0.05	13.96	0.05	15.08	0.05	14.77	0.08	14.35	0.05
Wback [g/kg]	7.88	0.05	8.24	0.04	8.32	0.04	7.72	0.05	7.95	0.07	8.00	0.05
Water Flow Rate [kg/s]	0.050	0.000	0.071	0.000	0.092	0.000	0.050	0.000	0.071	0.000	0.092	0.000
Water Inlet [C]	4.99	0.05	5.04	0.05	5.00	0.05	5.08	0.05	5.08	0.05	4.99	0.05
Water Outlet [C]	5.82	0.05	6.04	0.05	6.20	0.05	6.04	0.05	6.09	0.05	5.99	0.05
Calculated Measurements	Value	Error	Value	Error	Value	Error	Value	Error	Value	Error	Value	Error
Air Mass Flow Rate [kg/s]	0.083	0.003	0.082	0.003	0.082	0.003	0.083	0.003	0.083	0.003	0.083	0.003
Air Side Heat Transfer [W]	238.7	18.0	330.1	19.6	460.1	23.3	204.6	18.5	277.3	25.2	363.1	22.2
Air Side Sensible Heat Transfer [W]	419.6	22.5	565.8	26.5	724.6	32.1	359.2	22.3	481.4	30.6	580.5	29.2
Water Side Heat Transfer [W]	174.6	11.0	295.1	15.6	463.0	20.2	204.1	11.0	300.4	15.5	383.2	20.3
% difference	36.7		11.9		-0.6		0.2		-7.7		-5.2	
Sensible UA Value CF [W/C]	22.4	0.7	32.0	0.9	44.0	1.2	18.9	0.7	26.4	0.9	32.9	1.0
LTMD [C]	18.75	0.05	17.66	0.05	16.49	0.05	18.99	0.05	18.23	0.05	17.64	0.05
Epsilon	0.132		0.184		0.257		0.113		0.153		0.201	
Fp	0.117		0.164		0.235		0.102		0.139		0.182	
Epsilon (sensible)	0.232		0.316		0.405		0.199		0.266		0.322	
Enthalpy In [kJ/kg]	44.78	0.14	45.02	0.14	44.83	0.15	44.69	0.15	44.71	0.21	44.66	0.17
Enthalpy Out [kJ/kg]	41.91	0.13	41.02	0.12	39.23	0.12	42.23	0.13	41.38	0.18	40.27	0.13
Air Specific Volume [m3/kg]	0.8545	0.0002	0.8501	0.0002	0.8451	0.0002	0.8564	0.0002	0.8526	0.0002	0.8494	0.0002

Test Information												
Date Tested:	1/16/07		1/16/07		1/16/07		1/18/07		1/18/07		1/18/07	
Nozzle:	8015		8015		8015		8009		8009		8009	
Nozzle Area [m2]	4.48E-06		4.48E-06		4.48E-06		2.85E-06		2.85E-06		2.85E-06	
Nozzle Pressure [psi][Pa]	10.5	72395.0	22.0	151684.7	38.0	262000.8	30.0	206842.7	62.0	427475.0	105.0	723949.5
Measurements	Value	Error	Value	Error	Value	Error	Value	Error	Value	Error	Value	Error
Barometric Pressure [pa]	100664.3	1.3	100664.3	1.3	100664.3	1.3	100664.3	1.3	100664.3	1.3	100664.3	1.3
Air Face Velocity [m/s]	0.99	0.11	0.98	0.11	0.97	0.11	0.99	0.11	0.98	0.11	0.95	0.11
Front Tdb [C]	26.76	0.05	26.72	0.05	26.66	0.05	26.77	0.05	26.69	0.05	26.72	0.05
Front Twb [C]	15.69	0.15	16.01	0.06	16.09	0.07	16.03	0.05	16.09	0.06	16.00	0.08
Wfront [g/kg]	6.63	0.12	7.02	0.05	7.14	0.06	7.02	0.05	7.12	0.05	7.02	0.07
Back Tdb [C] Zeroed	19.44	0.05	17.43	0.05	15.48	0.05	17.94	0.05	15.74	0.05	14.66	0.05
Back Twb [C] Zeroed	14.99	0.05	14.42	0.04	14.00	0.05	14.87	0.04	14.18	0.05	13.79	0.05
Wback [g/kg]	8.86	0.04	9.07	0.04	9.42	0.04	9.36	0.04	9.51	0.04	9.54	0.04
Water Flow Rate [kg/s]	0.050	0.000	0.071	0.000	0.092	0.000	0.050	0.000	0.071	0.000	0.091	0.000
Water Inlet [C]	9.96	0.05	9.88	0.05	9.93	0.05	9.94	0.05	9.95	0.05	10.03	0.05
Water Outlet [C]	10.48	0.05	10.40	0.05	10.46	0.05	10.62	0.05	10.64	0.05	10.68	0.05
Calculated Measurements	Value	Error	Value	Error	Value	Error	Value	Error	Value	Error	Value	Error
Air Mass Flow Rate [kg/s]	0.027	0.003	0.027	0.003	0.027	0.003	0.027	0.003	0.027	0.003	0.026	0.003
Air Side Heat Transfer [W]	48.7	10.5	114.7	13.2	150.4	17.2	83.0	10.0	137.5	15.7	153.8	18.0
Air Side Sensible Heat Transfer [W]	201.2	24.6	254.2	27.9	304.6	33.7	243.3	26.4	299.4	32.9	320.4	36.3
Water Side Heat Transfer [W]	110.3	11.0	153.3	15.5	204.3	20.0	143.8	11.0	206.9	15.5	250.2	19.9
% difference	-55.9		-25.2		-26.4		-42.3		-33.6		-38.5	
Sensible UA Value CF [W/C]	16.0	1.1	22.4	1.4	30.7	2.0	21.0	1.2	29.7	1.8	34.9	2.3
LTMD [C]	12.58	0.05	11.37	0.05	9.94	0.06	11.60	0.05	10.07	0.06	9.19	0.06
Epsilon	0.107		0.253		0.335		0.182		0.305		0.352	
Fp	0.129		0.293		0.385		0.218		0.361		0.426	
Epsilon (sensible)	0.442		0.560		0.679		0.533		0.664		0.733	
Enthalpy In [kJ/kg]	43.83	0.32	44.78	0.14	45.02	0.16	44.82	0.13	45.02	0.15	44.76	0.18
Enthalpy Out [kJ/kg]	42.03	0.12	40.51	0.12	39.39	0.11	41.75	0.12	39.89	0.11	38.87	0.12
Air Specific Volume [m3/kg]	0.8536	0.0002	0.8498	0.0002	0.8465	0.0002	0.8514	0.0002	0.8478	0.0002	0.8462	0.0002

Test Information												
Date Tested:	1/18/07		1/18/07		1/18/07		1/20/07		1/20/07		1/20/07	
Nozzle:	2x8005		2x8005		2x8005		8015		8015		8015	
Nozzle Area [m2]	3.18E-06		3.18E-06		3.18E-06		4.48E-06		4.48E-06		4.48E-06	
Nozzle Pressure [psi][Pa]	24.0	165474.2	49.0	337843.1	85.0	586054.4	10.5	72395.0	22.0	151684.7	38.0	262000.8
Measurements	Value	Error	Value	Error	Value	Error	Value	Error	Value	Error	Value	Error
Barometric Pressure [pa]	100664.3	1.3	100664.3	1.3	100664.3	1.3	100664.3	1.3	100664.3	1.3	100664.3	1.3
Air Face Velocity [m/s]	1.00	0.11	0.98	0.11	0.99	0.11	1.00	0.11	0.99	0.11	0.98	0.11
Front Tdb [C]	26.68	0.05	26.69	0.05	26.71	0.05	26.72	0.05	26.73	0.05	26.76	0.05
Front Twb [C]	15.98	0.07	16.08	0.07	15.88	0.10	16.03	0.06	15.98	0.05	16.03	0.06
Wfront [g/kg]	7.00	0.06	7.12	0.06	6.87	0.09	7.04	0.05	6.98	0.05	7.02	0.05
Back Tdb [C] Zeroed	16.20	0.05	14.44	0.05	12.99	0.05	17.78	0.05	15.86	0.05	13.75	0.05
Back Twb [C] Zeroed	14.31	0.05	13.62	0.05	12.87	0.05	13.99	0.04	13.23	0.04	12.47	0.04
Wback [g/kg]	9.46	0.04	9.44	0.04	9.26	0.04	8.47	0.04	8.45	0.04	8.54	0.04
Water Flow Rate [kg/s]	0.051	0.000	0.071	0.000	0.092	0.000	0.051	0.000	0.071	0.000	0.092	0.000
Water Inlet [C]	9.93	0.05	9.96	0.05	10.02	0.05	5.01	0.05	5.05	0.05	4.97	0.05
Water Outlet [C]	10.66	0.05	10.67	0.05	10.71	0.05	5.54	0.05	5.65	0.05	5.61	0.05
Calculated Measurements	Value	Error	Value	Error	Value	Error	Value	Error	Value	Error	Value	Error
Air Mass Flow Rate [kg/s]	0.027	0.003	0.027	0.003	0.027	0.003	0.027	0.003	0.027	0.003	0.027	0.003
Air Side Heat Transfer [W]	122.1	14.0	178.2	20.0	217.0	24.4	150.2	16.6	199.3	21.9	253.0	28.0
Air Side Sensible Heat Transfer [W]	291.9	31.6	337.3	36.9	381.9	42.0	248.4	26.8	300.6	32.6	356.4	39.2
Water Side Heat Transfer [W]	154.4	11.1	209.1	15.5	264.4	20.0	112.1	11.1	180.0	16.0	249.9	20.3
% difference	-20.9		-14.7		-17.9		34.0		10.7		1.3	
Sensible UA Value CF [W/C]	28.1	1.6	37.2	2.2	49.4	3.0	14.9	0.9	19.6	1.2	25.3	1.6
LTMD [C]	10.39	0.06	9.05	0.06	7.73	0.07	16.62	0.05	15.37	0.05	14.07	0.05
Epsilon	0.266		0.393		0.474		0.253		0.338		0.431	
Fp	0.323		0.469		0.594		0.219		0.296		0.376	
Epsilon (sensible)	0.636		0.744		0.835		0.418		0.509		0.606	
Enthalpy In [kJ/kg]	44.69	0.16	44.99	0.16	44.39	0.23	44.84	0.14	44.68	0.13	44.82	0.14
Enthalpy Out [kJ/kg]	40.22	0.12	38.39	0.11	36.44	0.11	39.33	0.11	37.34	0.11	35.41	0.11
Air Specific Volume [m3/kg]	0.8487	0.0002	0.8457	0.0002	0.8413	0.0002	0.8506	0.0001	0.8468	0.0002	0.8436	0.0002

Test Information												
Date Tested:	1/20/07		1/20/07		1/20/07		1/20/07		1/20/07		1/20/07	
Nozzle:	8009		8009		8009		2x8005		2x8005		2x8005	
Nozzle Area [m2]	2.85E-06		2.85E-06		2.85E-06		3.18E-06		3.18E-06		3.18E-06	
Nozzle Pressure [psi][Pa]	30.0	206842.7	62.0	427475.0	105.0	723949.5	24.0	165474.2	49.0	337843.1	85.0	586054.4
Measurements	Value	Error	Value	Error	Value	Error	Value	Error	Value	Error	Value	Error
Barometric Pressure [pa]	100664.3	1.3	100664.3	1.3	100664.3	1.3	100664.3	1.3	100664.3	1.3	100664.3	1.3
Air Face Velocity [m/s]	1.00	0.11	0.98	0.11	0.94	0.11	1.00	0.11	0.98	0.11	0.98	0.11
Front Tdb [C]	26.70	0.05	26.67	0.05	26.74	0.05	26.74	0.05	26.66	0.05	26.62	0.05
Front Twb [C]	16.45	0.08	15.96	0.10	16.02	0.07	16.05	0.06	15.96	0.08	16.14	0.07
Wfront [g/kg]	7.54	0.07	6.98	0.09	7.03	0.06	7.05	0.06	6.99	0.07	7.21	0.06
Back Tdb [C] Zeroed	16.36	0.05	13.54	0.05	12.24	0.05	15.30	0.05	12.68	0.05	10.68	0.05
Back Twb [C] Zeroed	13.96	0.05	12.45	0.05	11.76	0.05	13.56	0.04	12.12	0.05	10.86	0.04
Wback [g/kg]	9.01	0.04	8.60	0.04	8.45	0.04	9.02	0.04	8.63	0.04	8.22	0.04
Water Flow Rate [kg/s]	0.051	0.000	0.071	0.000	0.092	0.000	0.050	0.000	0.071	0.000	0.091	0.000
Water Inlet [C]	4.95	0.05	4.89	0.05	5.01	0.05	5.07	0.05	5.03	0.05	5.06	0.05
Water Outlet [C]	5.71	0.05	5.69	0.05	5.79	0.05	6.25	0.05	6.24	0.05	6.25	0.05
Calculated Measurements	Value	Error	Value	Error	Value	Error	Value	Error	Value	Error	Value	Error
Air Mass Flow Rate [kg/s]	0.027	0.003	0.027	0.003	0.026	0.003	0.027	0.003	0.027	0.003	0.027	0.003
Air Side Heat Transfer [W]	185.7	20.8	249.5	28.1	291.6	33.3	182.7	20.1	274.7	30.3	372.6	41.1
Air Side Sensible Heat Transfer [W]	287.3	31.5	359.8	40.2	385.5	43.8	319.6	34.5	386.9	42.5	441.8	48.7
Water Side Heat Transfer [W]	162.4	11.1	237.6	15.6	300.4	20.4	250.2	11.1	359.8	15.8	454.4	20.1
% difference	14.3		5.0		-2.9		-27.0		-23.7		-18.0	
Sensible UA Value CF [W/C]	18.3	1.1	25.9	1.6	29.9	1.9	21.6	1.2	29.7	1.7	38.6	2.3
LTMD [C]	15.71	0.05	13.91	0.06	12.90	0.06	14.78	0.05	13.01	0.06	11.46	0.06
Epsilon	0.312		0.425		0.513		0.306		0.466		0.633	
Fp	0.261		0.376		0.454		0.280		0.430		0.571	
Epsilon (sensible)	0.483		0.612		0.678		0.536		0.657		0.751	
Enthalpy In [kJ/kg]	46.08	0.20	44.63	0.23	44.81	0.16	44.88	0.15	44.64	0.18	45.16	0.16
Enthalpy Out [kJ/kg]	39.27	0.12	35.35	0.12	33.64	0.11	38.22	0.11	34.52	0.11	31.46	0.10
Air Specific Volume [m3/kg]	0.8483	0.0002	0.8427	0.0002	0.8406	0.0002	0.8460	0.0001	0.8406	0.0002	0.8354	0.0001

Test Information												
Date Tested:	1/21/07		1/21/07		1/21/07		1/21/07		1/21/07		1/21/07	
Nozzle:	8015		8015		8015		8009		8009		8009	
Nozzle Area [m2]	4.48E-06		4.48E-06		4.48E-06		2.85E-06		2.85E-06		2.85E-06	
Nozzle Pressure [psi][Pa]	10.5	72395.0	22.0	151684.7	38.0	262000.8	30.0	206842.7	62.0	427475.0	105.0	723949.5
Measurements	Value	Error	Value	Error	Value	Error	Value	Error	Value	Error	Value	Error
Barometric Pressure [pa]	99555.6	1.3	99555.6	1.3	99555.6	1.3	99555.6	1.3	99555.6	1.3	99555.6	1.3
Air Face Velocity [m/s]	3.07	0.11	3.04	0.11	3.01	0.11	3.04	0.11	2.99	0.11	2.94	0.11
Front Tdb [C]	32.98	0.05	32.99	0.05	33.02	0.05	32.97	0.05	32.96	0.05	32.97	0.05
Front Twb [C]	20.63	0.06	20.58	0.06	20.50	0.06	20.62	0.05	20.49	0.06	20.57	0.06
Wfront [g/kg]	10.41	0.07	10.34	0.06	10.22	0.07	10.40	0.06	10.23	0.06	10.33	0.07
Back Tdb [C] Zeroed	28.32	0.05	26.79	0.05	25.27	0.05	27.30	0.05	24.43	0.05	21.87	0.05
Back Twb [C] Zeroed	19.61	0.05	19.25	0.05	18.77	0.05	19.30	0.05	18.70	0.05	18.01	0.05
Wback [g/kg]	10.96	0.06	11.12	0.05	11.12	0.06	10.97	0.05	11.38	0.05	11.56	0.05
Water Flow Rate [kg/s]	0.051	0.000	0.070	0.000	0.092	0.000	0.050	0.000	0.072	0.000	0.092	0.000
Water Inlet [C]	10.04	0.05	9.91	0.05	10.00	0.05	9.94	0.05	10.01	0.05	10.02	0.05
Water Outlet [C]	10.60	0.05	10.64	0.05	10.70	0.05	10.67	0.05	10.97	0.05	11.26	0.05
Calculated Measurements	Value	Error	Value	Error	Value	Error	Value	Error	Value	Error	Value	Error
Air Mass Flow Rate [kg/s]	0.080	0.003	0.080	0.003	0.080	0.003	0.080	0.003	0.079	0.003	0.079	0.003
Air Side Heat Transfer [W]	271.7	21.5	350.4	21.3	450.7	25.2	347.8	21.0	462.1	24.2	649.1	29.8
Air Side Sensible Heat Transfer [W]	384.4	24.8	508.8	26.1	633.4	31.1	465.0	24.8	694.2	31.7	895.7	38.6
Water Side Heat Transfer [W]	118.3	11.1	215.9	15.3	269.1	20.2	154.8	11.1	285.3	15.7	480.2	21.0
% difference	129.7		62.3		67.5		124.7		61.9		35.2	
Sensible UA Value CF [W/C]	19.0	0.7	26.1	0.8	34.1	1.0	23.6	0.7	38.7	1.0	55.0	1.4
LTMD [C]	20.27	0.05	19.49	0.05	18.57	0.05	19.73	0.05	17.94	0.05	16.28	0.05
Epsilon	0.147		0.189		0.245		0.188		0.253		0.358	
Fp	0.116		0.152		0.199		0.150		0.210		0.303	
Epsilon (sensible)	0.208		0.274		0.344		0.251		0.380		0.494	
Enthalpy In [kJ/kg]	59.84	0.18	59.67	0.16	59.38	0.19	59.79	0.16	59.35	0.17	59.61	0.18
Enthalpy Out [kJ/kg]	56.47	0.15	55.29	0.14	53.73	0.15	55.45	0.14	53.53	0.14	51.37	0.13
Air Specific Volume [m3/kg]	0.8849	0.0002	0.8807	0.0002	0.8770	0.0002	0.8821	0.0002	0.8749	0.0002	0.8685	0.0002

Test Information												
Date Tested:	1/21/07		1/21/07		1/21/07		1/25/07		1/25/07		1/25/07	
Nozzle:	2X 8005		2X 8005		2X 8005		8015		8015		8015	
Nozzle Area [m2]	3.18E-06		3.18E-06		3.18E-06		4.48E-06		4.48E-06		4.48E-06	
Nozzle Pressure [psi][Pa]	24.0	165474.2	49.0	337843.1	85.0	586054.4	10.5	72395.0	22.0	151684.7	38.0	262000.8
Measurements	Value	Error	Value	Error	Value	Error	Value	Error	Value	Error	Value	Error
Barometric Pressure [pa]	99555.6	1.3	99555.6	1.3	99555.6	1.3	100781.3	1.3	100781.3	1.3	100781.3	1.3
Air Face Velocity [m/s]	3.05	0.11	3.02	0.11	2.99	0.11	3.07	0.11	3.04	0.11	3.01	0.11
Front Tdb [C]	32.98	0.05	33.00	0.05	32.97	0.05	33.04	0.05	33.08	0.05	33.04	0.05
Front Twb [C]	20.44	0.05	20.49	0.05	20.47	0.05	20.47	0.05	20.59	0.05	20.55	0.05
Wfront [g/kg]	10.15	0.06	10.20	0.06	10.20	0.06	9.98	0.06	10.12	0.06	10.09	0.06
Back Tdb [C] Zeroed	26.04	0.05	23.77	0.05	20.94	0.05	27.90	0.05	26.39	0.05	24.77	0.05
Back Twb [C] Zeroed	18.80	0.05	18.38	0.04	17.62	0.04	19.19	0.05	18.98	0.05	18.49	0.05
Wback [g/kg]	10.84	0.05	11.25	0.05	11.47	0.05	10.39	0.05	10.76	0.05	10.80	0.05
Water Flow Rate [kg/s]	0.050	0.000	0.071	0.000	0.093	0.000	0.050	0.000	0.071	0.000	0.092	0.000
Water Inlet [C]	9.97	0.05	10.01	0.05	10.05	0.05	5.04	0.05	5.08	0.05	5.00	0.05
Water Outlet [C]	11.41	0.05	11.53	0.05	11.72	0.05	6.36	0.05	6.54	0.05	6.45	0.05
Calculated Measurements	Value	Error	Value	Error	Value	Error	Value	Error	Value	Error	Value	Error
Air Mass Flow Rate [kg/s]	0.081	0.003	0.080	0.003	0.080	0.003	0.082	0.003	0.081	0.003	0.081	0.003
Air Side Heat Transfer [W]	430.0	22.8	546.4	25.7	729.9	31.5	342.9	20.6	425.2	22.8	539.2	25.6
Air Side Sensible Heat Transfer [W]	572.9	27.4	759.6	32.8	987.6	40.6	429.9	23.5	556.8	27.0	686.6	30.7
Water Side Heat Transfer [W]	304.4	11.2	453.0	15.6	647.6	20.4	278.6	11.1	434.2	15.8	562.0	20.5
% difference	41.3		20.6		12.7		23.1		-2.1		-4.1	
Sensible UA Value CF [W/C]	30.7	0.8	43.8	1.1	63.7	1.5	17.4	0.5	23.4	0.7	29.8	0.8
LTMD [C]	18.68	0.05	17.33	0.05	15.49	0.05	24.71	0.05	23.82	0.05	23.01	0.05
Epsilon	0.231		0.295		0.396		0.150		0.186		0.237	
Fp	0.202		0.259		0.355		0.112		0.139		0.177	
Epsilon (sensible)	0.308		0.410		0.536		0.187		0.244		0.301	
Enthalpy In [kJ/kg]	59.16	0.16	59.33	0.16	59.28	0.16	58.78	0.15	59.20	0.16	59.07	0.16
Enthalpy Out [kJ/kg]	53.83	0.13	52.53	0.13	50.17	0.13	54.59	0.13	53.97	0.14	52.41	0.13
Air Specific Volume [m3/kg]	0.8786	0.0002	0.8729	0.0002	0.8657	0.0002	0.8725	0.0002	0.8685	0.0002	0.8645	0.0002

Test Information												
Date Tested:	1/23/07		1/23/07		1/23/07		1/22/07		1/22/07		1/22/07	
Nozzle:	8009		8009		8009		2x 8005		2x 8005		2x 8005	
Nozzle Area [m2]	2.85E-06		2.85E-06		2.85E-06		3.18E-06		3.18E-06		3.18E-06	
Nozzle Pressure [psi][Pa]	30.0	206842.7	62.0	427475.0	105.0	723949.5	24.0	165474.2	49.0	337843.1	85.0	586054.4
Measurements	Value	Error	Value	Error	Value	Error	Value	Error	Value	Error	Value	Error
Barometric Pressure [pa]	100088.0	1.3	100088.0	1.3	100088.0	1.3	100088.0	1.3	100088.0	1.3	100088.0	1.3
Air Face Velocity [m/s]	3.05	0.11	2.99	0.11	2.95	0.11	3.05	0.11	3.02	0.11	2.99	0.11
Front Tdb [C]	33.02	0.05	33.01	0.05	33.04	0.05	32.99	0.05	32.96	0.05	32.98	0.05
Front Twb [C]	20.63	0.05	20.44	0.05	20.61	0.05	20.48	0.05	20.62	0.05	20.63	0.05
Wfront [g/kg]	10.30	0.06	10.06	0.06	10.27	0.06	10.12	0.06	10.32	0.06	10.32	0.06
Back Tdb [C] Zeroed	27.32	0.05	24.07	0.05	21.39	0.05	25.89	0.05	23.58	0.05	20.12	0.05
Back Twb [C] Zeroed	19.31	0.05	18.40	0.04	17.49	0.05	18.71	0.05	18.12	0.05	16.85	0.04
Wback [g/kg]	10.90	0.05	11.07	0.05	11.05	0.05	10.71	0.05	10.92	0.05	10.80	0.04
Water Flow Rate [kg/s]	0.051	0.000	0.071	0.000	0.092	0.000	0.051	0.000	0.071	0.000	0.093	0.000
Water Inlet [C]	5.06	0.05	5.12	0.05	5.08	0.05	5.07	0.05	5.04	0.05	5.03	0.05
Water Outlet [C]	6.73	0.05	6.91	0.05	7.11	0.05	6.95	0.05	7.03	0.05	7.42	0.05
Calculated Measurements	Value	Error	Value	Error	Value	Error	Value	Error	Value	Error	Value	Error
Air Mass Flow Rate [kg/s]	0.081	0.003	0.080	0.003	0.079	0.003	0.081	0.003	0.081	0.003	0.081	0.003
Air Side Heat Transfer [W]	348.6	21.1	525.3	24.9	790.3	33.6	467.6	23.5	652.4	29.0	968.2	39.1
Air Side Sensible Heat Transfer [W]	471.6	24.7	731.7	31.8	947.8	39.6	590.5	27.5	777.2	33.6	1066.1	43.1
Water Side Heat Transfer [W]	356.4	11.3	535.4	15.7	784.7	20.6	402.2	11.3	595.2	15.8	931.4	20.6
% difference	-2.2		-1.9		0.7		16.3		9.6		3.9	
Sensible UA Value CF [W/C]	19.5	0.6	32.8	0.8	45.7	1.1	25.3	0.6	35.3	0.8	53.7	1.2
LTMD [C]	24.22	0.05	22.34	0.05	20.75	0.05	23.34	0.05	22.03	0.05	19.87	0.05
Epsilon	0.154		0.235		0.355		0.205		0.288		0.427	
Fp	0.115		0.180		0.272		0.157		0.219		0.332	
Epsilon (sensible)	0.208		0.327		0.426		0.260		0.343		0.470	
Enthalpy In [kJ/kg]	59.60	0.16	58.96	0.15	59.54	0.16	59.09	0.15	59.58	0.16	59.61	0.16
Enthalpy Out [kJ/kg]	55.28	0.14	52.39	0.13	49.59	0.13	53.34	0.13	51.51	0.13	47.64	0.12
Air Specific Volume [m3/kg]	0.8767	0.0002	0.8688	0.0002	0.8619	0.0002	0.8728	0.0002	0.8669	0.0002	0.8581	0.0002

Test Information												
Date Tested:	1/26/07		1/26/07		1/26/07		1/26/07		1/26/07		1/26/07	
Nozzle:	8015		8015		8015		8009		8009		8009	
Nozzle Area [m2]	4.48E-06		4.48E-06		4.48E-06		2.85E-06		2.85E-06		2.85E-06	
Nozzle Pressure [psi][Pa]	10.0	68947.6	22.0	151684.7	38.0	262000.8	30.0	206842.7	62.0	427475.0	105.0	723949.5
Measurements	Value	Error	Value	Error	Value	Error	Value	Error	Value	Error	Value	Error
Barometric Pressure [pa]	99462.3	1.3	99462.3	1.3	99462.3	1.3	99462.3	1.3	99462.3	1.3	99462.3	1.3
Air Face Velocity [m/s]	0.98	0.10	0.97	0.10	0.96	0.11	0.97	0.11	0.96	0.11	0.94	0.11
Front Tdb [C]	33.01	0.05	33.01	0.05	32.94	0.05	32.96	0.05	32.94	0.05	32.99	0.05
Front Twb [C]	20.46	0.07	20.47	0.08	20.51	0.08	20.48	0.07	20.45	0.08	20.53	0.07
Wfront [g/kg]	10.18	0.08	10.20	0.09	10.27	0.09	10.23	0.08	10.19	0.09	10.29	0.08
Back Tdb [C] Zeroed	24.54	0.05	21.85	0.05	18.97	0.05	20.90	0.05	17.79	0.05	16.45	0.05
Back Twb [C] Zeroed	18.86	0.05	18.02	0.05	16.98	0.05	18.00	0.06	16.32	0.05	15.70	0.04
Wback [g/kg]	11.55	0.05	11.60	0.05	11.51	0.05	11.96	0.06	11.21	0.05	11.05	0.04
Water Flow Rate [kg/s]	0.050	0.000	0.071	0.000	0.092	0.000	0.050	0.000	0.071	0.000	0.093	0.000
Water Inlet [C]	10.06	0.05	9.99	0.05	9.99	0.05	9.99	0.05	10.04	0.05	9.92	0.05
Water Outlet [C]	10.87	0.05	10.88	0.05	10.93	0.05	11.17	0.05	11.15	0.05	11.05	0.05
Calculated Measurements	Value	Error	Value	Error	Value	Error	Value	Error	Value	Error	Value	Error
Air Mass Flow Rate [kg/s]	0.026	0.003	0.026	0.003	0.026	0.003	0.026	0.003	0.026	0.003	0.025	0.003
Air Side Heat Transfer [W]	134.9	15.7	202.9	23.0	285.4	32.2	205.2	23.2	331.7	37.2	380.6	43.2
Air Side Sensible Heat Transfer [W]	225.6	25.1	294.7	33.0	365.9	41.2	319.0	35.4	398.5	44.7	429.5	48.8
Water Side Heat Transfer [W]	172.8	11.0	266.7	15.6	361.4	20.1	248.2	10.9	329.3	15.6	441.5	20.6
% difference	-21.9		-23.9		-21.0		-17.3		0.7		-13.8	
Sensible UA Value CF [W/C]	12.5	0.8	17.9	1.1	25.2	1.6	20.3	1.2	29.3	1.7	33.8	2.1
LTMD [C]	18.04	0.05	16.46	0.05	14.54	0.06	15.73	0.05	13.58	0.06	12.71	0.06
Epsilon	0.226		0.341		0.485		0.345		0.562		0.649	
Fp	0.187		0.283		0.402		0.293		0.479		0.546	
Epsilon (sensible)	0.377		0.495		0.622		0.536		0.676		0.732	
Enthalpy In [kJ/kg]	59.28	0.20	59.32	0.22	59.44	0.23	59.34	0.21	59.22	0.23	59.53	0.20
Enthalpy Out [kJ/kg]	54.09	0.13	51.45	0.14	48.28	0.13	51.40	0.16	46.30	0.13	44.52	0.12
Air Specific Volume [m3/kg]	0.8785	0.0002	0.8734	0.0002	0.8684	0.0002	0.8728	0.0002	0.8660	0.0002	0.8632	0.0002

Test Information												
Date Tested:	1/27/07		1/27/07		1/27/07		1/28/07		1/28/07		1/28/07	
Nozzle:	2x 8005		2x 8005		2x 8005		8015		8015		8015	
Nozzle Area [m2]	3.18E-06		3.18E-06		3.18E-06		4.48E-06		4.48E-06		4.48E-06	
Nozzle Pressure [psi][Pa]	24.0	165474.2	49.0	337843.1	85.0	586054.4	10.5	72395.0	22.0	151684.7	38.0	262000.8
Measurements	Value	Error	Value	Error	Value	Error	Value	Error	Value	Error	Value	Error
Barometric Pressure [pa]	100101.3	1.3	100101.3	1.3	100101.3	1.3	100501.3	1.3	100501.3	1.3	100501.3	1.3
Air Face Velocity [m/s]	0.98	0.11	0.97	0.11	0.96	0.11	0.99	0.11	0.98	0.11	0.97	0.11
Front Tdb [C]	33.04	0.05	32.98	0.05	32.97	0.05	32.99	0.05	33.03	0.05	32.98	0.05
Front Twb [C]	20.57	0.09	20.75	0.07	20.72	0.07	20.47	0.06	20.48	0.12	20.67	0.07
Wfront [g/kg]	10.21	0.10	10.49	0.07	10.45	0.08	10.04	0.06	10.04	0.13	10.32	0.08
Back Tdb [C] Zeroed	19.82	0.05	17.34	0.05	15.25	0.05	22.00	0.05	19.44	0.05	16.97	0.05
Back Twb [C] Zeroed	16.98	0.05	15.94	0.05	14.83	0.05	16.75	0.05	15.73	0.06	14.75	0.05
Wback [g/kg]	11.08	0.05	10.89	0.04	10.49	0.04	9.85	0.04	9.72	0.06	9.64	0.04
Water Flow Rate [kg/s]	0.051	0.000	0.070	0.000	0.093	0.000	0.051	0.000	0.071	0.000	0.092	0.000
Water Inlet [C]	9.92	0.05	9.93	0.05	10.03	0.05	4.99	0.05	4.85	0.05	4.98	0.05
Water Outlet [C]	10.92	0.05	11.01	0.05	11.10	0.05	6.18	0.05	6.09	0.05	6.21	0.05
Calculated Measurements	Value	Error	Value	Error	Value	Error	Value	Error	Value	Error	Value	Error
Air Mass Flow Rate [kg/s]	0.026	0.003	0.026	0.003	0.026	0.003	0.027	0.003	0.027	0.003	0.027	0.003
Air Side Heat Transfer [W]	300.4	33.1	394.9	43.5	473.7	52.7	314.0	33.7	393.4	43.3	481.7	52.8
Air Side Sensible Heat Transfer [W]	358.4	39.7	421.6	46.5	476.0	53.1	301.3	32.6	372.0	41.8	435.9	48.0
Water Side Heat Transfer [W]	215.6	11.3	317.6	15.4	413.6	20.4	257.0	11.3	374.1	15.7	474.9	20.4
% difference	39.3		24.3		14.5		22.2		5.2		1.4	
Sensible UA Value CF [W/C]	23.6	1.4	31.5	1.8	41.0	2.5	14.0	0.8	18.5	1.1	23.7	1.4
LTMD [C]	15.20	0.05	13.40	0.06	11.62	0.06	21.54	0.05	20.14	0.05	18.40	0.05
Epsilon	0.489		0.650		0.785		0.418		0.521		0.646	
Fp	0.407		0.532		0.648		0.309		0.386		0.470	
Epsilon (sensible)	0.584		0.693		0.789		0.401		0.493		0.584	
Enthalpy In [kJ/kg]	59.39	0.26	60.03	0.19	59.93	0.21	58.89	0.17	58.94	0.33	59.60	0.21
Enthalpy Out [kJ/kg]	48.04	0.14	45.01	0.13	41.87	0.12	47.17	0.12	44.21	0.15	41.47	0.12
Air Specific Volume [m3/kg]	0.8624	0.0002	0.8574	0.0002	0.8522	0.0002	0.8610	0.0002	0.8559	0.0002	0.8514	0.0002

Test Information												
Date Tested:	1/28/07		1/28/07		1/28/07		1/27/07		1/27/07		1/27/07	
Nozzle:	8009		8009		8009		2x 8005		2x 8005		2x 8005	
Nozzle Area [m2]	2.85E-06		2.85E-06		2.85E-06		3.18E-06		3.18E-06		3.18E-06	
Nozzle Pressure [psi][Pa]	30.0	206842.7	62.0	427475.0	105.0	723949.5	24.0	165474.2	49.0	337843.1	85.0	586054.4
Measurements	Value	Error	Value	Error	Value	Error	Value	Error	Value	Error	Value	Error
Barometric Pressure [pa]	100501.3	1.3	100501.3	1.3	100501.3	1.3	100101.3	1.3	100101.3	1.3	100101.3	1.3
Air Face Velocity [m/s]	0.98	0.11	0.97	0.11	0.94	0.11	0.99	0.11	0.98	0.11	0.97	0.11
Front Tdb [C]	32.97	0.05	33.05	0.05	33.03	0.05	32.98	0.05	32.99	0.05	32.99	0.05
Front Twb [C]	20.54	0.09	20.30	0.06	20.49	0.06	20.51	0.07	20.52	0.07	20.54	0.07
Wfront [g/kg]	10.15	0.09	9.78	0.07	10.04	0.06	10.16	0.07	10.16	0.08	10.20	0.08
Back Tdb [C] Zeroed	19.50	0.05	16.39	0.05	14.50	0.05	18.20	0.05	15.00	0.05	12.71	0.05
Back Twb [C] Zeroed	16.23	0.05	14.58	0.05	13.45	0.04	15.69	0.04	13.90	0.05	12.46	0.04
Wback [g/kg]	10.27	0.05	9.70	0.04	9.26	0.04	10.23	0.04	9.56	0.04	9.01	0.04
Water Flow Rate [kg/s]	0.052	0.000	0.071	0.000	0.093	0.000	0.050	0.000	0.071	0.000	0.093	0.000
Water Inlet [C]	5.01	0.05	5.02	0.05	4.93	0.05	5.00	0.05	4.98	0.05	5.02	0.05
Water Outlet [C]	6.59	0.05	6.57	0.05	6.44	0.05	6.37	0.05	6.37	0.05	6.45	0.05
Calculated Measurements	Value	Error	Value	Error	Value	Error	Value	Error	Value	Error	Value	Error
Air Mass Flow Rate [kg/s]	0.027	0.003	0.026	0.003	0.026	0.003	0.027	0.003	0.027	0.003	0.027	0.003
Air Side Heat Transfer [W]	357.2	39.2	456.6	50.2	542.2	61.2	401.0	43.2	531.3	58.1	630.4	69.9
Air Side Sensible Heat Transfer [W]	365.9	40.5	451.2	49.8	491.0	55.6	405.7	43.9	490.9	53.9	550.8	61.3
Water Side Heat Transfer [W]	340.5	11.4	461.0	15.7	591.1	20.7	289.9	11.0	418.5	15.8	557.5	20.8
% difference	4.9		-1.0		-8.3		38.3		26.9		13.1	
Sensible UA Value CF [W/C]	18.4	1.1	25.2	1.5	29.5	1.8	21.2	1.2	28.9	1.7	36.2	2.1
LTMD [C]	19.84	0.05	17.87	0.05	16.66	0.06	19.13	0.05	16.99	0.06	15.22	0.06
Epsilon	0.481		0.614		0.743		0.533		0.710		0.847	
Fp	0.360		0.473		0.560		0.396		0.528		0.631	
Epsilon (sensible)	0.492		0.607		0.673		0.539		0.656		0.740	
Enthalpy In [kJ/kg]	59.14	0.25	58.28	0.17	58.94	0.16	59.20	0.19	59.22	0.21	59.31	0.21
Enthalpy Out [kJ/kg]	45.67	0.13	41.03	0.12	38.00	0.11	44.23	0.12	39.28	0.12	35.53	0.11
Air Specific Volume [m3/kg]	0.8568	0.0002	0.8504	0.0002	0.8467	0.0002	0.8583	0.0002	0.8514	0.0002	0.8458	0.0002

Test Information												
Date Tested:	1/29/07		1/29/07		1/29/07		1/29/07		1/29/07		1/29/07	
Nozzle:	8015		8015		8015		8015		8015		8015	
Nozzle Area [m2]	4.48E-06		4.48E-06		4.48E-06		4.48E-06		4.48E-06		4.48E-06	
Nozzle Pressure [psi][Pa]	10.5	72395.0	22.0	151684.7	38.0	262000.8	10.5	72395.0	22.0	151684.7	38.0	262000.8
Measurements	Value	Error	Value	Error	Value	Error	Value	Error	Value	Error	Value	Error
Barometric Pressure [pa]	100061.3	1.3	100061.3	1.3	100061.3	1.3	100061.3	1.3	100061.3	1.3	100061.3	1.3
Air Face Velocity [m/s]	3.05	0.11	3.03	0.11	3.01	0.11	3.05	0.11	3.02	0.11	3.00	0.11
Front Tdb [C]	26.71	0.05	26.70	0.05	26.72	0.05	26.65	0.05	26.74	0.05	26.71	0.05
Front Twb [C]	22.18	0.05	22.21	0.05	22.15	0.05	20.17	0.05	20.29	0.05	20.30	0.05
Wfront [g/kg]	15.17	0.06	15.22	0.06	15.11	0.06	12.33	0.06	12.46	0.06	12.49	0.06
Back Tdb [C] Zeroed	24.19	0.05	23.61	0.05	22.79	0.05	23.83	0.05	22.92	0.05	22.15	0.05
Back Twb [C] Zeroed	21.24	0.04	21.08	0.04	20.65	0.04	19.43	0.04	19.31	0.04	19.01	0.05
Wback [g/kg]	14.85	0.05	14.88	0.05	14.62	0.05	12.51	0.05	12.73	0.05	12.67	0.05
Water Flow Rate [kg/s]	0.051	0.000	0.071	0.000	0.094	0.000	0.051	0.000	0.071	0.000	0.092	0.000
Water Inlet [C]	10.05	0.05	10.08	0.05	10.09	0.06	10.01	0.05	10.00	0.05	10.04	0.05
Water Outlet [C]	11.28	0.05	11.36	0.05	11.31	0.05	10.99	0.05	11.03	0.05	11.05	0.05
Calculated Measurements	Value	Error	Value	Error	Value	Error	Value	Error	Value	Error	Value	Error
Air Mass Flow Rate [kg/s]	0.081	0.003	0.081	0.003	0.080	0.003	0.081	0.003	0.081	0.003	0.080	0.003
Air Side Heat Transfer [W]	277.2	20.4	326.8	21.1	427.8	23.3	198.7	18.0	259.8	19.0	340.0	20.6
Air Side Sensible Heat Transfer [W]	211.1	20.5	257.1	20.9	326.8	22.2	236.0	19.5	316.5	21.1	376.8	22.3
Water Side Heat Transfer [W]	260.6	11.1	382.8	15.7	479.7	23.1	208.6	11.1	308.0	15.6	389.7	20.1
% difference	6.4		-14.6		-10.8		-4.8		-15.7		-12.8	
Sensible UA Value CF [W/C]	14.3	0.8	17.8	0.9	23.3	1.1	16.0	0.8	22.2	0.9	27.3	1.1
LTMD [C]	14.77	0.05	14.42	0.05	14.01	0.05	14.72	0.05	14.27	0.05	13.81	0.05
Epsilon	0.205		0.243		0.319		0.146		0.192		0.253	
Fp	0.247		0.284		0.352		0.217		0.271		0.337	
Epsilon (sensible)	0.156		0.191		0.244		0.174		0.234		0.280	
Enthalpy In [kJ/kg]	65.54	0.17	65.65	0.16	65.40	0.16	58.23	0.15	58.65	0.15	58.69	0.15
Enthalpy Out [kJ/kg]	62.12	0.14	61.59	0.14	60.08	0.14	55.79	0.13	55.43	0.13	54.46	0.13
Air Specific Volume [m3/kg]	0.8748	0.0002	0.8729	0.0002	0.8704	0.0002	0.8707	0.0002	0.8686	0.0002	0.8665	0.0002

Test Information												
Date Tested:	1/30/07		1/30/07		1/30/07		1/31/07		1/31/07		1/31/07	
Nozzle:	8009		8009		8009		8009		8009		8009	
Nozzle Area [m2]	2.85E-06		2.85E-06		2.85E-06		2.85E-06		2.85E-06		2.85E-06	
Nozzle Pressure [psi][Pa]	30.0	206842.7	62.0	427475.0	105.0	723949.5	30.0	206842.7	62.0	427475.0	105.0	723949.5
Measurements	Value	Error	Value	Error	Value	Error	Value	Error	Value	Error	Value	Error
Barometric Pressure [pa]	100234.6	1.3	100234.6	1.3	100234.6	1.3	100140.3	1.3	100140.3	1.3	100140.3	1.3
Air Face Velocity [m/s]	3.07	0.11	3.03	0.11	2.99	0.11	3.06	0.11	3.01	0.11	2.97	0.11
Front Tdb [C]	26.69	0.05	26.68	0.05	26.76	0.05	26.73	0.05	26.67	0.05	26.70	0.05
Front Twb [C]	22.13	0.05	22.18	0.05	22.28	0.05	20.19	0.06	20.28	0.06	20.26	0.06
Wfront [g/kg]	15.07	0.06	15.14	0.06	15.27	0.06	12.31	0.06	12.47	0.06	12.43	0.06
Back Tdb [C] Zeroed	23.78	0.05	22.58	0.05	21.18	0.05	23.21	0.05	21.68	0.05	20.14	0.05
Back Twb [C] Zeroed	20.90	0.05	20.51	0.04	19.80	0.04	19.01	0.05	18.73	0.05	18.07	0.05
Wback [g/kg]	14.51	0.05	14.47	0.05	14.09	0.05	12.21	0.05	12.48	0.05	12.28	0.05
Water Flow Rate [kg/s]	0.050	0.000	0.070	0.000	0.092	0.000	0.050	0.000	0.071	0.000	0.092	0.000
Water Inlet [C]	10.06	0.05	9.96	0.05	10.02	0.06	10.01	0.05	9.81	0.05	10.05	0.06
Water Outlet [C]	11.55	0.05	11.56	0.05	11.86	0.05	11.20	0.05	11.15	0.05	11.56	0.06
Calculated Measurements	Value	Error	Value	Error	Value	Error	Value	Error	Value	Error	Value	Error
Air Mass Flow Rate [kg/s]	0.082	0.003	0.081	0.003	0.080	0.003	0.082	0.003	0.081	0.003	0.080	0.003
Air Side Heat Transfer [W]	362.3	22.3	482.4	24.7	705.2	31.1	316.6	20.8	412.2	23.5	571.7	27.2
Air Side Sensible Heat Transfer [W]	246.7	21.4	344.1	22.7	463.9	25.3	297.1	21.4	416.0	24.9	541.8	27.6
Water Side Heat Transfer [W]	312.5	11.0	471.4	15.6	706.9	21.6	251.8	11.2	396.0	15.5	582.9	24.3
% difference	15.9		2.3		-0.2		25.7		4.1		-1.9	
Sensible UA Value CF [W/C]	17.1	0.8	24.9	1.0	35.9	1.3	20.7	0.8	30.6	1.1	43.5	1.5
LTMD [C]	14.42	0.05	13.83	0.05	12.94	0.05	14.34	0.05	13.62	0.05	12.45	0.05
Epsilon	0.265		0.354		0.522		0.230		0.301		0.426	
Fp	0.311		0.387		0.512		0.321		0.391		0.511	
Epsilon (sensible)	0.181		0.253		0.343		0.216		0.303		0.404	
Enthalpy In [kJ/kg]	65.26	0.17	65.45	0.16	65.84	0.16	58.26	0.16	58.61	0.17	58.54	0.17
Enthalpy Out [kJ/kg]	60.84	0.14	59.50	0.14	57.08	0.13	54.40	0.14	53.53	0.14	51.42	0.13
Air Specific Volume [m3/kg]	0.8710	0.0002	0.8675	0.0002	0.8631	0.0002	0.8666	0.0002	0.8630	0.0002	0.8588	0.0002

Test Information												
Date Tested:	2/1/07		2/1/07		2/1/07		2/2/07		2/2/07		2/2/07	
Nozzle:	2x 8005		2x 8005		2x 8005		2x 8005		2x 8005		2x 8005	
Nozzle Area [m2]	3.18E-06		3.18E-06		3.18E-06		3.18E-06		3.18E-06		3.18E-06	
Nozzle Pressure [psi][Pa]	24.0	165474.2	49.0	337843.1	85.0	586054.4	24.0	165474.2	49.0	337843.1	85.0	586054.4
Measurements	Value	Error	Value	Error	Value	Error	Value	Error	Value	Error	Value	Error
Barometric Pressure [pa]	99513.7	1.3	99513.7	1.3	99513.7	1.3	99513.7	1.3	99513.7	1.3	99513.7	1.3
Air Face Velocity [m/s]	3.02	0.11	3.02	0.11	2.98	0.11	3.04	0.11	3.02	0.11	2.99	0.11
Front Tdb [C]	26.70	0.05	26.73	0.05	26.67	0.05	26.72	0.05	26.67	0.05	26.67	0.05
Front Twb [C]	22.17	0.05	22.17	0.05	22.23	0.05	20.25	0.05	20.23	0.05	20.24	0.05
Wfront [g/kg]	15.26	0.06	15.23	0.06	15.35	0.06	12.49	0.06	12.49	0.06	12.50	0.06
Back Tdb [C] Zeroed	23.22	0.05	22.30	0.05	20.33	0.05	22.81	0.05	21.49	0.05	19.43	0.05
Back Twb [C] Zeroed	20.90	0.04	20.44	0.04	19.42	0.04	19.34	0.04	18.78	0.04	17.94	0.04
Wback [g/kg]	14.87	0.05	14.60	0.05	14.04	0.05	12.90	0.05	12.71	0.05	12.51	0.05
Water Flow Rate [kg/s]	0.051	0.000	0.070	0.000	0.092	0.000	0.050	0.000	0.071	0.000	0.093	0.000
Water Inlet [C]	10.10	0.05	10.01	0.05	10.16	0.05	10.04	0.05	10.06	0.05	10.05	0.05
Water Outlet [C]	11.81	0.05	11.83	0.05	12.27	0.05	11.48	0.05	11.57	0.05	11.73	0.05
Calculated Measurements	Value	Error	Value	Error	Value	Error	Value	Error	Value	Error	Value	Error
Air Mass Flow Rate [kg/s]	0.080	0.003	0.080	0.003	0.080	0.003	0.081	0.003	0.081	0.003	0.080	0.003
Air Side Heat Transfer [W]	367.6	21.9	495.7	25.0	789.8	33.8	240.8	18.5	383.9	21.6	597.4	27.4
Air Side Sensible Heat Transfer [W]	288.8	21.4	367.6	23.1	524.0	27.1	325.6	21.0	430.8	23.7	599.6	28.4
Water Side Heat Transfer [W]	370.4	11.3	535.0	15.5	810.4	21.1	302.7	11.2	445.9	15.6	651.4	20.4
% difference	-0.7		-7.4		-2.5		-20.5		-13.9		-8.3	
Sensible UA Value CF [W/C]	20.6	0.9	27.1	1.0	43.1	1.4	23.3	0.9	32.7	1.1	50.2	1.5
LTMD [C]	13.99	0.05	13.55	0.05	12.16	0.05	13.97	0.05	13.18	0.05	11.94	0.05
Epsilon	0.275		0.368		0.597		0.178		0.285		0.446	
Fp	0.324		0.406		0.568		0.266		0.386		0.533	
Epsilon (sensible)	0.216		0.273		0.396		0.240		0.319		0.447	
Enthalpy In [kJ/kg]	65.75	0.16	65.72	0.17	65.96	0.17	58.73	0.15	58.65	0.15	58.69	0.16
Enthalpy Out [kJ/kg]	61.17	0.14	59.54	0.14	56.08	0.13	55.75	0.13	53.91	0.13	51.26	0.13
Air Specific Volume [m3/kg]	0.8758	0.0002	0.8726	0.0002	0.8669	0.0002	0.8717	0.0002	0.8677	0.0002	0.8624	0.0002

Test Information												
Date Tested:	2/17/07		2/17/07		2/17/07		2/17/07		2/17/07		2/17/07	
Nozzle:	8015		8015		8015		8015		8015		8015	
Nozzle Area [m2]	4.48E-06		4.48E-06		4.48E-06		4.48E-06		4.48E-06		4.48E-06	
Nozzle Pressure [psi][Pa]	10.5	72395.0	22.0	151684.7	38.0	262000.8	10.5	72395.0	22.0	151684.7	38.0	262000.8
Measurements	Value	Error	Value	Error	Value	Error	Value	Error	Value	Error	Value	Error
Barometric Pressure [pa]	100273.7	1.3	100273.7	1.3	100273.7	1.3	100273.7	1.3	100273.7	1.3	100273.7	1.3
Air Face Velocity [m/s]	3.09	0.11	3.06	0.11	3.02	0.11	3.10	0.11	3.08	0.11	3.04	0.11
Front Tdb [C]	26.74	0.05	26.68	0.05	26.72	0.05	26.70	0.05	26.72	0.05	26.72	0.05
Front Twb [C]	22.19	0.05	22.12	0.05	22.21	0.05	20.27	0.06	20.20	0.05	20.19	0.05
Wfront [g/kg]	15.13	0.06	15.05	0.06	15.16	0.06	12.41	0.06	12.30	0.06	12.29	0.06
Back Tdb [C] Zeroed	23.68	0.05	22.73	0.05	22.13	0.05	23.26	0.05	22.30	0.05	21.34	0.05
Back Twb [C] Zeroed	20.86	0.04	20.47	0.05	20.17	0.04	19.00	0.05	18.61	0.04	18.23	0.04
Wback [g/kg]	14.50	0.05	14.35	0.05	14.19	0.05	12.15	0.05	12.06	0.05	11.97	0.05
Water Flow Rate [kg/s]	0.051	0.000	0.071	0.000	0.092	0.000	0.050	0.000	0.071	0.000	0.093	0.000
Water Inlet [C]	5.10	0.06	4.94	0.06	4.94	0.06	5.08	0.06	5.01	0.06	4.92	0.06
Water Outlet [C]	6.33	0.05	6.28	0.06	6.28	0.05	6.08	0.05	6.11	0.05	6.02	0.06
Calculated Measurements	Value	Error	Value	Error	Value	Error	Value	Error	Value	Error	Value	Error
Air Mass Flow Rate [kg/s]	0.083	0.003	0.082	0.003	0.081	0.003	0.083	0.003	0.083	0.003	0.082	0.003
Air Side Heat Transfer [W]	395.3	22.9	481.4	25.1	584.4	27.5	348.3	22.0	429.5	22.5	521.9	25.0
Air Side Sensible Heat Transfer [W]	261.3	21.8	334.6	23.0	384.7	23.7	293.9	22.4	376.9	22.3	455.0	24.2
Water Side Heat Transfer [W]	262.4	13.2	401.9	19.2	517.9	21.7	211.6	12.1	327.1	17.3	428.0	24.3
% difference	50.6		19.8		12.8		64.6		31.3		21.9	
Sensible UA Value CF [W/C]	13.4	0.7	17.5	0.8	20.5	0.9	15.2	0.7	19.9	0.7	24.6	0.9
LTMD [C]	19.48	0.05	19.07	0.05	18.77	0.05	19.37	0.05	18.90	0.05	18.47	0.05
Epsilon	0.220		0.269		0.330		0.193		0.238		0.290	
Fp	0.108		0.133		0.162		0.111		0.138		0.169	
Epsilon (sensible)	0.146		0.187		0.217		0.163		0.209		0.253	
Enthalpy In [kJ/kg]	65.48	0.17	65.21	0.17	65.53	0.17	58.49	0.17	58.25	0.15	58.22	0.15
Enthalpy Out [kJ/kg]	60.70	0.14	59.34	0.14	58.33	0.14	54.30	0.14	53.07	0.13	51.87	0.13
Air Specific Volume [m3/kg]	0.8703	0.0002	0.8671	0.0002	0.8651	0.0002	0.8661	0.0002	0.8630	0.0002	0.8602	0.0002

Test Information												
Date Tested:	2/18/07		2/18/07		2/18/07		2/18/07		2/18/07		2/18/07	
Nozzle:	8009		8009		8009		8009		8009		8009	
Nozzle Area [m2]	2.85E-06		2.85E-06		2.85E-06		2.85E-06		2.85E-06		2.85E-06	
Nozzle Pressure [psi][Pa]	30.0	206842.7	62.0	427475.0	105.0	723949.5	30.0	206842.7	62.0	427475.0	105.0	723949.5
Measurements	Value	Error	Value	Error	Value	Error	Value	Error	Value	Error	Value	Error
Barometric Pressure [pa]	100113.7	1.3	100113.7	1.3	100113.7	1.3	100113.7	1.3	100113.7	1.3	100113.7	1.3
Air Face Velocity [m/s]	3.09	0.11	3.02	0.11	2.95	0.11	3.04	0.11	2.99	0.11	2.93	0.11
Front Tdb [C]	26.76	0.05	26.70	0.05	26.79	0.05	26.70	0.05	26.74	0.05	26.66	0.05
Front Twb [C]	22.24	0.05	22.18	0.05	22.22	0.05	20.16	0.05	20.24	0.05	20.28	0.05
Wfront [g/kg]	15.22	0.06	15.16	0.07	15.18	0.06	12.28	0.06	12.38	0.06	12.47	0.06
Back Tdb [C] Zeroed	23.37	0.05	21.57	0.05	19.64	0.05	22.32	0.05	20.51	0.05	18.62	0.05
Back Twb [C] Zeroed	20.80	0.04	19.89	0.04	18.70	0.04	18.69	0.05	18.01	0.04	17.01	0.04
Wback [g/kg]	14.58	0.05	14.07	0.05	13.30	0.05	12.18	0.05	12.06	0.05	11.61	0.04
Water Flow Rate [kg/s]	0.050	0.000	0.071	0.000	0.092	0.000	0.050	0.000	0.071	0.000	0.092	0.000
Water Inlet [C]	5.11	0.06	4.83	0.05	5.05	0.05	5.09	0.06	4.99	0.05	5.01	0.05
Water Outlet [C]	6.31	0.06	6.43	0.05	7.10	0.05	6.05	0.06	6.39	0.05	6.66	0.05
Calculated Measurements	Value	Error	Value	Error	Value	Error	Value	Error	Value	Error	Value	Error
Air Mass Flow Rate [kg/s]	0.083	0.003	0.081	0.003	0.080	0.003	0.082	0.003	0.081	0.003	0.080	0.003
Air Side Heat Transfer [W]	424.0	23.4	653.3	29.8	970.8	40.0	390.6	22.1	584.3	26.9	831.7	35.0
Air Side Sensible Heat Transfer [W]	289.5	21.9	430.2	25.3	590.0	29.0	368.0	22.6	517.2	25.9	659.0	30.1
Water Side Heat Transfer [W]	251.6	12.3	476.5	15.7	796.0	20.3	200.1	12.3	417.5	16.2	643.6	20.3
% difference	68.6		37.1		22.0		95.2		40.0		29.2	
Sensible UA Value CF [W/C]	15.0	0.7	23.3	0.8	34.7	1.0	19.5	0.7	29.0	0.9	39.7	1.1
LTMD [C]	19.33	0.05	18.45	0.05	17.02	0.05	18.89	0.05	17.82	0.05	16.60	0.05
Epsilon	0.237		0.367		0.557		0.221		0.332		0.481	
Fp	0.115		0.183		0.284		0.128		0.195		0.285	
Epsilon (sensible)	0.162		0.242		0.339		0.208		0.294		0.381	
Enthalpy In [kJ/kg]	65.71	0.17	65.50	0.17	65.64	0.17	58.18	0.16	58.47	0.15	58.60	0.15
Enthalpy Out [kJ/kg]	60.58	0.14	57.44	0.14	53.50	0.13	53.39	0.14	51.23	0.13	48.16	0.12
Air Specific Volume [m3/kg]	0.8701	0.0002	0.8646	0.0002	0.8584	0.0002	0.8650	0.0002	0.8596	0.0002	0.8542	0.0002

Test Information												
Date Tested:	2/6/07		2/6/07		2/6/07		2/6/07		2/6/07		2/6/07	
Nozzle:	2x 8005		2x 8005		2x 8005		2x 8005		2x 8005		2x 8005	
Nozzle Area [m2]	3.18E-06		3.18E-06		3.18E-06		3.18E-06		3.18E-06		3.18E-06	
Nozzle Pressure [psi][Pa]	24.0	165474.2	49.0	337843.1	85.0	586054.4	24.0	165474.2	49.0	337843.1	85.0	586054.4
Measurements	Value	Error	Value	Error	Value	Error	Value	Error	Value	Error	Value	Error
Barometric Pressure [pa]	99952.7	1.3	99952.7	1.3	99952.7	1.3	99952.7	1.3	99952.7	1.3	99952.7	1.3
Air Face Velocity [m/s]	3.03	0.11	3.00	0.11	2.97	0.11	3.02	0.11	2.99	0.11	2.97	0.11
Front Tdb [C]	26.74	0.05	26.75	0.05	26.67	0.05	26.72	0.05	26.70	0.05	26.66	0.05
Front Twb [C]	22.23	0.05	22.17	0.05	22.12	0.05	20.31	0.05	20.23	0.05	20.22	0.05
Wfront [g/kg]	15.25	0.06	15.15	0.06	15.12	0.06	12.52	0.06	12.41	0.06	12.41	0.06
Back Tdb [C] Zeroed	22.82	0.05	21.22	0.05	19.24	0.05	22.34	0.05	20.55	0.05	18.25	0.05
Back Twb [C] Zeroed	20.58	0.04	19.60	0.04	18.29	0.04	18.82	0.05	17.95	0.05	16.67	0.05
Wback [g/kg]	14.51	0.05	13.84	0.05	12.97	0.05	12.36	0.05	11.99	0.05	11.37	0.05
Water Flow Rate [kg/s]	0.050	0.000	0.071	0.000	0.092	0.000	0.049	0.000	0.071	0.000	0.092	0.000
Water Inlet [C]	5.17	0.05	5.09	0.05	5.06	0.05	4.99	0.05	5.01	0.05	5.11	0.05
Water Outlet [C]	7.04	0.05	7.18	0.05	7.46	0.05	6.48	0.05	6.72	0.05	7.10	0.05
Calculated Measurements	Value	Error	Value	Error	Value	Error	Value	Error	Value	Error	Value	Error
Air Mass Flow Rate [kg/s]	0.081	0.003	0.080	0.003	0.080	0.003	0.081	0.003	0.081	0.003	0.081	0.003
Air Side Heat Transfer [W]	478.7	24.6	726.6	31.7	1054.1	42.6	397.2	22.4	595.8	27.3	908.2	37.5
Air Side Sensible Heat Transfer [W]	326.9	22.4	459.0	25.2	616.9	29.7	364.5	22.6	509.7	25.8	696.8	31.5
Water Side Heat Transfer [W]	397.0	11.1	619.2	15.8	925.9	20.3	308.2	11.0	509.2	15.8	771.6	20.4
% difference	20.6		17.4		13.8		28.9		17.0		17.7	
Sensible UA Value CF [W/C]	17.5	0.7	25.8	0.8	37.2	1.1	19.4	0.7	28.9	0.9	43.2	1.2
LTMD [C]	18.66	0.05	17.79	0.05	16.56	0.05	18.76	0.05	17.66	0.05	16.14	0.05
Epsilon	0.274		0.416		0.606		0.225		0.340		0.521	
Fp	0.138		0.213		0.315		0.132		0.203		0.317	
Epsilon (sensible)	0.187		0.263		0.355		0.207		0.291		0.400	
Enthalpy In [kJ/kg]	65.77	0.17	65.54	0.17	65.36	0.17	58.79	0.16	58.50	0.16	58.45	0.16
Enthalpy Out [kJ/kg]	59.85	0.14	56.50	0.13	52.23	0.13	53.88	0.14	51.11	0.13	47.18	0.12
Air Specific Volume [m3/kg]	0.8710	0.0002	0.8659	0.0002	0.8595	0.0002	0.8670	0.0002	0.8617	0.0002	0.8548	0.0002

Test Information												
Date Tested:	2/21/07		2/21/07		2/21/07		2/21/07		2/21/07		2/21/07	
Nozzle:	8015		8015		8015		8015		8015		8015	
Nozzle Area [m2]	4.48E-06		4.48E-06		4.48E-06		4.48E-06		4.48E-06		4.48E-06	
Nozzle Pressure [psi][Pa]	10.5	72395.0	22.0	151684.7	38.0	262000.8	10.5	72395.0	22.0	151684.7	38.0	262000.8
Measurements	Value	Error	Value	Error	Value	Error	Value	Error	Value	Error	Value	Error
Barometric Pressure [pa]	98780.4	1.3	98780.4	1.3	98780.4	1.3	98780.4	1.3	98780.4	1.3	98780.4	1.3
Air Face Velocity [m/s]	1.04	0.11	1.03	0.11	1.01	0.11	1.03	0.11	1.02	0.11	1.01	0.11
Front Tdb [C]	26.70	0.05	26.71	0.05	26.74	0.05	26.76	0.05	26.71	0.05	26.64	0.05
Front Twb [C]	22.28	0.08	22.18	0.06	22.27	0.06	20.06	0.06	20.35	0.06	20.17	0.06
Wfront [g/kg]	15.55	0.09	15.39	0.07	15.51	0.07	12.33	0.07	12.75	0.06	12.53	0.06
Back Tdb [C] Zeroed	21.77	0.05	20.07	0.05	18.78	0.05	21.29	0.05	19.37	0.05	17.91	0.05
Back Twb [C] Zeroed	19.87	0.06	18.51	0.04	17.67	0.05	18.44	0.05	17.55	0.04	16.69	0.04
Wback [g/kg]	14.16	0.06	13.07	0.05	12.53	0.05	12.47	0.05	12.14	0.05	11.69	0.04
Water Flow Rate [kg/s]	0.049	0.000	0.071	0.000	0.092	0.000	0.050	0.000	0.070	0.000	0.092	0.000
Water Inlet [C]	10.12	0.05	10.06	0.07	10.03	0.06	9.90	0.06	10.10	0.06	10.15	0.06
Water Outlet [C]	10.90	0.05	10.91	0.06	10.91	0.05	10.51	0.05	10.84	0.05	10.88	0.05
Calculated Measurements	Value	Error	Value	Error	Value	Error	Value	Error	Value	Error	Value	Error
Air Mass Flow Rate [kg/s]	0.027	0.003	0.027	0.003	0.027	0.003	0.027	0.003	0.027	0.003	0.027	0.003
Air Side Heat Transfer [W]	237.4	25.3	347.5	36.3	424.1	44.9	144.3	16.0	248.0	26.3	298.3	31.9
Air Side Sensible Heat Transfer [W]	140.0	16.9	186.8	20.4	221.2	24.2	154.0	17.1	205.8	22.2	241.3	26.2
Water Side Heat Transfer [W]	159.6	11.2	252.3	19.5	335.9	21.8	128.3	12.1	217.8	16.8	281.1	22.3
% difference	48.8		37.7		26.3		12.5		13.9		6.1	
Sensible UA Value CF [W/C]	10.3	0.7	14.7	1.1	18.5	1.4	11.3	0.8	16.8	1.1	21.4	1.5
LTMD [C]	13.62	0.05	12.69	0.06	11.94	0.05	13.67	0.05	12.27	0.05	11.30	0.06
Epsilon	0.520		0.764		0.942		0.312		0.547		0.671	
Fp	0.248		0.372		0.456		0.191		0.328		0.411	
Epsilon (sensible)	0.307		0.411		0.491		0.333		0.454		0.543	
Enthalpy In [kJ/kg]	66.51	0.23	66.11	0.18	66.44	0.18	58.35	0.18	59.37	0.17	58.73	0.17
Enthalpy Out [kJ/kg]	57.87	0.17	53.34	0.13	50.66	0.13	53.08	0.14	50.26	0.13	47.63	0.12
Air Specific Volume [m3/kg]	0.8797	0.0002	0.8750	0.0002	0.8720	0.0002	0.8776	0.0002	0.8729	0.0002	0.8697	0.0002

Test Information												
Date Tested:	2/19/07		2/19/07		2/19/07		2/19/07		2/19/07		2/19/07	
Nozzle:	8009		8009		8009		8009		8009		8009	
Nozzle Area [m2]	2.85E-06		2.85E-06		2.85E-06		2.85E-06		2.85E-06		2.85E-06	
Nozzle Pressure [psi][Pa]	30.0	206842.7	62.0	427475.0	105.0	723949.5	30.0	206842.7	62.0	427475.0	105.0	723949.5
Measurements	Value	Error	Value	Error	Value	Error	Value	Error	Value	Error	Value	Error
Barometric Pressure [pa]	98753.8	1.3	98753.8	1.3	98753.8	1.3	98753.8	1.3	98753.8	1.3	98753.8	1.3
Air Face Velocity [m/s]	1.01	0.11	1.00	0.11	0.99	0.11	1.02	0.11	1.01	0.11	0.99	0.11
Front Tdb [C]	26.69	0.05	26.73	0.05	26.71	0.05	26.70	0.05	26.71	0.05	26.74	0.05
Front Twb [C]	22.16	0.06	22.12	0.08	22.21	0.05	20.28	0.06	20.34	0.06	20.29	0.07
Wfront [g/kg]	15.37	0.07	15.30	0.10	15.44	0.07	12.66	0.07	12.75	0.07	12.66	0.08
Back Tdb [C] Zeroed	19.76	0.05	18.16	0.05	17.11	0.05	18.44	0.05	17.04	0.05	16.04	0.05
Back Twb [C] Zeroed	18.81	0.04	17.49	0.05	16.66	0.04	17.28	0.05	16.33	0.05	15.58	0.04
Wback [g/kg]	13.58	0.05	12.58	0.05	11.99	0.04	12.19	0.05	11.62	0.04	11.16	0.04
Water Flow Rate [kg/s]	0.050	0.000	0.071	0.000	0.092	0.000	0.050	0.000	0.071	0.000	0.092	0.000
Water Inlet [C]	9.91	0.06	10.09	0.06	10.12	0.06	10.07	0.06	10.14	0.06	10.00	0.05
Water Outlet [C]	11.17	0.06	11.38	0.05	11.42	0.05	11.18	0.05	11.22	0.06	11.05	0.05
Calculated Measurements	Value	Error	Value	Error	Value	Error	Value	Error	Value	Error	Value	Error
Air Mass Flow Rate [kg/s]	0.027	0.003	0.027	0.003	0.027	0.003	0.027	0.003	0.027	0.003	0.027	0.003
Air Side Heat Transfer [W]	313.1	33.3	417.4	45.0	496.0	53.1	262.3	28.0	344.1	36.8	394.9	42.6
Air Side Sensible Heat Transfer [W]	191.5	21.1	234.8	26.7	263.7	28.8	229.9	24.9	267.3	29.0	293.6	32.2
Water Side Heat Transfer [W]	263.8	12.6	381.2	17.2	499.5	21.5	234.4	12.0	320.9	18.8	403.7	20.9
% difference	18.7		9.5		-0.7		11.9		7.2		-2.2	
Sensible UA Value CF [W/C]	15.4	1.0	20.8	1.4	24.9	1.7	19.8	1.2	25.2	1.6	29.1	1.9
LTMD [C]	12.47	0.05	11.32	0.05	10.60	0.05	11.58	0.05	10.61	0.06	10.11	0.06
Epsilon	0.695		0.944		1.122		0.581		0.771		0.882	
Fp	0.348		0.479		0.563		0.364		0.479		0.549	
Epsilon (sensible)	0.425		0.531		0.596		0.509		0.599		0.656	
Enthalpy In [kJ/kg]	66.04	0.18	65.88	0.25	66.24	0.17	59.13	0.18	59.37	0.19	59.17	0.20
Enthalpy Out [kJ/kg]	54.34	0.13	50.13	0.13	47.57	0.12	49.44	0.13	46.56	0.12	44.37	0.12
Air Specific Volume [m3/kg]	0.8766	0.0002	0.8728	0.0002	0.8697	0.0002	0.8726	0.0002	0.8693	0.0002	0.8663	0.0002

Test Information												
Date Tested:	2/20/07		2/20/07		2/20/07		2/20/07		2/20/07		2/20/07	
Nozzle:	2x 8005		2x 8005		2x 8005		2x 8005		2x 8005		2x 8005	
Nozzle Area [m2]	3.18E-06		3.18E-06		3.18E-06		3.18E-06		3.18E-06		3.18E-06	
Nozzle Pressure [psi][Pa]	24.0	165474.2	49.0	337843.1	85.0	586054.4	24.0	165474.2	49.0	337843.1	85.0	586054.4
Measurements	Value	Error	Value	Error	Value	Error	Value	Error	Value	Error	Value	Error
Barometric Pressure [pa]	98807.1	1.3	98807.1	1.3	98807.1	1.3	98807.1	1.3	98807.1	1.3	98807.1	1.3
Air Face Velocity [m/s]	1.02	0.11	1.00	0.11	1.01	0.11	1.02	0.11	1.01	0.11	1.01	0.11
Front Tdb [C]	26.72	0.05	26.65	0.05	26.80	0.05	26.69	0.05	26.74	0.05	26.68	0.05
Front Twb [C]	22.20	0.06	22.21	0.06	22.16	0.06	20.18	0.06	20.33	0.06	20.01	0.07
Wfront [g/kg]	15.41	0.07	15.46	0.07	15.32	0.08	12.52	0.07	12.71	0.07	12.29	0.08
Back Tdb [C] Zeroed	19.36	0.05	17.60	0.05	15.64	0.05	17.96	0.05	16.33	0.05	14.60	0.05
Back Twb [C] Zeroed	18.36	0.05	17.08	0.04	15.41	0.04	17.04	0.05	15.89	0.05	14.52	0.04
Wback [g/kg]	13.17	0.05	12.29	0.05	11.13	0.04	12.09	0.05	11.40	0.04	10.55	0.04
Water Flow Rate [kg/s]	0.051	0.000	0.071	0.000	0.092	0.000	0.050	0.000	0.071	0.000	0.092	0.000
Water Inlet [C]	9.99	0.06	10.13	0.07	10.03	0.06	10.04	0.06	9.97	0.06	9.88	0.07
Water Outlet [C]	11.68	0.05	11.82	0.06	11.71	0.05	11.52	0.05	11.47	0.05	11.29	0.06
Calculated Measurements	Value	Error	Value	Error	Value	Error	Value	Error	Value	Error	Value	Error
Air Mass Flow Rate [kg/s]	0.027	0.003	0.027	0.003	0.027	0.003	0.027	0.003	0.027	0.003	0.027	0.003
Air Side Heat Transfer [W]	361.6	37.9	466.6	49.7	601.8	63.7	274.2	29.0	379.2	40.3	458.7	48.8
Air Side Sensible Heat Transfer [W]	206.8	22.6	251.1	27.4	313.7	34.0	244.8	26.2	289.5	31.3	338.5	36.5
Water Side Heat Transfer [W]	357.7	12.5	502.9	21.1	648.8	22.9	312.5	12.8	445.8	18.4	544.1	25.9
% difference	1.1		-7.2		-7.2		-12.3		-14.9		-15.7	
Sensible UA Value CF [W/C]	17.3	1.1	23.4	1.6	32.7	2.2	21.9	1.3	28.4	1.8	37.5	2.5
LTMD [C]	11.98	0.05	10.73	0.06	9.58	0.06	11.16	0.05	10.18	0.06	9.02	0.07
Epsilon	0.793		1.049		1.316		0.602		0.833		0.999	
Fp	0.410		0.541		0.688		0.395		0.538		0.664	
Epsilon (sensible)	0.454		0.565		0.686		0.538		0.636		0.737	
Enthalpy In [kJ/kg]	66.17	0.19	66.23	0.18	66.02	0.20	58.77	0.17	59.29	0.19	58.18	0.20
Enthalpy Out [kJ/kg]	52.87	0.13	48.84	0.13	43.89	0.12	48.71	0.13	45.27	0.12	41.34	0.12
Air Specific Volume [m3/kg]	0.8733	0.0002	0.8688	0.0002	0.8626	0.0002	0.8706	0.0002	0.8668	0.0002	0.8606	0.0002

Test Information												
Date Tested:	2/24/07		2/24/07		2/24/07		2/24/07		2/24/07		2/24/07	
Nozzle:	8015		8015		8015		8015		8015		8015	
Nozzle Area [m2]	4.48E-06		4.48E-06		4.48E-06		4.48E-06		4.48E-06		4.48E-06	
Nozzle Pressure [psi][Pa]	10.5	72395.0	22.0	151684.7	38.0	262000.8	10.5	72395.0	22.0	151684.7	38.0	262000.8
Measurements	Value	Error	Value	Error	Value	Error	Value	Error	Value	Error	Value	Error
Barometric Pressure [pa]	97662.3	1.3	97662.3	1.3	97662.3	1.3	97662.3	1.3	97662.3	1.3	97662.3	1.3
Air Face Velocity [m/s]	1.02	0.11	1.00	0.11	0.99	0.11	1.02	0.11	1.00	0.11	0.99	0.11
Front Tdb [C]	26.69	0.05	26.68	0.05	26.73	0.05	26.70	0.05	26.71	0.05	26.72	0.05
Front Twb [C]	22.19	0.06	22.27	0.05	22.26	0.06	20.21	0.08	20.36	0.07	20.33	0.09
Wfront [g/kg]	15.62	0.08	15.74	0.07	15.71	0.08	12.74	0.09	12.94	0.08	12.89	0.10
Back Tdb [C] Zeroed	21.45	0.05	19.28	0.05	17.36	0.05	20.30	0.05	18.40	0.05	16.95	0.06
Back Twb [C] Zeroed	19.55	0.05	17.92	0.05	16.55	0.05	17.83	0.06	16.72	0.05	15.75	0.05
Wback [g/kg]	14.04	0.05	12.79	0.05	11.89	0.05	12.25	0.06	11.66	0.05	11.10	0.05
Water Flow Rate [kg/s]	0.050	0.000	0.071	0.000	0.092	0.000	0.051	0.000	0.071	0.000	0.092	0.000
Water Inlet [C]	5.04	0.06	4.93	0.05	5.03	0.06	4.99	0.06	4.97	0.06	5.10	0.06
Water Outlet [C]	5.93	0.06	5.99	0.05	6.10	0.05	5.76	0.06	5.89	0.05	6.02	0.05
Calculated Measurements	Value	Error	Value	Error	Value	Error	Value	Error	Value	Error	Value	Error
Air Mass Flow Rate [kg/s]	0.027	0.003	0.026	0.003	0.026	0.003	0.027	0.003	0.027	0.003	0.026	0.003
Air Side Heat Transfer [W]	251.2	26.9	400.1	42.5	506.1	54.7	208.8	23.0	312.5	33.6	381.1	41.7
Air Side Sensible Heat Transfer [W]	144.2	16.8	202.3	22.3	253.5	28.2	175.6	20.3	226.7	25.2	262.8	29.8
Water Side Heat Transfer [W]	189.5	12.8	315.9	16.3	410.6	21.2	165.5	12.6	276.2	17.3	357.0	21.7
% difference	32.6		26.6		23.2		26.2		13.1		6.8	
Sensible UA Value CF [W/C]	7.8	0.6	11.7	0.8	15.7	1.1	9.8	0.7	13.4	0.9	16.6	1.2
LTMD [C]	18.50	0.05	17.32	0.05	16.13	0.05	17.97	0.05	16.86	0.05	15.87	0.06
Epsilon	0.435		0.694		0.889		0.360		0.540		0.672	
Fp	0.206		0.329		0.423		0.202		0.302		0.377	
Epsilon (sensible)	0.250		0.351		0.445		0.302		0.392		0.464	
Enthalpy In [kJ/kg]	66.67	0.20	66.97	0.18	66.93	0.20	59.34	0.24	59.86	0.21	59.75	0.25
Enthalpy Out [kJ/kg]	57.23	0.15	51.83	0.13	47.58	0.13	51.51	0.16	48.07	0.14	45.17	0.14
Air Specific Volume [m3/kg]	0.8886	0.0002	0.8827	0.0002	0.8780	0.0002	0.8844	0.0002	0.8798	0.0002	0.8765	0.0002

Test Information												
Date Tested:	2/25/07		2/25/07		2/25/07		2/25/07		2/25/07		2/25/07	
Nozzle:	8009		8009		8009		8009		8009		8009	
Nozzle Area [m2]	2.85E-06		2.85E-06		2.85E-06		2.85E-06		2.85E-06		2.85E-06	
Nozzle Pressure [psi][Pa]	30.0	206842.7	62.0	427475.0	105.0	723949.5	30.0	206842.7	62.0	427475.0	105.0	723949.5
Measurements	Value	Error	Value	Error	Value	Error	Value	Error	Value	Error	Value	Error
Barometric Pressure [pa]	98449.0	1.3	98449.0	1.3	98449.0	1.3	98449.0	1.3	98449.0	1.3	98449.0	1.3
Air Face Velocity [m/s]	0.98	0.11	0.96	0.11	0.95	0.11	0.98	0.11	0.97	0.11	0.95	0.11
Front Tdb [C]	26.73	0.05	26.84	0.05	26.64	0.05	26.74	0.05	26.67	0.05	26.71	0.05
Front Twb [C]	22.15	0.07	22.22	0.07	22.15	0.06	20.16	0.08	20.39	0.07	20.36	0.06
Wfront [g/kg]	15.40	0.08	15.46	0.08	15.43	0.08	12.53	0.09	12.88	0.08	12.83	0.07
Back Tdb [C] Zeroed	19.26	0.05	16.78	0.05	14.31	0.05	17.04	0.05	15.30	0.05	13.79	0.05
Back Twb [C] Zeroed	17.96	0.05	16.02	0.04	14.05	0.04	15.91	0.05	14.53	0.04	13.35	0.04
Wback [g/kg]	12.75	0.05	11.40	0.04	10.20	0.04	11.16	0.05	10.32	0.04	9.65	0.04
Water Flow Rate [kg/s]	0.051	0.000	0.071	0.000	0.092	0.000	0.051	0.000	0.071	0.000	0.092	0.000
Water Inlet [C]	5.07	0.06	5.11	0.05	4.98	0.05	5.10	0.06	5.18	0.06	4.98	0.05
Water Outlet [C]	5.92	0.06	5.95	0.05	5.91	0.05	5.56	0.06	5.87	0.05	5.76	0.05
Calculated Measurements	Value	Error	Value	Error	Value	Error	Value	Error	Value	Error	Value	Error
Air Mass Flow Rate [kg/s]	0.026	0.003	0.026	0.003	0.026	0.003	0.026	0.003	0.026	0.003	0.026	0.003
Air Side Heat Transfer [W]	375.0	41.2	531.7	59.1	662.9	75.1	354.7	38.9	475.8	52.4	546.1	61.7
Air Side Sensible Heat Transfer [W]	200.4	23.2	267.6	30.6	325.3	37.4	263.2	29.6	306.5	34.4	340.6	38.9
Water Side Heat Transfer [W]	182.4	12.7	253.2	16.0	359.9	20.2	98.4	12.4	205.6	16.8	300.8	20.6
% difference	105.6		110.0		84.2		260.5		131.4		81.5	
Sensible UA Value CF [W/C]	11.6	0.8	16.9	1.1	22.8	1.5	16.3	1.0	20.7	1.3	24.3	1.6
LTMD [C]	17.29	0.05	15.84	0.05	14.28	0.05	16.12	0.06	14.82	0.06	14.02	0.05
Epsilon	0.665		0.948		1.196		0.620		0.843		0.978	
Fp	0.318		0.453		0.572		0.346		0.466		0.545	
Epsilon (sensible)	0.356		0.477		0.587		0.460		0.543		0.610	
Enthalpy In [kJ/kg]	66.16	0.22	66.41	0.21	66.14	0.20	58.85	0.23	59.65	0.20	59.56	0.17
Enthalpy Out [kJ/kg]	51.70	0.13	45.75	0.12	40.16	0.12	45.40	0.13	41.48	0.12	38.26	0.11
Air Specific Volume [m3/kg]	0.8741	0.0002	0.8672	0.0002	0.8603	0.0002	0.8677	0.0002	0.8630	0.0002	0.8588	0.0002

Test Information												
Date Tested:	2/24/07		2/24/07		2/24/07		2/24/07		2/24/07		2/24/07	
Nozzle:	2x 8005		2x 8005		2x 8005		2x 8005		2x 8005		2x 8005	
Nozzle Area [m2]	3.18E-06		3.18E-06		3.18E-06		3.18E-06		3.18E-06		3.18E-06	
Nozzle Pressure [psi][Pa]	24.0	165474.2	49.0	337843.1	85.0	586054.4	24.0	165474.2	49.0	337843.1	85.0	586054.4
Measurements	Value	Error	Value	Error	Value	Error	Value	Error	Value	Error	Value	Error
Barometric Pressure [pa]	97662.3	1.3	97662.3	1.3	97662.3	1.3	97662.3	1.3	97662.3	1.3	97662.3	1.3
Air Face Velocity [m/s]	1.01	0.11	1.00	0.11	0.99	0.11	1.02	0.11	1.00	0.11	0.99	0.11
Front Tdb [C]	26.70	0.05	26.70	0.05	26.70	0.05	26.70	0.05	26.71	0.05	26.72	0.05
Front Twb [C]	22.08	0.10	22.22	0.08	22.21	0.09	20.21	0.08	20.35	0.07	20.30	0.08
Wfront [g/kg]	15.44	0.12	15.66	0.10	15.65	0.11	12.74	0.09	12.93	0.08	12.86	0.09
Back Tdb [C] Zeroed	17.95	0.05	15.51	0.05	13.10	0.05	20.30	0.05	18.40	0.05	16.97	0.06
Back Twb [C] Zeroed	17.25	0.05	15.30	0.05	13.30	0.04	17.83	0.06	16.71	0.05	15.75	0.05
Wback [g/kg]	12.50	0.05	11.19	0.04	9.97	0.04	12.25	0.06	11.66	0.05	11.10	0.05
Water Flow Rate [kg/s]	0.050	0.000	0.071	0.000	0.092	0.000	0.051	0.000	0.071	0.000	0.092	0.000
Water Inlet [C]	5.14	0.05	4.91	0.06	4.85	0.05	5.00	0.06	4.97	0.06	5.10	0.06
Water Outlet [C]	7.24	0.05	7.02	0.05	6.86	0.05	5.77	0.06	5.89	0.05	6.02	0.05
Calculated Measurements	Value	Error	Value	Error	Value	Error	Value	Error	Value	Error	Value	Error
Air Mass Flow Rate [kg/s]	0.027	0.003	0.027	0.003	0.027	0.003	0.027	0.003	0.027	0.003	0.026	0.003
Air Side Heat Transfer [W]	441.1	47.0	606.7	65.1	753.9	81.8	208.7	23.0	312.1	33.6	378.8	41.3
Air Side Sensible Heat Transfer [W]	242.1	27.9	307.0	34.1	373.3	41.7	175.5	20.3	226.8	25.1	262.4	29.4
Water Side Heat Transfer [W]	444.6	11.2	625.9	16.4	772.4	20.3	165.8	12.6	275.7	17.4	357.9	21.8
% difference	-0.8		-3.1		-2.4		25.9		13.2		5.8	
Sensible UA Value CF [W/C]	15.2	0.9	20.9	1.3	28.3	1.8	9.8	0.7	13.5	0.9	16.5	1.2
LTMD [C]	15.90	0.05	14.68	0.05	13.21	0.06	17.97	0.05	16.86	0.05	15.88	0.06
Epsilon	0.763		1.046		1.296		0.360		0.540		0.668	
Fp	0.387		0.525		0.647		0.202		0.302		0.375	
Epsilon (sensible)	0.419		0.530		0.642		0.302		0.392		0.463	
Enthalpy In [kJ/kg]	66.23	0.31	66.77	0.25	66.76	0.28	59.33	0.23	59.83	0.21	59.67	0.22
Enthalpy Out [kJ/kg]	49.73	0.14	43.90	0.12	38.35	0.11	51.51	0.16	48.05	0.14	45.17	0.14
Air Specific Volume [m3/kg]	0.8806	0.0002	0.8734	0.0002	0.8661	0.0002	0.8845	0.0002	0.8798	0.0002	0.8765	0.0002

Test Information												
Date Tested:	3/1/07		3/1/07		3/1/07		3/2/07		3/2/07		3/2/07	
Nozzle:	8015		8015		8015		8015		8015		8015	
Nozzle Area [m2]	4.48E-06		4.48E-06		4.48E-06		4.48E-06		4.48E-06		4.48E-06	
Nozzle Pressure [psi][Pa]	10.5	72395.0	22.0	151684.7	38.0	262000.8	10.5	72395.0	22.0	151684.7	38.0	262000.8
Measurements	Value	Error	Value	Error	Value	Error	Value	Error	Value	Error	Value	Error
Barometric Pressure [pa]	99728.9	1.3	99728.9	1.3	99728.9	1.3	98633.8	1.3	98633.8	1.3	98633.8	1.3
Air Face Velocity [m/s]	3.06	0.11	3.04	0.11	3.07	0.11	3.09	0.11	3.09	0.11	3.05	0.11
Front Tdb [C]	32.99	0.05	33.01	0.05	33.09	0.05	32.96	0.05	33.03	0.05	32.94	0.05
Front Twb [C]	27.92	0.06	27.80	0.06	27.91	0.08	25.59	0.06	25.53	0.05	25.61	0.06
Wfront [g/kg]	22.22	0.10	21.99	0.09	22.15	0.13	18.27	0.08	18.14	0.08	18.31	0.08
Back Tdb [C] Zeroed	29.77	0.05	29.00	0.05	28.50	0.05	29.35	0.05	28.48	0.05	27.54	0.05
Back Twb [C] Zeroed	27.29	0.05	26.94	0.05	26.78	0.06	25.35	0.05	25.04	0.04	24.69	0.04
Wback [g/kg]	22.43	0.07	22.10	0.07	22.02	0.08	19.39	0.06	19.24	0.06	19.05	0.06
Water Flow Rate [kg/s]	0.050	0.000	0.071	0.000	0.092	0.000	0.050	0.000	0.071	0.000	0.092	0.000
Water Inlet [C]	10.01	0.07	10.19	0.05	10.01	0.06	9.98	0.06	10.10	0.07	9.98	0.06
Water Outlet [C]	11.95	0.06	12.25	0.05	12.07	0.05	11.60	0.05	11.83	0.06	11.67	0.06
Calculated Measurements	Value	Error	Value	Error	Value	Error	Value	Error	Value	Error	Value	Error
Air Mass Flow Rate [kg/s]	0.079	0.003	0.079	0.003	0.080	0.003	0.079	0.003	0.079	0.003	0.079	0.003
Air Side Heat Transfer [W]	224.5	26.6	306.9	26.4	409.1	35.1	70.7	21.5	152.0	21.3	294.0	23.4
Air Side Sensible Heat Transfer [W]	265.3	30.4	330.0	29.4	382.2	39.9	297.0	25.5	375.2	26.0	442.3	28.0
Water Side Heat Transfer [W]	411.2	14.7	612.3	16.1	792.0	21.8	339.3	12.3	510.4	19.5	650.4	24.1
% difference	-45.4		-49.9		-48.3		-79.2		-70.2		-54.8	
Sensible UA Value CF [W/C]	13.0	0.8	16.7	0.8	19.4	1.2	14.6	0.7	19.0	0.8	22.8	1.0
LTMD [C]	20.39	0.06	19.77	0.05	19.73	0.05	20.35	0.05	19.75	0.06	19.36	0.05
Epsilon	0.124		0.170		0.222		0.039		0.083		0.162	
Fp	0.051		0.071		0.092		0.019		0.042		0.080	
Epsilon (sensible)	0.146		0.183		0.207		0.163		0.206		0.244	
Enthalpy In [kJ/kg]	90.09	0.26	89.51	0.24	90.02	0.33	79.95	0.21	79.68	0.20	80.03	0.21
Enthalpy Out [kJ/kg]	87.23	0.19	85.61	0.19	84.88	0.22	79.05	0.17	77.76	0.17	76.30	0.16
Air Specific Volume [m3/kg]	0.9016	0.0002	0.8986	0.0002	0.8972	0.0002	0.9062	0.0002	0.9032	0.0002	0.9001	0.0002

Test Information												
Date Tested:	2/27/07		2/27/07		2/27/07		2/27/07		2/27/07		2/27/07	
Nozzle:	8009		8009		8009		8009		8009		8009	
Nozzle Area [m2]	2.85E-06		2.85E-06		2.85E-06		2.85E-06		2.85E-06		2.85E-06	
Nozzle Pressure [psi][Pa]	30.0	206842.7	62.0	427475.0	105.0	723949.5	30.0	206842.7	62.0	427475.0	105.0	723949.5
Measurements	Value	Error	Value	Error	Value	Error	Value	Error	Value	Error	Value	Error
Barometric Pressure [pa]	99795.6	1.3	99795.6	1.3	99795.6	1.3	99795.6	1.3	99795.6	1.3	99795.6	1.3
Air Face Velocity [m/s]	3.05	0.11	3.00	0.11	2.94	0.11	3.01	0.11	2.97	0.11	2.92	0.11
Front Tdb [C]	33.03	0.05	33.01	0.05	33.01	0.05	33.00	0.05	33.02	0.05	32.98	0.05
Front Twb [C]	27.94	0.08	27.89	0.08	27.99	0.07	25.58	0.06	25.56	0.06	25.46	0.09
Wfront [g/kg]	22.23	0.12	22.15	0.12	22.33	0.12	17.98	0.08	17.94	0.08	17.78	0.13
Back Tdb [C] Zeroed	29.25	0.05	27.96	0.05	26.10	0.05	28.53	0.05	26.84	0.05	24.70	0.05
Back Twb [C] Zeroed	26.14	0.05	25.44	0.05	24.32	0.05	23.85	0.05	23.20	0.04	22.00	0.06
Wback [g/kg]	20.55	0.07	19.88	0.07	18.80	0.06	17.01	0.06	16.71	0.06	15.79	0.07
Water Flow Rate [kg/s]	0.051	0.000	0.071	0.000	0.092	0.000	0.050	0.000	0.071	0.000	0.091	0.000
Water Inlet [C]	10.10	0.06	10.13	0.05	10.14	0.05	10.05	0.06	10.12	0.06	10.08	0.05
Water Outlet [C]	10.96	0.05	11.35	0.05	12.04	0.05	10.50	0.05	11.02	0.06	11.59	0.05
Calculated Measurements	Value	Error	Value	Error	Value	Error	Value	Error	Value	Error	Value	Error
Air Mass Flow Rate [kg/s]	0.079	0.003	0.078	0.003	0.077	0.003	0.079	0.003	0.078	0.003	0.077	0.003
Air Side Heat Transfer [W]	650.4	36.8	864.5	42.1	1250.7	53.5	557.9	29.4	746.0	33.9	1056.2	48.8
Air Side Sensible Heat Transfer [W]	312.5	36.0	412.5	37.1	557.4	38.8	364.7	27.5	500.4	29.0	664.1	43.2
Water Side Heat Transfer [W]	182.6	12.6	363.5	16.0	734.2	20.2	95.0	12.1	266.5	18.2	579.3	20.1
% difference	256.2		137.9		70.3		487.5		179.9		82.3	
Sensible UA Value CF [W/C]	15.2	0.9	21.0	1.0	30.4	1.2	17.9	0.7	26.0	0.9	37.3	1.3
LTMD [C]	20.58	0.05	19.68	0.05	18.35	0.05	20.43	0.05	19.24	0.05	17.79	0.05
Epsilon	0.358		0.483		0.707		0.309		0.417		0.595	
Fp	0.140		0.193		0.289		0.146		0.202		0.300	
Epsilon (sensible)	0.172		0.230		0.315		0.202		0.279		0.374	
Enthalpy In [kJ/kg]	90.15	0.31	89.92	0.31	90.38	0.30	79.24	0.22	79.16	0.20	78.71	0.32
Enthalpy Out [kJ/kg]	81.91	0.19	78.85	0.19	74.16	0.17	72.13	0.17	69.59	0.16	65.05	0.18
Air Specific Volume [m3/kg]	0.8972	0.0002	0.8926	0.0002	0.8862	0.0002	0.8909	0.0002	0.8855	0.0002	0.8786	0.0002

Test Information												
Date Tested:	3/3/07		3/3/07		3/3/07		3/4/07		3/4/07		3/4/07	
Nozzle:	2x 8005		2x 8005		2x 8005		2x 8005		2x 8005		2x 8005	
Nozzle Area [m2]	3.18E-06		3.18E-06		3.18E-06		3.18E-06		3.18E-06		3.18E-06	
Nozzle Pressure [psi][Pa]	24.0	165474.2	49.0	337843.1	85.0	586054.4	24.0	165474.2	49.0	337843.1	85.0	586054.4
Measurements	Value	Error	Value	Error	Value	Error	Value	Error	Value	Error	Value	Error
Barometric Pressure [pa]	98660.4	1.3	98660.4	1.3	98660.4	1.3	100580.3	1.3	100580.3	1.3	100580.3	1.3
Air Face Velocity [m/s]	3.12	0.11	3.09	0.11	3.06	0.11	3.09	0.11	3.07	0.11	3.03	0.11
Front Tdb [C]	33.00	0.05	33.02	0.05	33.02	0.05	33.00	0.05	33.01	0.05	32.92	0.05
Front Twb [C]	27.86	0.06	27.86	0.06	27.81	0.06	25.57	0.05	25.73	0.05	25.59	0.05
Wfront [g/kg]	22.38	0.10	22.36	0.09	22.27	0.09	17.79	0.07	18.06	0.07	17.86	0.07
Back Tdb [C] Zeroed	28.78	0.05	27.36	0.05	25.49	0.05	28.13	0.05	26.52	0.05	24.27	0.05
Back Twb [C] Zeroed	27.22	0.05	26.22	0.04	24.80	0.04	24.56	0.04	23.85	0.05	22.50	0.04
Wback [g/kg]	22.98	0.07	21.77	0.07	20.09	0.06	18.18	0.06	17.71	0.06	16.57	0.05
Water Flow Rate [kg/s]	0.051	0.000	0.071	0.000	0.092	0.000	0.050	0.000	0.071	0.000	0.092	0.000
Water Inlet [C]	9.99	0.07	10.08	0.07	10.10	0.06	9.90	0.05	10.12	0.06	10.12	0.05
Water Outlet [C]	12.21	0.05	12.58	0.06	13.00	0.05	11.58	0.05	12.13	0.06	12.32	0.05
Calculated Measurements	Value	Error	Value	Error	Value	Error	Value	Error	Value	Error	Value	Error
Air Mass Flow Rate [kg/s]	0.080	0.003	0.079	0.003	0.079	0.003	0.081	0.003	0.081	0.003	0.081	0.003
Air Side Heat Transfer [W]	228.1	26.4	591.3	31.2	1065.3	44.5	331.0	23.6	618.9	30.1	989.2	40.8
Air Side Sensible Heat Transfer [W]	351.5	30.8	470.0	31.0	625.2	34.7	410.2	26.4	546.3	29.7	725.3	34.2
Water Side Heat Transfer [W]	469.4	15.3	743.9	21.6	1113.4	24.9	352.0	11.2	595.8	17.4	844.2	20.7
% difference	-51.4		-20.5		-4.3		-6.0		3.9		17.2	
Sensible UA Value CF [W/C]	17.8	0.9	25.0	1.0	35.5	1.2	20.7	0.7	29.5	0.9	42.2	1.2
LTMD [C]	19.77	0.06	18.82	0.06	17.61	0.05	19.78	0.05	18.55	0.05	17.18	0.05
Epsilon	0.124		0.324		0.584		0.176		0.332		0.536	
Fp	0.051		0.136		0.252		0.089		0.169		0.278	
Epsilon (sensible)	0.191		0.257		0.343		0.218		0.294		0.393	
Enthalpy In [kJ/kg]	90.49	0.25	90.49	0.23	90.25	0.24	78.76	0.19	79.45	0.20	78.85	0.19
Enthalpy Out [kJ/kg]	87.63	0.19	83.04	0.18	76.82	0.17	74.69	0.16	71.81	0.16	66.59	0.15
Air Specific Volume [m3/kg]	0.9093	0.0002	0.9034	0.0002	0.8960	0.0002	0.8839	0.0002	0.8784	0.0002	0.8710	0.0002

Test Information												
Date Tested:	3/5/07		3/5/07		3/5/07		3/6/07		3/6/07		3/6/07	
Nozzle:	8015		8015		8015		8015		8015		8015	
Nozzle Area [m2]	4.48E-06		4.48E-06		4.48E-06		4.48E-06		4.48E-06		4.48E-06	
Nozzle Pressure [psi][Pa]	10.5	72395.0	22.0	151684.7	38.0	262000.8	10.5	72395.0	22.0	151684.7	38.0	262000.8
Measurements	Value	Error	Value	Error	Value	Error	Value	Error	Value	Error	Value	Error
Barometric Pressure [pa]	100687.0	1.3	100687.0	1.3	100687.0	1.3	100541.3	1.3	100541.3	1.3	100541.3	1.3
Air Face Velocity [m/s]	3.09	0.11	3.07	0.11	3.05	0.11	3.09	0.11	3.08	0.11	3.04	0.11
Front Tdb [C]	32.98	0.05	33.03	0.05	32.99	0.05	32.99	0.05	33.01	0.05	33.04	0.05
Front Twb [C]	27.98	0.06	27.50	0.14	27.88	0.05	25.63	0.05	25.67	0.07	25.73	0.05
Wfront [g/kg]	22.09	0.09	21.18	0.21	21.91	0.08	17.92	0.07	17.97	0.09	18.06	0.08
Back Tdb [C] Zeroed	29.41	0.05	28.05	0.09	27.55	0.05	29.07	0.05	27.94	0.05	26.85	0.05
Back Twb [C] Zeroed	26.66	0.04	25.61	0.18	25.61	0.04	24.42	0.05	24.14	0.05	23.68	0.05
Wback [g/kg]	21.19	0.07	19.94	0.25	20.16	0.06	17.55	0.06	17.58	0.07	17.31	0.06
Water Flow Rate [kg/s]	0.050	0.000	0.071	0.000	0.092	0.000	0.050	0.000	0.071	0.000	0.092	0.000
Water Inlet [C]	5.04	0.05	4.75	0.07	5.01	0.05	5.01	0.05	5.00	0.06	5.02	0.05
Water Outlet [C]	7.47	0.05	7.28	0.08	7.64	0.05	7.07	0.05	7.26	0.05	7.21	0.05
Calculated Measurements	Value	Error	Value	Error	Value	Error	Value	Error	Value	Error	Value	Error
Air Mass Flow Rate [kg/s]	0.080	0.003	0.081	0.003	0.080	0.003	0.081	0.003	0.081	0.003	0.080	0.003
Air Side Heat Transfer [W]	484.2	28.9	674.7	71.9	814.3	36.5	405.8	25.1	505.5	30.6	669.8	31.6
Air Side Sensible Heat Transfer [W]	300.0	28.2	419.5	64.3	455.5	29.5	329.4	25.3	425.8	31.5	516.0	29.3
Water Side Heat Transfer [W]	514.2	11.6	755.0	20.2	1013.4	20.3	430.6	11.4	671.2	16.4	848.9	20.8
% difference	-5.8		-10.6		-19.6		-5.8		-24.7		-21.1	
Sensible UA Value CF [W/C]	12.0	0.6	17.1	1.4	19.0	0.8	13.2	0.6	17.5	0.7	21.7	0.8
LTMD [C]	24.93	0.05	24.51	0.08	23.92	0.05	24.98	0.05	24.31	0.05	23.77	0.05
Epsilon	0.215		0.295		0.362		0.179		0.222		0.297	
Fp	0.091		0.130		0.155		0.089		0.111		0.148	
Epsilon (sensible)	0.133		0.184		0.203		0.145		0.187		0.229	
Enthalpy In [kJ/kg]	89.74	0.23	87.47	0.55	89.29	0.22	79.07	0.20	79.22	0.24	79.48	0.20
Enthalpy Out [kJ/kg]	83.71	0.18	79.10	0.64	79.13	0.17	74.06	0.16	72.98	0.19	71.14	0.16
Air Specific Volume [m3/kg]	0.8925	0.0002	0.8861	0.0004	0.8853	0.0002	0.8864	0.0002	0.8831	0.0002	0.8799	0.0002

Test Information												
Date Tested:	3/6/07		3/6/07		3/6/07		3/6/07		3/6/07		3/6/07	
Nozzle:	8009		8009		8009		8009		8009		8009	
Nozzle Area [m2]	2.85E-06		2.85E-06		2.85E-06		2.85E-06		2.85E-06		2.85E-06	
Nozzle Pressure [psi][Pa]	30.0	206842.7	62.0	427475.0	85.0	586054.4	30.0	206842.7	62.0	427475.0	105.0	723949.5
Measurements	Value	Error	Value	Error	Value	Error	Value	Error	Value	Error	Value	Error
Barometric Pressure [pa]	100541.3	1.3	100541.3	1.3	100541.3	1.3	100541.3	1.3	100541.3	1.3	100541.3	1.3
Air Face Velocity [m/s]	3.01	0.11	2.97	0.11	2.92	0.11	3.04	0.11	2.98	0.11	2.92	0.11
Front Tdb [C]	33.00	0.05	33.00	0.05	32.98	0.05	33.02	0.05	33.00	0.05	33.01	0.05
Front Twb [C]	27.78	0.06	27.75	0.05	27.77	0.06	25.74	0.05	25.75	0.05	25.68	0.05
Wfront [g/kg]	21.75	0.09	21.69	0.08	21.75	0.09	18.09	0.07	18.11	0.08	17.98	0.08
Back Tdb [C] Zeroed	28.86	0.05	26.95	0.05	24.93	0.05	28.40	0.05	26.35	0.05	23.70	0.05
Back Twb [C] Zeroed	26.53	0.04	25.44	0.04	24.01	0.04	24.41	0.04	23.50	0.04	21.95	0.05
Wback [g/kg]	21.24	0.07	20.15	0.06	18.66	0.06	17.83	0.06	17.25	0.06	16.01	0.06
Water Flow Rate [kg/s]	0.050	0.000	0.071	0.000	0.092	0.000	0.050	0.000	0.071	0.000	0.092	0.000
Water Inlet [C]	5.07	0.05	4.99	0.05	5.05	0.05	5.08	0.05	5.06	0.05	5.01	0.05
Water Outlet [C]	7.19	0.05	7.76	0.05	8.45	0.05	6.60	0.05	7.11	0.05	7.80	0.05
Calculated Measurements	Value	Error	Value	Error	Value	Error	Value	Error	Value	Error	Value	Error
Air Mass Flow Rate [kg/s]	0.079	0.003	0.078	0.003	0.077	0.003	0.080	0.003	0.079	0.003	0.078	0.003
Air Side Heat Transfer [W]	441.9	28.1	798.9	36.4	1257.8	51.7	436.5	25.5	715.3	32.9	1143.6	47.1
Air Side Sensible Heat Transfer [W]	339.7	28.8	492.8	30.1	650.4	34.8	382.2	25.9	543.6	29.9	753.0	35.9
Water Side Heat Transfer [W]	445.7	11.0	829.5	16.1	1312.9	20.5	323.2	11.1	612.6	15.8	1073.8	20.5
% difference	-0.8		-3.7		-4.2		35.1		16.8		6.5	
Sensible UA Value CF [W/C]	13.7	0.6	20.9	0.7	29.4	0.9	15.4	0.6	23.1	0.7	34.6	1.0
LTMD [C]	24.79	0.05	23.56	0.05	22.12	0.05	24.83	0.05	23.52	0.05	21.79	0.05
Epsilon	0.201		0.365		0.581		0.196		0.325		0.523	
Fp	0.085		0.159		0.258		0.095		0.160		0.267	
Epsilon (sensible)	0.154		0.225		0.300		0.171		0.247		0.344	
Enthalpy In [kJ/kg]	88.88	0.24	88.74	0.22	88.86	0.23	79.54	0.19	79.56	0.20	79.25	0.20
Enthalpy Out [kJ/kg]	83.25	0.18	78.48	0.17	72.58	0.16	74.06	0.16	70.47	0.16	64.56	0.15
Air Specific Volume [m3/kg]	0.8912	0.0002	0.8844	0.0002	0.8768	0.0002	0.8854	0.0002	0.8790	0.0002	0.8704	0.0002

Test Information												
Date Tested:	3/5/07		3/5/07		3/5/07		3/4/07		3/4/07		3/4/07	
Nozzle:	2x 8005		2x 8005		2x 8005		2x 8005		2x 8005		2x 8005	
Nozzle Area [m2]	3.18E-06		3.18E-06		3.18E-06		3.18E-06		3.18E-06		3.18E-06	
Nozzle Pressure [psi][Pa]	24.0	165474.2	49.0	337843.1	85.0	586054.4	24.0	165474.2	49.0	337843.1	85.0	586054.4
Measurements	Value	Error	Value	Error	Value	Error	Value	Error	Value	Error	Value	Error
Barometric Pressure [pa]	100687.0	1.3	100687.0	1.3	100687.0	1.3	100580.3	1.3	100580.3	1.3	100580.3	1.3
Air Face Velocity [m/s]	3.07	0.11	3.04	0.11	3.00	0.11	3.08	0.11	3.05	0.11	3.01	0.11
Front Tdb [C]	32.97	0.05	33.00	0.05	33.01	0.05	33.03	0.05	32.99	0.05	33.03	0.05
Front Twb [C]	27.81	0.06	27.74	0.06	27.63	0.07	25.72	0.05	25.74	0.05	25.61	0.05
Wfront [g/kg]	21.78	0.09	21.63	0.09	21.42	0.11	18.04	0.08	18.09	0.07	17.84	0.08
Back Tdb [C] Zeroed	28.37	0.05	26.64	0.05	24.30	0.05	27.42	0.05	25.55	0.05	22.91	0.05
Back Twb [C] Zeroed	26.15	0.05	25.00	0.05	23.26	0.05	24.20	0.04	23.17	0.04	21.39	0.05
Wback [g/kg]	20.74	0.07	19.52	0.07	17.70	0.06	17.89	0.06	17.07	0.06	15.52	0.06
Water Flow Rate [kg/s]	0.052	0.000	0.071	0.000	0.092	0.000	0.051	0.000	0.071	0.000	0.092	0.000
Water Inlet [C]	5.13	0.06	5.00	0.06	5.14	0.05	5.03	0.06	5.02	0.06	4.95	0.06
Water Outlet [C]	7.20	0.05	7.58	0.05	8.21	0.05	7.01	0.05	7.40	0.05	7.67	0.05
Calculated Measurements	Value	Error	Value	Error	Value	Error	Value	Error	Value	Error	Value	Error
Air Mass Flow Rate [kg/s]	0.080	0.003	0.080	0.003	0.080	0.003	0.081	0.003	0.081	0.003	0.081	0.003
Air Side Heat Transfer [W]	601.2	31.2	962.5	42.1	1482.1	60.4	502.5	27.3	837.2	36.2	1326.4	52.3
Air Side Sensible Heat Transfer [W]	386.7	28.9	531.8	33.5	726.5	42.5	472.5	28.3	625.5	31.8	849.3	38.4
Water Side Heat Transfer [W]	447.8	12.9	766.3	17.3	1183.0	20.7	421.8	13.4	710.0	17.5	1046.1	22.7
% difference	34.2		25.6		25.3		19.1		17.9		26.8	
Sensible UA Value CF [W/C]	15.8	0.6	22.7	0.8	33.2	1.1	19.6	0.6	27.2	0.8	39.6	1.0
LTMD [C]	24.48	0.05	23.47	0.05	21.86	0.05	24.16	0.05	22.97	0.05	21.45	0.05
Epsilon	0.268		0.429		0.664		0.221		0.369		0.583	
Fp	0.113		0.186		0.295		0.109		0.184		0.299	
Epsilon (sensible)	0.172		0.237		0.326		0.207		0.275		0.373	
Enthalpy In [kJ/kg]	88.94	0.22	88.59	0.24	88.06	0.29	79.42	0.20	79.52	0.20	78.92	0.20
Enthalpy Out [kJ/kg]	81.46	0.18	76.55	0.17	69.50	0.17	73.23	0.16	69.17	0.15	62.51	0.15
Air Specific Volume [m3/kg]	0.8882	0.0002	0.8816	0.0002	0.8729	0.0002	0.8826	0.0002	0.8759	0.0002	0.8666	0.0002

Test Information												
Date Tested:	3/12/07		3/12/07		3/12/07		3/12/07		3/12/07		3/12/07	
Nozzle:	8015		8015		8015		8015		8015		8015	
Nozzle Area [m2]	4.48E-06		4.48E-06		4.48E-06		4.48E-06		4.48E-06		4.48E-06	
Nozzle Pressure [psi][Pa]	10.5	72395.0	22.0	151684.7	38.0	262000.8	10.5	72395.0	22.0	151684.7	38.0	262000.8
Measurements	Value	Error	Value	Error	Value	Error	Value	Error	Value	Error	Value	Error
Barometric Pressure [pa]	100381.3	1.3	100381.3	1.3	100381.3	1.3	100381.3	1.3	100381.3	1.3	100381.3	1.3
Air Face Velocity [m/s]	0.97	0.10	0.96	0.10	0.94	0.10	0.96	0.10	0.95	0.10	0.94	0.10
Front Tdb [C]	33.04	0.05	32.97	0.05	33.06	0.05	32.93	0.05	32.94	0.05	33.00	0.05
Front Twb [C]	27.93	0.10	27.58	0.07	27.75	0.06	25.75	0.06	25.59	0.08	25.59	0.06
Wfront [g/kg]	22.06	0.15	21.43	0.11	21.70	0.09	18.17	0.08	17.90	0.11	17.87	0.08
Back Tdb [C] Zeroed	27.42	0.05	24.96	0.05	22.90	0.05	26.11	0.05	23.70	0.05	21.78	0.05
Back Twb [C] Zeroed	25.92	0.05	23.86	0.05	22.13	0.05	23.33	0.05	21.81	0.05	20.50	0.04
Wback [g/kg]	20.81	0.08	18.43	0.06	16.64	0.06	17.11	0.06	15.83	0.06	14.78	0.05
Water Flow Rate [kg/s]	0.050	0.000	0.071	0.000	0.092	0.000	0.051	0.000	0.071	0.000	0.092	0.000
Water Inlet [C]	10.10	0.06	10.12	0.06	9.98	0.06	9.82	0.05	9.91	0.07	10.00	0.06
Water Outlet [C]	11.81	0.05	11.95	0.05	11.91	0.05	11.33	0.05	11.49	0.06	11.62	0.05
Calculated Measurements	Value	Error	Value	Error	Value	Error	Value	Error	Value	Error	Value	Error
Air Mass Flow Rate [kg/s]	0.025	0.003	0.025	0.003	0.025	0.003	0.025	0.003	0.025	0.003	0.025	0.003
Air Side Heat Transfer [W]	230.6	27.1	404.4	44.9	586.8	65.7	248.2	27.7	376.3	42.1	489.3	55.0
Air Side Sensible Heat Transfer [W]	149.3	21.1	211.4	25.2	265.4	30.7	179.8	20.9	242.8	28.6	292.3	33.5
Water Side Heat Transfer [W]	362.1	11.8	541.3	16.9	740.9	22.7	321.8	11.6	467.3	20.2	622.1	22.3
% difference	-36.3		-25.3		-20.8		-22.9		-19.5		-21.4	
Sensible UA Value CF [W/C]	7.8	0.6	11.9	0.9	15.9	1.1	9.6	0.6	14.0	1.0	18.1	1.3
LTMD [C]	19.21	0.05	17.75	0.05	16.70	0.05	18.82	0.05	17.34	0.06	16.11	0.05
Epsilon	0.394		0.699		1.014		0.422		0.643		0.845	
Fp	0.161		0.296		0.427		0.207		0.322		0.426	
Epsilon (sensible)	0.255		0.365		0.459		0.305		0.415		0.505	
Enthalpy In [kJ/kg]	89.72	0.38	88.03	0.29	88.82	0.24	79.65	0.22	78.98	0.29	78.95	0.22
Enthalpy Out [kJ/kg]	80.66	0.21	72.02	0.17	65.34	0.15	69.87	0.16	64.12	0.15	59.45	0.14
Air Specific Volume [m3/kg]	0.8882	0.0002	0.8810	0.0002	0.8750	0.0002	0.8816	0.0002	0.8748	0.0002	0.8700	0.0002

Test Information												
Date Tested:	3/9/07		3/9/07		3/9/07		3/9/07		3/9/07		3/9/07	
Nozzle:	8009		8009		8009		8009		8009		8009	
Nozzle Area [m2]	2.85E-06		2.85E-06		2.85E-06		2.85E-06		2.85E-06		2.85E-06	
Nozzle Pressure [psi][Pa]	30.0	206842.7	62.0	427475.0	105.0	723949.5	30.0	206842.7	62.0	427475.0	105.0	723949.5
Measurements	Value	Error	Value	Error	Value	Error	Value	Error	Value	Error	Value	Error
Barometric Pressure [pa]	99807.0	1.3	99807.0	1.3	99807.0	1.3	99807.0	1.3	99807.0	1.3	99807.0	1.3
Air Face Velocity [m/s]	0.98	0.10	0.96	0.11	0.94	0.11	0.98	0.10	0.97	0.11	0.95	0.11
Front Tdb [C]	33.16	0.05	33.06	0.05	32.97	0.05	33.03	0.05	33.02	0.05	33.07	0.05
Front Twb [C]	27.90	0.05	27.65	0.06	27.82	0.07	25.61	0.06	25.69	0.06	25.60	0.06
Wfront [g/kg]	22.09	0.08	21.66	0.09	22.02	0.11	18.02	0.09	18.17	0.08	17.98	0.09
Back Tdb [C] Zeroed	24.60	0.05	22.21	0.05	20.37	0.05	22.92	0.05	20.53	0.05	18.93	0.05
Back Twb [C] Zeroed	23.55	0.05	21.75	0.04	20.10	0.05	21.40	0.05	19.71	0.04	18.48	0.04
Wback [g/kg]	18.21	0.06	16.48	0.05	14.90	0.05	15.66	0.05	14.30	0.05	13.35	0.05
Water Flow Rate [kg/s]	0.051	0.000	0.071	0.000	0.092	0.000	0.051	0.000	0.071	0.000	0.092	0.000
Water Inlet [C]	9.95	0.06	10.02	0.05	10.11	0.05	9.85	0.06	9.97	0.06	10.00	0.06
Water Outlet [C]	12.05	0.05	12.05	0.05	12.19	0.05	11.56	0.05	11.72	0.06	11.72	0.05
Calculated Measurements	Value	Error	Value	Error	Value	Error	Value	Error	Value	Error	Value	Error
Air Mass Flow Rate [kg/s]	0.026	0.003	0.025	0.003	0.025	0.003	0.026	0.003	0.026	0.003	0.025	0.003
Air Side Heat Transfer [W]	483.3	52.4	623.4	68.6	786.4	88.0	426.8	46.3	586.7	64.3	672.1	75.0
Air Side Sensible Heat Transfer [W]	229.7	25.9	288.3	32.8	331.7	38.3	271.5	30.3	334.2	37.2	373.5	42.3
Water Side Heat Transfer [W]	444.5	12.2	604.6	16.3	799.3	20.7	361.7	11.9	519.3	18.2	659.4	21.5
% difference	8.7		3.1		-1.6		18.0		13.0		1.9	
Sensible UA Value CF [W/C]	13.0	0.8	17.8	1.1	22.3	1.5	16.0	1.0	21.8	1.4	26.2	1.7
LTMD [C]	17.68	0.05	16.20	0.05	14.91	0.05	16.92	0.05	15.31	0.06	14.24	0.06
Epsilon	0.810		1.061		1.362		0.710		0.985		1.142	
Fp	0.339		0.451		0.570		0.357		0.493		0.578	
Epsilon (sensible)	0.385		0.491		0.575		0.452		0.561		0.635	
Enthalpy In [kJ/kg]	89.94	0.22	88.73	0.25	89.54	0.28	79.36	0.23	79.73	0.21	79.32	0.22
Enthalpy Out [kJ/kg]	71.09	0.16	64.21	0.15	58.31	0.14	62.86	0.15	56.95	0.14	52.89	0.13
Air Specific Volume [m3/kg]	0.8838	0.0002	0.8773	0.0002	0.8715	0.0002	0.8779	0.0002	0.8714	0.0002	0.8667	0.0002

Test Information												
Date Tested:	3/16/07		3/16/07		3/16/07		3/16/07		3/16/07		3/16/07	
Nozzle:	2x 8005		2x 8005		2x 8005		2x 8005		2x 8005		2x 8005	
Nozzle Area [m2]	3.18E-06		3.18E-06		3.18E-06		3.18E-06		3.18E-06		3.18E-06	
Nozzle Pressure [psi][Pa]	24.0	165474.2	49.0	337843.1	85.0	586054.4	24.0	165474.2	49.0	337843.1	85.0	586054.4
Measurements	Value	Error	Value	Error	Value	Error	Value	Error	Value	Error	Value	Error
Barometric Pressure [pa]	100940.3	1.3	100940.3	1.3	100940.3	1.3	100940.3	1.3	100940.3	1.3	100940.3	1.3
Air Face Velocity [m/s]	0.94	0.11	0.93	0.11	0.93	0.11	0.95	0.11	0.94	0.11	0.94	0.11
Front Tdb [C]	33.04	0.05	33.10	0.05	33.08	0.05	32.93	0.05	32.97	0.05	33.00	0.05
Front Twb [C]	27.81	0.07	27.72	0.08	27.71	0.09	25.69	0.07	25.35	0.16	25.80	0.07
Wfront [g/kg]	21.68	0.10	21.50	0.12	21.49	0.14	17.95	0.10	17.36	0.22	18.12	0.09
Back Tdb [C] Zeroed	24.09	0.05	21.34	0.05	18.37	0.05	22.68	0.05	19.39	0.06	17.54	0.05
Back Twb [C] Zeroed	23.62	0.05	21.07	0.05	18.18	0.05	21.62	0.05	18.97	0.07	17.26	0.04
Wback [g/kg]	18.31	0.06	15.67	0.05	13.06	0.05	15.89	0.05	13.64	0.07	12.26	0.04
Water Flow Rate [kg/s]	0.050	0.000	0.071	0.000	0.093	0.000	0.050	0.000	0.071	0.000	0.092	0.000
Water Inlet [C]	10.00	0.07	10.01	0.05	9.99	0.05	10.14	0.06	9.91	0.06	10.04	0.06
Water Outlet [C]	12.83	0.06	12.84	0.05	12.91	0.05	12.64	0.05	12.30	0.05	12.51	0.05
Calculated Measurements	Value	Error	Value	Error	Value	Error	Value	Error	Value	Error	Value	Error
Air Mass Flow Rate [kg/s]	0.025	0.003	0.025	0.003	0.025	0.003	0.025	0.003	0.025	0.003	0.026	0.003
Air Side Heat Transfer [W]	449.8	50.9	678.2	77.6	931.9	106.8	403.2	45.4	597.6	69.0	790.6	89.7
Air Side Sensible Heat Transfer [W]	234.8	27.8	307.6	36.6	389.9	46.3	270.2	31.3	358.0	45.1	411.0	47.3
Water Side Heat Transfer [W]	591.1	14.5	836.7	16.2	1131.3	21.4	520.6	12.6	714.8	17.8	950.4	22.6
% difference	-23.9		-18.9		-17.6		-22.5		-16.4		-16.8	
Sensible UA Value CF [W/C]	13.8	0.9	20.0	1.3	29.0	1.9	16.8	1.1	24.9	1.7	31.8	2.0
LTMD [C]	16.97	0.06	15.37	0.05	13.42	0.06	16.11	0.05	14.36	0.06	12.92	0.06
Epsilon	0.776		1.170		1.586		0.695		1.016		1.341	
Fp	0.340		0.518		0.707		0.365		0.549		0.698	
Epsilon (sensible)	0.405		0.530		0.664		0.465		0.609		0.697	
Enthalpy In [kJ/kg]	88.77	0.26	88.36	0.31	88.32	0.36	79.08	0.25	77.61	0.56	79.58	0.24
Enthalpy Out [kJ/kg]	70.83	0.16	61.28	0.14	51.58	0.14	63.20	0.15	54.10	0.19	48.71	0.12
Air Specific Volume [m3/kg]	0.8699	0.0002	0.8604	0.0002	0.8505	0.0002	0.8656	0.0002	0.8561	0.0002	0.8496	0.0002

Test Information												
Date Tested:	3/13/07		3/13/07		3/13/07		3/13/07		3/13/07		3/13/07	
Nozzle:	8015		8015		8015		8015		8015		8015	
Nozzle Area [m2]	4.48E-06		4.48E-06		4.48E-06		4.48E-06		4.48E-06		4.48E-06	
Nozzle Pressure [psi][Pa]	10.5	72395.0	22.0	151684.7	38.0	262000.8	10.5	72395.0	22.0	151684.7	38.0	262000.8
Measurements	Value	Error	Value	Error	Value	Error	Value	Error	Value	Error	Value	Error
Barometric Pressure [pa]	99488.9	1.3	99488.9	1.3	99488.9	1.3	99488.9	1.3	99488.9	1.3	99488.9	1.3
Air Face Velocity [m/s]	0.96	0.10	0.94	0.10	0.93	0.11	0.95	0.10	0.94	0.10	0.92	0.11
Front Tdb [C]	32.98	0.05	33.00	0.05	32.97	0.05	32.97	0.05	32.95	0.05	33.04	0.05
Front Twb [C]	27.69	0.05	27.85	0.06	27.83	0.06	25.78	0.08	25.62	0.06	25.58	0.07
Wfront [g/kg]	21.84	0.08	22.14	0.09	22.11	0.09	18.41	0.11	18.14	0.08	18.03	0.10
Back Tdb [C] Zeroed	26.89	0.05	24.21	0.05	21.52	0.05	25.29	0.05	22.30	0.05	20.18	0.05
Back Twb [C] Zeroed	25.23	0.05	23.32	0.04	20.91	0.04	22.79	0.06	20.56	0.05	18.98	0.05
Wback [g/kg]	20.05	0.07	18.07	0.06	15.60	0.05	16.78	0.07	14.78	0.05	13.52	0.05
Water Flow Rate [kg/s]	0.051	0.000	0.071	0.000	0.092	0.000	0.051	0.000	0.071	0.000	0.092	0.000
Water Inlet [C]	5.17	0.06	5.17	0.05	4.99	0.05	5.00	0.06	5.02	0.05	5.00	0.05
Water Outlet [C]	7.19	0.06	7.40	0.05	7.29	0.05	6.84	0.05	6.94	0.05	6.93	0.05
Calculated Measurements	Value	Error	Value	Error	Value	Error	Value	Error	Value	Error	Value	Error
Air Mass Flow Rate [kg/s]	0.025	0.003	0.025	0.003	0.025	0.003	0.025	0.003	0.025	0.003	0.024	0.003
Air Side Heat Transfer [W]	272.0	30.5	484.1	54.1	699.7	79.5	301.5	34.3	484.0	54.6	605.0	69.5
Air Side Sensible Heat Transfer [W]	158.4	18.9	227.6	26.4	294.0	34.3	198.6	24.1	273.2	31.5	325.9	38.3
Water Side Heat Transfer [W]	427.9	13.0	668.4	15.9	884.9	20.3	392.6	12.1	571.4	16.2	740.7	20.7
% difference	-36.4		-27.6		-20.9		-23.2		-15.3		-18.3	
Sensible UA Value CF [W/C]	6.7	0.5	10.3	0.7	14.2	1.0	8.6	0.6	12.8	0.8	16.2	1.1
LTMD [C]	23.70	0.05	22.16	0.05	20.77	0.05	23.09	0.05	21.35	0.05	20.15	0.05
Epsilon	0.392		0.701		1.016		0.432		0.700		0.882	
Fp	0.166		0.295		0.429		0.209		0.344		0.437	
Epsilon (sensible)	0.228		0.329		0.427		0.285		0.395		0.475	
Enthalpy In [kJ/kg]	89.11	0.22	89.88	0.23	89.78	0.24	80.30	0.29	79.59	0.21	79.40	0.25
Enthalpy Out [kJ/kg]	78.18	0.19	70.33	0.16	61.27	0.14	68.17	0.19	59.99	0.14	54.62	0.14
Air Specific Volume [m3/kg]	0.8934	0.0002	0.8864	0.0002	0.8784	0.0002	0.8875	0.0002	0.8797	0.0002	0.8746	0.0002

Test Information												
Date Tested:	3/11/07		3/11/07		3/11/07		3/11/07		3/11/07		3/11/07	
Nozzle:	8009		8009		8009		8009		8009		8009	
Nozzle Area [m2]	2.85E-06		2.85E-06		2.85E-06		2.85E-06		2.85E-06		2.85E-06	
Nozzle Pressure [psi][Pa]	30.0	206842.7	62.0	427475.0	105.0	723949.5	30.0	206842.7	62.0	427475.0	105.0	723949.5
Measurements	Value	Error	Value	Error	Value	Error	Value	Error	Value	Error	Value	Error
Barometric Pressure [pa]	100873.6	1.3	100873.6	1.3	100873.6	1.3	100873.6	1.3	100873.6	1.3	100873.6	1.3
Air Face Velocity [m/s]	0.98	0.10	0.96	0.11	0.94	0.11	0.98	0.11	0.97	0.11	0.94	0.11
Front Tdb [C]	32.97	0.05	33.04	0.05	32.94	0.05	32.97	0.05	32.95	0.05	33.03	0.05
Front Twb [C]	27.86	0.06	27.93	0.06	27.58	0.12	25.66	0.10	25.70	0.08	25.85	0.07
Wfront [g/kg]	21.84	0.09	21.94	0.09	21.33	0.19	17.90	0.13	17.98	0.10	18.21	0.10
Back Tdb [C] Zeroed	23.66	0.05	20.76	0.05	18.44	0.05	21.72	0.05	19.28	0.05	17.30	0.05
Back Twb [C] Zeroed	23.10	0.04	20.38	0.05	18.11	0.05	20.65	0.06	18.52	0.05	16.84	0.05
Wback [g/kg]	17.69	0.06	14.97	0.05	12.95	0.05	14.93	0.06	13.12	0.05	11.87	0.05
Water Flow Rate [kg/s]	0.050	0.000	0.071	0.000	0.092	0.000	0.050	0.000	0.071	0.000	0.092	0.000
Water Inlet [C]	5.18	0.06	5.08	0.05	4.95	0.05	5.00	0.06	5.06	0.05	4.91	0.05
Water Outlet [C]	7.70	0.05	7.60	0.05	7.43	0.05	7.15	0.05	7.29	0.05	7.11	0.05
Calculated Measurements	Value	Error	Value	Error	Value	Error	Value	Error	Value	Error	Value	Error
Air Mass Flow Rate [kg/s]	0.026	0.003	0.026	0.003	0.026	0.003	0.026	0.003	0.026	0.003	0.026	0.003
Air Side Heat Transfer [W]	527.8	57.1	792.0	86.9	930.7	105.2	506.8	55.3	693.8	76.3	831.5	93.8
Air Side Sensible Heat Transfer [W]	253.5	28.5	333.1	37.5	387.2	46.7	307.8	35.4	371.5	41.8	419.4	48.1
Water Side Heat Transfer [W]	531.6	11.7	750.1	15.8	955.4	20.1	457.0	11.8	661.6	15.8	847.6	20.2
% difference	-0.7		5.6		-2.6		10.9		4.9		-1.9	
Sensible UA Value CF [W/C]	11.7	0.7	16.5	1.0	20.5	1.4	14.7	0.9	19.2	1.2	22.9	1.4
LTMD [C]	21.70	0.05	20.17	0.05	18.86	0.05	20.94	0.05	19.38	0.05	18.33	0.05
Epsilon	0.727		1.089		1.296		0.685		0.948		1.149	
Fp	0.312		0.466		0.566		0.342		0.474		0.568	
Epsilon (sensible)	0.349		0.458		0.539		0.416		0.508		0.579	
Enthalpy In [kJ/kg]	89.09	0.23	89.41	0.24	87.75	0.48	79.00	0.35	79.18	0.27	79.85	0.26
Enthalpy Out [kJ/kg]	68.81	0.15	58.88	0.14	51.37	0.15	59.77	0.17	52.66	0.14	47.45	0.13
Air Specific Volume [m3/kg]	0.8718	0.0002	0.8626	0.0002	0.8553	0.0002	0.8641	0.0002	0.8572	0.0002	0.8518	0.0002

Test Information												
Date Tested:	3/17/07		3/17/07		3/17/07		3/17/07		3/17/07		3/17/07	
Nozzle:	2x 8005		2x 8005		2x 8005		2x 8005		2x 8005		2x 8005	
Nozzle Area [m2]	3.18E-06		3.18E-06		3.18E-06		3.18E-06		3.18E-06		3.18E-06	
Nozzle Pressure [psi][Pa]	24.0	165474.2	49.0	337843.1	85.0	586054.4	24.0	165474.2	49.0	337843.1	85.0	586054.4
Measurements	Value	Error	Value	Error	Value	Error	Value	Error	Value	Error	Value	Error
Barometric Pressure [pa]	100847.0	1.3	100847.0	1.3	100847.0	1.3	100847.0	1.3	100847.0	1.3	100847.0	1.3
Air Face Velocity [m/s]	0.95	0.11	0.94	0.11	0.94	0.11	0.95	0.11	0.94	0.11	0.94	0.11
Front Tdb [C]	32.91	0.05	32.99	0.05	32.98	0.05	32.95	0.05	32.92	0.05	33.00	0.05
Front Twb [C]	27.80	0.06	27.81	0.06	27.78	0.06	25.69	0.08	25.60	0.06	25.38	0.15
Wfront [g/kg]	21.75	0.10	21.74	0.10	21.68	0.09	17.96	0.11	17.82	0.09	17.42	0.20
Back Tdb [C] Zeroed	23.51	0.05	19.85	0.05	16.75	0.05	21.67	0.05	18.47	0.05	15.02	0.06
Back Twb [C] Zeroed	23.08	0.04	19.75	0.04	16.55	0.04	20.93	0.05	18.04	0.04	14.79	0.06
Wback [g/kg]	17.74	0.06	14.50	0.05	11.76	0.04	15.35	0.05	12.85	0.05	10.46	0.05
Water Flow Rate [kg/s]	0.050	0.000	0.071	0.000	0.092	0.000	0.050	0.000	0.071	0.000	0.092	0.000
Water Inlet [C]	4.97	0.06	5.08	0.05	5.08	0.05	5.03	0.05	5.00	0.05	4.98	0.05
Water Outlet [C]	8.40	0.05	8.68	0.05	8.68	0.05	8.26	0.05	8.21	0.05	8.06	0.06
Calculated Measurements	Value	Error	Value	Error	Value	Error	Value	Error	Value	Error	Value	Error
Air Mass Flow Rate [kg/s]	0.025	0.003	0.026	0.003	0.026	0.003	0.026	0.003	0.026	0.003	0.026	0.003
Air Side Heat Transfer [W]	509.2	56.9	819.9	92.6	1088.1	123.2	468.1	52.8	705.6	80.1	939.9	107.8
Air Side Sensible Heat Transfer [W]	250.0	29.2	350.7	40.6	438.5	50.4	299.0	34.8	383.4	44.2	483.9	58.2
Water Side Heat Transfer [W]	727.6	12.7	1070.7	15.8	1386.3	20.3	674.7	11.6	951.3	15.9	1190.7	20.5
% difference	-30.0		-23.4		-21.5		-30.6		-25.8		-21.1	
Sensible UA Value CF [W/C]	11.7	0.7	18.3	1.1	25.5	1.6	14.7	0.9	20.7	1.3	29.6	1.9
LTMD [C]	21.39	0.05	19.14	0.05	17.22	0.05	20.40	0.05	18.53	0.05	16.37	0.06
Epsilon	0.714		1.147		1.504		0.655		0.986		1.290	
Fp	0.316		0.513		0.674		0.340		0.515		0.685	
Epsilon (sensible)	0.350		0.491		0.606		0.418		0.536		0.664	
Enthalpy In [kJ/kg]	88.80	0.25	88.86	0.26	88.69	0.24	79.14	0.27	78.75	0.23	77.80	0.52
Enthalpy Out [kJ/kg]	68.78	0.15	56.74	0.14	46.61	0.12	60.79	0.15	51.15	0.13	41.56	0.14
Air Specific Volume [m3/kg]	0.8676	0.0002	0.8555	0.0002	0.8451	0.0002	0.8614	0.0002	0.8514	0.0002	0.8402	0.0002

8.7 MatLab Code

MCdrops.m (note that some figure outputs are not shown for sake of space)

```
function MCdrops(vo, theta, phi,d, U, Winfi, Tinfi, Td)

clear; clear global; format long; format compact
tic

global  g K rhow miua theta U vo k ka Cs
global  Tinfi hfg Pr cpw cpv cpa Cinfi brad cva cvv Rs rhoa

inc=1;
AirTemp=[27.6, 33.0];     %'Freestream temperature [C]'
AirVelocity=[1, 3]; %'Freestream velocity [m/s]'
WaterTemp=[5, 10];  %'Initial drop temperature [C]'
DropRadii=[237,345,430];
AirHumidity=[.00699, .01234, .01505]; %'Freestream humidity ratio [kgw/kga(dry)]'
WaterFlow=[3.00, 4.25, 5.50]; %Water flow rate [kg/min]
Lavg=.18395;                   %[m]
Axsect=.02322576;              %Test section cross sectional area [m^2]
OrifaceArea=[3.178e-6, 2.8514e-6, 4.47726e-6];
%%Initializing the free stream and drop conditions

for DR=3:-1:2
    for AH=1:3
       for WF=1:3


            wdot=WaterFlow(WF)
            miurdi=DropRadii(DR)
            Winfi=AirHumidity(AH)
            U=AirVelocity(1)
            Tdi=WaterTemp(2)
            Tinfi=AirTemp(1)

            %%Initializing constants and other metrics
            rhow=999.7;             %Density of water [kg/m^3]
            rhoa=1.23;              %Density of air [kg/m^3]

            Cinfi=Winfi*rhoa;       %Vapor concentration at inf.

            g=9.81;                 %Acceleration due to gravity [m/s^2]
            miua=184.6e-7;          %The viscosity of air
            ka=.0263;               %Conductivity of air [W/m K]
            gamma=1.4;              %Specific heat ratio
            cpv=1874;               %Specific heat of vapor [J/kg K] 1874
            cpw=4179;               %Specific heat of water [J/kg K]
            cpa=1008;               %Specific heat of air [J/kg K]
            cva=720;                %Specific heat of air [J/kg K]
            cvv=1338;               %Specific heat of vapor [J/kg K]
            Pr=.707;                %Prandlt number
            hfg=2438e3;             %Enthalpy of vaporization [J/kg]
            Rs=461.5;               %Gas constant for steam [J/kg K]
            ufg=2361300;           %Internal energy of vaporization [J/kg]

            tf=Lavg./((wdot/60)./(rhow.*OrifaceArea(DR))) %average flight time
            ND=round(((wdot/60).*tf/rhow)./((4/3)*pi.*(miurdi.*10^-6).^3))  %number of
drops in the simulation
            miuvo=(wdot/60)./(rhow.*OrifaceArea(DR))%drop mean initial velocity

            %%Figuring brad
            brad=((miurdi.*10^-6)^3*(1+(rhow*U*Axsect)/(wdot/60)))^(1/3)

            sprintf('Test (inc) %3.0f started', inc)

            %%Initializing the random variable matricies
            vo=zeros(1,ND);
            rdi=zeros(1,ND);
            zeta=zeros(1,ND);
```

```
theta=zeros(1,ND);
%%RV characteristics STDEV and Mean
sigmavo=.1;
%miuvo=miuvo;
sigmardi=10;
%miurdi=miurdi;
sigmazeta=25;
miuzeta=0;
sigmatheta=.15;
miutheta=-90;      %'Nozzle angle from x-axis [degrees]'

%%Building the RV matricies
for i=1:ND
    vo(i)=randn*sigmavo+miuvo;
    %'Velocity at nozzle exit [m/s]'
    rdi(i)=randn*sigmardi+miurdi;
    %'Droplet radius [micrometers]'
    zeta(i)=randn*sigmazeta+miuzeta;
    %'Spray launch Angle from normal-axis[degrees]'
    theta(i)=randn*sigmatheta+miutheta;
    %'Fanning angle from set launch angle [degrees]'
end

%%Units conversions
rdi=rdi.*10^-6;
Tinfi=Tinfi+273.15;
Tdi=Tdi+273.15;
theta=theta.*(pi/180);
zeta=zeta.*(pi/180);

options=odeset('RelTol', 1e-12);
TSPAN=[0:.0002:.02,.03:.01:.2]; %The flight timespan in question

%%Sending info to DE solver - This is the 3D version of the code
for j=1:ND
    X0=[0; vo(j)*cos(theta(j)); 0; vo(j)*sin(theta(j)); rdi(j);
        Tdi; Cinfi; Tinfi; 0; vo(j)*sin(zeta(j))];
    %Initial conditions
    [tfgd(:,j), xdatagd(:,:,j)]=ode45('MCdropeqns3d', TSPAN,
        X0, options);
end

%%Refining computational domain
xdatagdtrim=[];
for m=1:ND
    for i=1:length(TSPAN)
        if (xdatagd(i,3,m)>xdatagd(i,9,m)-0.21552)&&...
                (xdatagd(i,3,m)>-xdatagd(i,9,m)-0.21552)
            xdatagdtrim(i,:,m)=xdatagd(i,:,m);
        end
    end
end
%%Refining the trimmed matrix (making a temporary matrix)
%%for plotting purposes.
[Rw,Cm,Lr]=size(xdatagdtrim);

%%Energy calcualtions for the spray
drop_mass_sum=0;
q_spray_sens=0;
q_spray_sens2=0;
q_spray_latn=0;
q_spray_tot=0;
q_spray_tot2=0;
air_mass_sum=0;
humidity_ratio=Winfi;
qair_sens=0;
qair_tot=0;
qair_latn=0;
flight_time=zeros(1,ND);
final_drop_temp=zeros(1,ND);
final_air_temp=zeros(1,ND);
for m=1:ND
```

```
                xtemp=[];
                for i=1:Rw
                    if xdatagdtrim(i,5,m)~=0
                        xtemp(i,:,m)=xdatagdtrim(i,:,m);
                    end
                end
                [tempRw,tempCm,tempLr]=size(xtemp);

                deltadropvol=(4/3)*pi*(xtemp(tempRw,5,m)^3-xtemp(1,5,m)^3);
                drop_mass_sum=drop_mass_sum+deltadropvol*rhow;


               q_drop_sens=(4/3)*pi*rhow*(cpw*(xtemp(tempRw,6,m)*xtemp(tempRw,5,m)^3-
       ...
                    xtemp(1,6,m)*xtemp(1,5,m)^3)-...
                    (xtemp(tempRw,5,m)^3-xtemp(1,5,m)^3)*...
                    (3146253+(Rs-2822)*(xtemp(tempRw,6,m)-
xtemp(1,6,m))))/TSPAN(tempRw);

                q_spray_sens=q_spray_sens+q_drop_sens;

                q_drop_tot=(4/3)*pi*rhow*cpw*(xtemp(tempRw,6,m)*xtemp(tempRw,5,m).^3-
...
                    xtemp(1,6,m)*xtemp(1,5,m).^3)/TSPAN(tempRw);
                q_spray_tot=q_spray_tot+q_drop_tot;

                q_spray_latn=q_spray_latn+(q_drop_tot-q_drop_sens);

                deltaairmass=(4/3)*pi*((brad^3-xtemp(tempRw,5,m)^3)*xtemp(tempRw,7,m)-
...
                    (brad^3-xtemp(1,5,m)^3)*xtemp(1,7,m));
                air_mass_sum=air_mass_sum+deltaairmass;

                humidity_ratio=(humidity_ratio+(xtemp(tempRw,7,m)/rhoa))/2;

                flight_time(m)=TSPAN(tempRw);
                avg_flight_time=mean(flight_time);
                final_drop_temp(m)=xtemp(tempRw,6,m);
                final_air_temp(m)=xtemp(tempRw,8,m);



            end

            mdotequiv=(4/3)*pi*mean(rdi)^3*rhow*ND/TSPAN(tempRw);
            OutPut(1,1)=Tinfi;
            OutPut(1,2)=U;
            OutPut(1,3)=Tdi;
            OutPut(1,4)=miurdi;
            OutPut(1,5)=Winfi;
            OutPut(1,6)=wdot;
            OutPut(1,7)=brad;
            OutPut(1,8)=mdotequiv;
            OutPut(1,9)=drop_mass_sum;
            OutPut(1,10)=air_mass_sum;
            OutPut(1,11)=q_spray_sens;
            OutPut(1,12)=q_spray_tot;
            OutPut(1,13)=q_spray_latn;
            OutPut(1,14)=humidity_ratio;
            OutPut(1,15)=mean(final_drop_temp)-273.15;
            OutPut(1,16)=mean(final_air_temp)-273.15;
            OutPut(1,17)=avg_flight_time;
            OutPut(1,18)=ND;
            OutPut(1,19)=miuvo;
            OutPut(1,20)=inc;

            if inc<10
                filename=['testHMX00',num2str(inc),'.dat']
            elseif inc>=10 && inc<100
                filename=['testHMX0',num2str(inc),'.dat']
            else
                filename=['testHMX',num2str(inc),'.dat']
```

```
            end

            eval(['save ', filename, ' OutPut -ascii -double -tabs'])
            sprintf('Test (inc) %3.0f completed', inc)
            inc=inc+1;
        end
    end
end

toc
```

MCdropeqns3d.m (this is called by MCdrops.m and contains the differential equations defining the problem)

```
function datadot=MCdropeqns3d(t, x)

global g K rhow miua theta U vo k ka Cs Tinfi hfg Pr cpw cpv cpa Cinfi brad cva cvv Rs
rhoa rdinit

%xdatagd(:,1) is the drop x position
%xdatagd(:,2) is the drop x velocity
%xdatagd(:,3) is the drop y position
%xdatagd(:,4) is the drop y velocity
%xdatagd(:,5) is the drop radius
%xdatagd(:,6) is the drop temperature
%xdatagd(:,7) is the free stream vapor concentration
%xdatagd(:,8) is the free stream temeprature
%xdatagd(:,9) is the drop z position
%xdatagd(:,10)is the drop z velocity

Dv=2.495e-5.*(x(8)./292.88).^2.334; %Vapor Diffusivity [m^2/s]
Sc=miua./(rhoa*Dv);  %Schmidt Number
Re=rhoa.*sqrt((abs(x(10))).^2+(U-x(2)).^2+x(4).^2).*2.*x(5)/miua;
Sh=2+0.6*Re.^(1/2).*Sc.^(1/3);
cs=((.11708164-.014327228.*(x(6).^0.5)+.00043884997.*x(6))/...
    (1-.0951059.*(x(6).^0.5)+.0022436935.*x(6)))*rhoa;
Nu=2+0.6*Re.^(1/2).*Pr.^(1/3);
ufgTd=3146253-2822.*x(6);

xdot(1)=x(2);
xdot(2)=(3/(rhow*pi*4.*x(5).^3))*(rhoa*.5.*x(5).^2*pi*((24*miua./(...
    rhoa.*sqrt((abs(x(10))).^2+(abs(x(4))).^2+(abs(U-x(2))).^2).*...
    x(5)*2))*(1+(1/6).*(((rhoa/miua).*sqrt((abs(x(10))).^2+...
    (abs(x(4))).^2+(abs(U-x(2))).^2)*2.*x(5))^(2/3)))))).*...
    (U-x(2)).*abs(U-x(2));
xdot(3)=x(4);
xdot(4)=(3/(rhow*4*pi.*x(5).^3))*(-(rhoa*.5.*x(5).^2*pi*((24*miua./(...
    rhoa.*sqrt((abs(x(10))).^2+(abs(x(4))).^2+(abs(U-x(2))).^2).*...
    x(5)*2))*(1+(1/6).*((rhoa/miua).*sqrt((abs(x(10))).^2+...
    (abs(x(4))).^2+(abs(U-x(2))).^2)*2.*x(5))^(2/3))))).*...
    x(4).*abs(x(4)))-g;
xdot(5)=(-1/(2.*rhow.*x(5))).*...
    Dv.*Sh.*(cs-x(7));
xdot(6)=(3/(2*rhow*cpw.*(x(5).^2))).*...
    (ka.*Nu.*(x(8)-x(6))-...
    Dv.*Sh.*(cs-x(7)).*(ufgTd+Rs.*x(6)));
xdot(7)=(3.*x(5)./(2.*(brad^3-rdinit.^3))).*Dv.*Sh.*(cs-x(7));
xdot(8)=(3.*x(5)./(2.*(brad^3-rdinit.^3).*(rhoa*cva+x(7)*cvv))).*...
    (-ka.*Nu.*(x(8)-x(6))+...
    Dv.*Sh.*(cs-x(7)).*(cvv.*(x(6)-x(8))+Rs.*x(6)));
xdot(9)=x(10);
xdot(10)=(3/(rhow*pi*4.*x(5).^3))*(-(rhoa*.5.*x(5).^2*pi*((24*miua/(...
    rhoa.*sqrt((abs(x(10))).^2+(abs(x(4))).^2+(abs(U-x(2))).^2).*...
    x(5)*2))*(1+(1/6)*(((rhoa/miua).*sqrt((abs(x(10))).^2+...
```

```
    (abs(x(4))).^2+(abs(U-x(2))).^2)*2.*x(5))^(2/3))))).*...
    x(10).*abs(x(10)));

datadot=[xdot(1); xdot(2); xdot(3); xdot(4); xdot(5); xdot(6); xdot(7);
xdot(8);xdot(9);xdot(10)];
```

8.8 Model Calibration – Method of 'Effective b'

Before application, the model must be calibrated by adjusting the size of the air volume defined by the variable *b*. There are two basic methods explored for calibrating the model. The first method involves the use of experimental data to calculate an 'effective *b*,' i.e. the value of *b* is adjusted until the exiting air temperature and humidity ratio agrees with the experimental data. The second method, described earlier in the text, requires calculation of an air volume based on the simulation information including the spray volume and air volume to be treated, i.e. the volume of air being treated is divided equally amongst the drops in the simulation.

Exiting air temperature and vapor concentration for a simulation is known a priori via experimental testing. The method of effective *b* then uses this information by simply adjusting the sizes of the treated air volume until the simulation results match experimental results.

To explore this method, a series of simulations were run in which a single drop was tested in different size air volumes. The results of each test were logged and then plotted, as shown in Fig. H1. The first point to mention is that the temperature and moisture changes required slightly different *b* values. This is not surprising given some of the differences between the experiments and the simulation. Table H1 shows what averaged values of *b* were finally used for the investigation.

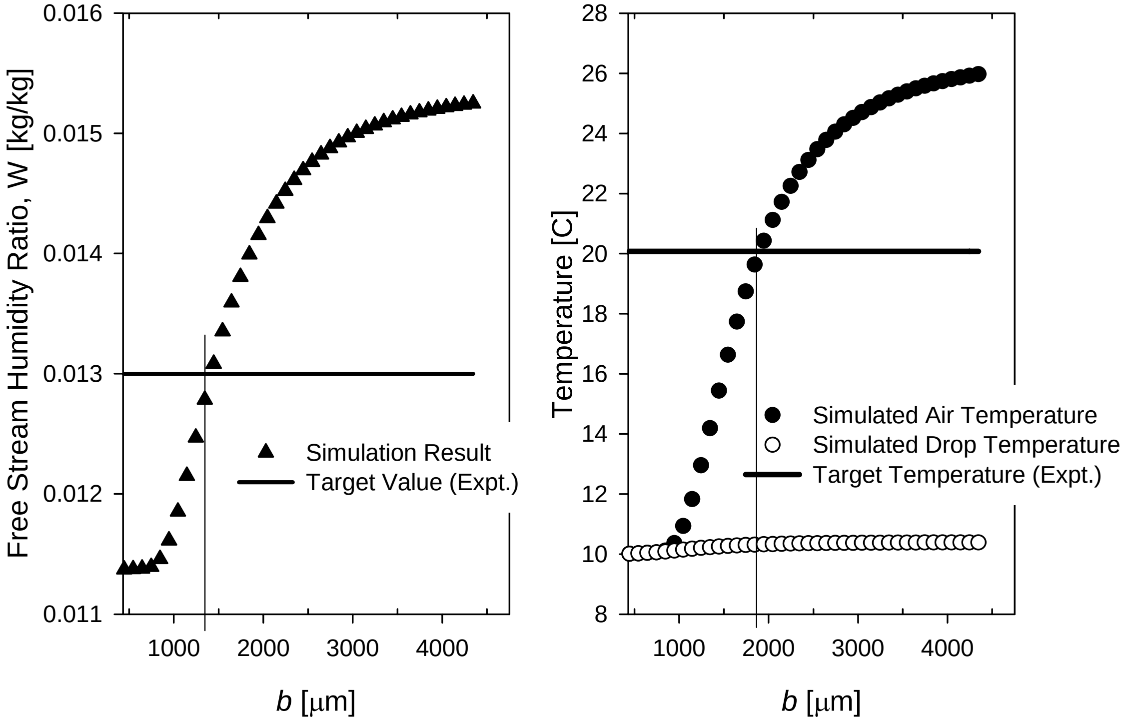

Figure H1 Variation of simulation results with *b*.

Table H1 Results of calibration showing how the optimum value of *b* was not the same for humidity and temperature. Also shown is the averaged value used in the computations.

Drop Size	Optimum *b*		Average Used
	Humidity	Temperature	
237.5	940	1300	1120
345	1600	1500	1550
430	1500	1950	1725

Note that these values of *b* produce an air volume that is nominally two times smaller than the volume of the area affected by the spray. Initially, this could be seen as capturing a ‘blow-by’ effect. However, what this really means is that the total exit air temperature is much higher (for this case of cooling). In other words, the small volume of air defined by *b* is at the proper exiting temperature, however, when that volume of air is mixed with the remaining untreated volume, the true exiting air temperature will be some kind of average of the exiting calibrated temperature, and what is effectively the inlet temperature (from the untreated air). Note that the same argument can be made for the moisture concentration.

The detailed experimental results are not presented as they essentially agree with what is shown in section 5.4.3, i.e. the heat transfer is virtually the same for both processes. However, because this method not only requires experimental results for calibration, but also requires extra post processing, it is not used in the simulations.